Colloidal Spheres under Shear:

The Interplay between Macroscopic Deformation and Microscopic Properties

Inaugural-Dissertation

zur Erlangung des Doktorgrades
der Mathematisch-Naturwissenschaftlichen Fakultät
der Heinrich-Heine-Universität Düsseldorf

vorgelegt von

Philipp Maßhoff
aus Essen

Düsseldorf, November 2019

aus dem Institut für experimentelle Physik der kondensierten Materie
der Heinrich-Heine-Universität Düsseldorf

Gedruckt mit der Genehmigung der
Mathematisch-Naturwissenschaftlichen Fakultät der
Heinrich-Heine-Universität Düsseldorf

Berichterstatter:

1. Prof. Dr. Stefan U. Egelhaaf

2. Prof. Dr. Thomas Voigtmann

Tag der mündlichen Prüfung: 28. Januar 2020

Eidesstattliche Versicherung

Ich versichere an Eides Statt, dass die Dissertation von mir selbständig und ohne unzulässige fremde Hilfe unter Beachtung der "Grundsätze zur Sicherung guter wissenschaftlicher Praxis an der Heinrich-Heine-Universität Düsseldorf" erstellt worden ist. Ich habe diese Dissertation keiner anderen Fakultät vorgelegt und außerdem bisher weder einen erfolgreichen noch einen erfolglosen Promotionsversuch unternommen. Im Fall von Zusammenarbeiten sind meine Beiträge umseitig aufgeführt.

Düsseldorf, 28. November 2019

Philipp Maßhoff

Experiments in **chapter 8** were conceived by S. U. Egelhaaf (supervisor) and M. A. Escobedo Sánchez. Samples were prepared by I. Elsner and the candidate. A. Pamvouxoglou designed the experimental setup (i.e., the shear cell) and provided a script to control it. The experimental protocol was developed by the candidate, in collaboration with A. P. and I. E. Presented results are based on measurements by the candidate. Data analysis and writing of the chapter was done by the candidate. Based on this chapter, a first manuscript has been written by the candidate, revised by S. U. E., and is intended for submission.

Experiments in **chapter 9** were initiated by S. U. E. The candidate prepared samples, designed the experimental protocol, performed measurements, analyzed the data, and wrote the chapter.

Experiments in **chapter 10** were conceived by S. U. E., A. P., and the candidate. A. P. and the candidate designed the experiments, prepared samples, and performed the measurements in equal parts. Data analysis and writing of the chapter has been done by the candidate. Results were interpreted by the candidate, A. P., and S. U. E. A first manuscript has been written by A. P., revised by S. U. E., and is intended for submission.

Chapter 11 contains three different experiments: **Section 11.1** has been done entirely by the candidate. The experiments in **section 11.2** were conceived by S. U. E. Samples have been prepared by the candidate. L. Gilson performed the experiments. Data analysis and writing have been done by the candidate. Experiments in **section 11.3** were initiated by J. Lauko. Samples were prepared by J. L. and the candidate. The design and execution of the measurements were done by the candidate, in collaboration with J. L. The candidate analyzed the data and wrote the chapter.

Summary

$\pi\acute{\alpha}\nu\tau\alpha\ \grave{\rho}\epsilon\tilde{\imath}$ (pantha rhei, Heraclitus 535 - 475 BC) – "everything flows"

So too do colloidal spheres. But how do they flow? This work investigates their behavior under shear intending to establish a link between the macroscopic (i.e., bulk) rheological response and the microscopic (i.e., single-particle level) structure and dynamics. Suspensions of colloidal spheres, that is, micrometer size particles dispersed in a liquid are a fascinating model system on their own, but can also mimic paints, pastes, or blood cells in our bodies.

In this work, I study single and multi-component systems of colloidal hard spheres. Shear, in the form of large-amplitude oscillatory shear (LAOS) experiments and start-up tests, is imposed by a rheometer or a shear cell. At the same time, thousands of small fluorescent spheres are imaged with high-resolution confocal microscopy. The particle motions are either analyzed with image velocimetry or tracked using customized computer algorithms.

Samples in the vicinity of the colloidal glass transition are known to yield at strain amplitudes of roughly 12%. This study confirms that their macroscopic elastic and viscous response is microscopically related to reversible and irreversible particle motions, respectively. Besides, it is found that some particles occasionally display different behavior than expected. For instance, transient nonlinear velocity profiles are observed during start-up shear at low shear rates. On a single-particle level, this is expressed in time-dependent dynamical quantities, such as local nonaffine motions and mean squared displacements. This work suggests that there is a link between the microscopic properties and the mesoscopic velocity profiles. Caution is required here since the phenomena are history-dependent, and not directly visible in the macroscopic rheological response. Another observation is that, given a sufficiently small polydispersity and a suitable external shear protocol, one can switch from amorphous to crystalline states of matter. For instance, binary mixtures can crystallize under oscillatory shear unless the size difference between particle species exceeds about 15%.

Altogether, the combination of confocal microscopy and rheology is found to be advantageous in revealing the links between microscopic and macroscopic properties. As implied in the very last section, the techniques and methods developed in this thesis can be readily applied to other soft systems.

Contents

Acronyms

AAm	acrylamide
AOD	acousto-optic deflector
bcc	body-centered cubic
C	crystal
CAD	computer-aided design
cis-decalin	*cis*-decahydronaphthalene
CHB	cycloheptyl or cyclohexyl bromide
CHB6	cyclohexyl bromide
CHB7	cycloheptyl bromide
CLSM	confocal laser scanning microscopy
CNT	classical nucleation theory
CMT	combined motor transducer
CST	continuous shear thickening
DFS	dynamic frequency sweep
DFT	discrete Fourier transform
DSS	dynamic strain sweep
DST	or discontinuous shear thickening
DWS	diffusing wave spectroscopy
F	fluid
G	glass
fcc	face-centered cubic
FOV	field of view
H_2O	water
HB	Herschel-Bulkley
HS	hard spheres
hcp	hexagonal close-packed
icos	icosahedron
LAOS	large amplitude oscillatory shear
LVE	linear viscoelasticity, linear viscoelastic
magn	magnification

MCT	mode-coupling theory
MSD	mean squared displacement
NBD	4-methylaminoethylmethacrylate-7-nitro-benzo-2-oxal,3-diazol
PHS	poly(12-hydroxy stearic acid)
PIC	polyisocyanopeptide
PMMA	poly(methyl methacrylate)
PMT	photomultiplier tube
PTFE	polytetrafluoroethylene
rhcp	random hexagonal close packing
S	solid
sc	single cubic
SD	standard deviation
SLS	static light scattering
SMT	separate motor transducer
tetralin	tetrahydronaphthalene
TCE	tetrachloroethylene
WD	working distance

Symbols

a	image
a'	edge length of an fcc unit cell
a''	edge length of a bcc unit cell
a_i, a_j	images i and j
a_{backg}	image background
a_{proc}	processed image
a_{raw}	raw image
A	area
$\mathcal{A}$	Fourier transform of a
$\boldsymbol{A}$	affine transformation
b	image
$\mathcal{B}$	Fourier transform of b
c	concentration
c_n, c'_m	coefficients
cc_{ij}	elements of $\boldsymbol{cc}$
$\boldsymbol{cc}$	cross-correlation matrix
d	diameter
dx	scalar displacement in the x-direction
$d\boldsymbol{x}$	displacement vector in the x-direction
d_{xy}	lateral resolution
dy	scalar displacement in the y-direction
$d\boldsymbol{y}$	displacement vector in the y-direction
d_z	axial resolution
D	diffusion coefficient
D_l	long-time diffusion coefficient
D_s	short-time diffusion coefficient
D^2_{min}	a measure for the nonaffine motion
e	elementary charge
$e(\ldots)$	residual
E	internal energy

$Err(f^{\mathrm{conf}})$	relative error of f^{conf}
$Err(\Delta x_0^{\mathrm{conf}})$	relative error of $\Delta x_0^{\mathrm{conf}}$
f	frequency
f_{xy}	frame rate for 2D images
f^{conf}	frequency measured with CLSM
$f(\theta')$	function within CNT
F	force
F_g	gravitational force
F_{H}	Helmholtz free energy
F_γ	strain constant
F_σ	stress constant
$\boldsymbol{F}$	material deformation gradient tensor
$\mathcal{F}$	Fourier transform
$\mathcal{F}^{-1}$	inverse Fourier transform
g	acceleration of gravity
$g(r)$	radial distribution function
$g^2(\tau)$	correlation function (DLS)
G	rigidity modulus
G'	elastic modulus
G''	viscous modulus
G'_L	large-strain modulus
G'_M	minimum-strain modulus
$\lvert G^* \rvert$	complex shear modulus
ΔG	energy barrier
ΔG_{het}	energy barrier for heterogeneous nucleation
ΔG_{hom}	energy barrier for homogeneous nucleation
h	height, gap height
h_z	vertical distance covered by a 3D image stack
H	Hamaker constant
i	integer
I	(total) instrument inertia
I_{drive}	drive inertia
I_{tool}	tool inertia
$\boldsymbol{J}$	material displacement gradient tensor

k	integer
k_p	fitting parameter
k_B	Boltzmann constant
l	integer
l_B	Bjerrum length
l_DH	Debye screening length
m	integer number
M	torque
M_min	minimum torque
n	integer number
n'	flow index in the HB law
n_r	refractive index
n_s	number of images (slices) in a z-stack
N	integer number
N_b	number of neighbors
N_c	contact number
N_e, N_f, N_v	number of edges, faces, vertices
NA	numerical aperture
o_0	fitting parameter
p	fitting parameter in the Krieger-Dougherty model
P, P'	points
$P(\ldots)$	probability for ...
Pe	Péclet number (steady shear)
Pe_ω	Péclet number (oscillatory shear)
$\boldsymbol{cp}$	phase correlation matrix
PCC	Pearson correlation coefficient
Q, Q'	points
$\boldsymbol{Q}$	transformation matrix for a pure rotation
q_l	(local) bond order parameter (e.g., q_4, q_6)
$\overline{q}_l$	averaged (local) bond order parameter
$\langle \overline{q}_l \rangle$	global bond order parameter
r	distance, radial distance
r_1, r_2, r_3	specific positions in $g(r)$
r_cutoff	cutoff-radius

$\boldsymbol{r}_0$	position vector of the reference particle
$\boldsymbol{r}_n$	position vector of particle n
R	radius
R_b	radius of big species
R_s	radius of the small species
R_n	radius of a nucleus
R_{CNT}	nucleation rate (within CNT)
$\widetilde{R}$	parameter for secondary flows
$\mathbb{R}^n$	n-dimensional space
S	entropy
$\widetilde{S}$	strain-stiffening ratio
$\boldsymbol{S}$	transformation matrix for simple shear
t	time
t_p	time of one period
$\delta t, \Delta t$	time interval
Δt_{2D}	time interval to capture one 2D image
Δt_{3D}	time interval to capture one 3D image stack
T	temperature
$\widetilde{T}$	shear-thickening ratio
u	fitting parameter
U	potential
U_0	maximum value of U_{edl}
U_{edl}	electrostatic double layer potential
U_{vdw}	van der Waals potential
$\boldsymbol{U}$	transformation matrix for pure stretching ($\neq \boldsymbol{V}$)
v	velocity
v_s	sedimentation velocity
v_{s0}	terminal sedimentation velocity
v_x	velocity in the x-direction
v_{norm}	normalized velocity
v_{wall}	velocity of the moving wall
V	volume
V_b	volume occupied by big spheres
V_s	volume occupied by small spheres

V_{spheres}	volume occupied by (colloidal) spheres
V_{total}	total volume
$\boldsymbol{V}$	transformation matrix for pure stretching ($\neq \boldsymbol{U}$)
w_l	(local) third-order bond order parameter
$\overline{w}_l$	averaged (local) third-order bond order parameter
W_L	lost work per cycle
x	spatial coordinate
X	relative volume fraction of the big spheres
$\boldsymbol{X}$	matrix needed for D^2_{min}
Δx	displacement in the x-direction
Δx^{conf}	displacement measured with CLSM
Δx_0	expected displacement amplitude
Δx_0^{conf}	fitted displacement amplitude
y	spatial coordinate
$\langle \Delta x^2 \rangle$	MSD in the x-direction
$\langle \Delta y^2 \rangle$	MSD in the y-direction
$\boldsymbol{Y}$	matrix needed for D^2_{min}
z	spatial coordinate
z_{step}	vertical distance between images in a z-stack

α	size ratio
β	cone angle
β_{max}	maximum cone angle
γ	strain
γ_0	strain amplitude
γ_0^{true}	strain amplitude with slip correction from CLSM
γ_c	characteristic shear strain
γ_c^{conf}	critical shear strain determined with CLSM
γ_c^{free}	critical shear strain according to the free volume
γ_c^{p1}	characteristic shear strain
γ_{lc}	tension of crystal-liquid interface
γ_{dist}	apparent shear strain
γ_{norm}	normalized strain
$\gamma_{\text{threshold}}$	threshold strain

$\dot{\gamma}$	strain rate
$\dot{\gamma}^*$	critical shear rate (shear banding)
$\dot{\gamma}_0$	strain rate amplitude
$\dot{\gamma}_{\text{appl.}}$	applied shear rate
$\dot{\gamma}_{\text{local}}$	local shear rate
$\dot{\gamma}_{\text{norm}}$	normalized shear rate
δ	polydispersity
δ_i	displacement of a particle
δ_t	terminal polydispersity
ϵ_0	vacuum permittivity
ϵ_r	relative dielectric constant
ϵ_{zz}	unit elongation in the z-direction
$\boldsymbol{\epsilon}$	infinitesimal strain tensor
ζ	parameter for a distance to the yield stress
η	(shear) viscosity
η_0	viscosity of the dispersion medium
η_p	plastic viscosity
η_r	relative viscosity
$\eta_L^{'}$	large-rate dynamic viscosity
$\eta_M^{'}$	minimum-rate dynamic viscosity
$[\eta]$	fitting parameter in Krieger-Dougherty model
θ	angle
θ_0	angle related to γ_0
θ_0^{true}	angle related to γ_0^{true}
$\theta^{'}$	contact angle
ϑ	phase (angle) shift / mechanical loss angle
Θ	motor angular displacement
$\dot{\Theta}$	angular velocity
κ	consistency index in the HB law
λ	wavelength
λ_i	wavelength of the light illuminating the sample
λ_f	wavelength of the fluorescent light
$\Delta\mu$	difference in chemical potential
ν	kinematic viscosity

ξ	friction coefficient
ρ	density
ρ_n	density of bulk phase
$\Delta\rho$	density difference
σ	shear stress
σ^*	onset stress (shear thickening)
σ_0	shear stress amplitude
σ_c	critical stress
σ_n	nth stress harmonic
σ_s	steady state stress
σ_y	yield stress
σ_{ij}	elements of the stress tensor
$\sigma_{\min}$	minimum stress
σ_{norm}	normalized stress
$\boldsymbol{\sigma}$	stress tensor
τ	lag time
τ^*	a diffusion time scale
τ_w	waiting time
τ_{ij}	off-diagonal elements of the stress tensor (engineering notation)
τ_{B}	characteristic time of Brownian motion
τ_M	parameter in the Maxwell model
τ_α	α-relaxation time
τ_β	β-relaxation time
υ	flow index in the HB law
ϕ	volume fraction
ϕ_g	glass transition
ϕ_m	volume fraction after sedimentation
ϕ_p	fitting parameter
ϕ_J	maximum jamming sphere packing
ϕ_{fp}	freezing point
ϕ_{mp}	melting point
$\phi_{\max}$	maximum volume fraction
ψ	fitting parameter
ω	angular frequency

Part I

Fundamentals

1

Rheology: Get the Juices Flowing

Rheology is used to measure, model, and predict material properties of deformable and flowing systems. It answers the question: "What happens when I poke it?[1, p.207]" The term "rheology" was coined in the 1920s and is said to be invented by Professor Bingham of Lafayette College [2]. It can be derived from the Greek word $\rho\acute{\epsilon}\omega\lambda o\gamma\acute{\iota}\alpha$, where $\rho\acute{\epsilon}\omega$ means "flow" and $-\lambda o\gamma\acute{\iota}\alpha$ "the study of."

We will start with a generic description of the concepts of stress, strain, and simple shear in section 1.1. Afterward, we will introduce models that describe linear (section 1.2) and nonlinear (section 1.3) relations between stress and strain. Special emphasis is put on oscillatory shear (section 1.4), as well as the instrumental constraints that experimentalists have to bear in mind (section 1.5).

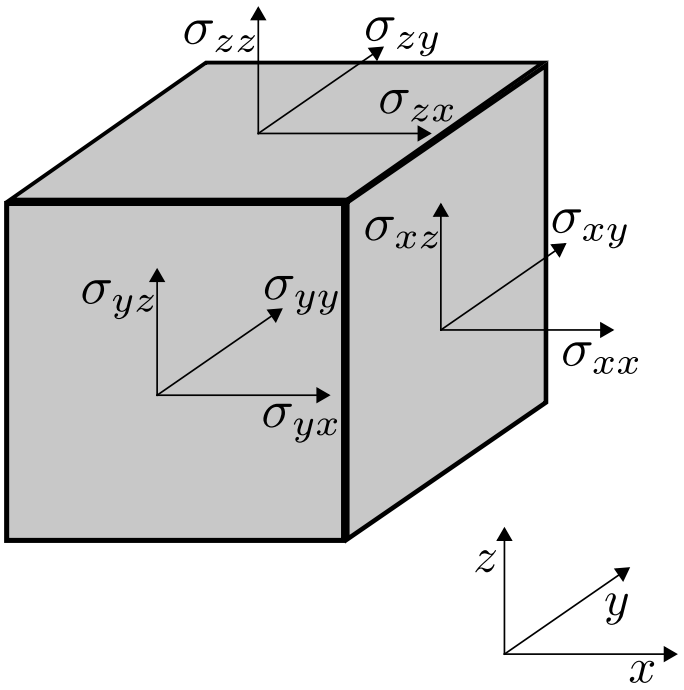

Fig. 1.1 Illustration of stress elements σ_{ij} acting on an infinitesimal cubic element. Stresses σ_{ij} act on the surface i in the direction j.

1.1 Basic Concepts

1.1.1 Stress Tensor

Considering the deformation of a small cubic element, as illustrated in figure 1.1, is a typical introduction to rheology. In order to "poke" the cube, external forces have to act on the surfaces of this element. The force per area is called stress.

In the general case, the stress is a 3×3 tensor

$$\boldsymbol{\sigma} = \underbrace{\begin{pmatrix} \sigma_{xx} & \sigma_{xy} & \sigma_{xz} \\ \sigma_{yx} & \sigma_{yy} & \sigma_{yz} \\ \sigma_{zx} & \sigma_{zy} & \sigma_{zz} \end{pmatrix}}_{\text{scientific}} = \underbrace{\begin{pmatrix} \sigma_{x} & \tau_{xy} & \tau_{xz} \\ \tau_{yx} & \sigma_{y} & \tau_{yz} \\ \tau_{zx} & \tau_{zy} & \sigma_{z} \end{pmatrix}}_{\text{engineering}} \tag{1.1}$$

with elements σ_{ij}. Here, i indicates the orientation of the surface, and j refers to the direction of the stress. This convention is regularly used (e.g., [2–6]), but one should be cautious as, for example, in "Colloidal suspension rheology" by Mewis and Wagner [7], the reverse notation is used. The number of independent elements in equation (1.1) can be reduced from 9 to 6 using the relation $\sigma_{ij} = \sigma_{ji}$, which is equivalent to the statement that no angular momentum is present inside the cube. The elements σ_{ii} are called *normal stresses* and the remaining ones *shear stresses*.

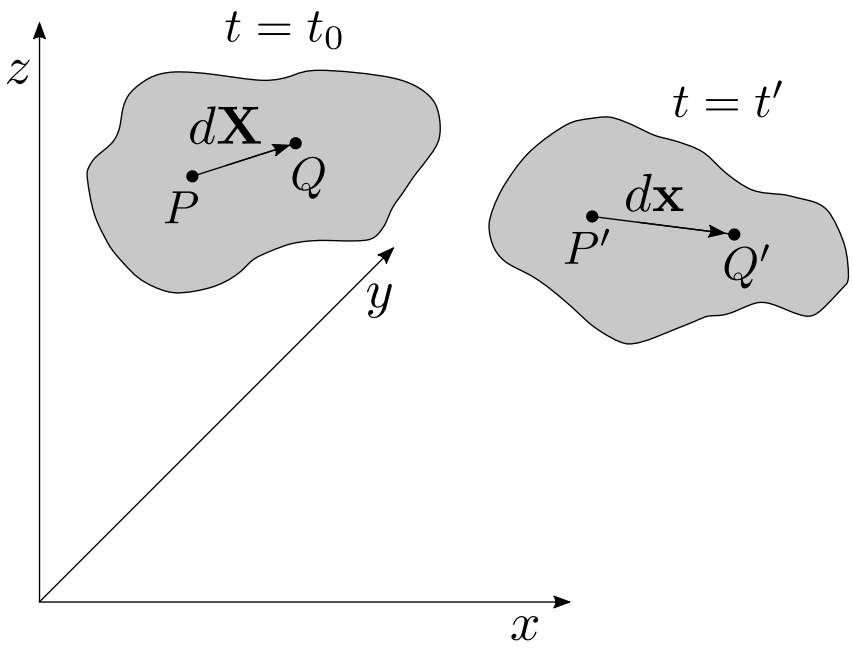

Fig. 1.2 Schematic deformation of a material element (gray cloud). At time $t = t_0$, two points P and Q of the material element are separated by the vector $d\boldsymbol{X}$. At a later time $t = t'$, the two points P and Q have changed their absolute positions to P' and Q' and are connected by the vector $d\boldsymbol{x}$.

1.1.2 Strain Tensor

How can one describe a deformation that is caused by the stress $\boldsymbol{\sigma}$? As with the stress tensor, different authors use different notations. This section will follow the notation and definitions from reference [6].

A small piece of material could be deformed in a way, as depicted in figure 1.2. Let there be two points P and Q inside the small element at time t_0. The points P and Q live in a three-dimensional space and can be defined by their coordinates in x-, y- and z-direction. For the description to follow, only their relative positions are important. Thus, let the vector that starts at P and ends at Q be denoted by $d\boldsymbol{X} = (dX_x, dX_y, dX_z)$. At a later time t', the two points are now at P' and Q' instead of P and Q, and the vector connecting both points is now $d\boldsymbol{x} = (dx_x, dx_y, dx_z)$.

The fundamental equation of deformation that relates $d\boldsymbol{X}$ and $d\boldsymbol{x}$ is

$$d\boldsymbol{x} = \boldsymbol{F} \cdot d\boldsymbol{X} \,, \tag{1.2}$$

where $\boldsymbol{F}$ is the *material deformation gradient tensor*. Typically, $\boldsymbol{F}$ is assumed to be given. If $d\boldsymbol{X}$ and $\boldsymbol{F}$ are known, then $d\boldsymbol{x}$ can be calculated for any time according to equation (1.2). In experiments with particle tracking (cf., section 3.4 and chapter 6), rather the particle positions at different times (and thus $d\boldsymbol{x}$ and $d\boldsymbol{X}$) are known. Finding an affine transformation $\boldsymbol{F}$ for a given set of vectors $d\boldsymbol{x}$ and $d\boldsymbol{X}$ (in $\mathbb{R}^n$)

can be solved by a least-squares minimization [8, 9]

$$e(\boldsymbol{F}) = \sum_{i=1}^{n} \|dx_i - F dX_i\|^2 \,, \tag{1.3}$$

where $\|\ldots\|$ is the Euclidean distance. Given $\boldsymbol{F}$, the *material displacement gradient tensor*

$$\boldsymbol{J} = \boldsymbol{F} - \mathbb{1} \tag{1.4}$$

is calculated by subtracting the identity matrix $\mathbb{1}$. Then, the *infinitesimal strain tensor* reads

$$\boldsymbol{\epsilon} = \frac{1}{2}\left(\boldsymbol{J} + \boldsymbol{J}^\top\right) \tag{1.5}$$

with its components

$$\boldsymbol{\epsilon} = \underbrace{\begin{pmatrix} \epsilon_{xx} & \epsilon_{xy} & \epsilon_{xz} \\ \epsilon_{yx} & \epsilon_{yy} & \epsilon_{yz} \\ \epsilon_{zx} & \epsilon_{zy} & \epsilon_{zz} \end{pmatrix}}_{\text{scientific}} = \underbrace{\begin{pmatrix} \epsilon_x & \gamma_{xy}/2 & \gamma_{xz}/2 \\ \gamma_{yx}/2 & \epsilon_y & \gamma_{yz}/2 \\ \gamma_{zx}/2 & \gamma_{zy}/2 & \epsilon_z \end{pmatrix}}_{\text{engineering}}, \tag{1.6}$$

written in both the scientific and engineering notation [6]. Here, $\boldsymbol{J}^\top$ is the transpose. The entries in the main diagonal of $\boldsymbol{\epsilon}$ are unit elongations, and the off-diagonal entries contain information about the decrements of angles in the ij-planes. Furthermore, $\epsilon_{ij} = \epsilon_{ji}$ (and $\gamma_{ij} = \gamma_{ji}$). The interpretation of the off-diagonal entries will become clearer in the next section using a specific example.

1.1.3 Simple Shear

From now on we will focus on the zx-component of the shear stress and shear strain and use the shorthand notations [1]

$$\sigma \equiv \sigma_{zx} \tag{1.7}$$

and

$$\gamma \equiv \gamma_{zx} \,. \tag{1.8}$$

Let us consider again a cube. Now let there be a force F acting on the top surface A in the x-direction, as illustrated in figure 1.3. Hence, we will have a non-zero shear stress

$$\sigma = \frac{F}{A} \,. \tag{1.9}$$

[1] This shorthand notation is strictly speaking a mixture between the scientific (σ_{zx}) and engineering (γ_{zx}) notation, but this combination is frequently used.

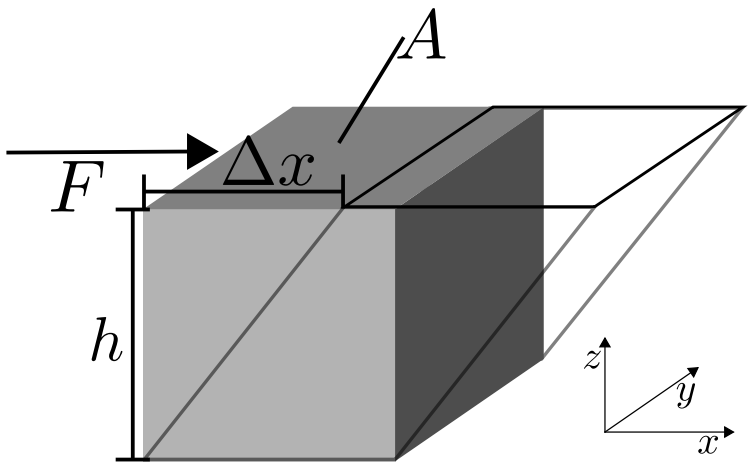

Fig. 1.3 Illustration of simple shear. The force F acts on the top surface with area A. As a consequence, the top part of the cube is displaced by Δx.

The affine deformation of this cube is measured by the shear strain

$$\gamma = \frac{\Delta x}{h} \,. \tag{1.10}$$

where Δx is the displacement in the x-direction and h the height of the cube. The scenario from figure 1.3 is called *simple shear*, but it is not that simple after all since it can be decomposed into a combination of a pure rotation and pure strain as shown in figure 1.4.

This can also be described analytically involving full tensor analysis. The tensor $\boldsymbol{S}$, which describes simple shear, can be decomposed into a rotation ($\boldsymbol{Q}$) plus stretching ($\boldsymbol{U}$ and $\boldsymbol{V}$). Both decompositions ($\boldsymbol{S} = \boldsymbol{QU}$ and $\boldsymbol{S} = \boldsymbol{VQ}$) are visualized in figure 1.5. As can be seen in figure 1.5, the angle θ between the x-axis and the extension axis is, in fact, close to but not identical to 45° and becomes smaller for larger strains.

1.2 Linear Viscoelasticity

Having introduced the shear stress σ and shear strain γ now raises the question of whether and what exactly is their relation. Within *linear viscoelasticity* (LVE), stress and strain are connected via linear differential equations, where the general differential equation has the form

$$\left(1 + c_1 \frac{\partial}{\partial t} + \ldots + c_n \frac{\partial^n}{\partial t^n}\right) \sigma = \left(c'_0 + c'_1 \frac{\partial}{\partial t} + \ldots + c'_m \frac{\partial^m}{\partial t^m}\right) \gamma \tag{1.11}$$

with coefficients c_n and c'_m and $n \leq m$. The symbols $\frac{\partial^n}{\partial t^n}$ denote the nth partial derivative with respect to time.

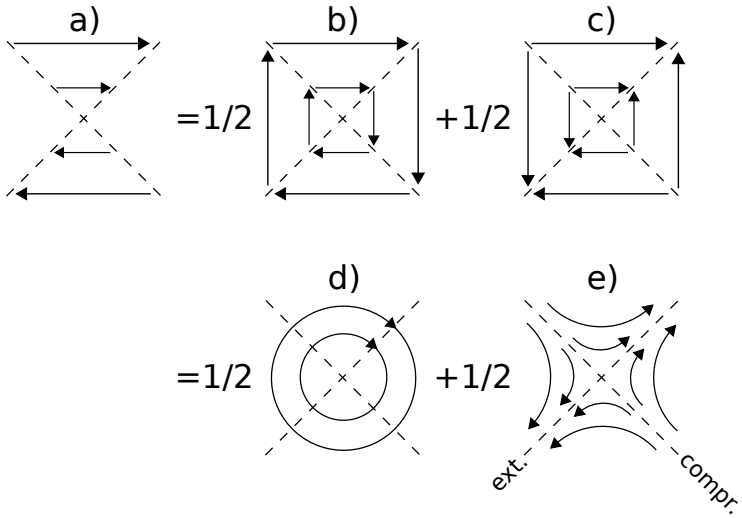

Fig. 1.4 Simple shear (a) can be decomposed into a linear combination of a pure rotation (d) and pure strain (e) as can be seen either directly or with the help of an intermediate step involving (b) and (c). Redrawn with permission of J. Bergenholtz [10].

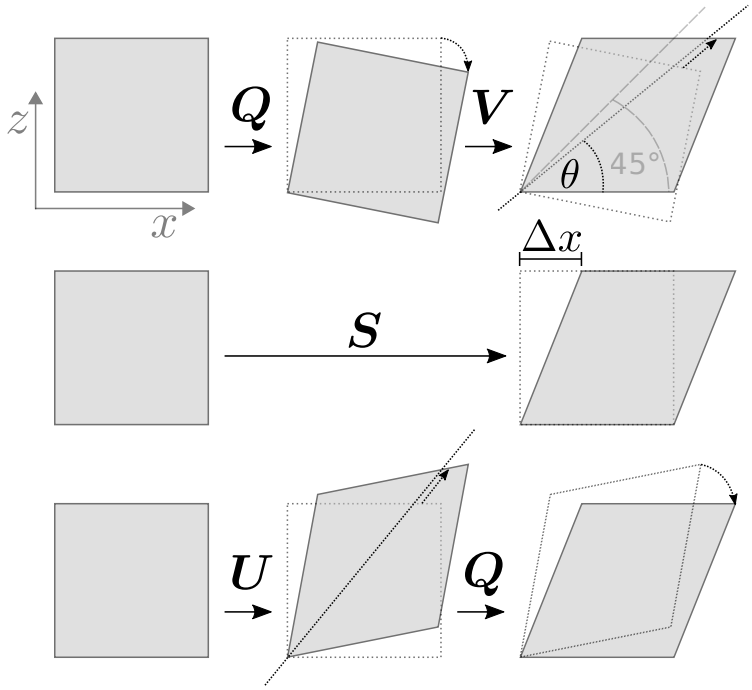

Fig. 1.5 Decomposition of simple shear $\boldsymbol{S}$ (middle) into a combination of rotation $\boldsymbol{Q}$ and pure stretching $\boldsymbol{V}$ (top), and into a combination of pure stretching $\boldsymbol{U}$ and rotation $\boldsymbol{Q}$ (bottom). The angle θ between the extension axis and the x-axis slightly deviates from 45°.

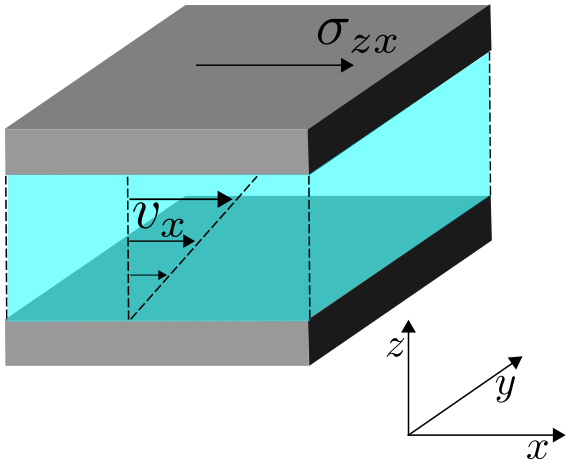

Fig. 1.6 Illustration of simple shear flow of a Newtonian fluid. When a stress σ_{zx} is applied, the velocity v_x inside the Newtonian fluid increases linearly with height z.

1.2.1 Common Models

A general equation like equation (1.11) might be difficult to solve and to use in everyday life. And since rheology is applied to materials like mayonnaise, plastics, paints, and oils, it is tempting to use rather simplified models. The simplest model is probably *Hooks law*. Hooks law is obtained, if the coefficient $c_0^{'}$ from equation (1.11) is the only non-zero coefficient. Setting $c'_0 \equiv G$ we get

$$\sigma = G\gamma\,, \tag{1.12}$$

where we introduced the rigidity modulus G. The rigidity modulus is measured in units of Pascal (Pa) and typical values range from 5 Pa for salad dressing to 80 GPa for steel [11]. The corresponding picture for Hooks law is the one from figure 1.3. Hooks law is the equation for an *ideal solid*, whose stress is proportional to the applied strain. However, this simplified model is not valid for all solid materials.

Similar to ideal solids, there is a model describing an idealized fluid. If $c'_1 \equiv \eta$ is the only non-zero coefficient, we get

$$\sigma = \eta\dot{\gamma} \tag{1.13}$$

with the shear viscosity η. The shear rate

$$\dot{\gamma} = \frac{\partial\gamma}{\partial t} = \frac{v_x}{z} \tag{1.14}$$

is constant across the gap as illustrated in figure 1.6. A material following this model is called *Newtonian fluid*. The shear viscosity is measured in units of Pa s (pascal-second) and typical values are $\eta = 10\,\mathrm{Pa\,s}$ for liquid honey and $\eta = 1\,\mathrm{mPa\,s}$

for water at room temperature. Here it is worth noting that equation (1.13) is used as the definition of the shear viscosity

$$\eta = \frac{\sigma}{\dot{\gamma}}\,, \tag{1.15}$$

that is, the shear viscosity is the shear stress divided by the shear rate (and not $\partial\sigma/\partial\dot{\gamma}$). The shear viscosity η, often just called viscosity, is not necessarily a material constant but depends, for example, on temperature. It will be seen in the following that the viscosity will also be, amongst others, a function of the strain, shear rate or stress.

Another model is the so-called *Maxwell model*. The non-zero parameters are now $c_1 \equiv \tau_M$ and $c'_1 \equiv \eta$, hence the equation for the Maxwell model reads

$$\sigma + \tau_M \dot{\sigma} = \eta\dot{\gamma}\,, \tag{1.16}$$

where η is again denoted viscosity. Essentially, the coefficient $c'_1 \equiv \eta$ is only equivalent to the shear viscosity as introduced in equation (1.15) once the shear stress reached a steady-state value ($\dot{\sigma} = 0$), which is the case for longer times. The equation $\sigma = \eta\dot{\gamma}[1 - \exp(-t/\tau_M)]$ is a solution for $\sigma(t = 0) = 0$. The parameter τ_M has the dimension of time and hence can be referred to as a characteristic time. For times $t >> \tau_M$ the Maxwell model describes a Newtonian fluid. Although just a special case, the Maxwell model is often used to describe colloidal suspension rheology [7, p.12].

1.3 Nonlinear Viscoelasticity

Fortunately, many real materials can be modeled under certain circumstances (e.g., within a specific range of γ, $\dot{\gamma}$ or σ) using the models of linear viscoelasticity. Unfortunately, most materials will also show nonlinear responses. Be aware that this section will still not cover all possible material responses but it will go one step further towards the description of more complex materials.

A typical approach is to start with one of the linear models and to add a nonlinear term. The description of the Newtonian fluid (equation (1.13)) can be easily extended to a group of *generalized Newtonian fluids*. One model out of the generalized Newtonian fluids is the *Bingham model*

$$\sigma = \sigma_y + \eta_p\dot{\gamma}\,, \tag{1.17}$$

where the constant σ_y was added. Here η_p is called plastic viscosity in order to avoid confusion with the shear viscosity (cf., equation (1.15)). As long as $\sigma < \sigma_y$, there is no flow ($\dot{\gamma} = 0$). Only, if $\sigma > \sigma_y$, flow sets in, and the material yields. Therefore, σ_y is called *yield stress*.

Another regularly used model out of the generalized Newtonian fluids is the Herschel-Bulkley law

$$\sigma = \sigma_y + \kappa\dot{\gamma}^{\upsilon} \tag{1.18}$$

with the consistency index κ and the flow index υ. It is $\upsilon < 1$ for shear thinning and $\upsilon > 1$ for shear thickening behavior [11]. For colloidal suspensions, a typical value is $\upsilon = 0.47 - 0.59$ [12]. Shear thinning and thickening will be treated separately in section 2.5.4.1.

1.4 Oscillatory Shear

Oscillatory measurements are a powerful technique within rheology. Either an oscillating strain or stress is applied. Then, the response to the strain (stress) is recorded and can be used to distinguish between elastic, viscous and viscoelastic behavior. Using different angular frequencies $\omega = 2\pi f$, with period time $t_p = 1/f$, oscillatory shear offers the ability to probe the response at different time scales. Many rheological instruments use rotating measurement systems and typical configurations are for instance a cone-plate or a Couette system.

1.4.1 Linear Oscillatory Shear

The basic idea of oscillatory shear is to apply an oscillating deformation $\gamma(t)$ of the form

$$\gamma(t) = \gamma_0 \sin(\omega t) \tag{1.19}$$

with the strain amplitude γ_0 and the angular frequency ω. Here, the sine is used without loss of generality. The same could also be expressed with a cosine or as a complex quantity. Taking the time derivative of equation (1.19) we get

$$\dot{\gamma}(t) = \dot{\gamma}_0 \cos(\omega t)\,, \tag{1.20}$$

where we identified $\dot{\gamma}_0 = \gamma_0\omega$. Within the linear regime, the stress response is of the form

$$\sigma(t) = \sigma_0 \sin(\omega t + \vartheta) \tag{1.21}$$

with the phase angle shift ϑ (also called mechanical loss angle [13]). A phase shift angle $\vartheta = 0°$ corresponds to a perfectly elastic solid and $\vartheta = 90°$ to a perfectly viscous liquid. A sample with a phase shift $0° < \vartheta < 90°$ is a viscoelastic sample.

In analogy to Hooks law (cf., equation (1.12)), a *complex shear modulus* $|G^*|$ is defined by

$$|G^*| = \frac{\sigma_0}{\gamma_0}\,, \tag{1.22}$$

where σ_0 and γ_0 are the maximum stress and strain, respectively [14]. The modulus might also be denoted as *dynamic modulus* [13]. It is common to separate $|G^*|$ into a storage modulus (also called elastic modulus)

$$G' = \frac{\sigma_0}{\gamma_0}\cos(\vartheta) \tag{1.23}$$

and loss modulus (also called viscous modulus)

$$G'' = \frac{\sigma_0}{\gamma_0}\sin(\vartheta)\,. \tag{1.24}$$

The two moduli G', G'' and the phase angle shift ϑ or loss factor $\tan(\vartheta)$ are related via $\tan(\vartheta) = G''/G'$. The mechanical dissipation (lost work per cycle) is given by the circular integral of the stress with respect to strain

$$W_L = \oint \sigma d\gamma \tag{1.25}$$

and corresponds to the area of the ellipse in a stress-versus-strain plot.

1.4.1.1 Lissajous-Bowditch Curves

Often just called Lissajous curves, Lissajous-Bowditch curves are a classic way of visualizing and analyzing oscillatory shear measurements. They should better be called Lissajous-Bowditch curves since these kinds of diagrams have already been used by Bowditch in 1815 to study orbital trajectories [15]. Within oscillatory rheology, two typical ways of using them exist: The most common way is to plot, for a given strain amplitude γ_0, the stress $\sigma(t)$ as a function of the strain $\gamma(t)$. This will, for a linear response, result in an ellipse. The enclosed surface of the $\sigma(\gamma)$-ellipse corresponds to the dissipated energy per cycle as already stated above. For a pure elastic behavior, the Lissajous-Bowditch curve is a line (cf., Hooks law) and for pure viscous behavior, it is a circle (maximum energy dissipation) in the $\sigma(\gamma)$-plot. From Lissajous-Bowditch curves, the phase angle shift ϑ can be obtained using $\vartheta = \arcsin(\frac{\gamma|_{\sigma=0}}{\gamma_0})$, where $\gamma|_{\sigma=0}$ is the strain at zero stress and γ_0 is the strain amplitude [16]. Additionally, $\sigma(\dot{\gamma})$-curves (stress vs. shear rate) can be used, where pure viscous behavior is represented by a straight line through the origin.

1.4.2 Nonlinear Oscillatory shear

Within linear oscillatory shear, the stress as a function of time is well described by a sine (with the same frequency as the input signal) and a phase shift. But materials also show nonlinear responses. One example is the Xanthan Gum (XG) solution from reference [17] whose stress response $\sigma(t)$ clearly deviates from a linear response for large strain amplitudes γ_0. The deviation from pure sinusoidal stress/strain is

what distinguishes the nonlinear oscillatory shear from the linear oscillatory shear. Corresponding Lissajous-Bowditch figures will deviate from elliptical shapes and may become, for instance, rectangular or exhibit humps.

Several ways exist to describe, analyze and interpret the nonlinear response to large amplitude oscillatory shear (LAOS) [16, 18]: From a mathematical point of view, the nonlinear response can be described by a series of sines and cosines, similar to a Fourier series. Wilhelm and co-workers started using Fourier rheology in order to classify the nonlinear response with higher harmonics [19–21]. This is a widespread method and used frequently in rheology, but it originates from a purely mathematical approach. To this end, several notations exist, for example,

$$\sigma(t) = \sum_{n=1,\text{odd}} \sigma_n(\omega, \gamma_0) \sin(n\omega t + \vartheta_n(\omega, \gamma_0)) \,, \tag{1.26}$$

which is referred to as Fourier series [13] and another notation is

$$\sigma(t) = \gamma_0 \sum_{n=1,\text{odd}} \left[G_n^{'}(\omega, \gamma_0) \sin(n\omega t) + G_n^{''}(\omega, \gamma_0) \cos(n\omega t) \right] . \tag{1.27}$$

If not stated otherwise, the commonly used storage $G^{'}$ and loss $G^{''}$ moduli refer to the first-harmonic contributions of equation (1.27), that is, $G^{'} \equiv G_1^{'}$ and $G^{''} \equiv G_1^{''}$ [18].

The moduli $G^{'}$ and $G^{''}$ can be used to classify the nonlinear behavior into four classes as depicted in figure 1.7. In Type I (strain thinning, (a)), both $G^{'}$ and $G^{''}$ are decreasing with increasing strain amplitude, which is often observed in polymer solutions [18]. In Type II (strain hardening, (b)) instead, both $G^{'}$ and $G^{''}$ are increasing, which is typical for biological gels like collagen [22]. In Type III (weak strain overshoot, (c)), $G^{'}$ is decreasing and $G^{''}$ first exhibits a peak and is decreasing afterward. Finally, there is Type IV (strong strain overshoot, (d)), where both $G^{'}$ and $G^{''}$ first increase and then decrease as a function of strain.

Klein et al. proposed a superposition of basic function [23]. This is towards a more physical interpretation but they use basic functions that do not form an orthonormal basis and any superposition is not unique [18].

Cho et al. tried to classify the LAOS behavior from a purely physical approach in that they decompose the stress into a purely elastic and a purely viscous part [24]. The elastic stress $\sigma^{'}$ and the viscous stress $\sigma^{''}$ are obtained by the unique decomposition

$$\sigma^{'}(x, y) = \frac{\sigma(x, y) - \sigma(-x, y)}{2} \tag{1.28}$$

$$\sigma^{''}(x, y) = \frac{\sigma(x, y) - \sigma(x, -y)}{2} \tag{1.29}$$

with $x = \gamma$ and $y = \dot{\gamma}/\omega$ [24]. The area in the stress vs. strain plot is a measure of the mechanical dissipation and always zero if the elastic stress $\sigma^{'}$ is plotted versus

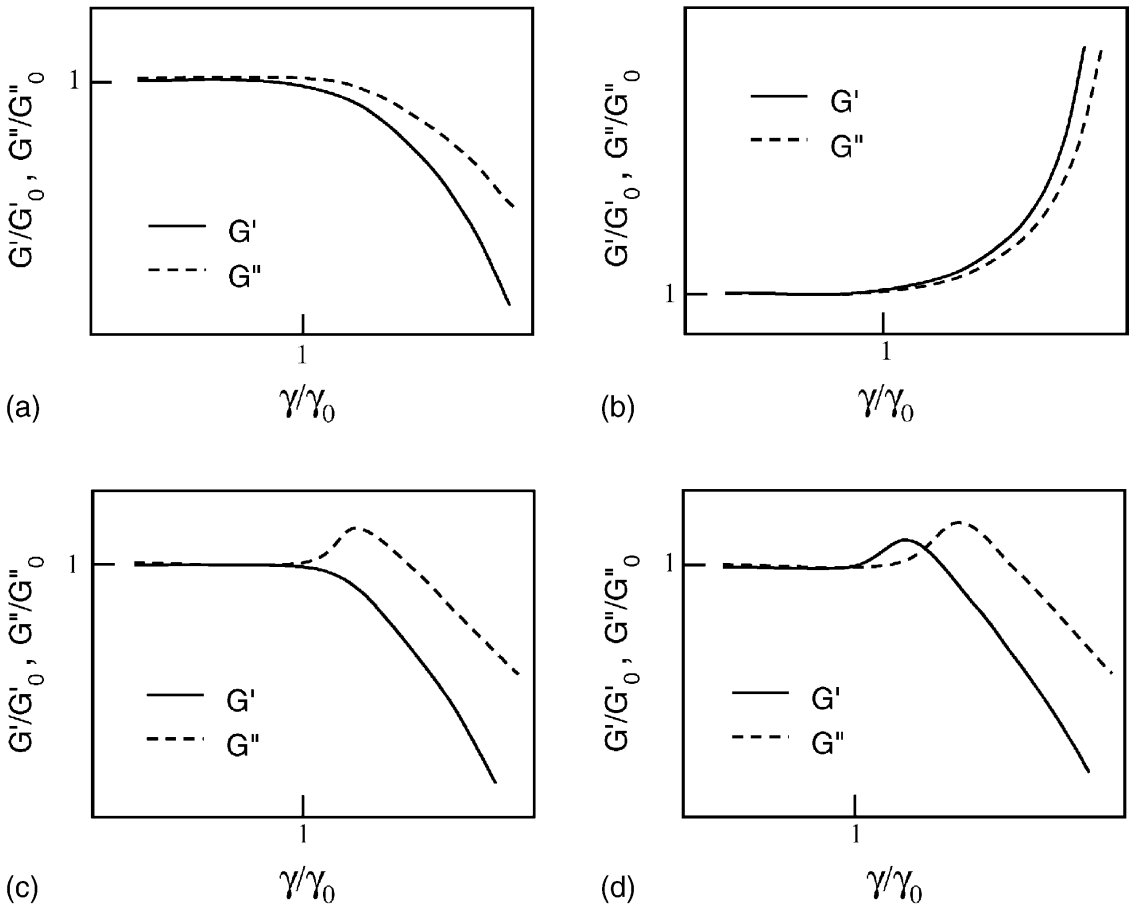

Fig. 1.7 Illustration of four different types of nonlinear behavior in oscillatory shear. (a) Type I (strain thinning): Both $G^{'}$ and $G^{''}$ are decreasing as a function of strain. (b) Type II (strain hardening): $G^{'}$ and $G^{''}$ are increasing. (c) Type III (weak strain overshoot): $G^{'}$ is decreasing and $G^{''}$ has a local maximum. (d) Type IV (strong strain overshoot): Both $G^{'}$ and $G^{''}$ first increase and then decrease as a function of strain. Reprinted from Journal of Non-Newtonian Fluid Mechanics, 107, K. Hyun et al., "Large amplitude oscillatory shear as a way to classify the complex fluids", pp. 51-65, Copyright (2002), with permission from Elsevier.

strain. We realize that equation (1.26) to equation (1.29) only allow odd harmonics. In other words, the stress response obeys the symmetry

$$\sigma(-\gamma(t), -\dot{\gamma}(t)) = -\sigma(\gamma(t), \dot{\gamma}(t))\,, \tag{1.30}$$

which means that the stress response is independent of the shear direction. In terms of Lissajous-Bowditch curves, this implies a rotational symmetry with respect to the origin [25]. This is reasonable for isotropic materials. Nevertheless, even harmonics have also been observed and attributed to wall slip or shear banding [18, 26, 27].

Ewoldt et al. [25] introduced new measures for nonlinearity, namely the minimum-strain modulus

$$G_M^{'} = \left.\frac{d\sigma}{d\gamma}\right|_{\gamma=0} \tag{1.31}$$

and the large-strain modulus

$$G_L^{'} = \left.\frac{\sigma}{\gamma}\right|_{\gamma=\pm\gamma_0}, \tag{1.32}$$

which reduce to the common storage and loss moduli in the LVE-regime. The corresponding two dynamic viscosities are the minimum-rate dynamic viscosity

$$\eta_M^{'} = \left.\frac{d\sigma}{d\dot{\gamma}}\right|_{\dot{\gamma}=0} \tag{1.33}$$

and the large-rate dynamic viscosity

$$\eta_L^{'} = \left.\frac{\sigma}{\dot{\gamma}}\right|_{\dot{\gamma}=\pm\dot{\gamma}_0}. \tag{1.34}$$

All four quantities can be best visualized in a Lissajous-Bowditch plot as shown in figure 1.8. These new measures can be combined to yield two dimensionless indices of nonlinearity, namely, the strain-stiffening ratio

$$\widetilde{S} = \frac{G_L^{'} - G_M^{'}}{G_L^{'}} \tag{1.35}$$

and the shear-thickening ratio

$$\widetilde{T} = \frac{\eta_L^{'} - \eta_M^{'}}{\eta_L^{'}}\,. \tag{1.36}$$

Vanishing indices (i.e., $\widetilde{S} = 0$, $\widetilde{T} = 0$) correspond to a linear response. A positive index $\widetilde{S} > 0$ ($\widetilde{T} > 0$) stands for intra-cycle strain stiffening (shear thickening) while a negative index $\widetilde{S} < 0$ ($\widetilde{T} < 0$) describes intra-cycle strain softening (shear thinning) [25].

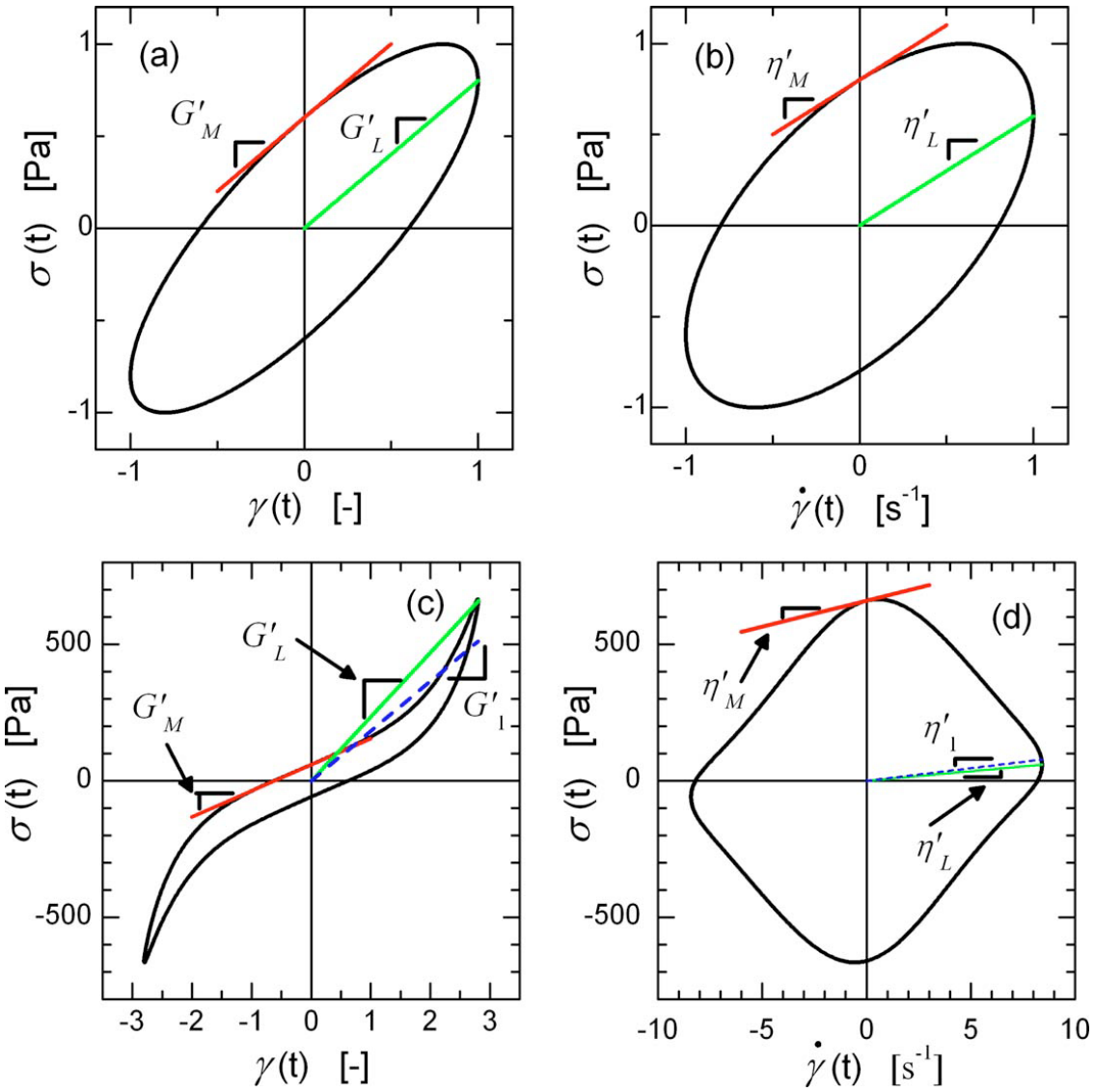

Fig. 1.8 Definitions of new measures of nonlinearity according to reference [25]. They are illustrated in Lissajous-Bowditch curves in σ-γ- (left) and σ-$\dot{\gamma}$-representation (right). The measure G'_M corresponds to the slope at $\gamma(t) = 0$, and G'_L corresponds to the ratio of $\sigma(t)$ and $\gamma(t)$ at the maximum strain. Analogous for the viscous moduli η'_M and η'_L. In (c) and (d), the moduli of the first harmonics are shown for comparison. Reprinted with permission from reference [25]. Copyright 2008, The Society of Rheology.

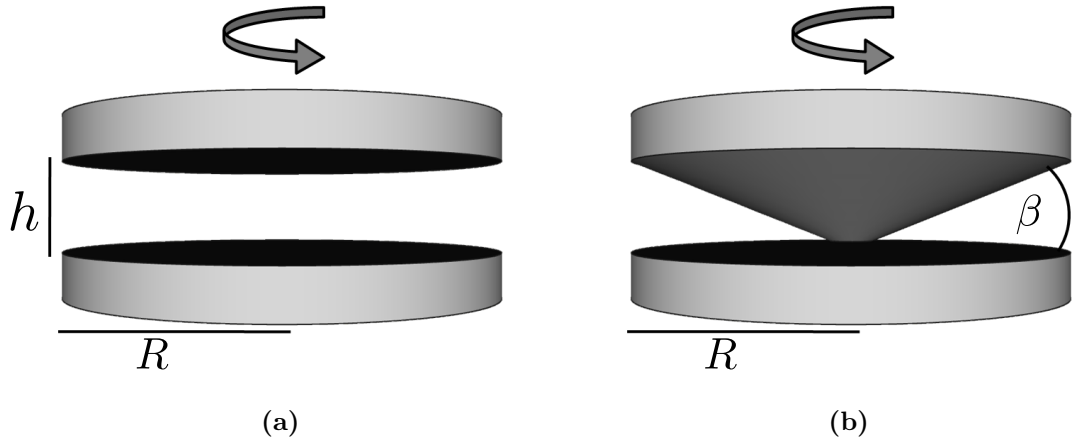

Fig. 1.9 Illustration of two measuring geometries: (a) the parallel plate geometry and (b) the cone and plate geometry.

1.5 Rheological Measurements

This section will focus on "practical rheology," that is, how to perform rheological measurements. Here, we will deal with the fundamentals of rotational rheometry that are relevant for one of the experimental setups (section 4.2) of this work.

Rotational rheometers can be grouped into the separate motor transducer (SMT) and combined motor transducer (CMT) design and both types can be equipped with a bunch of different so-called geometries. In the SMT design – historically called strain-controlled design – the motor drives one part of the geometry while a transducer measures the torque needed to keep the other part of the geometry in a fixed position. Instead, in the CMT design – historically called stress-controlled design – one part of the geometry is mechanically fixed and the torque is measured at the moving part of the geometry [28]. The detailed operating mode of stress- and strain-controlled rheometers is beyond the scope of this thesis and can be found elsewhere [29].

1.5.1 Geometries

Two commonly used measuring geometries for rotational rheometers are the *parallel plate* and the *cone and plate* geometry. A detailed description of further types of geometries can be found, for example, in a handbook of rheology [11]. The parallel and cone-plate geometries are both illustrated in figure 1.9. The parallel plate geometry (figure 1.9a) consists of two circular plates with radius R that are separated by a distance h. This distance h, called *gap height*, can be varied. Thus, the amount of sample needed for an experiment can be tuned by changing the gap height. This distance should be at least ten times larger than the particle size

[11]. One (or both) plates can be rotated in order to shear the sample. The main drawback of the parallel plate measuring system is that shear strain and stress are functions of the radial position and hence are not constant within the sample.

The cone and plate geometry overcomes this by the use of a cone with angle β, as shown in figure 1.9b. The cone angle needs to be smaller than a maximum angle of $\beta_{\max} = 4°$ [11]. Cones are truncated to prevent friction between cone and plate, which otherwise would distort the measurement. The cone truncation should be ten times larger than the particle size [11].

Geometries are usually made from stainless steel. The movement of the measuring geometries should be transferred to adjacent sample layers immediately and without slip. Therefore, the surface of the geometries might not be smooth as sketched in figure 1.9 but instead serrated or sandblasted [30–33].

The torque M that the motor can measure or apply is converted to the stress using

$$\sigma = F_\sigma M \tag{1.37}$$

with the conversion factor F_σ. Similarly, the strain is obtained from the motor angular displacement Θ via

$$\gamma = F_\gamma \Theta \tag{1.38}$$

with the conversion factor F_γ [1]. The conversion factors depend on the specifications of the geometry and are listed for selected types of geometries in table 1.1.

1.5.2 Experimental Challenges

What is the accuracy of an instrument? For instance, a typical ruler can be used to measure accurate to the millimeter and a bright-field microscope can be used to visualize objects with a minimum extent of several hundred nanometers. A rheometer can be used to measure ...? Good question! So what actually are the limitations of commercial rotational rheometers? This section is inspired by reference [1] and shall shed some light on what can be reasonably measured and where experimental challenges arise.

As introduced in section 1.1 and section 1.2, relevant rheological variables are the shear strain, shear stress, and shear rate. A rheometer does not measure these quantities directly. Instead, it measures, for instance, the displacement Θ and torque M of the motor.

Values of shear strain, shear rate, and shear stress are obtained by the equations

$$\sigma = F_\sigma M\,, \tag{1.39}$$

$$\gamma = F_\gamma \Theta\,, \tag{1.40}$$

$$\dot{\gamma} = F_\gamma \omega\,, \tag{1.41}$$

where the exact form of the stress and strain constants F_σ and F_γ depends on the specifications of the geometry (cf., table 1.1). The accuracy of the shear stress and

Geometry	F_γ	F_σ
Parallel plates	r/h	$2/(\pi r^3)$
Cone-plate	$1/\beta$	$3/(2\pi R^3)$

Tab. 1.1 Conversion factors for the stress F_σ and strain constants F_γ. They depend on the total radius R, the radial distance with respect to the center r, the gap height h and the cone angle β, respectively. For parallel plate measuring systems, the shear stress and strain depend on the radial position (i.e., $\sigma = \sigma(r)$, $\gamma = \gamma(r)$). Either the values at the total radius R are taken or a weighted average is used [11].

strain thus depends on the accuracy of the measured torque or displacement. This gives rise to the first restriction:

1.5.2.1 Minimum Torque

The torque needs to be larger than the minimum resolvable torque $M_{\min}$, leading to a minimum measurable stress

$$\sigma_{\min} > F_\sigma M_{\min} \tag{1.42}$$

or modulus

$$G_{\min} > \frac{F_\sigma M_{\min}}{\gamma_0} = \frac{F_\sigma M_{\min}}{F_\gamma \Theta_{\max}} \,. \tag{1.43}$$

This can help in choosing the most suitable measuring geometry. For example, in order to measure small moduli G' or G'', the factor F_σ/F_γ should be as small as possible, which can, among other parameters, be obtained by a large cone or plate radius.

1.5.2.2 Inertia Effects

Another criterion for obtaining reliable data is that the sample's torque M_{sample} should be dominant with respect to the instrument inertia torque $M_{\text{instrument}}$ [1]. Hence,

$$M_{\text{sample}} > M_{\text{instrument}} \,, \tag{1.44}$$

$$\frac{G\gamma_0}{F_\sigma} > I\Theta_0\omega^2 \,, \tag{1.45}$$

$$G > \frac{IF_\sigma}{F_\gamma}\omega^2 \,, \tag{1.46}$$

where I is the instrument inertia and γ_0 and Θ_0 are the amplitude of the strain and motor displacement, respectively. Once more, the factor F_σ/F_γ is an important limitation. Additionally, these inertia effects scale with the square of the angular frequency, that is, with ω^2.

1.5.2.3 Secondary Flows

Irrespectively of the instrument inertia, the sample inertia can lead to non-laminar flow at larger velocities. The idea is that due to inertia, sample material close to the (fast) rotating part of the geometry will have a non-zero movement in the radial direction. This outward movement is counterbalanced by an inwards movement close to the stationary plate [34]. To evaluate the flow behavior, Sdougos et al. [34] used a single parameter

$$\widetilde{R} = \frac{r^2 \dot{\Theta} \beta^2}{12\nu}\,, \tag{1.47}$$

which depends on the local radius r, the angular velocity of the cone $\dot{\Theta}$, the cone angle β and the fluid kinematic viscosity $\nu = \eta/\rho$, where η is the viscosity and ρ the density of the fluid sample. They concluded that laminar theory is valid for $\widetilde{R} < 0.5$ and turbulence sets in for $\widetilde{R} \gtrsim 4$ [34].

1.5.2.4 Slip

Wall slip affects rheological measurements. Recall for example the simple shear of a Newtonian liquid (cf., figure 1.6). It is assumed that the uppermost layer of the fluid has the same velocity as the top plate while the lowest layer of the fluid has the same velocity as the bottom plate. The underlying assumption is the no-slip condition. Only then, rheological variables like shear strain or shear rate do describe the sample's behavior correctly. If there is slip, then the sample does not experience the full deformation that is applied by the geometry. Then, the overall shear rate, and thus the measured stress, is smaller than in the case of no-slip. A possible way to reduce slip are roughened walls [35]. Wall slip of colloidal suspension has been studied by Ballesta et al. [36] and further information can be found, for instance, in a review on yield stress materials [33].

1.5.3 Measurement Protocols

Commercial rheometers can apply a sequential list of "jobs." Each job has its own measurement specifications. The two most important jobs of this work are a start-up test and a dynamic strain sweep (DSS): In the former, the shear rate is instantaneously increased from zero to a finite value. In the latter, an oscillatory strain signal with an increasing amplitude is applied. In both cases, the stress response is recorded. More details can be found, for example, in reference [11].

2

Colloidal Suspensions: Life in the Middle

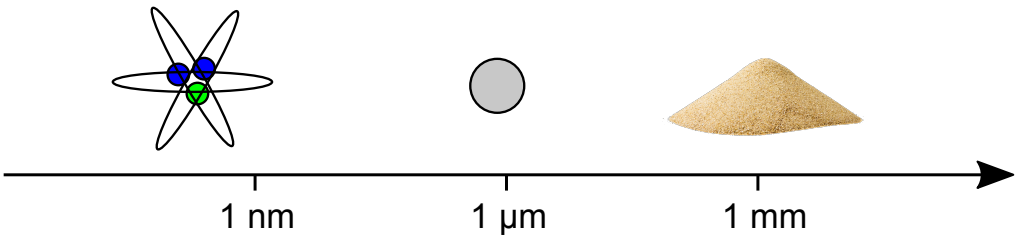

The term "colloid" is attributed to Thomas Graham, who first used it in 1861 [37]. Graham studied the diffusion of hydrates, phosphates, sugars, alcohols, acids, starch, gelatine, albumen, and many others through letter paper or animal skin. He called this method "dialysis," and he analyzed the velocity with which the materials "dialyze." Back in 1861, Graham said that colloids, such as gelatine, do not dialyze, whereas "crystalloids," such as dissolved salts, do dialyze. From today's point of view, Graham then wrongly linked the ability to dialyze with the ability to crystallize, but both of his terms ("colloid" and "dialyze") are still in use [38].

The definition of colloids was improved by Ostwald in 1913 [39]. According to Ostwald, a colloid is a dispersed system with typical dimensions between 1 nm and 100 nm, which is pretty close to today's definition, as shown in table 2.1.

During a series of lectures in 1913, Ostwald claimed that it is impossible to cover the full topic of colloidal chemistry within a few talks or even a one-year lecture [39]. It is still difficult to give a simple, compact summary. The following sections can, therefore, only contain a selection of relevant information without claiming completeness.

Colloids can exist in different states of matter as shown in table 2.2. They all have in common that the dimension of the dispersed phase is roughly between 1 nm and 1 µm, similar to the definition of Ostwald. The upper and lower boundaries might be historically linked to technical restrictions of filters or microscopes, but they can also be motivated physically. The lower boundary of 1 nm distinguishes colloids from atoms and small molecules. Colloids have – in contrast to atoms – a

disperse systems

coarse dispersions	colloids	molecular dispersions

$\longrightarrow$

decreasing size of particles

	$> 0.1\,\mu m$	$0.1\,\mu m$ - $1\,nm$	$< 1\,nm$
can be resolved with a microscope	✓		
pass paper filter		✓	✓
diffuse and dialyze			✓

Tab. 2.1 Definition of colloids according to Ostwald [39, p.20]. Although giving numbers, Ostwald emphasizes that the transition between the systems is not sharp but continuous. Note that Ostwald's definition is from 1913.

dispersion medium	dispersed phase	denomination	appearance
gaseous	gaseous	-	-
	liquid	liquid aerosol	fog
	solid	solid aerosol	smoke
liquid	gaseous	foam	foam
	liquid	emulsion	natural & synthetic emulsions, e.g., milk
	solid	suspension	most colloidal systems, e.g., paint
solid	gaseous	solid foam	minerals with gaseous ...
	liquid	solid emulsion	... liquid ...
	solid	solid suspension	... solid inclusions

Tab. 2.2 Possible appearances of colloids – grouped by the state of the dispersion medium and the dispersed phase. Adapted from reference [38, p.26].

well defined surface and can usually be treated classically (i.e., without quantum mechanics). We will focus, from now on, only on the most common occurrence of colloids: Colloidal suspensions. In a colloidal suspension, solid particles are dispersed in a liquid.

Typical examples of colloidal suspensions are paints, inks, pharmaceuticals, cosmetics, and food products. The upper boundary of 1-10 µm ensures that fluctuations and Brownian motion play an important role [40]. The bonding energy between individual colloids is of the order of the thermal energy $k_\mathrm{B}T$. Thus, there is a permanent reorganization of particle positions, which can lead to self-assembly [41]. The equilibrium state may not be reached in very concentrated suspensions or under external constraints. The size range of colloids also implies that colloids have a high surface area. If two units of the dispersed phase get in close contact, they tend to aggregate. This is often not desired and colloidal suspensions need to be stabilized. The following sections will first introduce Brownian motion (section 2.1) as well as relevant forces and interactions (section 2.2). Afterward, we will introduce our colloidal model system that will be used throughout this thesis (section 2.3) and discuss basic equilibrium (section 2.4) and nonequilibrium properties (section 2.5) thereof.

2.1 Brownian Motion

Colloidal suspensions undergo Brownian motion. Brownian motion is named after Robert Brown, a botanist, who investigated the motion of living and dead pollen in water in 1827 [42]. In his work, he states that the motion of the pollen particles has already been observed before. It may be claimed that Ingen-Housz was the first who discovered the random motion, 40 years before Robert Brown [43]. Albert Einstein succeeded in the theoretical description of the Brownian motion in 1905 [44]. In 1926, almost 100 years after Brown's experiments, Jean Baptist Perrin was awarded the Nobel Prize in Physics. He experimentally verified Einstein's theory using colloids.

Brownian motion of colloids is caused by random collisions with the solvent molecules. For illustration purposes, the zig-zag motion of a colloidal sphere in water is sketched in figure 2.1. The probability for collisions between colloids and surrounding molecules is the same in each direction, hence the averaged mean motion is zero. But at any time there will be some more collisions from one side, leading to a non-zero mean *squared* displacement. The mean squared displacement (MSD) is most generally defined as

$$\left\langle \Delta r^2(\tau) \right\rangle = \left\langle \left(\boldsymbol{r}_n(t+\tau) - \boldsymbol{r}_n(t) \right)^2 \right\rangle_{t,n} , \tag{2.1}$$

where the vector $\boldsymbol{r}_n$ points to the position of particle n. Here, the average is taken over all times t and all particles n, and the MSD only depends on the lag time τ.

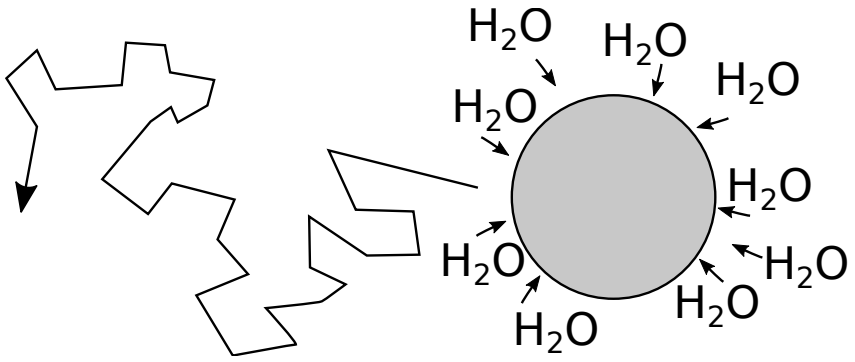

Fig. 2.1 Illustration of Brownian motion. A colloidal particle is constantly "bombarded" by water molecules. This leads to a zig-zag trajectory of the particle.

Einstein's equation for the MSD in one dimension reads

$$\left\langle \Delta x^2 \right\rangle_{t,n} = 2D\tau \tag{2.2}$$

with the diffusion coefficient D [44]. For a three-dimensional description, the prefactor in front of the diffusion coefficient is 6 instead of 2. The abovementioned equation for the MSD is valid only for dilute suspensions. Einstein also showed that one can link the diffusion coefficient D to the gas constant and Avogadro's number, making it possible to determine Avogadro's number experimentally [44]. The diffusion coefficient can also be linked to the particles radius R and the viscosity of the dispersion medium η_0 via the Stokes-Einstein relation

$$D = \frac{k_\mathrm{B}T}{6\pi\eta_0 R} \tag{2.3}$$

with Boltzmann constant k_B and absolute temperature T. Equation (2.3) is an example of a fluctuation-dissipation theorem, which becomes more obvious if written like

$$D = \frac{k_\mathrm{B}T}{\xi}\,, \tag{2.4}$$

where the diffusion coefficient accounts for fluctuations (cf., equation (2.2)) and the friction coefficient ξ describes dissipation. For a sphere in a fluid with viscosity η_0 the friction coefficient is $\xi = 6\pi\eta_0 R$. This is Stokes' law.

A characteristic time of Brownian motion is

$$\tau_\mathrm{B} = \frac{R^2}{D} = \frac{6\pi\eta_0 R^3}{k_\mathrm{B}T}\,, \tag{2.5}$$

which is about the time it takes a particle to diffuse a distance corresponding to its own size (cf., equation (2.2)). Brownian motion has also been theoretically described by Langevin (cf., e.g., [45]). Nowadays, Brownian motion is studied using optical microscopy [46] or dynamic light scattering [47].

2.2 Forces and Interactions

The dynamics of colloids are not only affected by random collisions with their surrounding molecules of the dispersion medium, but there are a number of forces acting on the colloids and some of them will be described below.

2.2.1 Gravity

Since colloids have a mass, they are affected by gravity. They may sediment or cream depending on the difference between their density and that of the dispersion medium, $\Delta\rho$. The gravitational force on a single colloid with radius R is

$$F_g = \frac{4}{3}\pi R^3 \Delta\rho g \,. \tag{2.6}$$

Gravity is competing with the fluctuations of colloids with thermal energy $k_\mathrm{B}T$. Thus, the effect of gravity is observable in a container with height L if $k_\mathrm{B}T \ll |F_g|L$. A single colloidal sphere in a dispersion medium with viscosity η_0 sediments with a terminal velocity

$$v_{s0} = \frac{2R^2\Delta\rho g}{9\eta_0} \,. \tag{2.7}$$

The sedimentation velocity from equation (2.7) is valid in the very dilute regime. The concentration is measured by the volume fraction $\phi = V_\mathrm{spheres}/V_\mathrm{total}$, where V_spheres is the volume occupied by the colloidal particles and V_total is the total volume, including particles and dispersion medium. For $0.01 < \phi < 0.2$, the sedimentation velocity is reduced due to hydrodynamic interactions [14] and for even higher particle concentrations an even more complex situation occurs. For instance, the sedimentation velocity v_s of a polystyrene suspension could be fitted by

$$v_s = v_{s0}\left(1 - \frac{\phi}{\phi_p}\right)^{k_p\phi_p} \tag{2.8}$$

using $\phi_p = 0.58$ and $k_p = 5.4$ (cf., [14, p.154])

2.2.2 Hard-Core Repulsion

If more than one colloidal particle is present, then they can interact with each other. One of the few things that rigid particles cannot do is to overlap or to interpenetrate each other. This hard-core repulsion is, in contrast to the following interactions, independent of the dispersion medium.

2.2.3 van der Waals Attraction

Another type of interaction, which in fact depends on the dispersion medium, is the van der Waals force (also named dispersion forces or London forces). The van der Waals interaction originates from quantum fluctuations. The simple picture is that there are fluctuating dipoles in each atom giving rise to an attractive interaction between colloids, which in fact consists of many atoms. The exact equation of the van der Waals attraction depends, among others, on the spatial distribution and distance between the interacting dipoles. In the limit of small separations $r \ll R$, the equation for two (colloidal) spheres with radius R is

$$U_{\mathrm{vdw}}(r) = -\frac{HR}{12r} \tag{2.9}$$

with the Hamaker constant H (cf., [48]). The Hamaker constant has the dimension of an energy and is typically of the order of $10\,k_{\mathrm{B}}T$. The Hamaker constant can be calculated using the physical properties of the involved materials. For non-polar systems, the Hamaker constant depends essentially on the refractive indices of the colloids and the dispersion medium. If the refractive index of colloidal spheres and of the dispersion medium is matched, then the van der Waals attraction becomes minimal [49].

2.2.4 Electrostatic Double Layer

A relevant interaction for charged colloidal suspensions arises from electrostatic double layer forces. For instance, colloids can have charged surfaces by synthesis or adsorption of ions. There can also be free ions within the dispersion medium that screen the surface charges. The result is an electrostatic double layer. For small potentials, the electrostatic double layer potential at a distance r is modeled by the Debye-Hückel approximation

$$U_{\mathrm{edl}}(r) = U_0 e^{-r/l_{\mathrm{DH}}}\,, \tag{2.10}$$

where U_0 is the potential for $r = 0$ and l_{DH} is known as the Debye screening length. It is $l_{\mathrm{DH}} \propto l_{\mathrm{B}}^{-0.5}$, where

$$l_B = \frac{e^2}{4\pi\epsilon_0\epsilon_r k_{\mathrm{B}}T} \tag{2.11}$$

is the Bjerrum length with the elementary charge e, the vacuum permittivity ϵ_0 and the relative dielectric constant ϵ_r [50, p.172]. Typical values of the relative dielectric constant are $\epsilon_r = 5 - 6$ for a mixture of the organic solvents cycloheptyl bromide and *cis*-decalin [51] and $\epsilon_r = 78.6$ for water at 25 °C [14]. The Bjerrum length is a characteristic length at which the electrostatic interaction between two point charges is equal to the thermal energy. In organic solvents, the electrostatic

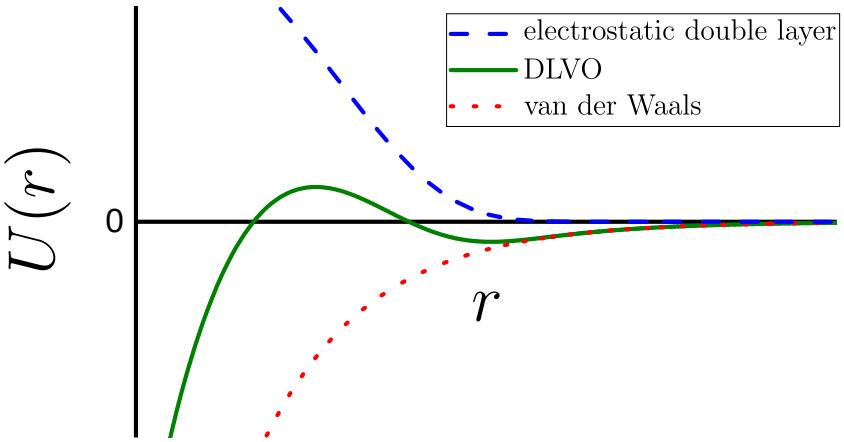

Fig. 2.2 Sketch of the DLVO potential (solid line), the electrostatic double layer potential (dashed line) and the van der Waals potential (dotted line) as a function of the interparticle distance r.

interactions are long-ranged with values of $l_B = 28\,\text{nm}$ as compared to $l_B < 1\,\text{nm}$ in water [52].

If the colloidal surface is – say – positively charged, then there will be a layer of negatively charged counterions from the dispersion medium close to the colloidal surface. Tightly bound counterions make up the so-called *Stern layer*. The remaining co- and counter-ions are diffusive. Upon particle approach, the repulsive interaction of the electric double layer will change and adjust to the new conditions. If two particles approach each other on a timescale faster than the relaxation time of the charges, the charges cannot rearrange to a new equilibrium. This leads to stronger repulsion [14].

2.2.5 DLVO Theory

The Deryaguin-Landau-Verwey-Overbeek (DLVO) theory [53, 54] is often used to describe the total interaction of colloids. It sums up the contributions of the van der Waals attraction and the electric double layer repulsion, assuming that they are additive. The DLVO theory describes the interaction between colloids with two energy minima at small and intermediate distances that are separated by an energy maximum. Depending on the relative contribution of either the van der Waals attraction or the electrostatic double layer repulsion, absolute heights and positions of the energy minima and the maximum change. The DLVO potential is sketched in figure 2.2. Particles may flocculate reversibly into the second minimum. Flocculation into the second minimum can also be observed as shear thinning or thixotropy. Under shear, the flocculation can be reversed, reducing the viscosity of the suspension with time and or shear rate. If particles get into close contact, such

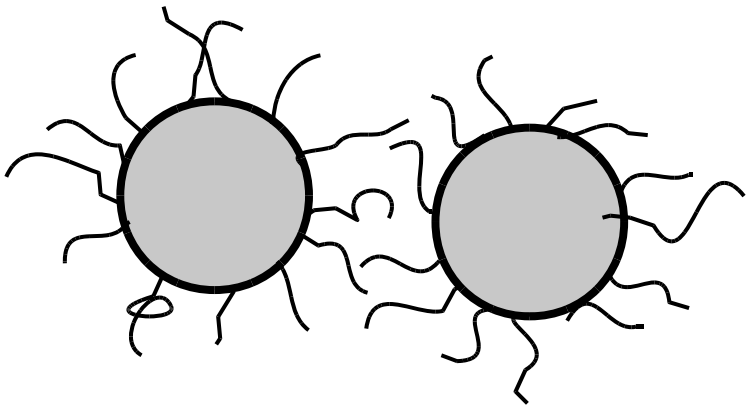

Fig. 2.3 Illustration of colloids with steric stabilization. The hairs are not drawn to scale. In practice, the length of the hairs is only a few percents of the particle size and would not be visible on the sketch.

that they enter the first minimum, they aggregate. The suspension is kinetically stable if the energy barrier for entering the first minimum exceeds $25\,k_\mathrm{B}T$ [14] and unstable for values below $5\,k_\mathrm{B}T$. Temperature also has an important impact on flocculation since it changes the solvency of stabilizing "hairs," which will be introduced below.

2.2.6 Steric Stabilization

In order to prevent flocculation of the colloidal system, two kinds of stabilizations are familiar. One is charge stabilization, where like-charged colloids repel each other. The other is steric stabilization. In the latter, polymer hairs are grafted onto the surface of the colloids as sketched in figure 2.3. This slightly increases the effective size of a colloid. Once two colloids approach each other, such that their stabilizing polymer hairs interpenetrate, the local density of polymer hairs increases leading to entropic repulsion. Depending on the exact way the hairs are arranged, they might also bend in a partially elastic way, also leading to a repulsion. The chances for a successful steric stabilization are increased under the following conditions [14]: The hairs should completely cover the whole surface of the particle. Also, the polymers should be chemically attached and strongly anchored. The hairs should be soluble in the dispersion medium or, in other words, the dispersion medium should be a good solvent for the hairs. The mixing of polymers and solvent is described by the Flory-Huggins theory [14, 55, 56]. Finally, the hairs should be larger than 75 nm to prevent flocculation [14, 57]. Further details including electrostatic stabilization may be found in a technical review [58].

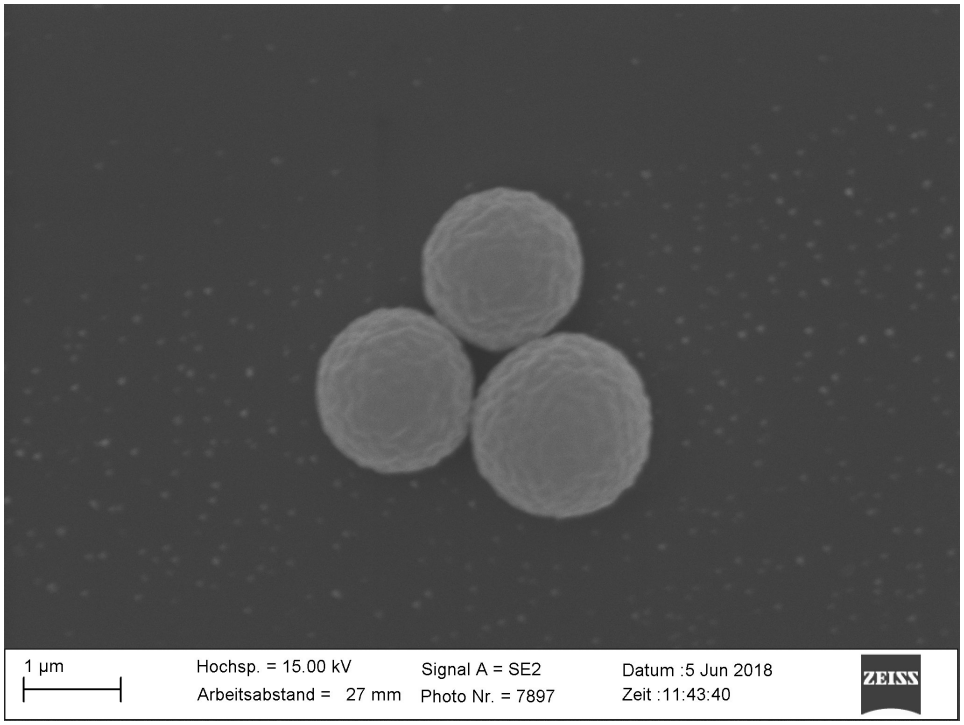

Fig. 2.4 Electron microscopy image of PMMA spheres as used in this work. The image has been recorded at CAi (HHU).

2.3 Model System: Spherical PMMA Particles

This section deals with the synthesis and specifications of one class of colloidal spheres, namely PMMA-PHS-spheres [59]. An electron microscopy image of PMMA spheres can be seen in figure 2.4.

In 1986, Antl published a recipe for monodisperse poly(methyl methacrylate) (PMMA) spheres stabilized by poly(12-hydroxy-stearic acid) (PHS) [60]. If the stabilizer is covalently bound to the particle's surface then the particles are "locked." If instead the stabilizer is adsorbed to the surface, the particles are referred to as "unlocked" [61]. Particle radii between 40 nm and 1.3 µm can be achieved by Antl's protocol. In contrast to atoms, colloids always have a size distribution, that is, they are polydisperse (cf., section 2.4.3). The polydispersity might be tuned by changing the relative amount of stabilizer [60]. The particles need to be washed after synthesis, that is, reaction products have to be replaced by a fresh solvent.

The PMMA-PHS particles can be density and refractive index matched if used, for example, in a mixture of cycloheptyl or cyclohexyl bromide (both abbreviated by CHB) and *cis*-decalin [51]. This minimizes gravity and van der Waals effects (cf., section 2.2.1 and section 2.2.3). This organic solvent mixture has a dielectric constant of $\epsilon = 5 - 6$ [51]. PMMA particles in CHB will acquire a charge [51, 52]

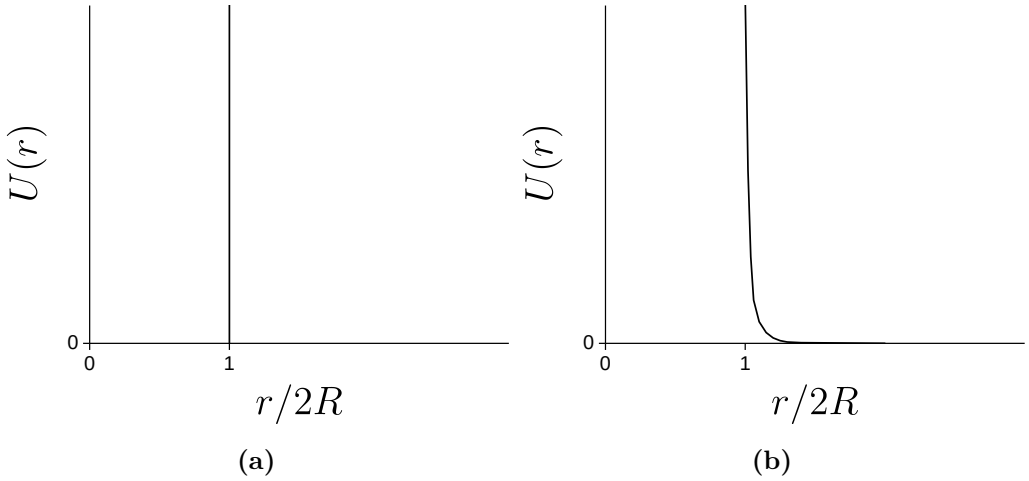

Fig. 2.5 Schematic of (a) an ideal hard-sphere potential and (b) a potential for sterically stabilized PMMA particles as a function of the center-to-center distance r. The particle diameter is $2R$.

where the amount of charging depends on whether the particles are locked or not. Locked particles have a higher charge [61]. Repulsive interactions due to charges can be reduced by adding the salt tetrabutylammonium chloride (TBAC) [51]. Care has to be taken since very high concentrations of TBAC can reverse the PMMA-PHS surface charge from positive to negative [61]. For confocal microscopy, the PMMA-PHS particles can be labeled with fluorescent dyes such as nitrobenzoxadiazole (NBD) or rhodamine, where rhodamine is known to also charge the particles [62]. In general, the behavior of PMMA particles may depend on particle size, solvent, stabilizer and fluorescent dye [52]. The charging due to CHB seems to be independent of the particle size [61], but it may be problematic to use CHB for bigger particles in confocal microscopy [63]. Density and refractive index matching can also be obtained without CHB, avoiding potential problems due to charging. But the use of, for example, tetrachloroethylene (TCE) can lead to particle swelling of up to 20-40% [63, 64]. The process of swelling can take weeks but may be reduced to a few hours by thermal heat shocks [64]. In the 1980s and 1990s, Pusey and van Megen used PMMA spheres in a mixture of *cis*-decalin and carbon disulfide [65–67], but the latter component is highly toxic. Quite recently, hard-sphere model systems have been used with a different stabilizer [68] or different monomers [69].

The interaction potential can have various contributions (cf., section 2.2). Nevertheless, sterically stabilized PMMA particles act essentially as *hard spheres* (HS) [70]. They can be thought of as tiny billiard balls, which only interact on contact. The interaction potential of ideal hard spheres is sketched in figure 2.5a. Sterically stabilized PMMA particles are nearly hard spheres [63] and their pairwise interaction potential is sketched in figure 2.5b. PMMA spheres show a liquid-solid phase

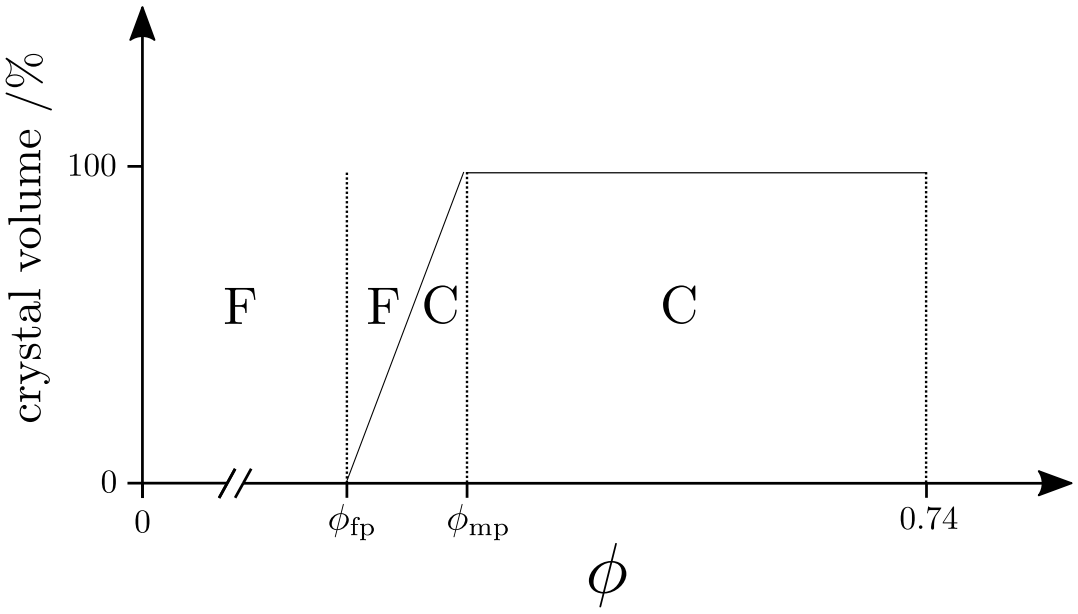

Fig. 2.6 Schematic equilibrium phase diagram of ideal hard spheres with fluid (F) and crystal (C) phases. A pure fluid phase exists between $\phi = 0$ and the freezing point $\phi_{\mathrm{fp}} = 0.494$, followed by a fluid-crystal coexistence region between ϕ_{fp} and the melting point $\phi_{\mathrm{mp}} = 0.545$, followed by a crystalline phase between ϕ_{mp} and the maximum packing for spheres at $\phi_{\mathrm{max}} = 0.74$.

transition (section 2.4.1) and can be regarded as a model system for atoms and molecules.

2.4 Equilibrium Properties of Hard Spheres

2.4.1 Phase Diagram of One-Component Systems

The phase diagram of colloids depends on their interaction potential and geometrical shape. This section will focus on the phase diagram of colloidal hard spheres. The only control parameter is the packing fraction

$$\phi = \frac{V_{\mathrm{spheres}}}{V_{\mathrm{total}}}\,, \tag{2.12}$$

which relates the volume of all spheres V_{spheres} to the total volume V_{total}.

Figure 2.6 shows the phase behavior of ideal hard spheres in three dimensions. The following is observed: Between $\phi = 0$ and the freezing point $\phi_{\mathrm{fp}} = 0.494$, the equilibrium phase is a fluid. Between ϕ_{fp} and the melting point $\phi_{\mathrm{mp}} = 0.545$, the colloids separate into a fluid and a crystal phase according to the lever rule. Above ϕ_{mp}, a crystalline structure is the thermodynamic stable phase. Hard spheres also

show a glass transition [70–72] (cf., section 2.5.2). Freezing and melting points have been first studied with Monte-Carlo simulations [73] in agreement with later density functional theory [74]. The phase behavior has been studied experimentally by Pusey and van Megan [70]. Actually, numerical values of ϕ_{mp} and ϕ_{fp} are from the Monte-Carlo simulations [73] and the experiments by Pusey and van Megen [70] were scaled to get the same freezing point. The maximum packing fraction of hard spheres is at $\phi_{\mathrm{max}} = 0.74$, corresponding to hexagonal close packing. Crystal structures are covered in section 2.4.2.

The abovementioned details on the phase diagram are valid only for monodisperse hard spheres. The phase diagram changes for polydisperse samples (cf., section 2.4.3) and binary mixtures (cf., section 2.4.4).

Even though hard spheres are non-attractive, they show a liquid-solid transition. In this context, Frenkel's commentary on "Order through entropy" is worth reading [75]. Ideal hard spheres are incompressible and have a constant volume. The interaction between two hard spheres is infinite at contact and zero else. Temperature does not change the shape of the interaction potential. The relevant thermodynamic quantity is the Helmholtz free energy $F_{\mathrm{H}} = E - TS$, and in the equilibrium state F_{H} is minimal [50, p.31]. Here, E is the internal energy of the system and constant for hard spheres [76]. Thus, the phase behavior of hard spheres is solely driven by entropy S (!) [75]. This means that an ordered state (i.e., a crystal) is entropically more favorable than a disordered structure.

The transition can be qualitatively understood with the help of a packing argument [77] as illustrated in figure 2.7. The same number of particles are arranged in boxes of equal size – in a disordered and in an ordered way. The disordered particles are lacking vibrational degrees of freedom. In contrast, the ordered particles share the total available volume such that they can all rattle around their lattice positions. In this respect, entropy does not maximize disorder but rather maximizes freedom.

2.4.2 Crystal Structures

For $0.545 < \phi < 0.74$ the phase diagram reveals that a crystalline state is the equilibrium state. Crystal structures are also found in colloidal systems [78–81].

Common crystal structures are the body-centered cubic (bcc), the face-centered cubic (fcc) and the hexagonal close-packed (hcp) structure. The unit cells of the fcc and bcc structures are visualized in figure 2.8. In the fcc structure, the particles are located both in the corners of a cube and in the centers of its surfaces. In the bcc structure, there are particles at each corner plus one additional particle in the center of the cube. The maximum packing fraction of a bcc crystal is $\phi_{\mathrm{max}} = 0.68$.

The hcp structure is very similar to the fcc structure and differs only in the stacking sequence (cf., figure 2.9): ABCABC... for fcc and ABABAB... for hcp. Any random stacking sequence (e.g., ABABCBCACB...) is referred to as a random hexagonal close packing (rhcp). The maximum packing fraction of the fcc, the hcp, and all

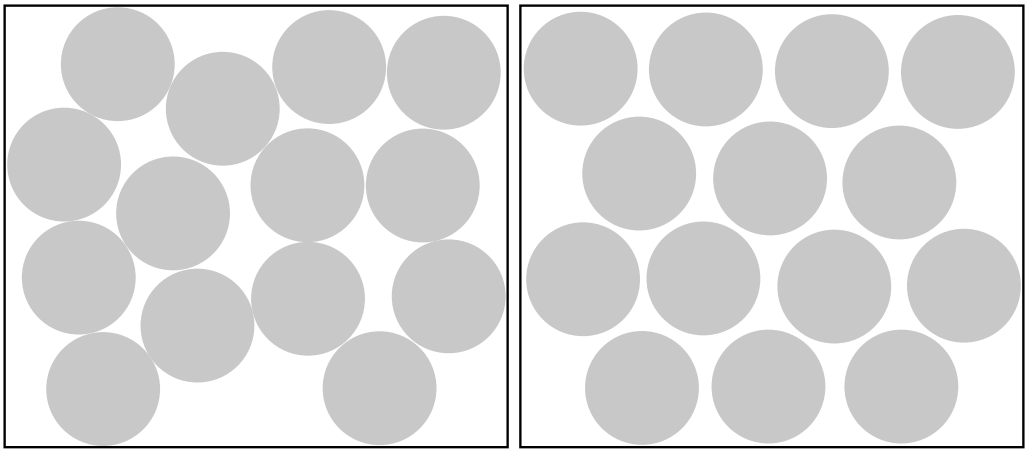

(a) **(b)**

Fig. 2.7 Comparison of (a) a disordered and (b) an ordered state of spheres at identical volume fraction. The disordered particles obstruct each other and have little freedom to change their positions. Instead, the ordered particles share the available space equally and can wiggle around. Thus, the ordered particles have higher freedom of movement. Adapted from reference [76].

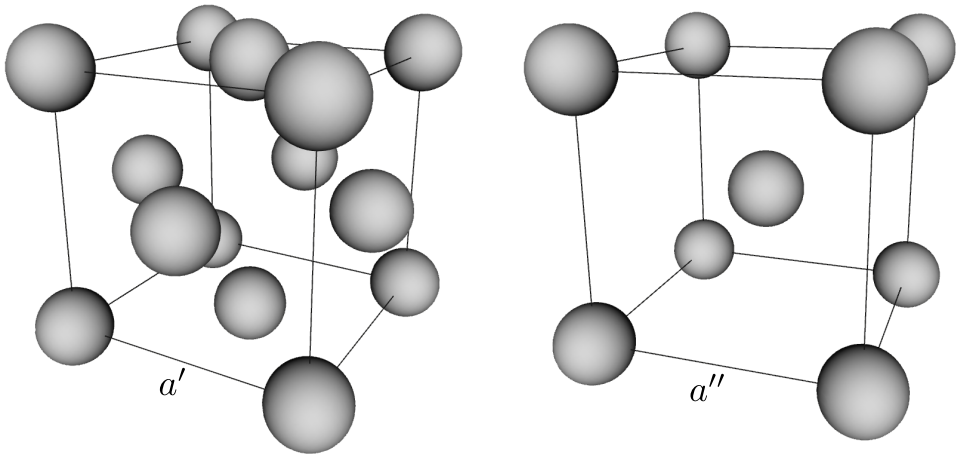

(a) **(b)**

Fig. 2.8 Renderings of particles placed in (a) an fcc crystal and (b) a bcc crystal. For the fcc unit cell, there are 8 particles placed at the vertices of the cube and 6 in the center of each face. The cube has volume a'^3. A particle in an fcc crystal has 12 nearest neighbors at a distance of $a'/\sqrt{2}$. For the bcc unit cell, there are 8 particles placed at the vertices of the cube and 1 is in the center of the cube. The cube has volume a''^3. A particle in a bcc crystal has 8 nearest neighbors at a distance of $(\sqrt{3}\,a'')/2$ and 6 next-nearest neighbors at a distance of a''.

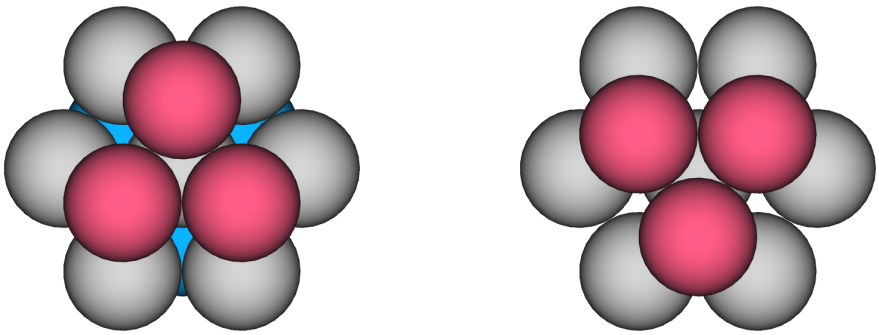

(a) **(b)**

Fig. 2.9 Comparison of the stacking sequence of (a) fcc and (b) hcp structures. Both structures differ only in their stacking order. The stacking sequence is ABCABC... for fcc and ABABAB... for hcp. Here, three layers of particles are labeled in blue, gray and red, respectively. In hcp, the third layer is arranged exactly in the same way as the first one. Accordingly, the blue particles are hidden below the red ones.

rhcp structures is $\phi_{\max} = \pi/\sqrt{18} \approx 0.74$. The proof of Kepler's conjecture that this is the maximum packing was given relatively recently by Hales [82]. Interestingly, small entropy differences have been found between fcc and hcp structures, which suggest that the fcc structure has slightly higher entropy than the hcp structure [81, p.216]. Therefore, the equilibrium crystal structures should be of fcc type.

Colloidal dispersions in the fluid-crystal coexisting region have been studied experimentally with confocal laser scanning microscopy (CLSM) [62] and light scattering experiments [70], and the structure of the nuclei, as well as the bulk structure, was found to be random hexagonal close-packed. An rhcp structure has also been found with simulations for polydisperse [83] and monodisperse hard spheres [84]. Although found in the early stages of nucleation, the rhcp structure is suggested to be metastable and expected to transform into an fcc structure at a later stage [84]. This goes in line with experimental observations: While the probabilities for fcc or hcp structures are equal at high nucleation ratios, slow nucleation rates favor fcc structures [85]. The bcc structure is uncommon for hard spheres but can be found in charged systems [78, p.793].

2.4.3 The Role of Polydispersity

Experimental hard spheres always have a distribution of particle sizes, which is quantified by the polydispersity. The polydispersity δ is typically defined as the standard deviation of the size distribution divided by the mean $\overline{R} = (1/N)\sum_{i=1}^{N} R_i$.

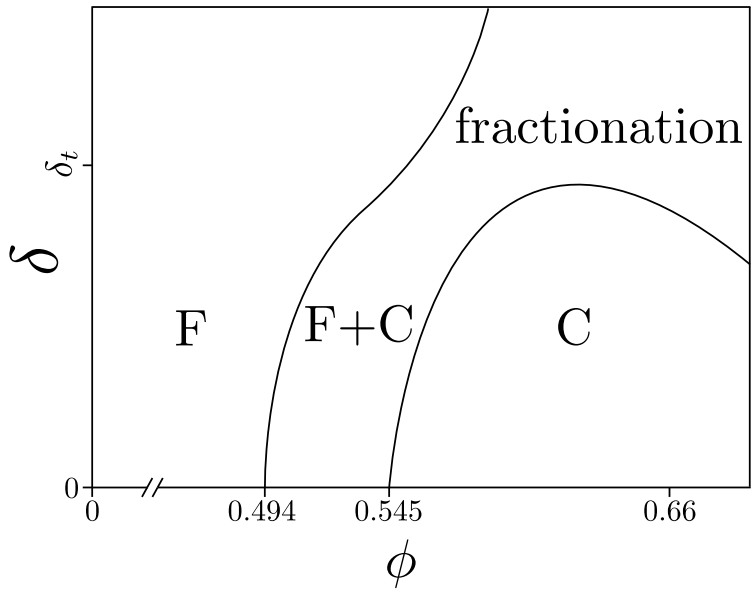

Fig. 2.10 Schematic equilibrium phase diagram for hard spheres including polydispersity δ as a function of the volume fractions ϕ, according to Fasolo and Sollich [90, 93]. For $\delta = 0$, the phase diagram reduces to the equilibrium phase diagram for monodisperse hard spheres as discussed in section 2.4.1. Crystals (C) are only stable below a terminal polydispersity δ_t. Fractionation includes combinations of multiple crystals with different daughter size distributions as well as multiple crystals coexisting with a fluid (F).

For a distribution of N particles with radii R_i, the polydispersity reads

$$\delta = \frac{1}{\overline{R}} \sqrt{\frac{1}{N-1} \sum_{i=1}^{N} (R_i - \overline{R})^2} \,. \tag{2.13}$$

The polydispersity does not contain full information about the size distribution of the particles. The size distribution might be Gaussian, triangular, flat or binary – just to name a few examples. Samples with small polydispersities are expected to behave essentially as hard spheres. For example, the PMMA particles that were used by Pusey and van Megen to study the equilibrium phase behavior of (nearly) hard spheres (cf., section 2.4.1) have a polydispersity of $\delta = 5\%$. Rules to map polydisperse hard sphere mixtures to a monocomponent hard sphere system work well in the fluid and reasonably good in the glass regime [86].

The equilibrium phase diagram changes for polydisperse samples [87–92]. A possible equilibrium phase diagram for polydisperse hard spheres that also incorporates for fractionation [90, 93] is sketched in figure 2.10. For polydispersities $\delta > 0$, the freezing and melting points shift to higher volume fractions. A single crystal is only stable below a terminal polydispersity δ_t. Reported values of the terminal polydispersity include $\delta_t \approx 5\%$ [94], $\delta_t = 5.7\%$ [95, 96], $\delta_t \approx 6\%$ [93] and $\delta_t \approx 7\%$

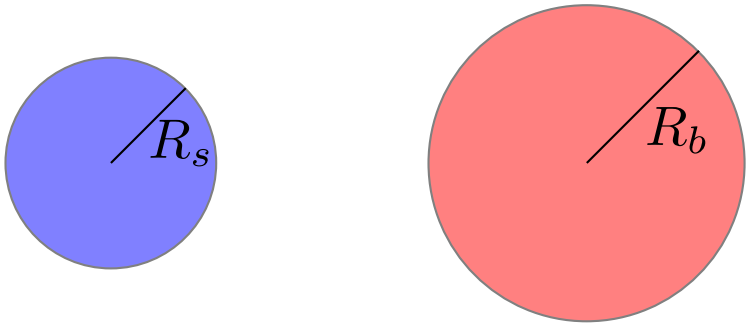

Fig. 2.11 Illustration of two spheres with radii R_s and $R_b \geq R_s$.

[90]. Crystallization is observed with PMMA spheres having polydispersities of, for example, $\delta = 5\%$ [97] and $\delta \approx 8\%$ [98].

In 1987, Pusey formulated a criterion for the terminal polydispersity [99], namely

$$\delta_t = \left(\frac{0.74}{\phi}\right)^{1/3} - 1\,. \tag{2.14}$$

His idea is that a crystal becomes unstable once the particle size distribution contains particles whose diameters are bigger than the average particle-particle distance. This idea is similar to Lindemann's melting criterion and generalized Lindemann measures have been studied with Monte Carlo simulations [100]. As indicated in the schematic phase diagram (figure 2.10) and Pusey's criterion (equation (2.14)), the terminal polydispersity depends on the volume fraction.

2.4.4 Binary Mixtures

Polydisperse systems can, within some restrictions, be mapped to an equivalent binary mixture [86, 101, 102]. Binaries are the simplest multi-component system. For the description to follow, the smaller particles will be denoted with subscript the s and the bigger ones with subscript b. Their radii are $R_s \leq R_b$ as illustrated in figure 2.11. Like one-component hard spheres are used to model atoms, binaries can be seen as a model system for molecules or metallic alloys. Depending on the properties of the individual components, binaries can develop very different structures.

Three independent parameters are necessary to describe binary mixtures, but the set of parameters is not unique. We will choose dimensionless parameters that are bound between zero and one.

The first parameter is the (total) volume fraction

$$\phi = \frac{V_{\text{spheres}}}{V_{\text{total}}} = \frac{V_s + V_b}{V_{\text{total}}}\,. \tag{2.15}$$

Here, the total volume V_{total} in the denominator is the sum of the volume of all small (V_s) and big spheres (V_b) plus the volume of the dispersion medium. Two additional parameters are the size ratio

$$\alpha = \frac{R_s}{R_b} \tag{2.16}$$

with the radii of the smaller and bigger spheres and the relative volume fraction of big spheres

$$X = \frac{V_b}{V_s + V_b}\,. \tag{2.17}$$

Having introduced the three independent variables ϕ, α, and X, we now end up with the question: What is the equilibrium phase behavior of binary hard spheres? According to Gibb's phase rule, a maximum of three coexisting phases is allowed in a two-component system. Let us now have a look at some limiting values of ϕ, α, and X:

For small volume fractions, that is, for $0 < \phi \lesssim 0.40$ [103] or $0 < \phi \lesssim 0.50$ [104], the equilibrium state is a fluid. For very high volume fractions (i.e., $\phi \gtrsim 0.74$), calculations predict the densest packings for almost any combinations of α and X [105, 106]. For $\alpha > 0.66$, the densest packing is achieved by a phase separation of small and big spheres [106]. In principle, binaries can always phase separate into a pure fcc crystal of small and a pure fcc crystal of big spheres, which leads to a total volume fraction of 0.74 (if boundary effects are neglected). A higher packing can be achieved for a suitable combination of α and X. Hopkins et al. found that the highest possible packing fraction is $\phi_{\max} \approx 0.91$ for $\alpha \approx 0.22$ and large X.

Let us now examine some special cases in terms of the size ratio α: We start with a hexagonal close-packed structure of big spheres and ask ourselves: How small need some smaller spheres be in order to fit into the holes of the bigger ones? First, we need to anticipate that there are holes of different sizes. Smaller spheres fit into the biggest holes if the size ratio obeys the inequality $\alpha < \sqrt{2} - 1 \approx 0.414$. For $\alpha < \sqrt{6}/2 - 1 \approx 0.225$, instead, even smaller holes in the closed packed structure could be filled [107], which leads to the high-density packing as described in the previous paragraph. Experiments have explored the region $0.1 < \alpha < 0.3$ at $\phi \approx 0.60$ [108], as well as $\alpha = 0.58$ for various compositions X and volume fractions ϕ [80, p.216]. Results for metallic alloys are available in the range $0.85 \lesssim \alpha \leq 1$ [104, 109–112]. Binary mixtures with larger size differences have been studied in experiments [113] and theory [114, 115] but are beyond the scope of this thesis.

Finally, we turn to some limiting values in terms of the relative volume fraction of big spheres. In terms of X, the one-component phase diagram is recovered for $X = 0$ (only small spheres) and $X = 1$ (only big spheres). Explicitly, there is no difference between $X = 0$ and $X = 1$ for colloidal hard spheres. Results from cell theory suggest that a fluid is most stable for $X \approx 0.5$ [115]. Further reading is found in reference [80, p.210-231] and [78, p.828].

2.4.4.1 Comparison to Metallic Alloys

Equivalent to (binary) mixtures in colloids are (binary) alloys in metals. An alloy is a mixture of chemical elements, where at least one element is a metal. Possible size ratios α between the elements of the periodic table range from $\alpha = 0.43$ to $\alpha = 1$ [116].

Depending on the composition of the alloy, there are three possible scenarios as sketched in figure 2.12. They can be separated into transformational, interstitial, and substitutional alloys. The transformational alloy has a completely different structure than the structure of the individual components. It may even be amorphous. Elements forming an interstitial alloy have to have very different sizes. If the sizes are quite similar, a substitutional alloy can be formed. The substitutional alloy can itself be separated into random, clustered or ordered alloys, depending on whether the (two) components are arranged in a random, clustered or regular order, respectively. In the case of the random ordered substitutional alloy, an empirical rule, the first Hume-Rothery rule, says that size differences up to 14% are allowed before the substitutional alloy becomes unstable [117]. In contrast to atomic or molecular systems, colloidal hard spheres do not consider electron valency or ionic charges, thus having fewer restrictions on crystal formation.

Barrat et al. [104] established three different phase diagrams for binary alloys with size ratios $0.85 \lesssim \alpha \leq 1$, visualized in figure 2.13. Starting from $\alpha = 1$, the first phase diagram that is observed is the *spindle* phase diagram: Big and small spheres are miscible in both the fluid and the solid state. With increasing temperature, the system goes from a solid phase to a fluid phase and vice versa. At fluid-solid coexistence, the solid phase has a higher amount of big spheres than the fluid phase. The *azeotropic* phase is found for $0.92 < \alpha < 0.94$. Details of the fluid-solid transition now depend on X. For some intermediate X, the fluid-solid transition is now at lower temperatures than for $X = 0$ or $X = 1$. In regions with fluid-solid coexistence, the solid phase may have a higher amount of smaller/bigger spheres for smaller/larger values of X, respectively. In the *eutectic* phase, big and small constituents are still miscible at the highest temperatures in the fluid but not in the solid. A solid now either consists of mainly small or big particles. Note here that the solid at larger X can still contain some small particles, while the solid at small X can only include a few large ones. All three phases are typically found in the range $0.85 < \alpha < 1$ [104, 109–112]. Barrat et al. state that below $\alpha = 0.85$, it is impossible to obtain a mechanically stable crystal [104]. Denton and Ashcroft found similar values for the eutectic phase but also studied smaller values of α and predict a disordered fcc to be the most stable phase in the region $0.76 < \alpha < 1$ [110].

In order to "translate" the findings on metallic alloys to colloidal suspensions, one could think of the mapping temperature to volume fraction by $(-T) \to \phi$. In terms of terminology, one could furthermore replace metallic *solids* to colloidal *crystals*. One should note here that there is a potential pitfall in the suggested translation:

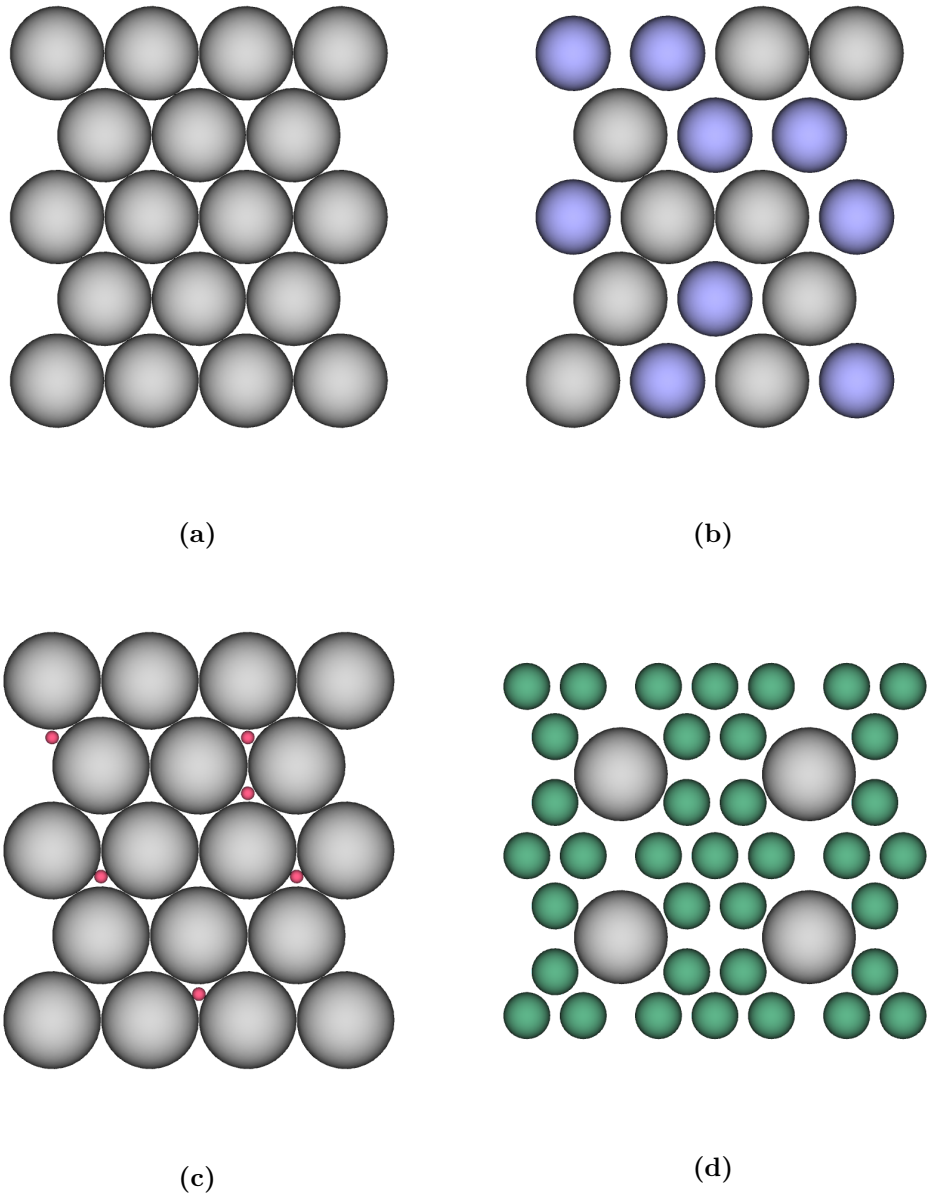

Fig. 2.12 Schematic showing (a) a pure metal, (b) a substitutional alloy, (c) an interstitial alloy and (d) a transformational alloy.

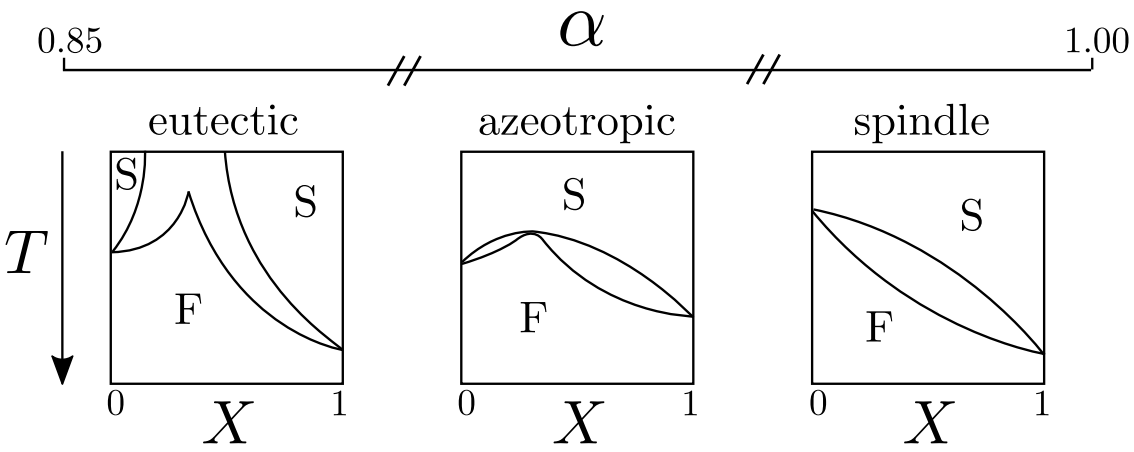

Fig. 2.13 Schematic phase diagrams of binary metallic alloys according to Barrat et al. [104]. These phase diagrams are given as a function of temperature T and relative volume fraction of big spheres X, and found for size ratios $0.85 < \alpha < 1$. For metallic alloys, the phase diagram shows regions of fluid (F) and solid (S) states. Adapted from reference [104]. More information in the text.

In the case of binary colloidal suspensions, the freezing point has to be the same for a system of only small (i.e., $X = 0$) or only big particles (i.e., $X = 1$). The freezing points in metallic alloys differ by a factor of α^3 between systems of only small and systems of only large spheres (cf., figure 2.13). This apparent discrepancy between metallic alloys and colloidal suspensions is due to units of pressure that are used to describe metallic alloys as pointed out by Denton at al. [110].

2.5 Nonequilibrium Properties of Hard Spheres

2.5.1 Digression: Nucleation Theory and Crystallization Kinetics

Nucleation is ubiquitous in daily life and directly connected to phase transitions. Examples are freezing of water, the formation of raindrops in the atmosphere or the condensation of a gas. Nucleation is an activated process [118]. While nucleation can occur in the bulk as *homogeneous nucleation*, the formation of a nucleus is often much likelier to occur at a surface – called *heterogeneous nucleation*. Within classical nucleation theory (CNT), the rate of forming a nucleus

$$R_{CNT} \propto \exp(-\Delta G/k_{\mathrm{B}}T) \tag{2.18}$$

is proportional to an exponential factor, where ΔG is the free energy cost of creating the nucleus. A prefactor (not shown here) in front of the exponential itself consists of three factors, namely, the number density of molecules, the rate of molecules entering or attaching to the nucleus and the so-called Zeldovich factor [118]. Nucleation

rates have been studied experimentally [62]. The energy barrier ΔG depends on two terms: A bulk term and a surface term. In order to form a nucleus, a surface is formed between the nucleus and the rest, which is energetically unfavorable. The nucleus is only stable once it reaches a critical size. In the case of homogeneous nucleation and a spherical nucleus, the equation for the Gibbs free energy cost reads

$$\Delta G_{\mathrm{hom}} = 4\pi R_n^2 \gamma_{lc} - \frac{4\pi}{3} R_n^3 \rho_n \Delta\mu \tag{2.19}$$

with the radius of the nucleus R_n, the number density of the bulk phase ρ_n, the difference in chemical potential between the bulk phase (liquid) and the phase of the nucleus (crystal) $\Delta\mu$, and the tension of the crystal-liquid interface γ_{lc}. Instead of being spherical, the nucleus of a colloidal crystal might rather be ellipsoidal and contains about 20 particles [62]. The energy barrier for heterogeneous nucleation ΔG_{het} at a flat surface reads

$$\Delta G_{\mathrm{het}} = G_{\mathrm{hom}} f(\theta^{'}) \,. \tag{2.20}$$

A flat surface is a reasonable and relevant assumption for heterogeneous crystallization of colloids since they are typically confined between two plates in a rheometer or in contact with a microscope coverslip. The function $f(\theta^{'})$ is a monotonically increasing function of the contact angle $\theta^{'}$. The limiting cases of the function $f(\theta^{'})$ are $f(\theta^{'} = 0°) = 0$ and $f(\theta^{'} = 180°) = 1$. The former is called *wetting* and the latter case is called *drying*.

2.5.2 The Colloidal Glass Transition

In contrast to the equilibrium phase behavior (cf., section 2.4.1), experiments on colloidal PMMA spheres [70] did not show crystals for some values of the volume fraction ϕ above the melting point $\phi_{\mathrm{mp}} = 0.545$. Instead, a metastable long-lived colloidal glass is found above $\phi_g \approx 0.58$, where ϕ_g is the glass transition volume fraction. In very simple words, a colloidal glass has a disordered structure similar to that of a fluid but behaves more like a solid.

A phase diagram for hard spheres including the glass transition is shown in figure 2.14. Reported values of ϕ_g include 0.56, 0.57, 0.59, and more values are listed, for example, in a book of Mewis and Wagner [7, p.96]. Computer simulations from Woodcock indicate a value $\phi_g \approx 0.57 - 0.58$ [71]. Differences in the values can originate, among other reasons, from uncertainties in determining absolute volume fractions [7, p.96] or effects from polydispersity [78, p.912-913]. The glass state does not continue up to the maximum packing for monodisperse spheres at $\phi_{\mathrm{max}} = 0.74$ but stops at $\phi_{\mathrm{rcp}} \approx 0.64$.

The random close packing ϕ_{rcp} is the maximum packing that a random configuration of spheres can reach. The random close packing is found as an empirical quantity and one might argue that a quantity whose name contains both the words

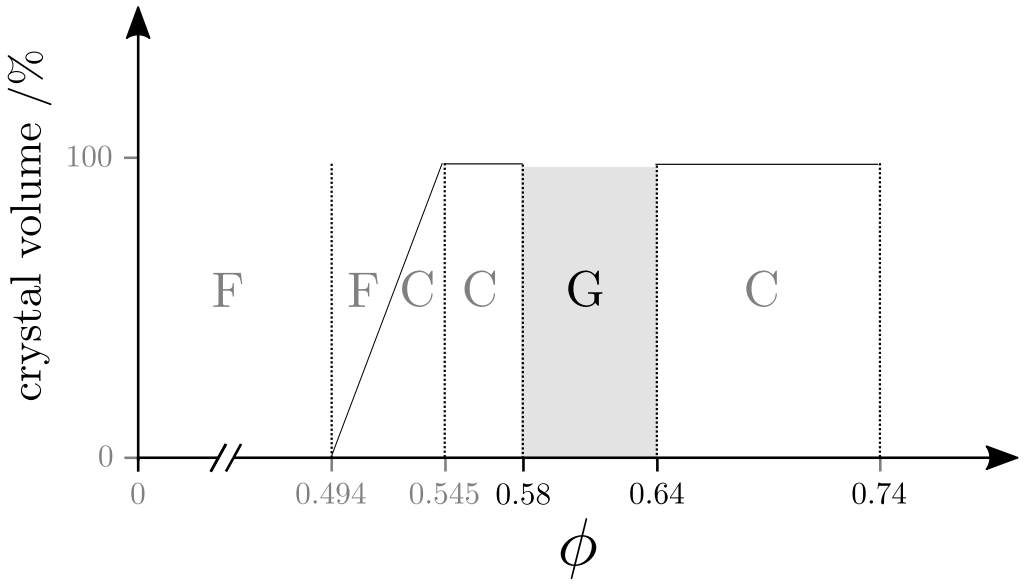

Fig. 2.14 Schematic nonequilibrium phase diagram of hard spheres incorporating the glass transition, which was first observed by Pusey and van Megen [65, 70]. In addition to the equilibrium phase diagram (section 2.4), an amorphous glassy state (G) is observed above the glass transition at $\phi_g \approx 0.56 - 0.59$, reaching up to the random close packing at $\phi_{\mathrm{rcp}} \approx 0.64$.

"random" and "packing" is an ill defined quantity [119, p.90]. It is very difficult or even impossible to define random close packing [50, p.198]. In fact, ϕ_{rcp} depends on the preparation protocol [120] and polydispersity [87, 91, 121]. Estimates for ϕ_{rcp} until the year 1983 range between $\phi = 0.61$ and $\phi = 0.665$ [122]. An empirical equation for ϕ_{rcp} depending on polydispersity was given by Desmond and Weeks [123]. Glasses can be considered as jammed systems [124]. Interestingly, a maximum jammed system can be defined rigorously and the maximum jamming sphere packing is at $\phi_J = 0.636$ [125, 126].

It has been argued that the glass transition is an effect of gravity. In fact, samples were able to crystallize in microgravity with volume fractions above ϕ_g and these crystals survived even when put back to normal gravity [127, 128]. A glass transition is often viewed as a dynamical transition [72] where particles are kinetically arrested (and therefore cannot reach equilibrium). Glasses also exist outside the colloidal world. Window glass is ubiquitous and molecular or metallic glasses are obtained by cooling a liquid below its freezing temperature with a very high cooling rate. While molecular glasses can be considered as supercooled liquids, colloidal glasses could be regarded as "supercompressed" [129]. Up to now, the physics of the colloidal glass transition and its link to molecular glasses remain to be fully understood [129, 130].

Glasses are out-of-equilibrium systems and their properties depend on the preparation (i.e., how fast they were "supercompressed"). The physics of glasses are

time-dependent, a phenomenon called *aging*. Their state depends on history and thus glasses "know their age."

Colloidal glasses can be observed easier than molecular counterparts and, therefore, serve as a convenient model for studying glasses. For this purpose, polydisperse samples are used to avoid crystallization [131]. The spread of polydispersities is relatively large. Researchers used, for example, polydispersities of 6% [132], 7% [133], 10% [134], 12% [12], 20% [135] and 23% [136]. Above a terminal polydispersity (cf., section 2.4.3, $\delta_t \gtrsim 8\%$) the glassy state can be the equilibrium state [137]. Besides polydisperse systems also binary mixtures are used to study glasses (e.g., [97, 138–140]).

Experimental methods to elucidate the physics of the glass transition include rheology (section 2.5.4) and confocal microscopy (section 2.5.3). Further reading in [7, 129, 130, 141, 142].

2.5.3 Microscopic Observations

Brownian motion, as characterized by $\langle \Delta x^2 \rangle_{t,n} = 6D\tau$ (equation (2.2)) is only observed for dilute suspensions. For concentrated colloidal suspensions, the MSD exhibits different trends depending on the lag time. This is illustrated in the right part of figure 2.15.

For very short and very large lag times τ, the MSD is still linear (i.e., $\langle \Delta x^2 \rangle \propto D_{l,s}\tau$), but the long-time diffusion coefficient D_l is considerably smaller than the short-time diffusion D_s, that is, $D_l \ll D_s$. At intermediate times, the MSD exhibits a plateau (cf., e.g., [143]). The inflection point inside the plateau has been used to define a characteristic time [144]. Confocal microscopy studies reveal that for $\phi \gtrsim \phi_g$, particles are "trapped in cages" formed by their neighbors [145, 146], as illustrated in the middle part of figure 2.15. Particles might only rearrange due to collective motion [147], which has been proposed by Adam and Gibbs [148]. The size of the collectively moving group of particles increases as the glass transition $\phi \approx \phi_g$ is approached [149]. Only for long times, particles are able to exit their cages, leading to a slow diffusive behavior.

Hence, timescales play an important role. Characteristic times can also be observed, for example, by mode-coupling theory (MCT) [150] or light scattering [66, 67, 72] by analyzing the decay times of the intermediate scattering function (ISF). Without going further into detail, the ISF develops a plateau, similar to the one in the MSD (cf., figure 2.15, middle right). There is always a relaxation for short times, the so-called β relaxation process with characteristic time τ_β. The second decay is the so-called α process, characterized by τ_α, and interpreted as particles leaving their cages [7, p.110].

Generally speaking, the dynamics of (colloidal) glasses are found to be non-ergodic and heterogeneous, giving rise to the term *dynamical heterogeneities*. Dynamical heterogeneities are found in quiescent samples and are manifested in a non-Gaussian

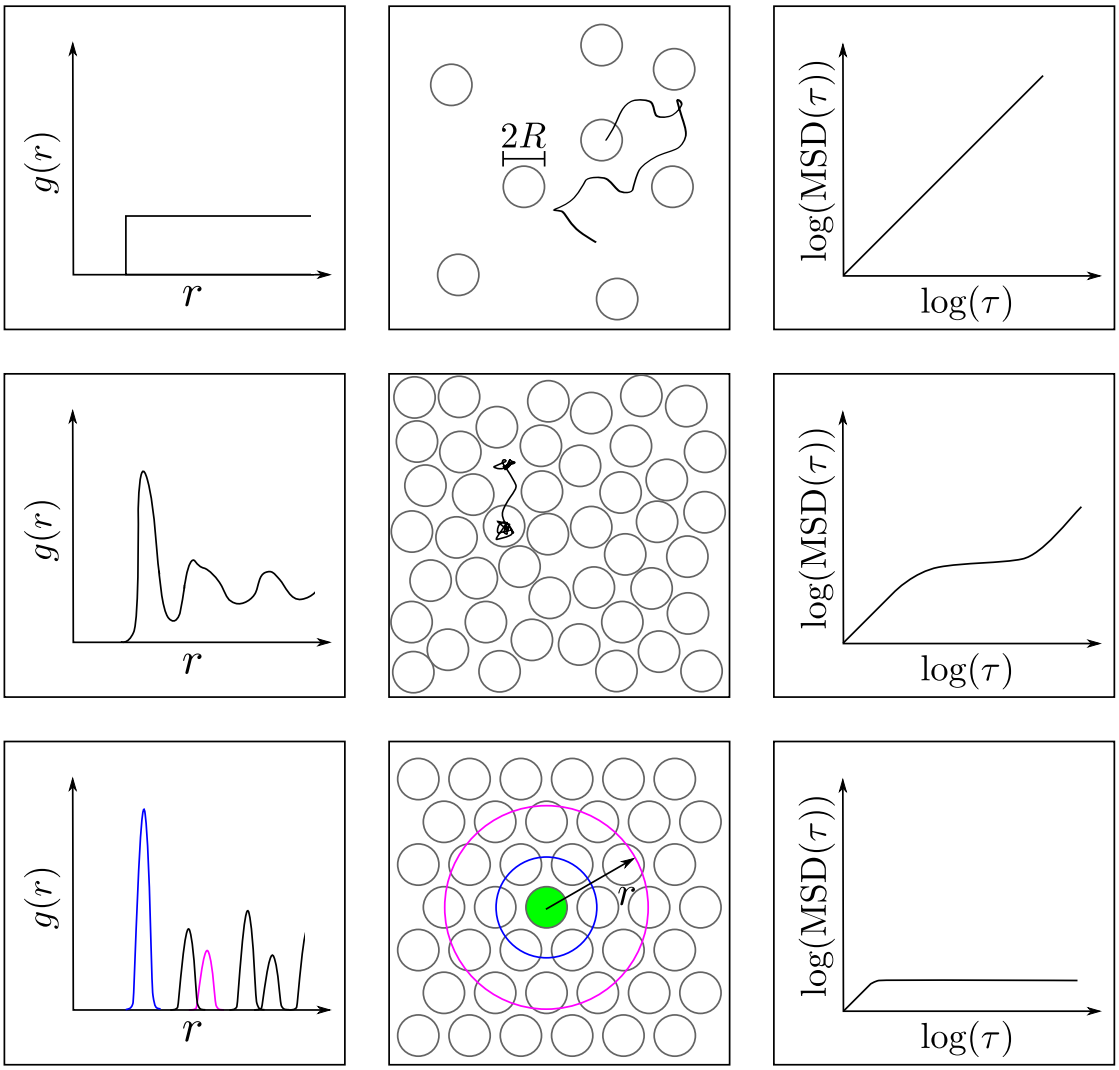

Fig. 2.15 Comparison of (from top to bottom) a fluid, a glass, and a crystal. Shown are sketches of particle arrangements (central column) together with corresponding pair correlation functions $g(r)$ (left column) and mean squared displacements (right column). The distance r is indicated inside the central box in the bottom. The pair correlation function measures how likely it is to find a particle at a distance r.

probability distribution of particle displacements [132]. They are observed in confocal microscopy experiments with PMMA particles [132, 145, 147], including binary mixtures [97], as well as in (molecular dynamics) simulations [151, 152] and (mode-coupling) theory [153]. Dynamical heterogeneities are also observed in colloidal gels [154–156] and other soft materials as well as under shear. Under shear, a measure for local (heterogeneous) dynamics are deviations from locally affine motion [157, 158].

2.5.4 Rheological Observations

The very basic rheological observation is that the viscosity of colloidal suspensions increases monotonically with increasing volume fraction ϕ and diverges for high ϕ.

For very dilute suspensions an equation has been given by Einstein, namely, $\eta_r = 1 + 2.5\phi$. Here, $\eta_r = \eta/\eta_0$ is the relative viscosity where η is the viscosity of the suspension and η_0 the viscosity of the dispersion medium. Improvements for semi-dilute suspensions have been made by Batchelor and Green, adding a term that is quadratic in ϕ. One out of many (phenomenological) models for concentrated suspensions is the Krieger-Dougherty model [159]

$$\eta_r = \left(1 - \frac{\phi}{p}\right)^{-[\eta]p} \tag{2.21}$$

with parameters $[\eta]$ and p. Other models are, for instance, the Doolittle-, Quemada- or mode-coupling model [160, 161]. Depending on the model used, the viscosity is usually expected to diverge at ϕ_g or ϕ_{RCP} [161]. Differences possibly depend on friction between particles [162, 163].

It has been shown by Krieger [159] that concentrated suspensions of differently sized colloidal spheres can be collapsed onto a master curve if plotted against dimensionless quantities [2, p.126]. In essence, to compare suspensions of different sizes, the shear stress σ, as well as the shear modulus $G^{'}$ and $G^{''}$, is given in units of $(k_{\mathrm{B}}T)/R^3$.

Similarly, the shear rate $\dot{\gamma}$ should be rescaled. A size-independent variable is the Péclet number Pe. Explicitly,

$$\mathrm{Pe} = \dot{\gamma}\tau_{\mathrm{B}} = \frac{6\pi\eta_0\dot{\gamma}R^3}{k_{\mathrm{B}}T} \propto \dot{\gamma}R^3 \tag{2.22}$$

with R being the particle radius, η_0 the viscosity of the dispersion medium under the condition of $\dot{\gamma} \to 0$, the Boltzmann constant k_{B} and the absolute temperature T. The Péclet number is a measure of whether shear ($\mathrm{Pe} > 1$) or Brownian motion ($\mathrm{Pe} < 1$) dominates. For oscillatory experiments, the shear rate $\dot{\gamma}$ is replaced by the angular frequency ω giving rise to the Péclet number for oscillatory shear

$$\mathrm{Pe}_{\omega} = \omega\tau_{\mathrm{B}} = \frac{6\pi\eta_0\omega R^3}{k_{\mathrm{B}}T} \propto \omega R^3\,. \tag{2.23}$$

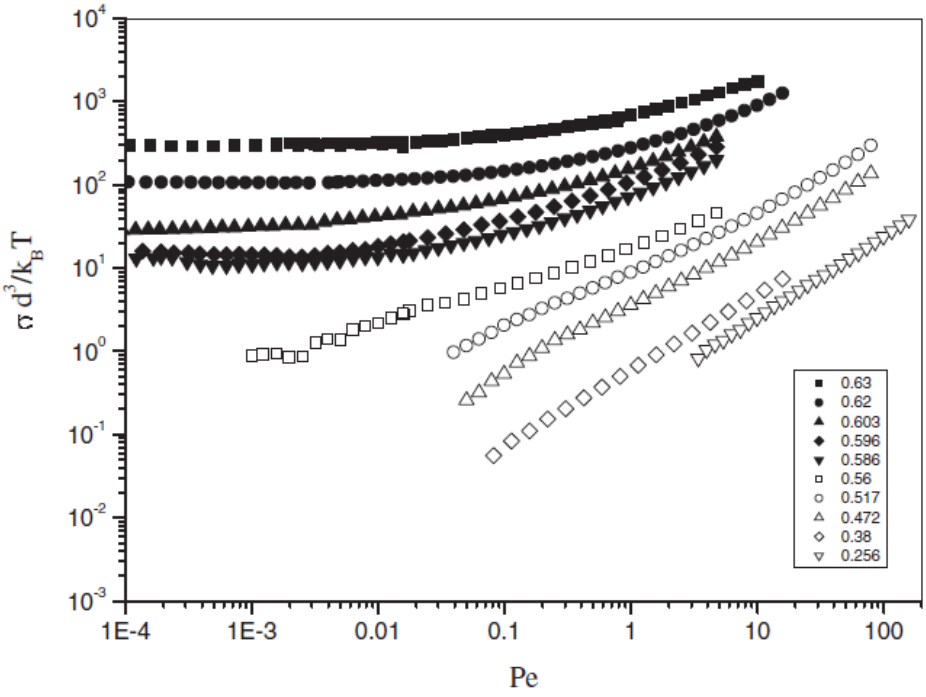

Fig. 2.16 Flow curves of liquid (open symbols) and glassy (filled symbols) colloidal suspensions. Volume fractions are given in the legend. Note that the ordinate is scaled with the diameter and not the radius. Figure reproduced from [164]. DOI: 10.1088/0953-8984/16/38/013 © IOP Publishing. Reproduced with permission. All rights reserved.

Colloidal suspensions do not only show a diverging viscosity above the glass transition but also a finite yield stress. This may, for instance, be seen from a set of flow curves of various volume fractions as shown in figure 2.16. Similarly, once shear on colloidal suspensions ceases, history-dependent residual stresses are left behind [165].

There are further characteristic signatures in other rheological variables close to the glass transition: Decay times can be deduced from rheology, typically from a dynamic frequency sweep (DFS). The response of colloidal suspensions to a DFS is shown in figure 2.17. The frequency where the viscous modulus G'' has a minimum corresponds to τ_β^{-1}, and the frequency where G'' has a peak (sometimes outside the experimental window) corresponds to τ_α^{-1} [7, p.111]. The frequency dependence of the elastic moduli G' is less pronounced close to the glass transition [135]. Relevant DFSs are also given in reference [166, fig. 5].

A DFS is performed at small strain amplitudes in the linear regime. The linear regime can be inferred from a dynamic strain sweep (DSS) as the region in which both G' and G'' are independent of strain amplitude γ_0. This is schematically shown in figure 2.18a. In a DSS, local rearrangements become irreversible above a

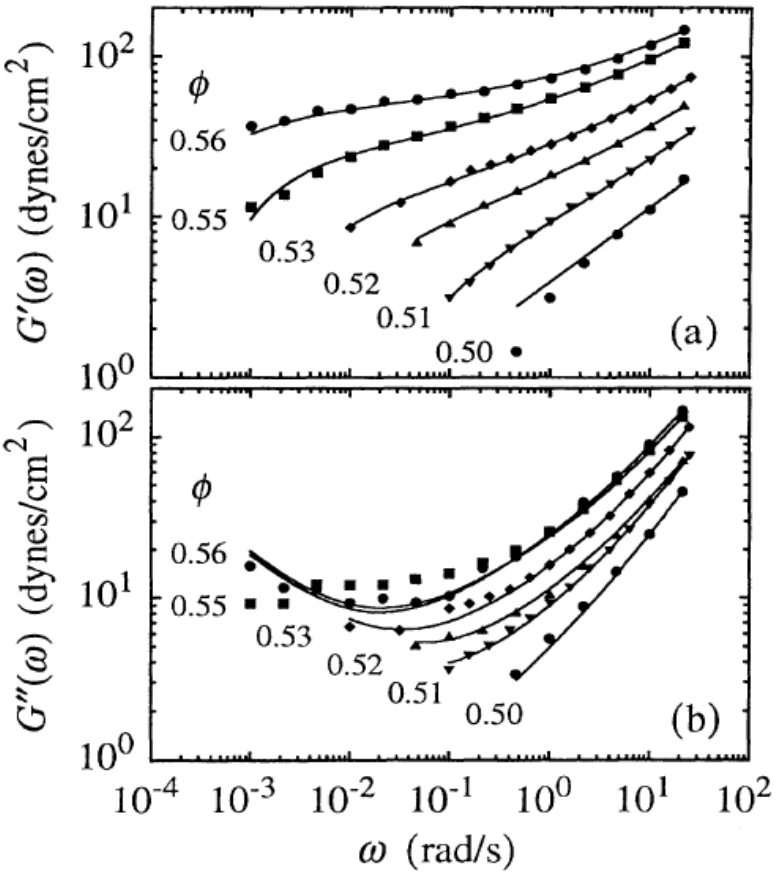

Fig. 2.17 Storage $G^{'}$ and loss modulus $G^{''}$ as a function of frequency for different volume fractions. Reprinted figure with permission from T. G. Mason and D. A. Weitz, Physical review letters, 75, 2770-2773, 2010. Copyright (1995) by the American Physical Society.

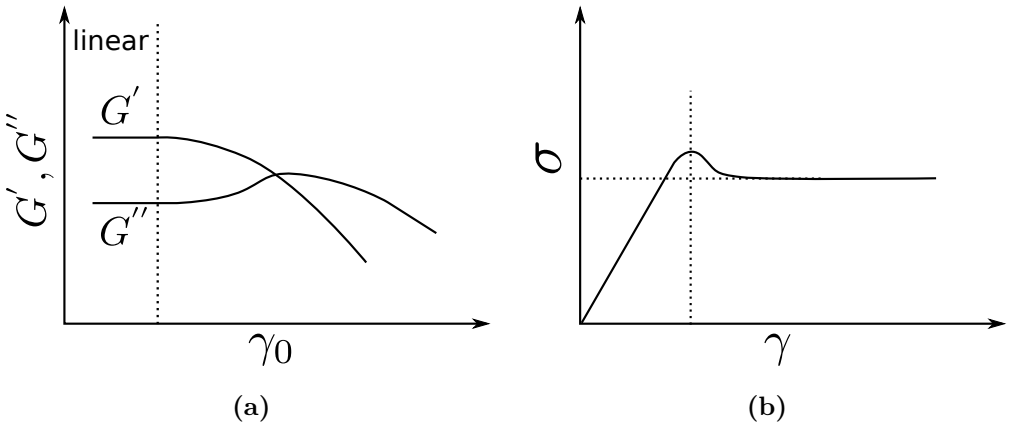

Fig. 2.18 Schematic response of colloidal glasses to (a) a DSS and (b) a start-up experiment. In the linear regime of the DSS, both $G^{'}$ and $G^{''}$ are independent of the strain amplitude γ_0.

certain yield strain, roughly located where $G^{'}$ and $G^{''}$ are crossing. Similar behavior is observed in steady shear flow. A schematic start-up experiment, depicted in figure 2.18b, shows a linear regime, followed by a stress overshoot and a regime with constant stress. In the linear regime, the stress σ increases linearly with strain γ. The height and position of the stress overshoot depend on the applied shear rate and volume fraction [167–169]. At the peak of the stress overshoot the microscopic cage – in which particles are trapped – is maximally distorted [169].

The next sections shall give a glimpse of some selected rheological topics, which are of special interest and to introduce relevant nomenclature. A better and broader overview of colloidal suspension rheology can be found, for instance, in reviews on yield stress materials [33] or amorphous systems [170].

2.5.4.1 Shear Thinning and Shear Thickening

Shear thinning (shear thickening) refers to a decrease (increase) of the viscosity η with increasing shear rate $\dot{\gamma}$, as illustrated in figure 2.19. Depending on whether the viscosity increases continuously or discontinuously, shear thickening is termed either continuous shear thickening (CST) or discontinuous shear thickening (DST). The (oversimplified) picture is the following: In the quiescent state, the colloids are arranged randomly but homogeneously. In the shear shinning regime, medium-concentrated dispersions are able to align in the direction of shear. Particles can be thought of moving in straight lanes, leading to fewer collisions and a reduced viscosity. At high shear rates, the lanes can no longer be maintained and the sample shear thickens. Particles are pushed into close contact and, due to hydrodynamic interactions, form so-called hydroclusters [171]. The critical shear rate, above which shear thickening sets in, decreases as a function of ϕ [7].

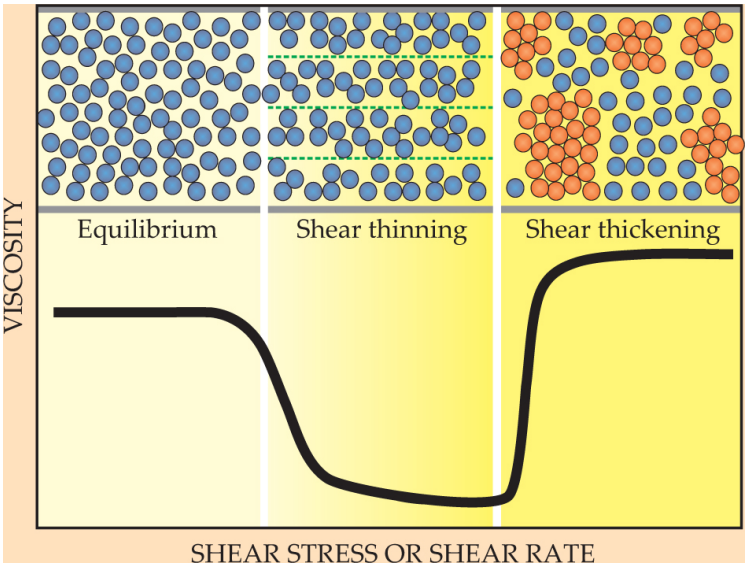

Fig. 2.19 Schematic diagram showing the viscosity as a function of shear rate for colloidal dispersion, together with the corresponding microstructure of the sample. In the shear thinning regime, particles align in layers. At higher shear stresses/rates, particles form "hydroclusters" (red) and shear thicken. Reproduced from Physics Today 62, 10, 27 (2009), with the permission of the American Institute of Physics.

But shear thickening can also be evaluated as a function of the shear stress instead of shear rate. Interestingly, the critical shear stress σ^* (also termed "onset stress"), above which shear thickening sets in, is found to be independent of the volume fraction [7]. Instead, it depends on the particle diameter. For instance, the critical shear stress is found to be $\sigma^* \approx 200\,\mathrm{Pa}$ for colloidal particles of size $2R = 404\,\mathrm{nm}$ and $\sigma^* \approx 0.5\,\mathrm{Pa}$ for $2R = 4500\,\mathrm{nm}$ [163].

Dynamic shear thickening is thought to be related to particle friction and sets in above $\phi \approx 0.55$ [162]. While contacts are lubricated at small strain rates, they get frictional for high shear rates or stresses. Therefore, the roughness of the particle surface plays a role [172]. Using numerical simulations, a diagram has been constructed, showing regions of shear thinning and thickening as a function of ϕ and σ for soft particles [139, 173]. Shear thinning and thickening can also be seen in oscillatory experiments. For instance, in a dynamic strain sweep, the region of shear thinning corresponds to the regime where the slope of $G^{'}$ (in a log-log plot) is twice as big as the slope of $G^{''}$. Shear thinning and thickening is reversible and should not to be mixed with thixotropy, which refers to a change of viscosity with time. Shear thickening was originally known as "dilatancy" but this term should also be avoided since it relates to an increase in volume, which is not needed for shear thickening [174].

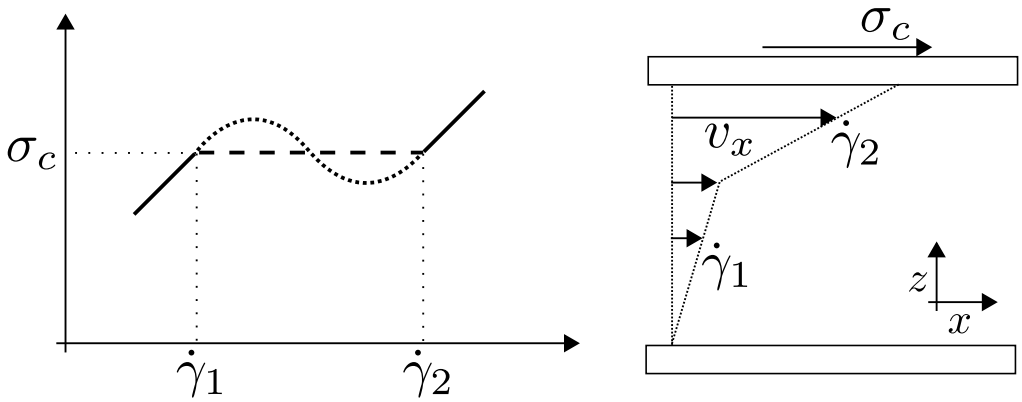

Fig. 2.20 (Left) Possible flow curve for a shear banding sample, where the same stress (in this case σ_c) corresponds to at least two shear rates $\dot{\gamma}_1$ and $\dot{\gamma}_2$. The dotted part of the flow curve is unstable [175] and would in practice be replaced by a horizontal line. Explicitly, the fraction of the dotted line with a negative slope is unstable, whereas the part with a positive slope is metastable. (Right) Illustration of a corresponding velocity profile.

2.5.4.2 Shear Banding and Flow Inhomogeneities

In order to describe shear banding, it may be helpful to recall the picture of simple shear (cf., figure 1.6). Complex materials like colloidal suspensions do not necessarily flow with simple shear but show flow inhomogeneities, that is, deviations from the simple linear shear profile. During shear banding, parts of the sample undergo larger strain deformations than other parts of the sample. Shear banding can be rather easily explained if two shear rates $\dot{\gamma}$ correspond to the same (critical) shear stress σ_c, as depicted in figure 2.20. Then, if the stress $\sigma = \sigma_c$ is applied, the sample can split into two regions, one with $\dot{\gamma} = \dot{\gamma}_1$ and a second one with $\dot{\gamma} = \dot{\gamma}_2$ (cf., figure 2.20). For the special case, where the applied stress is equal to the yield stress (i.e., $\sigma_c = \sigma_y$), one region with vanishing shear rate (i.e., $\dot{\gamma} = 0$) is expected [176].

Shear banding should refer to the nonlinear rheology of the sample and not be mixed with an inhomogeneous stress field that could be imposed by the geometry. Shear banding is observed in many systems including surfactant and polymer solutions, foams, biological gels, and granular media [177]. Inhomogeneous flow has also been seen in metallic glasses [178, 179], with enhanced diffusion [180] and density fluctuations [181] inside the shear bands. Inhomogeneous flow is not always denoted by the term shear banding. Related terms are layers, stripes and fractures [177]. The shear bands in metals typically have sharp borders, whereas, in colloids, the transition between shear bands might be rather continuous [182].

One might distinguish between transient and steady-state shear banding. Steady-state shear banding is usually attributed to a non-monotonic flow curve (cf., figure 2.20). On the other hand, there are experiments showing transient but no

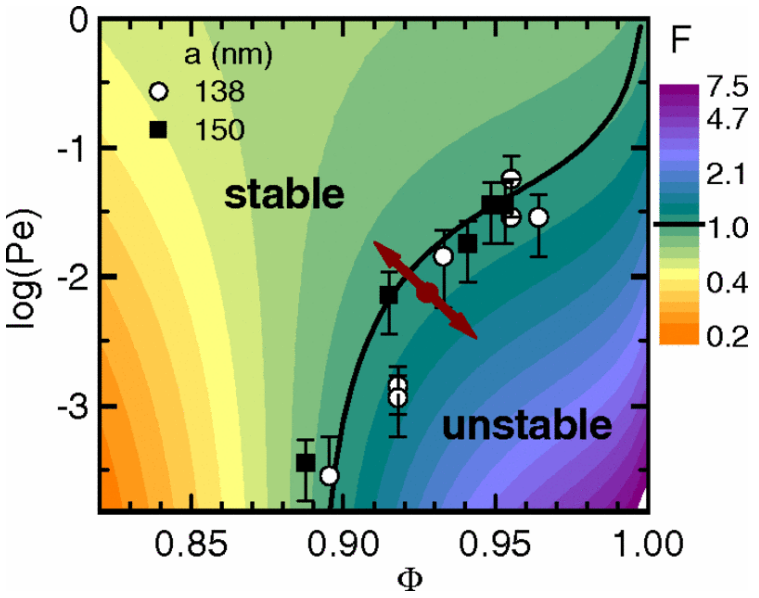

Fig. 2.21 The line shows the critical flow rate that separates the stable from the unstable regime according to reference [186]. Here, $\Phi = \phi/\phi_m$, with $\phi_m \approx 0.67$ being the volume fraction after sedimentation. Colors indicate values of the parameter F (cf., [186], Eq. 7) and instability sets in for $F > 1$. Symbols are experimental values from [186]. Reprinted figure with permission from R. Besseling, L. Isa, P. Ballesta, G. Petekidis, M. E. Cates, and W. C. K. Poon, Phys. Rev. Lett., 105, 268301, 2010. Copyright (2010) by the American Physical Society.

steady-state shear banding [183–185].

The remaining part of this subsection will deal with flow inhomogeneities on glassy colloidal suspensions, with a special focus on low shear rates or low Péclet numbers.

In 2007, Besseling et al. reported that discrepancies between the global rheology and the measured local shear rate could be due to shear banding [182]. In their case, shear banding occurs at shear rates lower than $\dot{\gamma} = 0.01\,\mathrm{s}^{-1}$ and is reflected in a nonlinear but smooth velocity profile. Three years later, Besseling et al. explain shear banding by flow-concentration coupling [186]. Their results are summarized in figure 2.21, where the stable and unstable flow regimes are shown as a function of volume fraction and Péclet number. Thus, flow gets unstable for volume fractions $\phi \gtrsim 0.6$ and low Péclets, that is, $\mathrm{Pe} \lesssim 1$ [186]. Additionally, the unsteady flow observed by Besseling et al. can be time-dependent and typically stays unsteady even at long times.

Experiments on a carbopol gel, which is a yield stress fluid made of polymer, show transient shear banding that eventually becomes stable after a long time [183]. Shear banding at low rates has also been observed in simulations [187], where the sheared system splits into a static and a fluidized region if the corresponding shear stress

is below the static yield stress (i.e., $\sigma(\dot{\gamma}) < \sigma_y$). In the abovementioned studies, inhomogeneous flow or shear banding sets in for low rates. Interestingly, also the opposite has been observed. Chikkadi et al. report that in a colloidal PMMA glass ($\phi \approx 0.60$), shear banding sets in above a critical shear rate $\dot{\gamma}^* = \dot{\gamma}\tau$, where τ is the structural relaxation time of the glass [188]. Below $\dot{\gamma}^*$, homogeneous flow is observed. Their results are for strains larger than 1, corresponding to the steady state. Strain heterogeneities for higher rates have also been observed with neutron scattering [140]. Similarly, molecular dynamics simulations on a non-aging glassy Lennard-Jones fluid also observe shear banding at high rates [189].

Additionally, Fuereder et al. showed that transient shear banding in a start-up experiment can be seen at strain values around the stress overshoot, and bigger overshoots are related to more pronounced shear banding. For very small as well as larger strains, a linear profile is observed [189]. In their simulations, they find structural differences in different shear bands [189]. Shear banding, in this case, might be due to spatial heterogeneities. Shear banding depends on the properties of the studied system. Experiments on core-shell particles, for example, have not shown shear banding [190], which is possibly attributed to the softness of the interaction potential [187]. Recent results suggest that also inertia and aging, often neglected in theoretical studies, can play an important role [191].

3

Confocal Laser Scanning Microscopy: Now You See Me

Microscopy is used to visualize objects that are too small to be observed by the naked eye. Optical microscopes based on the knowledge of diffraction were founded by Abbe in 1873 [192]. A specific arrangement of lenses ensures proper illumination of the sample and produces a magnified image of the object. Nevertheless, light microscopy also has fundamental resolution limits. The very basic limit originates from the diffraction of light, which only allows objects to resolved whose size is of the order of the wavelength of light.

This chapter deals with a specific class of optical microscopes, namely, *confocal laser scanning microscopes* (CLSM). As can be inferred from the name itself, the invention of the confocal principle, laser sources, fast scanning devices, and video acquisition were necessary for today's success of CLSMs. The confocal principle was patented by Minsky in 1957 [193], but the idea supposedly has been there before [194]. The first laser-scanning confocal microscope was used by Davidovitz and Egger in 1969, and corresponding microscopes became commercially available in 1982 [194]. The following sections will describe the basic principle (section 3.1) and experimental setup (section 3.2) of a CLSM. After a discussion on the achievable optical resolution (section 3.3), we will provide a brief survey of particle tracking (section 3.4), an important application of CLSM.

3.1 Confocal Principle

In short, a CLSM illuminates the sample point-wise with a laser, rejects out-of-focus light with a pinhole, collects the signal with a detector, and post-renders the image with the help of computational power. The biggest difference between confocal laser scanning microscopy (CLSM) and conventional optical microscopy is an additional pinhole that rejects out-of-focus light. The confocal principle is illustrated in figure 3.1. Only photons originating from the focal point pass the pinhole, while light from outside the focal point cannot pass the pinhole. There are ways to move the focal point in the x-, y-direction. An image of the sample is then reconstructed pixel by pixel. It is also possible to move the focal point in the z-direction. Many 2D images can thus be grouped to form a z-stack, which enables a 3D-reconstruction of the sample. This is illustrated in figure 3.2. Scanning always takes a finite time, and therefore, the sample should ideally not move during the scanning process.

3.2 CLSM Setup

The schematic setup of a CLSM is shown in figure 3.3. The sample shall be fluorescent, and from now on, CLSM will refer to fluorescent confocal laser scanning microscopy.

A laser acts as a light source. Laser power in the range of a few milliwatts (mW) is sufficient, else the florescent dye might easily bleach. The laser beam is expanded to use the full width of the objective. A filter after the laser, as sketched in figure 3.3, might remove tails of the beam. The laser beam is then reflected by a dichroic mirror and passes the rotating mirrors. There are several realizations of scanning the beam in the x- and y-direction (three possibilities are presented in reference [194]) and the scanning part of the CLSM is here schematically represented by two rotating mirrors. Then, the light passes through the microscope, where the objective focuses

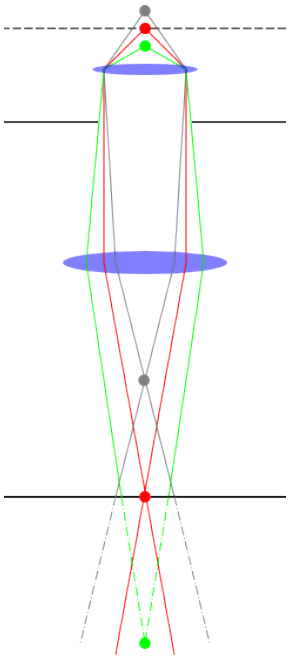

Fig. 3.1 Illustration of the confocal principle. Light from different vertical positions (gray, red, green) is imaged by an optical system (indicated by two blue lenses). Light from outside the focal plane (dotted line) is rejected by the pinhole (solid line at the bottom). Only light originating from the focal point (red) can pass through the pinhole. Reprinted from reference [195].

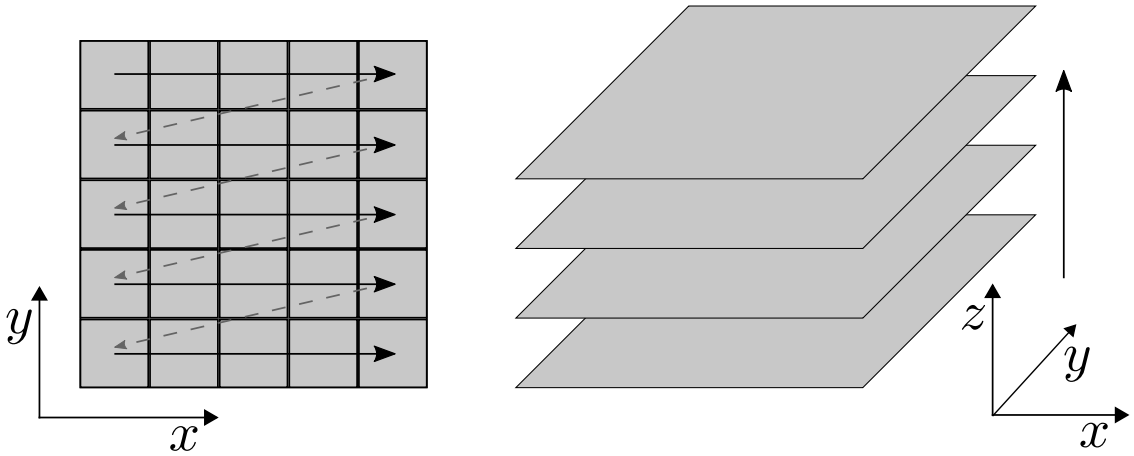

Fig. 3.2 Illustration of the scanning process and image formation. The left-hand side shows how pixels are scanned in the x- and y-direction to form a 2D image. On the right-hand side, many images from different z-heights are combined into a three-dimensional z-stack.

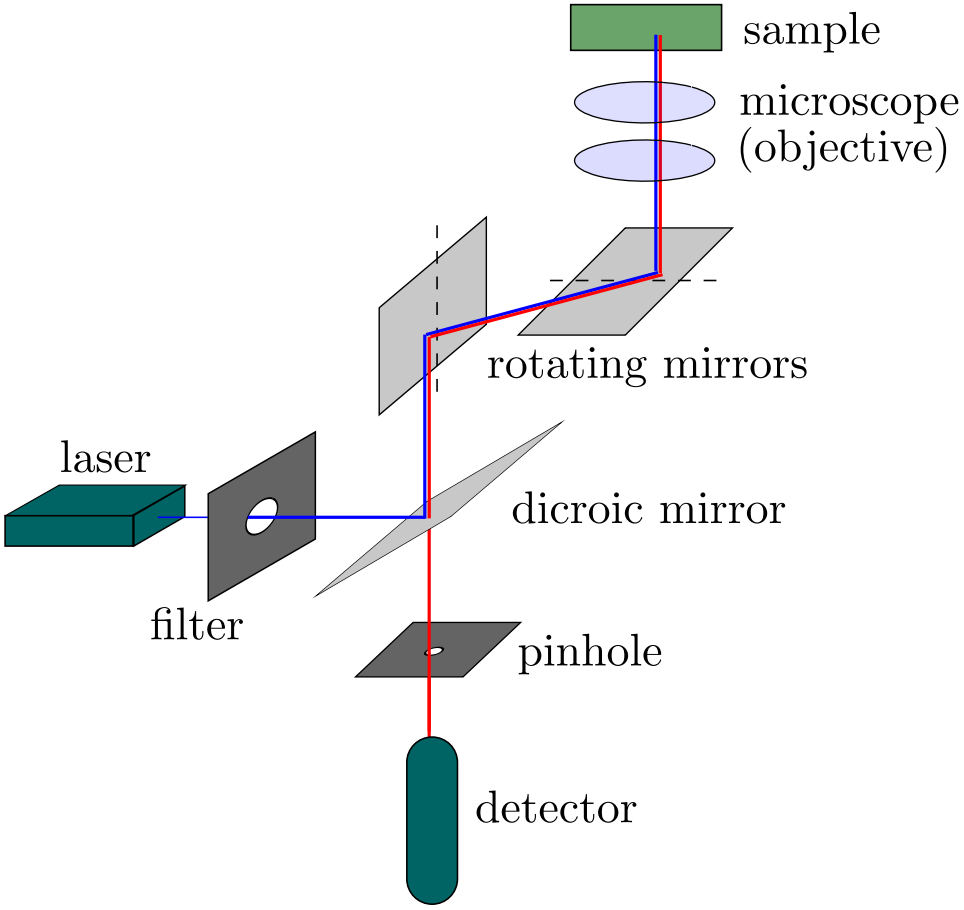

Fig. 3.3 Schematic setup of a CLSM. The sample is illuminated with a laser. A filter after the laser can change the profile or intensity of the beam. Scanning is done by means of two rotating mirrors. Fluorescent light is collected with the objective and guided to the detector. The dichroic mirror (below the rotating mirrors) reflects laser light (blue) and lets fluorescent light (red) pass through. Only light originating from the focal point inside the sample can pass the pinhole.

the light into the sample. Once the light reaches the focus spot inside the sample, fluorescent molecules are excited. Fluorescence is non-directional. For an objective, with a numerical aperture of NA = 1.4, only 30% of fluorescent photons can be collected by the objective [196, p.22]. Fluorescent photons collected by the objective then travel back along the same path the illumination photons took until they reach the dichroic mirror. The dichroic mirror is chosen such that it now transmits the fluorescent light. Afterward, the pinhole rejects out-of-focus light, therefore only photons originating from the focus spot in the sample (as well as some stray-light after the pinhole) are collected by the detector and translated to an electronic signal.

The scan-rate can be increased if one scanning-mirror is replaced by an acousto-optic deflector (AOD). In an AOD, a standing sound wave creates density patterns that act analogous to line gratings. By changing the frequency of the sound wave, the angle of the first diffraction order can be varied. The drawback of an AOD is that the diffraction angle also depends on the wavelength of the optical light. Thus, the implementation of the AOD has to be handled with care: For fluorescent samples, the wavelength of the light illuminating the sample λ_i and the wavelength of the fluorescent light λ_f originating from the sample are different, that is, $\lambda_i \neq \lambda_f$. Thus, they would be diffracted by the AOD with different angles. The fluorescent light, therefore, cannot move back completely along the same path that the illumination light took. If, for example, the AOD provides the fast scanning in the x-direction, then the fluorescent light from the sample is therefore only de-scanned in the y-direction, and the confocal pinhole is substituted by a confocal slit. This principle is shown in figure 3.4.

Besides the setup shown here, there exist several further variants like the Nipkow-scanning disk or systems with different illumination or detection components [194, 196].

3.3 Optical Resolution

If chromatic and spherical aberrations are eliminated, then the resolution of an optical system is ultimately limited by diffraction. The image of an ideal point-source, created by an ideal optical system, is not a point but corresponds to an Airy pattern. The intensity distribution of the Airy pattern can be seen in figure 3.5a,d. Two point-sources can be distinguished if one can distinguish their Airy discs (figure 3.5b). For two point-sources, there are different criteria for the diffraction limit, including the Rayleigh-, Abbe-, and Sparrow-criterion. They are also visualized in figure 3.5c, and more information can be found in reference [197]. Depending on the criterion, the equations for the optical resolution only differ in a numerical prefactor.

The lateral resolution is given by

$$d_{xy} = \mathcal{O}(1)\frac{\lambda}{\mathrm{NA}} \tag{3.1}$$

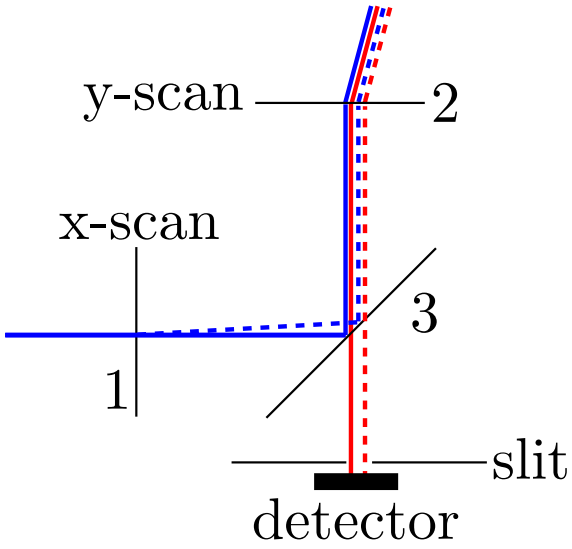

Fig. 3.4 Schematic of the confocal slit system as used with an AOD (x-scanning, 1) and a galvo-mirror (y-scanning, 2). Light from the laser with wavelength λ_i (blue) is scanned in the x- (AOD, 1) and y-direction (galvo, 2) on its way to the sample (to the top, not shown here). The solid and dashed lines correspond to two different points inside the focal plane of the sample. Fluorescent light originating from the sample with $\lambda_f \neq \lambda_i$ (red) is not de-scanned by the AOD (since the diffraction angle of the AOD depends on the wavelength) but passes through the dichroic mirror (3) and the confocal slit onto the detector.

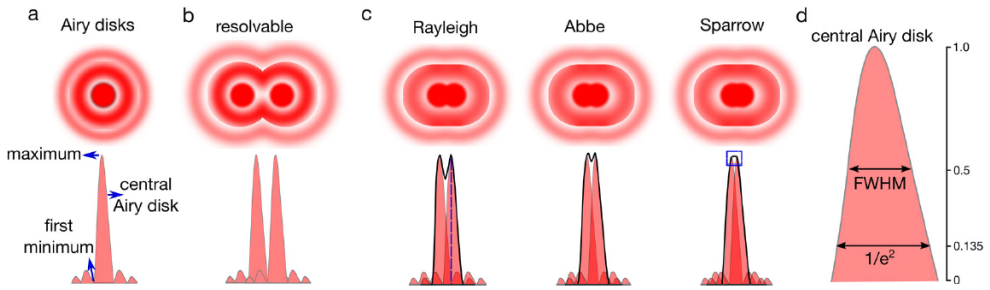

Fig. 3.5 Diffraction limits: (a) The image of a point-source has an intensity distribution that follows an Airy pattern with a central maximum and several minima. (b) In order to distinguish two point-sources one needs to be able to distinguish their images. Several criteria exist: shown are the (c) Rayleigh, Abbe, and Sparrow criterion. (d) Resolution is related to the width of the central Airy disk. The figure is reprinted from "Super-resolution optical microscopy for studying membrane structure and dynamics" by Erdinc Sezgin and is licensed under CC BY 3.0 [197].

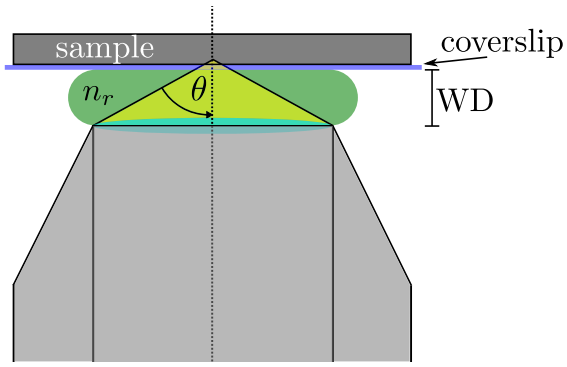

Fig. 3.6 Schematic of an objective close to a sample to illustrate the angle θ as well as the refractive index n_r that is used in the definition of the numerical aperture (cf., equation (3.3)). Here, the sample is placed on a coverslip and imaged from below. Objectives with high numerical apertures usually require oil-immersion but in principle, the medium between objective and coverslip can also be air. The working distance (WD) of the objective is the distance between its front lens and surface of the coverslip.

with the numerical aperture NA (cf., equation (3.3)) and a numerical prefactor of the order one. It can be shown that the lateral resolution in confocal microscopy using a pinhole is improved by a factor of 1.4 as compared to conventional microscopy [194]. In the literature on confocal microscopy, prefactor values like 0.32 can be found [198].

The axial resolution is given by

$$d_z = \mathcal{O}(1)\frac{n_r\lambda}{\mathrm{NA}^2} \tag{3.2}$$

with the refractive index n_r of the sample medium and a numerical prefactor of order one that is somewhere around 1.26 [198] or 2 [199]. For $\lambda = 500\,\mathrm{nm}$, $n_r = 1.51$, $\mathrm{NA} = 1.40$, and using the smallest prefactors given above, typical optical resolutions are $d_{xy} \approx 115\,\mathrm{nm}$ and $d_z \approx 485\,\mathrm{nm}$. Note that the axial resolution inversely depends on the squared numerical aperture.

The numerical aperture of an optical system is defined as

$$\mathrm{NA} = n_r \sin(\theta)\,, \tag{3.3}$$

where n_r is the refractive index of the medium between the optical system and the sample, and the angle θ can be inferred from figure 3.6. It is worth noting that an objective suitable for the refractive index of the sample should be used. Typical configurations include air ($n_r = 1$), water ($n_r = 1.33$), and oil ($n_r = 1.51$). Using samples or objectives with "wrong" refractive indices leads to incorrect measured axial distances [200].

3.4 Particle Tracking

Confocal laser scanning microscopy in modern laboratories is not only used to obtain high-quality images of fluorescent samples such as fluorescent particles or fluorescent cells but also to analyze the structure and or dynamics of the samples quantitatively [46, 201]. In the following, some relevant and representative particle tracking algorithms will be introduced. This section will not claim to have a complete list but it is aimed to classify and categorize tracking algorithms. In principle, particles of arbitrary shape can be tracked, but the focus of this section will be on the tracking of spherical objects.

Particle tracking generally involves the *localization* of particles (i.e., determination of the particle centers) as well as *linking* particle positions over time to form particle trajectories. The two steps are in most cases treated independently.

There are at least four different methods to locate the center of a spherical object: The centroid, Gaussian fit, cross-correlation, and sum-absolute difference method. All four are described in reference [202]. These methods can be further split into two subgroups since the centroid and Gaussian fit can be applied to each image independently, whereas the cross-correlation and sum-absolute difference method compare two images or at least one image and some kind of template.

The centroid method is maybe one of the simplest and computationally most efficient tracking algorithm [202]. It determines the center of a particle by calculating the centroid of its intensity distribution. Hence, particles should be dyed uniformly. In 1996, the centroid algorithm of Crocker and Grier was published [203], and corresponding software, written in the Interactive Data Language (IDL), can be found online [204]. It may be considered as the workhorse of colloidal science. More recent algorithms are modifications or extensions to this pioneering work [205–208], but also conceptually different algorithms exist [209, 210]. Worth mentioning is also "trackpy," a tracking algorithm written in Python and available on github [211].

The standard algorithm of Crocker and Grier [203] consists of five steps, namely, image restoration, particle location, location refinement, noise discrimination, and linking. In the first step, the image background, as well as noise, is removed by an appropriate convolution of the image with a Gaussian kernel. Second, local intensity maxima are found and act as candidates for the particle locations. Third, the neighborhood of these local intensity maxima is evaluated and the centroid (which then is assumed to be the particles' center) is calculated. The localization is refined by rejecting possible feature candidates, which are too small or too dim. Finally, the remaining centroid positions are linked by minimizing $\sum_{i=1}^{N} \delta_i^2$, where δ_i is the displacement of particle i between two frames. This is a reasonable assumption for non-interacting, diffusive particles [203].

Certainly, this linking step fails if the movement of the particles is affected by any kind of additional flow or shear. For small perturbations from Brownian diffusion, the standard linking process can be iterated [207]. Another option is to allow the

displacement of a particle δ_i to be directional. In reference [208], possible candidates are not searched for within a sphere, but within so-called Y bins. Also, a very recent adaptive linking algorithm exists, which estimates the particle movements from their previous steps [210].

A general idea is to subtract any convective motion, such that the remaining displacements are close to Brownian motion. This can be done by image velocimetry [207] and provides a robust way to handle many kinds of flow. No assumptions on the direction or magnitude of the flow are necessary since this information can be obtained by correlating the raw images. By correlating segments of the images, even non-uniform flow can be first measured and then subtracted from the coordinates [207]. Then again, in most of the cases, the standard linking process, which minimizes $\sum_{i=1}^{N} \delta_i^2$, is used.

Effort has been made to improve the feature location prior to the linking process. The standard code claims to be accurate up to 10 nm. Coordinates are refined making use of the point-spread function [206] or by improving the accuracy in the axial direction [205]. During this work, a method has been published in order to reduce the localization error down to 1 nm for light microscopy [212].

The concept of particle tracking is more powerful than just determining the center of spherical features. For instance, it is also possible to determine the orientation and shape of rod-like objects [200]. Even spherical objects have more parameters than just their center coordinates. An important parameter of spherical objects is their radius. The Crocker/Grier routine already determines radii from the intensity distribution of the features, but this is better used to discriminate features from noise and not for quantitative analysis. Actually, the size of all features should be similar, since the same convolution kernel is used for all features. Strictly speaking, the standard algorithm may fail in the case of very polydisperse systems [209], even though there are some clever extensions [213]. A multiscale tracking algorithm overcoming this issue has been developed quite recently [209] and is available in c++ and Python. Its underlying principle is the scale invariant feature transform. In other words, the images are convoluted with Gaussian kernels of – in this case – logarithmically increasing widths. Each convolution is related to a different size and thus spheres with different sizes can be tracked. The advantage of this scheme is that it acts on the image itself.

Last but not least, while instantaneous tracking *during* an experiment is in principle possible, all of the described particle tracking algorithms extract and link features *after* the experiment has finished.

Part II

Materials and Methods

4

Instruments: Play It by Ear

This section describes the main instruments and experimental setups used in this work. The setups are mainly based on commercially available devices and only the most important features will be briefly described in the following. Section 4.1 deals with the shear cell. Some details of the confocal-rheometer will be given in section 4.2 and both setups will be compared in section 4.3. Not *all* instruments are presented in this chapter. For example, pure rheology experiments are also carried out on a strain-controlled rheometer (TA, ARES G2), which can be equipped with standard tools and has a solvent trap to prevent evaporation.

4.1 Shear Cell

The shear cell is an improved version of shear cells that have previously been used in light scattering [214] and microscopy experiments [168, 215]. An early version is also discussed in a PhD thesis by Smith [216].

Figure 4.1 shows a model of the current version of the shear cell. The shear cell is a parallel plate device that can apply steady and oscillatory shear up to strains of the order one. A piezo (PI Instruments, model P-841.6B) drives the cell, more precisely, the bottom part of the cell (cf., figure 4.1a). In this configuration, the piezo only pushes. Two springs make sure that the movement can be reversed. They are located on the same side as the piezo but connected to the top part of the cell. The top and bottom parts of the cell are connected by means of a lever and move in opposite directions. The lever (and with that the zero velocity plane inside the sample) is adjustable in height.

The sample sits between a top and a bottom coverslip that act as top and bottom plate, respectively. Coverslips are glued (Norland, NBA 107) inside the shear cell. Furthermore, both coverslips are serrated to avoid slip. Scratching is done with the help of sandpaper, mounted onto a rotatory tool (Dremel, 400 digital). The top plate is adjustable with three micrometer heads (Mitutoyo, 148-152). Once aligned, it is fixed with three springs from the top.

For easy access, the top and bottom plate can be removed without dissembling the rest of the shear cell (cf., figure 4.1b). The transparent top plate has, furthermore, the advantage that the sample can be inspected by eye from the top (cf., figure 4.1c). This makes it easy to detect air bubbles inside the sample that may occur during loading. The gap height can theoretically be set between $h = 0\text{-}13\,\mathrm{mm}$. Since the piezo has a maximum travel range of $\Delta x = 90\,\mu\mathrm{m}$, the gap height directly influences the maximum strain $\gamma = \Delta x/h$. Typically, a gap height of $h = 100\text{-}150\,\mu\mathrm{m}$ is used.

For clarity, a few pieces are missing in the figure. For instance, the top and bottom parts of the shear cell have ball bearings. Furthermore, the whole cell is mounted in a frame. The frame has mounting devices such that it can be attached on an inverted microscope (Nikon, Eclipse Ti-E). A confocal head (Nikon, A1) converts the microscope to a confocal laser scanning microscope (CLSM). The CLSM is equipped with two lasers (Coherent, Sapphire$^{\mathrm{TM}}$) with a wavelength of $\lambda_1 = 488\,\mathrm{nm}$ and $\lambda_2 = 561\,\mathrm{nm}$, respectively. Light is collected with a photomultiplier tube. Two galvanometer scanners allow for frame rates up to 30fps for standard-sized images with 512×512 pixels.

Any objective suitable for the microscope can be used. Two are shown in figure 4.2. In principle, the shear cell may also be mounted on another (confocal) microscope and could also be used for scattering experiments.

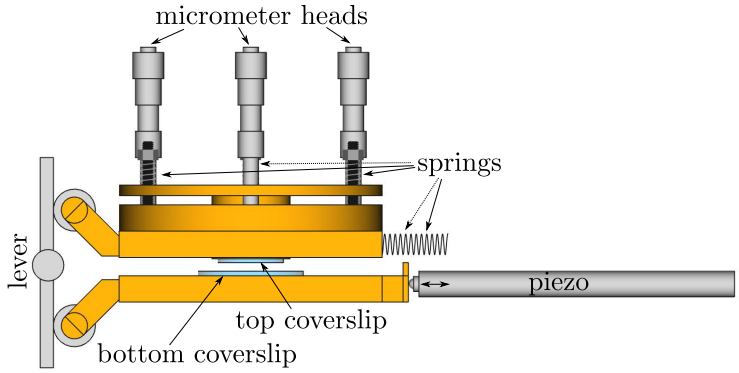

(a)

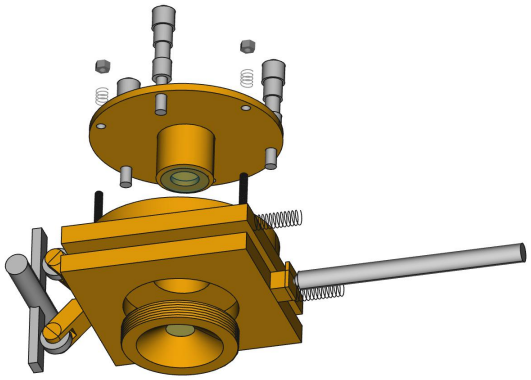

(b)

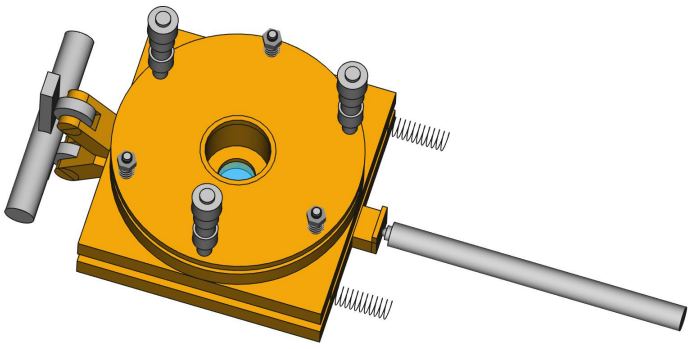

(c)

Fig. 4.1 CAD-drawing of the shear cell. (a) Side view with labeling. (b) Disassembled condition (e.g., for cleaning). (c) Top view, from which one can have a direct look into the sample chamber. Details in the text.

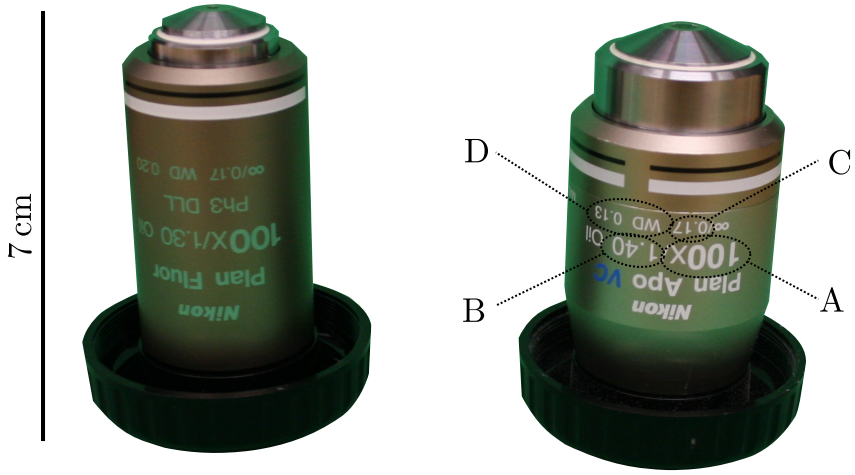

Fig. 4.2 Picture of two oil-immersion objectives that are frequently used. For the objective on the right-hand side, specifications of the magnification (A), numerical aperture (B), thickness of the coverslip (C), and the working distance (D) are highlighted. A scale bar is shown on the left. The image background has been removed.

4.2 Confocal Rheometer

The current setup of the confocal rheometer (sometimes also referred to as rheo-confocal) is shown in figure 4.3. It is mounted on an optical table (Standa, dimensions: 1.8 m × 1.2 m), which has a Pneumatic Vibration Isolation System. The confocal microscope consists of a confocal unit (Visitech, VT-Eye) attached to an inverted microscope (Nikon, Eclipse Ti). Illumination of the sample is done with a laser (Melles Griot, 85-BCD-050-230, $\lambda_1 = 488\,\mathrm{nm}$). (Fluorescent) light is collected with a PMT, which is located inside the confocal head. A piezo (PI, P-721, range: 100 µm) drives the objective in the vertical direction to allow for the acquisition of 3D image stacks.

Shear is applied with a stress-controlled rheometer (Anton Paar, MCR302 WESP) with plate-plate or cone-plate geometries. The term "stress-controlled" implies that torque and displacement are applied and measured at the same mobile part of the rheometer. Here, the bottom plate is stationary and the top plate/cone is moving.

Two cones are frequently used: A smaller one (Anton Paar, CP25-2/S, $d = 24.9826\,\mathrm{mm}$, $\beta = 2.001°$, $I_{\mathrm{tool}} = 0.0011336\ \mathrm{mN\,m\,s^2}$) and bigger one (HHU, $d = 40.1\,\mathrm{mm}$, $\beta = 3.03°$, $I_{\mathrm{tool}} = 0.0069421\ \mathrm{mN\,m\,s^2}$). Both cones have a roughened surface to reduce slip. The corresponding total inertia of the instrument $I = I_{\mathrm{tool}} + I_{\mathrm{drive}}$ is the sum of the inertia of the tool I_{tool} plus the drive inertia of the rheometer ($I_{\mathrm{drive}} = 0.0925\,\mathrm{mN\,m\,s^2}$). Minimum and maximum torque values that can be measured with the rheometer are $M_{\mathrm{min}} = 0.01\,\mu\mathrm{N\,m}$ and $M_{\mathrm{max}} = 200\,\mathrm{mN\,m}$, respectively. The rheometer itself is mounted on a home-build x-y-z-stage (cf., reference [217]), where the latter consists of two translational stages (Edmund

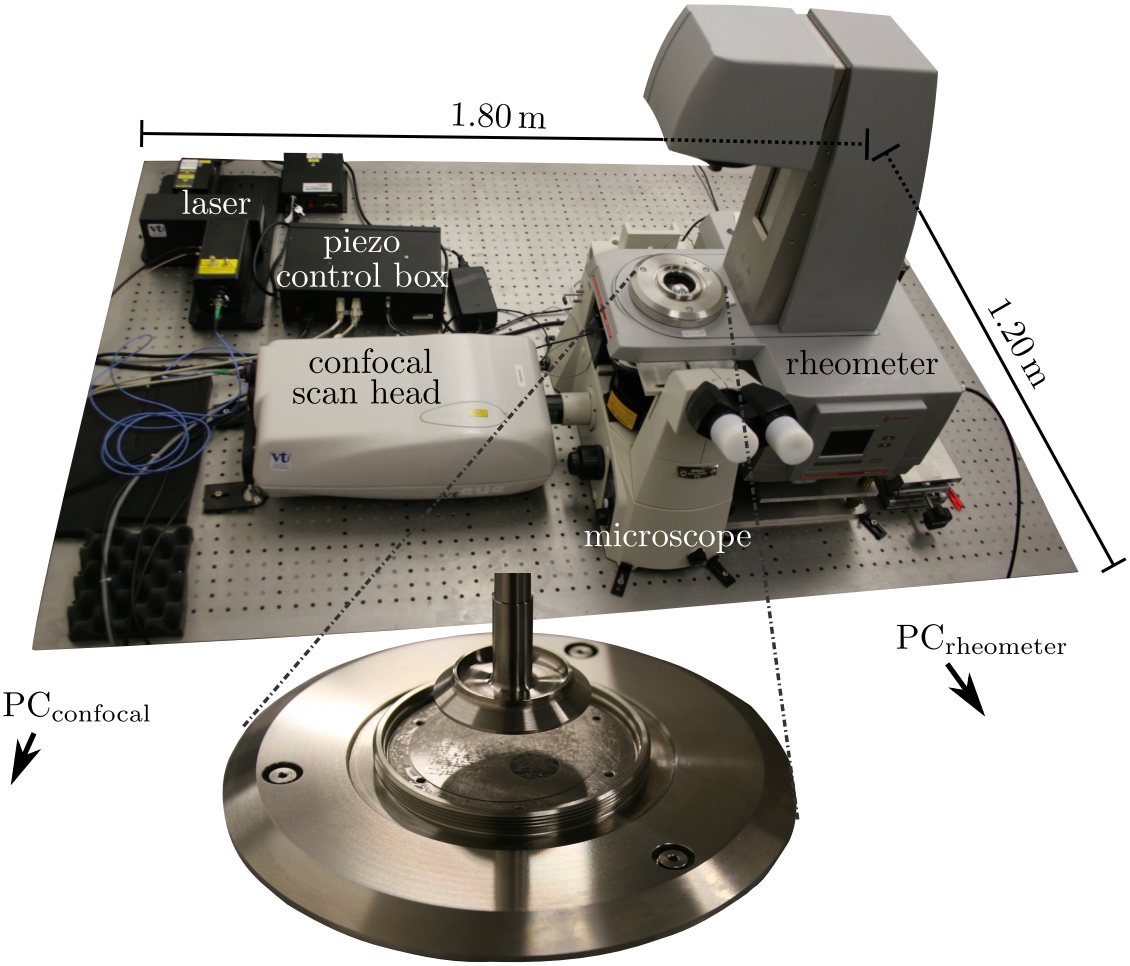

Fig. 4.3 Experimental setup of the confocal rheometer. (Major) components are labeled. Some (minor) control units are hidden beneath the optical table. The confocal microscope and the rheometer are controlled with two computers (not shown in the figure). The inset in the lower part of the figure shows the sample cell. A small hole below the coverslip allows for confocal imaging. Macroscopic deformation is applied and measured with various geometries. Here, the bottom part of a cone ($d = 40\,\text{mm}$) is visible. More information in the text.

Optics, 38-180) for alignment in x-y direction. A special feature of this MCR302 WESP rheometer is that the support plate is exposed – hence the name "With Exposed Support Plate (WESP)." This offers the opportunity to image the sample from below.

The measuring cell (visible in the magnified region at the bottom of figure 4.3) is based on an optical device (Anton Paar, P-PTD 200/GL) with a few additional home-build modifications: A coverslip (Menzel, #1.5, $d = 50\,\mathrm{mm}$) acts as the bottom plate. To reduce slip, the coverslip is scratched with the help of sandpaper and a rotatory tool (Dremel, 400 digital) and then glued (Norland, NBA 107) to its stainless steel support. The supporting plate has a hole ($d = 11\,\mathrm{mm}$) that enables optical access from below. Up to six screws (not present in the figure) keep the support plate – and thus the coverslip – in place.

The microscope and rheometer are mechanically connected with two aluminum plates [217]. Both instruments are also connected electronically with a BNC cable. In general, many details concerning the (original) design and the construction of the rheo-confocal setup as well as basic triggering settings can be found elsewhere [217]. Additional accessories that may be used in future experiments are part of the next section.

4.3 Comparison and Discussion

The two previous sections introduced the two main setups: the shear cell and the rheo-confocal. One might pose the question: "Why should one use the shear cell if a confocal rheometer is available?"

In principle, any shear cell experiment can be done with the rheo-confocal (although one can argue that the control of the shear cell offers more flexibility). The opposite is not necessarily the case, as shear stresses or other rheological quantities cannot be measured with the shear cell.

There are a few more subtle differences. The shear cell truly consists of two parallel plates and shear strains are limited to strains of about 100%. In contrast, the rheometer uses rotating cones or plates that allow for arbitrary strains. Tailored tools can be chosen depending on the properties of the sample. To this end, sample availability comes in: A typical rheo-confocal experiment needs ten times more sample volume than a typical shear cell experiment.

Also, the properties of the confocal unit matter. Currently, the shear cell is used in conjunction with the Nikon A1, and the rheo-confocal setup with the Visitech VT-Eye. The former has its strength in image quality and the latter in speed. If particle tracking has to meet specific demands, then the setup might be chosen on grounds of the confocal properties. Independent of the confocal unit is the optical degradation due to scratching of the coverslips. Both set-ups use #1.5 coverslips (borosilicate glass, thickness: 0.16-0.19 mm), which are very close to the requirements

of the objectives (cf., figure 4.2). The flat surface of the coverslip promotes wall slip. To prevent slip, surfaces have been coated with particles [31, 182] or roughened with sandpaper [218]. Coatings of dried particles may suck solvent and are usually nonpermanent. Coated particles might dissolve during measurement and propagate into the sample. Here, we sacrifice optical conditions due to scratching in favor of a permanent roughness. This also opens the opportunity to reuse and prepare particles for more than one experiment.

In both setups, the objective can be driven in the z-direction with a piezo to scan through the sample. Ideally, the movement of the piezo is not transmitted (e.g., via the immersion oil) into the sample. The rheo-confocal setup can monitor this by, for example, measuring normal forces. Signatures from z-scans are visible but can be weakened if abrupt z-movements are avoided. A good solution is to scan in upwards and downwards direction at the same speed [207]. In this respect, we also find that some immersion oils are more suitable than others. From a set of three different oils (Nikon Type N, Cargille Type 37, Cargille Type NF) we typically choose the third one.

Issues from z-scanning would be irrelevant if air objectives are used. Unfortunately, their magnification and numerical aperture are often too low to resolve colloids on a single-particle level. An elegant solution is to stick to oil-immersion objectives but to perform the scanning without any mechanical movements. This can be done with additional lenses that can change their focal point without mechanical movement. Preliminary experiments with such a lens (PhaseView, SmartScan) are promising, with the restriction that the focusing range is inverse proportional to the squared magnification of the objective. Another promising accessory is a home-build temperature controller. Temperatures are in general not relevant for PMMA particles but could be important for temperature-sensitive systems.

5

Sample Preparation: To Be Head Chef and Bottle Washer

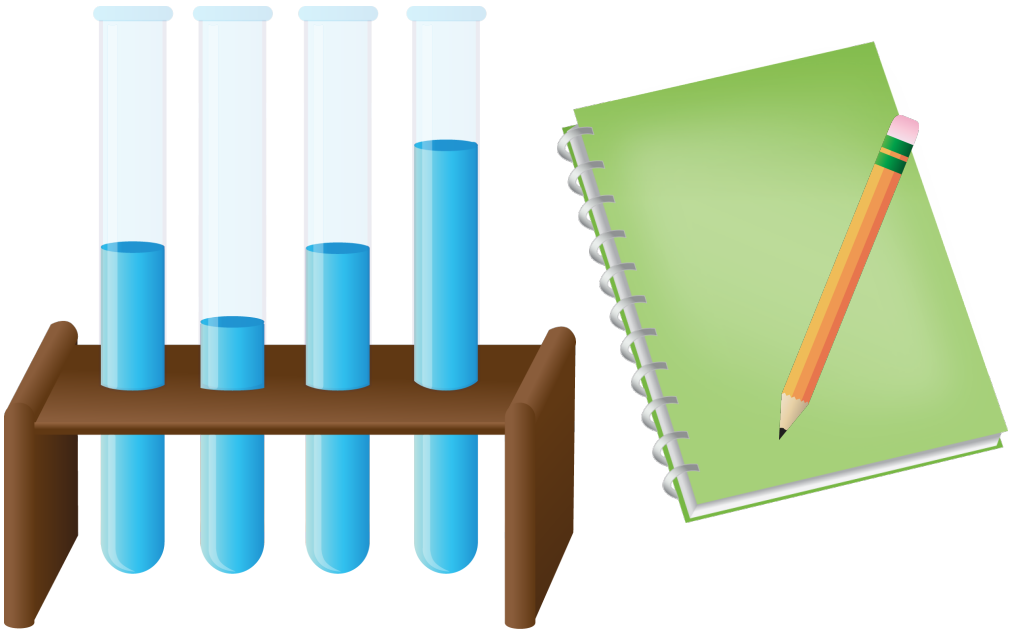

PMMA spheres are used as a model system for hard spheres (cf., section 2.3). In order to obtain this model system, several steps of sample preparation are needed. Individual steps, including the washing-process and the preparation of volume fractions, will be described below (section 5.1). In particular, this chapter draws attention to the role of the dispersion medium. We will compare possible candidates with respect to their refractive index, density, and evaporation rate. This chapter ends with an overview of the prepared samples.

solvent	ρ [g/ml]	n_r
cis-decalin	0.896102	1.48084
tetralin	0.967754	1.54105
CHB6	1.329860	1.49464
CHB7	1.300975	1.50434
TCE	1.620927	1.50590
squalene	0.854566	1.49593
octadecene	0.788563	1.44491

Tab. 5.1 Density ρ and refractive index n_r of possible dispersion media at $T = 21\,^{\circ}\mathrm{C}$. The densities are measured with an Anton Paar DMA 5000 density meter, and refractive indices with an Abbe refractometer model 60/LR at a wavelength of $\lambda = 589.3\,\mathrm{nm}$. For abbreviations see text or the list of acronyms.

5.1 Experimental Details

Stock solutions of PMMA-spheres (cf., section 2.3) are obtained externally from A. B. Schofield [219] or internally from M. A. Escobedo Sánchez and J. P. Segovia Gutiérrez. These stock solutions contain the "correct" colloidal spheres but the "wrong" dispersion medium. In order to remove reaction components and to change the dispersion medium, the samples are *washed* with *cis*-decahydronaphthalene (*cis*-decalin). A single cycle of washing incorporates centrifuging the dispersion, removing the supernatant liquid and adding pure *cis*-decalin. This procedure is repeated several times such that the final solvent consists of at least 98% of *cis*-decalin.

The density mismatch between PMMA-spheres $\rho_{\mathrm{PMMA}} \approx 1.19\,\mathrm{g/ml}$ and *cis*-decalin $\rho_{\mathrm{dec.}} \approx 0.89\,\mathrm{g/ml}$ is quite big with the consequence that particles sediment to the bottom (cf., section 2.2.1). Sedimentation can be avoided by adding a second solvent with a higher density.

For confocal microscopy, another constraint emerges: A transparent sample (which allows good imaging) can only be achieved if the refractive index of the dispersion medium closely matches the one of the PMMA-spheres. The refractive index of PMMA-spheres is $n_{r,\mathrm{PMMA}} \approx 1.49$. Exact numbers for the refractive index and density of PMMA-spheres depend on the synthesis and vary from batch to batch.

We now turn from the colloidal spheres to the dispersion medium. Frequently used organic solvents are *cis*-decahydronaphthalene (*cis*-decalin), tetrahydronaphthalene (tetralin), cyclohexyl bromide (CHB6), cycloheptyl bromide (CHB7), tetrachloroethylene (TCE), squalene (squalene), and octadecene (octadecene). The densities and refractive indices of these liquids are listed in table 5.1. The given solvents can be combined into a mixture that closely matches both the density as well as the

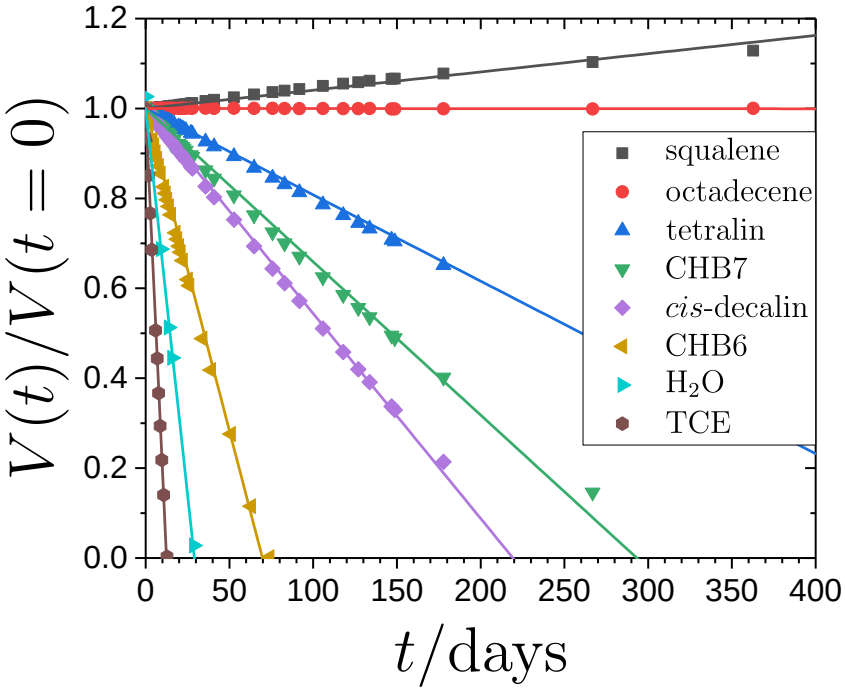

Fig. 5.1 Normalized solvent volumes $V/V(t=0)$ as a function of time t. Lines are linear fits to the data. Samples with an initial solvent volume of $V(t=0) = 1\,\mathrm{ml}$ are left undisturbed in open vials. Ambient conditions correspond to the ones of the confocal laboratory, which has an average temperature of 21 °C and a humidity between $60-70\%$.

refractive index of the particles. Density matching typically involves centrifugation of the sample at a relative centrifugal force (rcf) of about $2000g$. Density matching is completed if the sample does not show any sedimentation or creaming during one day. Else, either a low-density of a high-density solvent is added and the process is repeated.

Another aspect is important. While for pure (confocal) microscopy experiments the sample can be measured in a closed sample cell, it is typically exposed to its surroundings in rheology experiments. For combined rheo-confocal experiments, where the sample is not closed and sealed in a vial but rather in an open system, the solvent stability (especially its evaporation rate) plays a crucial role.

Information about evaporation rates is rarely available and furthermore depends on the temperature and humidity of the laboratory. Therefore, a small measurement series is performed to elucidate the evaporation rates of the solvents listed in table 5.1 under typical experimental conditions.

From each solvent, 1 ml is put into an open 5 ml-vial and left undisturbed. The mass of each vial is logged over time. Corresponding sample volumes are calculated under the assumption that densities of the solvents stay constant. Figure 5.1 shows the relative solvent volume $V(t)/V(t=0)$ as a function of time t. All solvents

show a nearly linear behavior and linear fits are included to guide the eye. The solvent with the highest evaporation rate is TCE. After 13 days, the TCE-vial is found empty – everything has evaporated. For comparison, water (H_2O) evaporates within 30 days at ambient conditions of the lab. The next four solvents are – sorted from fast to slow evaporation rates – CHB6, *cis*-decalin, CHB7, and tetralin. Note here that while CHB6 and CHB7 have similar chemical structures, densities, and refractive indices, their evaporation rates are strikingly different. CHB6 evaporates 4 times faster than CHB7. Hence, with respect to evaporation, measurements with CHB7 can last 4 times longer than with CHB6.

In terms of evaporation, an ideal candidate would be octadecene. Within one year, essentially no change in volume is detected. Thus, rheology experiments can even be performed without a solvent trap. Density matching may be achieved by combining octadecene with bromonaphthalene [166, 220, 221].

Another candidate is squalene. Squalene has the advantage that it directly matches the refractive index of PMMA as a one-component system. The disadvantage is that the density is low and particles will sediment. Apparently, squalene also gains volume with time (i.e., it absorbs humidity). Furthermore, squalene changes its color from transparent to yellowish if exposed to the environment. Similarly, CHB6 and CHB7 can have a yellowish color when bought. This effect has been reported previously [51]. After a filtering process incorporating aluminum oxide (Supelco, 06300), both CHB6 and CHB7 are transparent. The yellowish appearance may return if samples are exposed to light. Therefore, vials are usually covered with aluminum foil.

In terms of confocal microscopy experiments, the most commonly used mixture is perhaps the combination of *cis*-decalin with either cyclohexyl bromide (e.g., [222–227]) or cycloheptyl bromide (e.g., [168, 182, 188, 215, 221, 228–233]).

For some of the upcoming experiments, a solvent mixture of *cis*-decalin (TCI, D0009) and cycloheptyl bromide (Alfa Aesar, B23110 or Acros Organics, 111081000) is chosen for two reasons: On the one hand, this ensures consistency with previous work. On the other hand, this mixture minimizes evaporation (with respect to CHB6 and TCE) while at the same time being close to the density and refractive index of the PMMA-particles. In this case, the salt TBAC is added to screen charges. The amount of TBAC is under debate. Literature values range from molar concentrations of $c = 300\,\mathrm{nmol/l}$ [234], $c = 1\,\mu\mathrm{mol/l}$ [235], $c =$ 10-240 µmol/l [51], $c = 260\,\mu\mathrm{mol/l}$ [222, 236], $c = 1\,\mathrm{mmol/l}$ [237], $c = 4\,\mathrm{mmol/l}$ [169, 182, 207, 238] to saturated solutions [239]. In some cases, no value is given at all. In another study, the addition of salt shows no effect [163]. In this work, a concentration of $c = 4\,\mathrm{mmol/l}$ TBAC (Fluka, 86852) is added, simply following the apparent majority of previous work.

The addition of salt can be avoided if particles are dispersed, for example, in *cis*-decalin or a combination of *cis*-decalin and tetralin [240]. This comes along with a density mismatch and, therefore, the chosen dispersion medium depends on the specific experimental details.

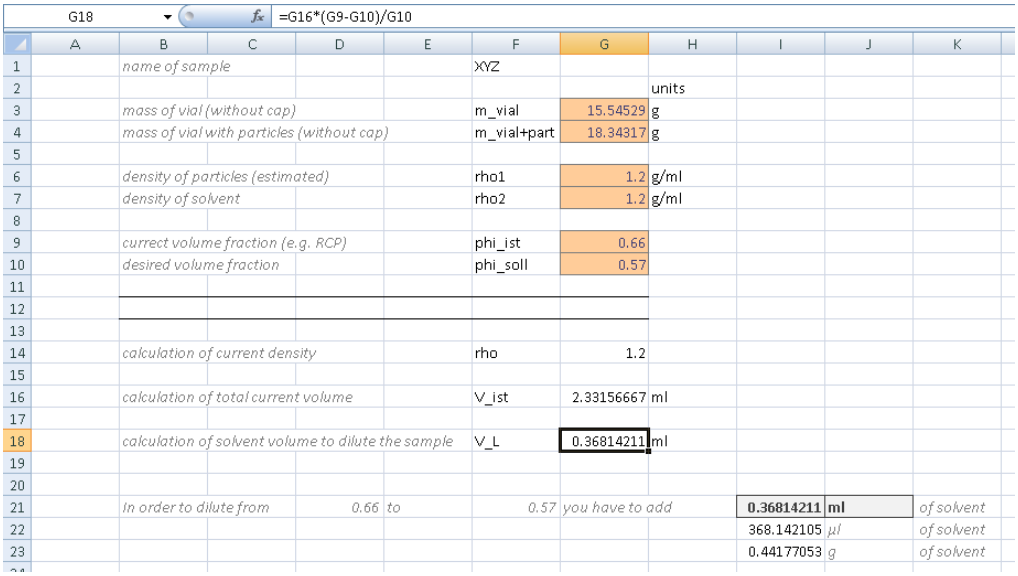

G18 =G16*(G9-G10)/G10

	A	B	C	D	E	F	G	H	I	J	K
1		name of sample				XYZ					
2								units			
3		mass of vial (without cap)				m_vial	15.54529	g			
4		mass of vial with particles (without cap)				m_vial+part	18.34317	g			
5											
6		density of particles (estimated)				rho1	1.2	g/ml			
7		density of solvent				rho2	1.2	g/ml			
8											
9		currect volume fraction (e.g. RCP)				phi_ist	0.66				
10		desired volume fraction				phi_soll	0.57				
11											
12											
13											
14		calculation of current density				rho	1.2				
15											
16		calculation of total current volume				V_ist	2.33156667	ml			
17											
18		calculation of solvent volume to dilute the sample				V_L	0.36814211	ml			
19											
20											
21		In order to dilute from		0.66	to	0.57	you have to add		**0.36814211**	**ml**	of solvent
22									368.142105	µl	of solvent
23									0.44177053	g	of solvent

Fig. 5.2 Screenshot of an excel sheet that is used to prepare volume fractions. Desired volume fractions are prepared by successive dilution of concentrated samples.

Volume fractions are set by sedimentation and subsequent dilution of samples. This is based on the assumption that the volume fraction of the sediment is equal to a random close packing as calculated by simulations [91]. In order to sediment density matched samples, we moderately increase the temperature inside the centrifuge (to $20\,°\mathrm{C} \lesssim T \lesssim 35\,°\mathrm{C}$). For consistency, as well as to minimize human errors, individual steps are done with the help of a home-written excel sheet (cf., figure 5.2). Actually, volumes are added by mass. For example, if 20 µl of *cis*-decalin shall be added, then the sample will be placed onto a balance and *cis*-decalin is added until an excess mass of $m = V\rho = 0.02\,\mathrm{ml} \times 0.896102\,\mathrm{g/ml} = 0.017922\,\mathrm{g}$ is reached.

With the balance (Sartorius, CP225D), a mass of 50 g can be measured within a permissible tolerance of 20 µg. Samples were weighted using gloves since a single fingerprint can lead to an absorption of up to 400 µg [241]. Furthermore, samples are weighted after adapting to room temperature. A sample colder than room temperature would appear heavier, and a sample hotter than room temperature would appear lighter than it is due to convection of air [241].

Densities are measured with a density meter (Anton Paar, DMA5000), which has a standard deviation of $10^{-6}\,\mathrm{g/ml}$. Accordingly, *relative* volume fractions, obtained by subsequent dilution, are very accurate thanks to the accuracy of the density meter and the balance. The biggest uncertainty in the preparation of *absolute* volume fraction stems from the assumption of the random close packing ϕ_{RCP}. Indeed, it is experimentally difficult to prepare and measure volume fractions. A corresponding review "On measuring colloidal volume fractions" is given by Poon et al. [64].

A few samples are shown in figure 5.3. The two vials on the left contain polystyrene

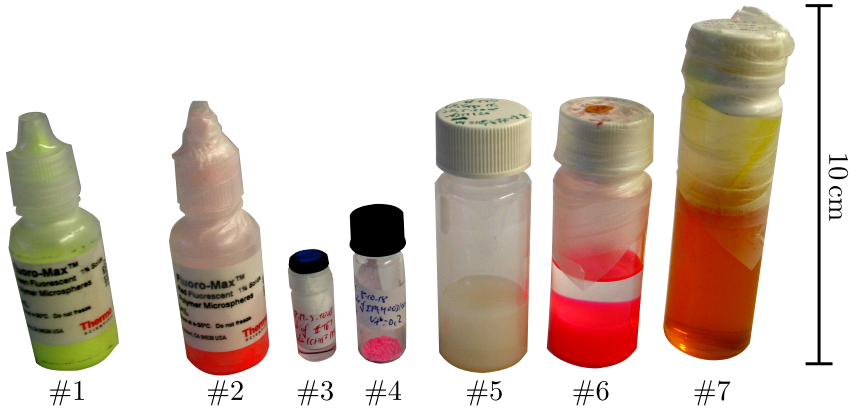

Fig. 5.3 Seven representative vials with samples, solvents, and leftovers, respectively. Shown are from left to right: (#1) Green and (#2) red polystyrene beads in water (externally procured from Thermo Scientific^{TM}). Vial #3 contains a mixture of *cis*-decalin and CHB7 and vial #4 has dried leftovers from a shear cell experiment. Vial #5 contains non-dyed PMMA particles at approximately random close packing. Vial #6 contains PMMA spheres labeled with rhodamine-B in *cis*-decalin. In vial #7, NBD-dyed PMMA spheres are dispersed in a density matching mixture of *cis*-decalin and CHB7. The image background has been removed, and contrast has been enhanced.

beads in water and are used for preliminary experiments in section 11.3. The other five vials are representatives for a large number of samples that are prepared during this thesis. They are selected for two reasons. First, the vials have different sizes ranging from 1.5 ml to 40 ml. Different types of experiments need different amounts of sample volumes. For instance, a single shear cell experiment consumes about 0.1 ml, while an experiment with the (confocal-)rheometer requires about 1 ml of sample. Second, the vials in figure 5.3 contain samples that are labeled with different fluorescent dyes. The polystyrene beads are dyed with Firefli^{TM} Fluorescent Green (468/508 nm, vial #1) and Firefli^{TM} Fluorescent Red (542/612 nm, vial #2). PMMA spheres are dyed, for example, with rhodamine-B (543/565 nm, vial #4 and #6) or 4-methylaminoethylmethacrylate-7-nitro-benzo-2-oxal,3-diazol (NBD) (vial #7). Vial #5 contains non-dyed spheres. Only dyed particles can be tracked with fluorescent laser scanning confocal microscopy.

6

Modified Particle Tracking: Catch Me If You Can

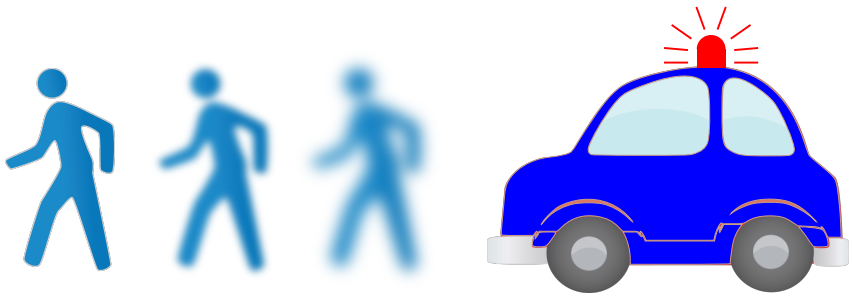

General concepts of particle tracking have been introduced in the fundamentals section (cf., section 3.4). Since many physically relevant quantities obtained from confocal laser scanning experiments depend directly or indirectly on the particle coordinates, accurate tracking is of great importance. In other words, the quantities obtained from those coordinates should be handled with care. It is tempting to assume that the coordinates obtained with particle tracking algorithms are true, real coordinates. It has been shown that the quality of the tracking methods is not always the same but depends on the specific set of measurements [202].

One may regard particle tracking as an annoying duty. The algorithms are in general described in the corresponding papers and often also in online tutorials. Yet, there is a need to explain, at least in some detail, how particle tracking is used in this work, such that it is possible to retrace the results.

The specific conditions of the instruments, in this case, the Visitech VTEye and the Nikon A1, plus the need to track particles under shear made it necessary to modify existing routines. Generally speaking, some routines are powerful in tracking particles with drift, while others are stronger in tracking particles from noisy images, while still others can determine the particle size directly. Depending on the system (one-component vs. binary), the microscope (Visitech VTEye vs. Nikon A1) and the amount of shear (with or without), different requirements need to be fulfilled by the tracking algorithm. Since, apparently, none of the existing algorithms fulfills *all* requirements, a workaround is to combine, modify or extend existing codes.

```
;PURPOSE:
;   Finds and measures roughly spheroidal 'features' within
;   a 3d image. Works best with dilute or separate feature,
;   i.e. non close-packed structures.
```

Listing 1 Excerpt from feature3d.pro

Explicitly, algorithms by Grocker and Grier [203, 204] and by Leocmach and Tanaka [209, 242] are used in this work.

The flowchart in figure 6.1 gives an overview of all major steps during particle tracking and shows a typical workflow. The combination of the steps always depends on the exact experimental protocol. Major steps during particle tracking are treated below in more detail: Image preprocessing and feature location will be described in section 6.1, and linking will be covered in section 6.2. Then, section 6.3 will explain how the location and linking results are checked. This chapter furthermore contains a critical discussion of particle tracking under shear in section 6.4 and ends with concluding remarks in section 6.5.

6.1 Particle Localization

The routines that will be addressed in the following make use of the a priori knowledge that the features, which shall be detected, are spherical. Depending on the image quality and the size distribution of the particles, different approaches are successful.

6.1.1 Small Polydispersity and Uneven Background

For fairly monodisperse samples, the feature localization routines from Grocker and Grier do a good job. Feature localization, in this case, involves two main steps: Filtering the image with `bpass3d.pro` and finding features with `feature3d.pro`. Both routines are available online [204]. `Feature3d.pro` works best with dilute or separate features, as can be inferred from the documentation. The relevant excerpt is shown in listing 1. Nevertheless, the Grocker/Grier algorithms are frequently used on colloidal glasses (i.e., concentrated, non-dilute samples).

In the following, we will get an impression of how images with uneven intensity distribution can be analyzed. Ideally, homogeneous illumination should be adjusted with the instrumental setup. Alternatively, the background could be calibrated once in order to correct for all upcoming measurements. With the current status of the Visitech VTEye confocal microscope, the illumination conditions can – unfortunately – change on a daily basis. Uneven illumination also occurs with other confocal setups

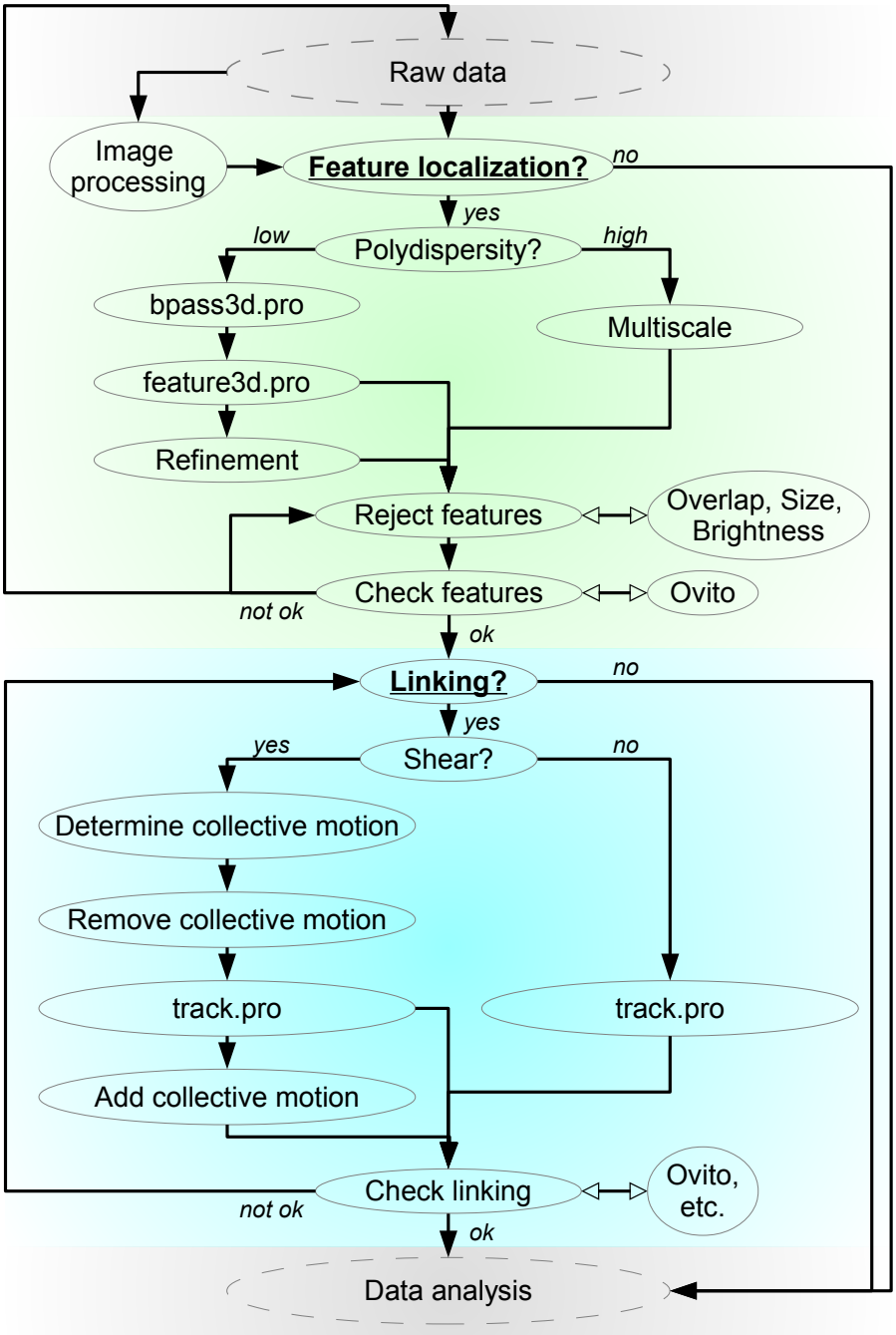

Fig. 6.1 Roadmap of particle tracking. There are many ways to get from raw data (at the very top) to particle positions that can be used for data analysis (at the very bottom). Particle tracking involves to main processes: The top half (green background) shows steps of feature localization (cf., section 6.1) and the bottom half (blue background) shows steps of the linking process (cf., section 6.2). Names having the suffix ".pro" represent major IDL-routines from reference [204].

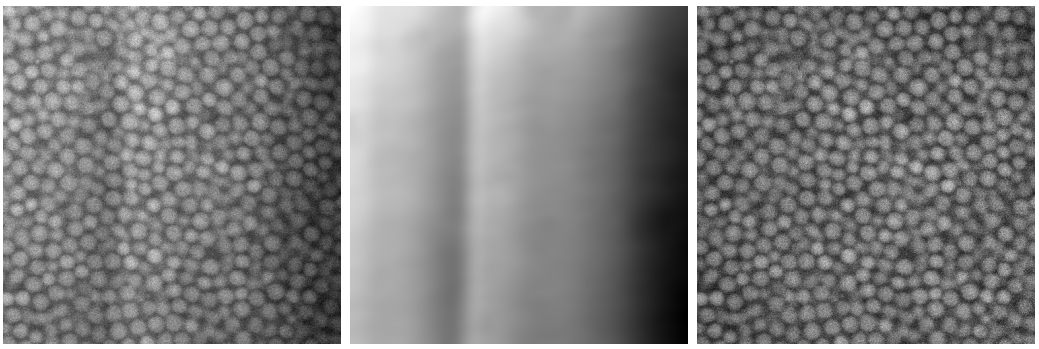

(a) **(b)** **(c)**

Fig. 6.2 (a) A raw image a_{raw} with inhomogeneous intensity distribution as obtained with the Visitech VTEye. (b) Image background a_{backg} as obtained by averaging many raw-images with essentially random particle positions plus an additional image smoothing. (c) Corrected image a_{proc} with homogeneous intensity distribution.

(cf., [142, fig. 12]). A brute force method turns out to be useful: The idea is to get an estimate of the background by averaging a big bunch of images. Typically, confocal images are acquired over time and at different positions. The brute force method to determine the background is to average all of these images. The underlying assumption is that every position in space is occupied by a particle with the same probability. For a system under shear, this assumption seems justifiable. Any residuals of individual particles are smeared out if the averaged background is smoothed with a boxcar average with a width of about a particle diameter. With this, a single "corrected" image a_{proc} is obtained by calculating

$$a_{\mathrm{proc}} = (a_{\mathrm{raw}} - a_{\mathrm{backg}})/a_{\mathrm{backg}}\,, \tag{6.1}$$

where a_{raw} is a single raw image and a_{backg} is the background as described above. A raw image with uneven illumination, an estimated background, and a corrected image are shown in figure 6.2.

The corrected image is then further processed by standard routines [203, 204], namely, `bpass` and `feature` or `bpass3d` and `feature3d` [204]. An output from `bpass3d.pro`, as well as a two-dimensional and a three-dimensional rendering of particle coordinates, are shown in figure 6.3.

The codes are written and executed in IDL (Interactive Data Language). A small but representative piece of code to locate particles is shown in listing 2. There, particle coordinates are also converted from pixel units to micrometers according to the experimental settings and saved for usage in later steps. In between, a refinement step can be added, which is explained in detail in reference [206].

Once all particle locations from all images (or image stacks) are saved, one can continue with the linking process (cf., section 6.2).

```
image_preprocessing_2, 'step*_1.tif'

for j=1,nf do begin
  l=STRING(j,FORMAT='(I4.4)')
  a=read_vteyetiff_pm('step'+[l]+'_1_preprocessed.tif')
  b=bpass3d(a,[1,1,1],[11,11,3])
  f=feature3d(b,[13,13,3],sep=[5,5,3],thresh=0.5)
  ref=ssf_refine_pm(a,f,[13,13,3])
  ref[0,*]*=0.0613
  ref[1,*]*=0.0617
  ref[2,*]*=0.18
  refd=remove_duplicates_pm(ref,min_distance)
  write_gdf,refd[0:6,*],'step'+[l]+'features.gdf'
  pretrack_to_ovito,ref,'step'+[l],3
endfor

pretrack_data=catptdata('step'+'*features.gdf')
write_gdf,pretrack_data,'all_features_'+'step'+'.gdf'
```

Listing 2 Simplified excerpt from a home-written analysis script written in IDL. Variables are written in black, numbers in gray, strings in red, build-in routines in light blue and home-written routines in dark blue. In the first line of code, the inhomogeneous background of the raw images is removed. The subsequent for-loop runs over nf image stacks. Each z-stack (suffix ".tif") is processed with **bpass3d** and **feature3d** [203, 204] and additionally, coordinates are refined with **ssf_refine_pm** (cf., [206]). Then, x-, y-, and z-coordinates are converted from pixel units to microns. Sometimes, one particle is detected multiple times and those duplicates are removed. At the end of the for-loop, data is saved for later usage as well as for visualization with the tool Ovito [243]. After the for-loop, individual files are merged to get one master-file for the whole experiment.

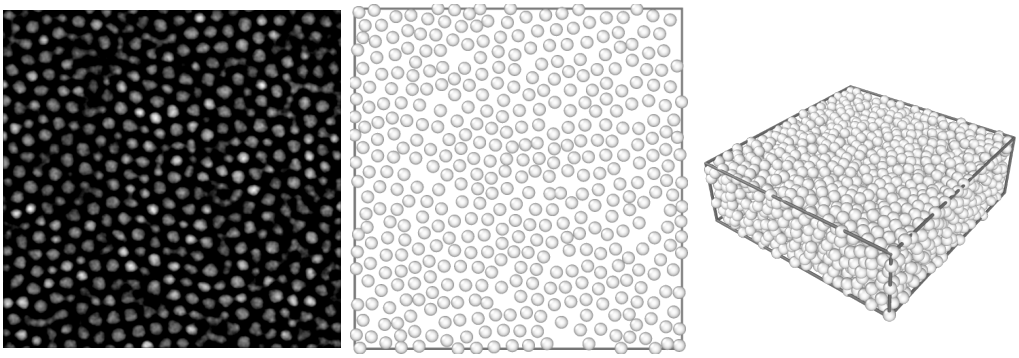

Fig. 6.3 Intermediate results after (a) application of bpass3d.pro and (b) feature3d.pro. These intermediate results belong to the same slice inside a z-stack. Small blobs in (a) correspond to particles outside the focal plane and are not visible in (b). (c) Reconstruction of particle coordinates as obtained from the full z-stack.

6.1.2 High Polydispersity and Good Image Quality

This subsection gives a brief overview, how (very) polydisperse particles, especially binaries with moderate size ratios, can be located.

The Grocker and Grier algorithm as described before is also used for polydisperse samples [238]. How is this possible? The idea is the following: One typically only takes the centers and not the radii as determined from the Grocker and Grier algorithm. To estimate the particle radii, one then uses a smart idea that is based solely on the knowledge of the particle positions [213]. The accuracy of this procedure has been tested for polydispersities up to 7% as well as a binary mixture with a size ratio of 1:1.3 [213].

Some experiments of this thesis will work on binaries with a higher size ratio (i.e., up to 1:1.55). Therefore, a different approach was searched for. The method of choice turns out to be the "Novel particle tracking method with individual particle size measurement" that was established by Leocmach and Tanaka [209] and is available online [209, 242]. In this case, particle sizes are determined directly from the images and not retroactively from measured particle coordinates. The core idea is to convolute the raw images not only with one kernel but with kernels of different width, to account for the different particle sizes. A typical raw image from a binary sample, measured with the Nikon A1, together with a two- and three-dimensional reconstruction based on the multiscale algorithm of Leocmach and Tanaka, is shown in figure 6.4. The workflow for locating particles with the multiscale approach of Leocmach and Tanaka is similar the one of Grocker and Grier. A shortened but representative piece of code can be seen in listing 3. The reader might notice that this code segment is written in Python instead of IDL. This is simply because the multiscale code is only available in either c++ or Python. For further processing

```
from pims import ND2_Reader
import pandas as pd
from colloids import track

im = ND2_Reader('/mnt/Mixture_001_002/001.nd2')
filename = '/mnt/Mixture_001_002/001_features.txt'
ffile=open(filename,'a')
f = []
fmax = im.sizes['t']
for i in range(0,fmax):
    imagei = im[i][:]
    finder = track.MultiscaleBlobFinder(imagei.shape, Octave0=False,
    ↪  nbOctaves=6)
    centers = finder(imagei,k=1.6, removeOverlap=False)
    x = centers[:,0]*0.124
    y = centers[:,1]*0.124
    z = centers[:,2]*0.124
    r = centers[:,-2]*0.124
    time = x*0+i
    d={'x':x, 'y':y, 'z':z, 'r':r, 'time':time}
    df=pd.DataFrame(d, columns=['x', 'y', 'z', 'r', 'time'])
    df.to_csv(ffile, sep = '\t', index = False, header = False, mode
    ↪  = 'a')
ffile.close()
```

Listing 3 Simplified excerpt from a home-written analysis script written in Python 2.7 to analyze .nd2-files as obtained with the Nikon A1. One .nd2-file contains all images of a single experiment (i.e., all z-stacks are stored in a single file). A couple of external modules need to be loaded in the preamble. Then, the following is done: The .nd2-file is opened, and a .txt-file – which will contain the tracking results – is created. Inside the for-loop, particle centers at times i are located with the **track** routine from the external **colloids** module. Obtained particle coordinates and radii are then converted from pixel units to microns and – together with a timestamp – successively appended to the .txt-file.

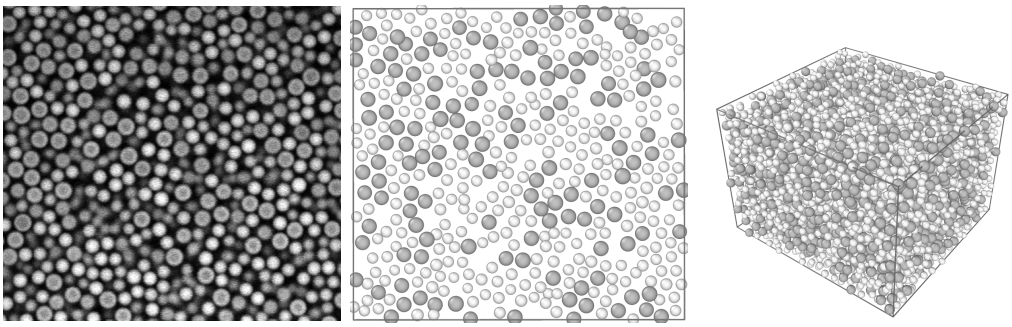

(a) (b) (c)

Fig. 6.4 (a) Raw image, recorded with the Nikon A1, showing a binary mixture of colloidal spheres. The raw image is part of a three-dimensional z-stack. (b) Corresponding reconstruction of particles after tracking. The multiscale algorithm is able to track and identify particles with different sizes. In the rendering, a size threshold is used to color bigger particles in gray and smaller ones in white. (c) Three-dimensional rendering of particle coordinates.

and data analysis, the individual particle positions and sizes are saved and then imported into IDL since most of the necessary codes were already written in IDL.

6.2 Linking of Trajectories

Once the localization process has finished, the particle positions can be linked to particle trajectories. The standard code is most likely `track.pro`, which finds trajectories by minimizing $\sum_{i=1}^{N} \delta_i^2$, where δ_i is the displacement of particle i between two images [203, 204]. This comes with the restriction that a particle should move less than its distance to a neighboring particle. Otherwise, the trajectories cannot be determined unambiguously. Thus, `track.pro` works well with Brownian motion but performs poorly for particles that experience large, directed movements, as in the case of colloids under shear.

A workaround is to subtract the shear-induced motion by means of particle velocimetry *before* running `track.pro`. A brief introduction to particle velocimetry may be found in reference [244, p.11]. This approach has been used, for example, by Besseling et al. for imaging of colloidal flows [207]. Particles are thus tracked in the "co-shearing" reference frame [245]. Computer codes along these lines were also written by K. J. Mutch. His codes (i.e., `affine_3d.pro` and `catsheardata.pro`) provided a helpful basis for this work. As stated before, every set of experiments may have different requirements on tracking. Accordingly, also the codes of K. J. M. were modified, extended and new code was written from scratch.

The linking process for a sheared system is divided into four individual steps:

```
displacements=affine_3d_pm('step'+'*_1.tif')
f_shifted=feature_reshear_pm(pretrack_data,displacements)
tr_shifted=track(f_shifted)
tr=backward_shift_tracks(tr_shifted)
tracking_efficiency,tr
write_gdf,tr,'tr_'+'step'+'.gdf'
```

Listing 4 Simplified excerpt of a home-written analysis file showing the workflow for tracking under shear. A few of the routines (colored in dark or light blue) can take more parameters but they are omitted for better readability. The variable "pretrack_data" is the same as in listing 2. More details in the text.

First, the collective motion is determined. This is done by image correlation with the help of a fast Fourier transform (cf., section 7.1). The home-written routine **affine_3D_pm** takes roughly 40 ms to determine the displacement between two images (512×512 pixels) with one core of an Intel *i*7 computer. So, the typical amount of images per measurement can be analyzed in a few minutes. As a second major linking step, the collective motion is subtracted from the previously determined particle positions. Third, the trajectories are calculated with `track.pro`. Fourth, the collective motion is added to the particle positions. Depending on what you want, you can then continue with the trajectories (either with or without subtraction of collective motion). Note here that any subtraction is somewhat arbitrary, and it is not guaranteed that "ideal" Brownian motion is retained after the subtraction. A representative piece of code incorporating all the four abovementioned steps is shown in listing 4.

6.3 Checking Results

Tracking algorithms will always return results as long as the syntax is correct. The user has to take care that the results are reliable. Especially for the localization process, methods to test the accuracy are well described in reference [237, p.111]. Just to name one method, a first crude estimate is to cross-check the determined particle positions by comparing particle renderings with raw data. Visualization can, for instance, be done with Ovito [243]. In the case of three-dimensional data, this is done for the full stack, as well as for small z-slices of about one to two particle diameters. More sophisticated measures – mainly for the localization process – are described elsewhere [204, 237].

How to check the linking process? If the localization process was correct, then one can be sure that particle positions (and not noise) were linked to trajectories. Still, one should check whether a trajectory belongs to one and the same particle. A quick

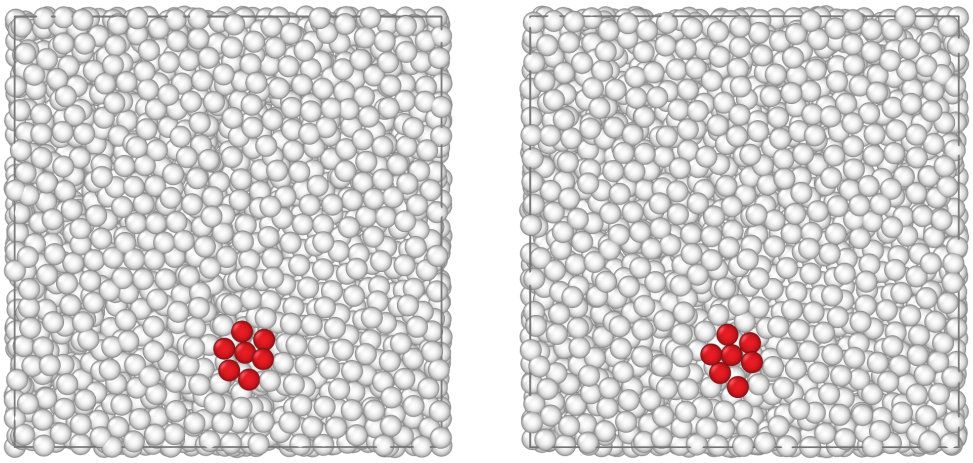

(a) **(b)**

Fig. 6.5 (a) Rendering of particle coordinates. Seven particles that are close together are highlighted in red. (b) Rendering of the same sample 12 time steps (i.e., 21.5 s) later. Data is taken from a rheo-confocal experiment where the sample is subjected to shear.

check is an inspection by eye. For example, it is convenient to visualize all particles, or a subgroup of particles, with a visualization program and then highlight one particle. In Ovito, a particle can be selected according to its ID-number, which is uniquely assigned by `track.pro`. Then one can check by eye if the selected particle appears to be the same for different time steps. A visualization of this procedure is given in figure 6.5.

Another way to check the result of the linking process is to look at the *length* of trajectories. By rule of thumb, longer trajectories are more reliable than shorter ones. In the simplest case, one calculates a histogram of trajectory lengths. Ideally, a particle is tracked during its total "lifetime". The trackable lifetime can be reduced due to bleaching of the fluorescent dye in long measurements, or if particles are leaving the FOV due to diffusion or external shear. Hence, the histogram should be somewhat peaked around typical lifetimes. They can certainly be smaller than the total duration of the experiment, but if the histogram is peaked around zero and decays rapidly, then tracking is certainly at its limits. Two histograms of trajectory length are given in figure 6.6. The first histogram is for a system under shear ($\phi_1 = 0.57$, $\dot{\gamma}_1 = 0.0025\,\mathrm{s}^{-1}$), where all particles are fluorescently labeled and tracked. The second one is for a quiescent system, where only a few tracer particles are fluorescently labeled ($\phi_2 = 0.57$, $\dot{\gamma}_2 = 0\,\mathrm{s}^{-1}$). The FOV is $31 \times 31 \times 10\,\mu\mathrm{m}$ in the first and $51 \times 54 \times 75\,\mu\mathrm{m}$ in the second case. In both cases, the fluorescently labeled particles have a radius of about $R \approx 800\,\mathrm{nm}$. A relative tracking length of 100% is achieved if a particle is tracked during the total duration of the measurement.

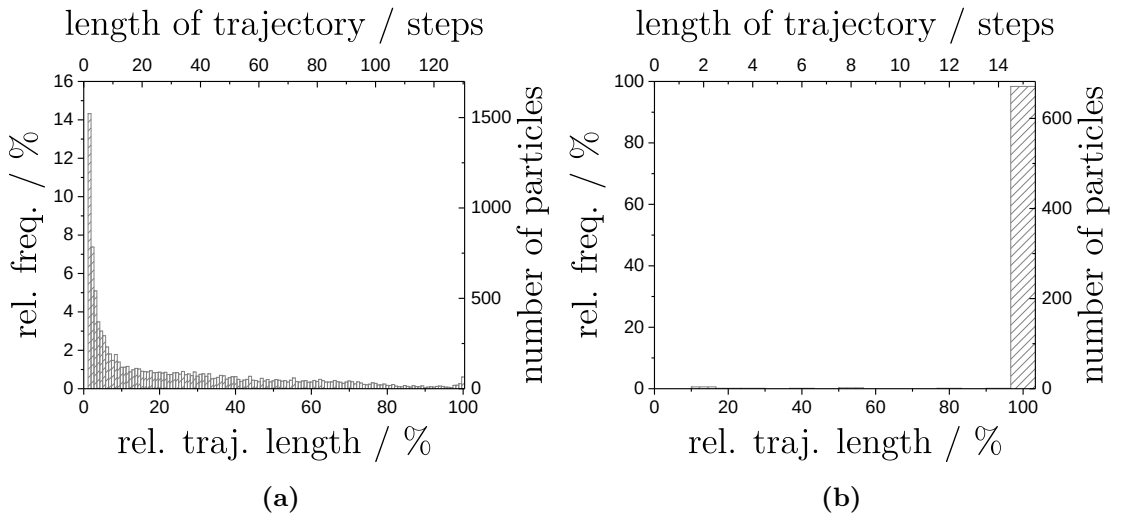

Fig. 6.6 Histograms with the length of particle trajectories. In both cases, the underlying raw data is taken from a series of z-stacks, measured with the rheo-confocal setup. A particle has a trajectory with a length of n steps if it is uniquely identified within $n+1$ z-stacks. The number of particles that are tracked for a given length is given on the right axis. For a better comparison, the left and bottom axis contain relative quantities that are normalized with the total number of all tracked particles and the longest trajectory length, respectively. Data in (a) belongs to fluorescently labeled, concentrated (i.e., $\phi_1 = 0.57$) and polydisperse colloidal spheres under shear. About 2500 particles are located within one z-stack. Due to shear, particles enter end leave the FOV. Here, the maximum possible lifetime of a particle within the FOV is around 140 time steps (see text). But trajectories are much shorter. Thus, only a fraction of particles is correctly tracked. (b) Tracking of tracer particles ($\phi_{2,\mathrm{tracer}} \lesssim 0.01$) within a concentrated sample ($\phi_2 = 0.57$). No shear is applied. Essentially, all tracer particles are tracked successfully.

While essentially all of the tracer particles reach a relative tracking length of 100%, this only applies to 1% in the case of shear, where all particles are labeled. For the system under shear (figure 6.6a), the average particle displacement between two images in the direction of shear is $\langle \delta_i \rangle_x = 220\,\mathrm{nm}$. The FOV in the direction of shear has a width of 31 µm, so on average, after 140 time steps, all particles have left the FOV. A way to circumvent this issue is to image and track particles in a plane of zero velocity, which can be achieved with suitable setups [168, 222].

6.4 A Discussion on Tracking under Shear

The previous section pointed out that *linking* particle positions to trajectories can be difficult under shear. In fact, also the *localization* process is a bit more involved than in the quiescent state. Recall that one gets three-dimensional reconstructions from confocal laser *scanning* microscopy. Thus, not all pixels are captured at the same time. If a particle does not move considerably during the acquisition time of a 3D-stack, everything is fine.

If shear is imposed, this assumption is not necessarily true. Then instead, there is a preferred direction of movement and all coordinates can be biased in a specific direction. This systematic error has to be considered. Figure 6.7 visualizes the described situation: Say, two people – Alice and Bob (i.e., B1 and B2 in the figure) – are taking a photograph of a boat (A1). The boat is moving to the right with a fixed velocity $v_x > 0$. Say, Alice is taking – essentially instantaneous – a picture of the full boat. Instead, Bob is taking a photo piecewise from bottom to top. Imagine that Bob has an aperture, which only allows him to image a small fraction at a time. If Alice would afterward look at her picture, she would see something like shown in (C1) and Bob would see something similar to what is shown in (C2). In the case of Bob, the boat almost looks as if it has been sheared. We can define an apparent shear strain

$$\gamma_{\mathrm{dist}} = \tan(\theta) = \frac{\Delta x}{h_z}\,, \tag{6.2}$$

which quantifies the distortion of the boat in Bob's picture. Here, h_z is the height of the boat and Δx is the translation of the top slice of the boat with respect to the bottom slice (cf., figure 6.7).

The same idea applies to CLSM when imaging moving objects. The important question is: "How far does an object move while being imaged?" To answer this, we will assume that a confocal laser scanning microscope takes two-dimensional images (in the xy-plane) with a constant frame rate f_{xy}. Thus, the time to capture one 2d-image is

$$\Delta t_{2\mathrm{D}} = \frac{1}{f_{xy}}\,. \tag{6.3}$$

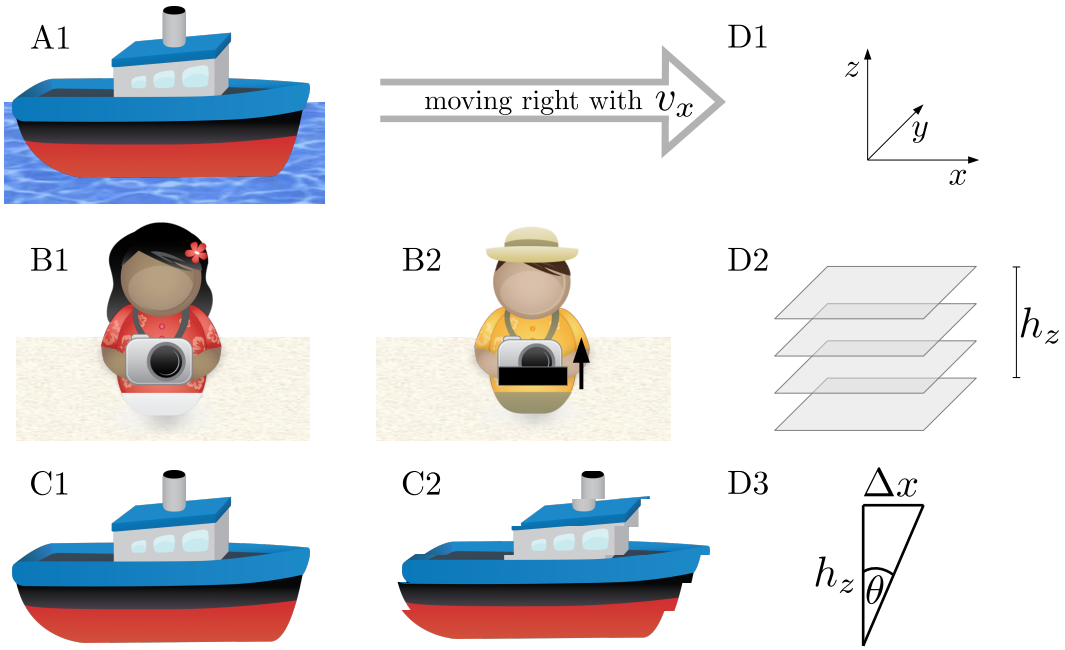

Fig. 6.7 Illustration of a potential problem of feature location under shear. Imagine that an object (A1) is moving to the right. If Alice (B1) takes a picture with essentially zero exposure time, she will get a picture showing the "true" object (C1). If Bob (B2) takes a picture of the same object by scanning it from bottom to top with a finite time $t > 0$, he will get a different result (C2). Any object with height h_z that is moving in the x-direction with a constant speed will be displaced by a distance Δx during a finite time $t > 0$. This leads to a distorted image with an apparent shear deformation $\gamma_{\text{dist}} = \tan(\theta) = \Delta x / h_z$.

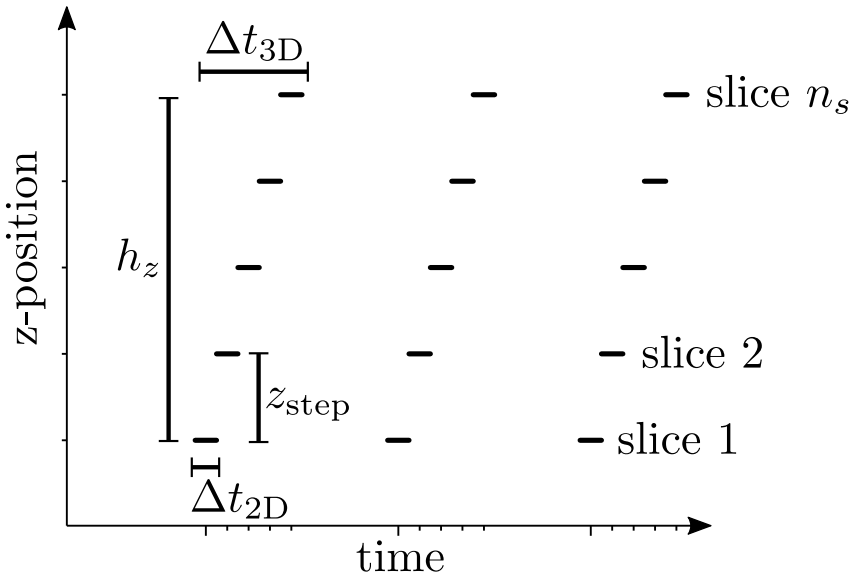

Fig. 6.8 Visualization of variables used in equation (6.3) to equation (6.5). It takes a finite time Δt_{3D} to capture a confocal z-stack of height h_z consisting of n_s slices separated by z_{step}. The time to capture a single slice $\Delta t_{2D} > 0$ is short but finite.

If all slices are separated by z_{step} then the total height of the 3D-stack will be

$$h_z = n_s z_{step} \,. \tag{6.4}$$

The 3D-stack is captured in a time interval

$$\Delta t_{3D} = n_s \Delta t_{2D} = \frac{n_s}{f_{xy}} \,, \tag{6.5}$$

if we neglect any additional delay due to the z-movement. The relevant quantities are visualized in figure 6.8. What is now the distance Δx that an object has traveled during the time Δt_{3D}? In the case of a directed motion with constant velocity v_x, we can write $\Delta x = v_x \Delta t_{3D}$. Thus,

$$\tan(\theta) = \frac{\Delta x}{h_z} = \frac{v_x \Delta t_{3D}}{n_s z_{step}} = \frac{v_x}{z_{step} f_{xy}} \,. \tag{6.6}$$

For any measurement, the frame rate f_{xy} and the distance between two slices z_{step} is given. From the definition of the shear rate (cf., equation (1.14)), we have $v_x = z\dot{\gamma}$, where z is the vertical distance with respect to the bottom plate. For a small 3D-volume in the vicinity of z, we may thus write

$$\tan(\theta) = \frac{z\dot{\gamma}}{z_{step} f_{xy}} \,. \tag{6.7}$$

Inserting typical values (i.e., $z = 20\,\mu\text{m}$, $z_{\text{step}} = 0.1\,\mu\text{m}$, $f_{xy} = 50\,\text{s}^{-1}$), we get

$$\tan(\theta) = 4\dot{\gamma}\,. \tag{6.8}$$

For $\dot{\gamma} = 0.1\,\text{s}^{-1}$ this is already $\theta \approx 22°$! To keep the apparent shear strain $\gamma_{\text{dist}} = \tan(\theta)$ below 1%, the shear rate needs to be small (i.e., $\dot{\gamma} \lesssim 0.0025\,\text{s}^{-1}$).

In chapter 7, methods to extract local strain values or other quantities based on particle trajectories will be presented. Will they necessarily be wrong? The answer is the following: While "static quantities" based on *one* 3D-stack can be biased as discussed in this section, "dynamic quantities" are less affected. Dynamic quantities are based on *pairs* of 3D-stacks. In the latter case, *relative* particle positions are used with the consequence that the static error is already subtracted.

6.5 Conclusion

Particle tracking is a powerful technique, which provides real-space information on the structure and dynamics of small objects – here: colloidal particles. Particles are first located (cf., section 6.1) and then linked to trajectories (cf., section 6.2). Methods to check the tracking results have been established in section 6.3. For dilute samples, the localization accuracy of the Crocker and Grier algorithm is 10 nm [203]. Effort has been made, to improve the localization accuracy. Refinement techniques are especially suited for quiescent systems. Care has to be taken under shear since particles might move considerably during the acquisition time of a 3D-image-stack (cf., section 6.4). This does not only affect the dynamics but primarily the structure of the imaged objects. A system might appear to be sheared even though it was only moving as a block. Always consider that images can show something different from reality (cf., figure 6.7).

7

Data Analysis: Crunching the Numbers

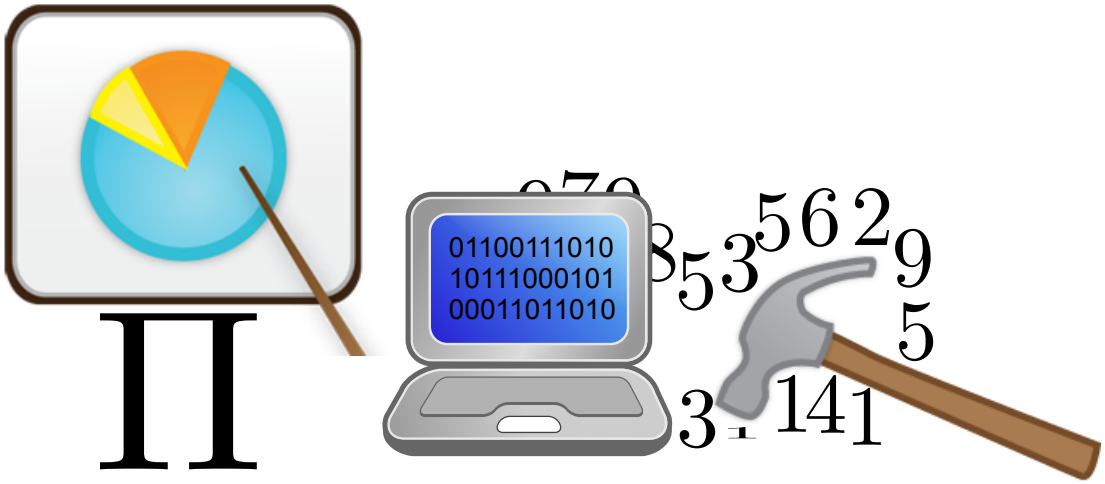

This chapter contains methods that are used to analyze the experimental data from confocal microscopy. We will address image correlations (section 7.1) that play an important role in the analysis of images in one of the experiments as well as for the modified particle tracking algorithm (chapter 6). Afterward, we will discuss single-particle properties and focus on local affine and nonaffine motions (section 7.2), the determination of neighbors (section 7.3) and local volumes (section 7.4) as well as the characterization of local structures. The mean-squared displacement (MSD) (equation (2.1)) was briefly introduced in section 2.1 and section 2.5.3 and is not covered here, but it is worth noting that noisy particle coordinates can lead to an apparent sub-diffusion for short lag times [246]. The pair correlation function $g(r)$ is described elsewhere [204].

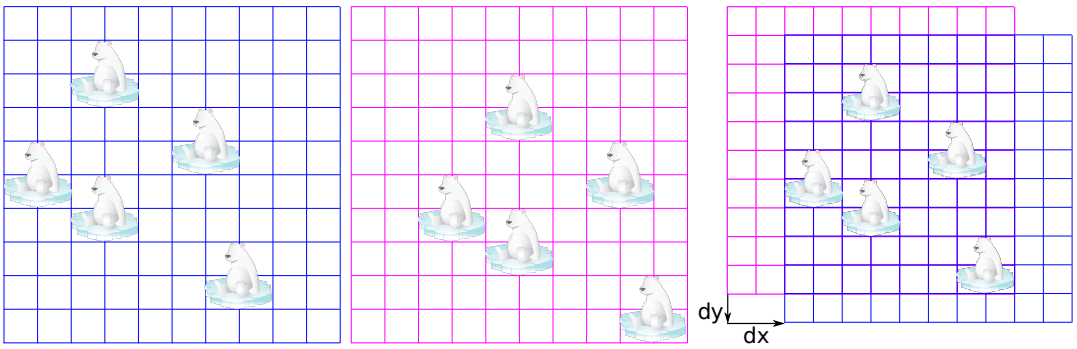

Fig. 7.1 Images in (a) and (b) have a relative offset (dx, dy) as indicated in (c).

7.1 Image Correlations

This thesis deals with colloids under shear. Routinely, images of moving particles are recorded and particle displacements between image pairs have to be determined. One way is to use particle tracking (cf., chapter 6). However, if particle displacements are large compared to their size, particle tracking reaches its limits. Image correlation can then be used to facilitate particle tracking (section 6.2).

A simplified example to determine the displacements (dx, dy) between two images is given in figure 7.1. One can easily see that from figure 7.1a to figure 7.1b all polar bears, sitting on floating ice sheets, have moved by two boxes to the right and by one box down, as can be inferred by superimposing both images (figure 7.1c). With experimental raw data from confocal microscopy, the situation is not that clear.

This section shall establish the basics of image correlation and explain what kind of image correlation is applied in some of the following experiments. Section 7.1.1 will introduce the cross- and phase correlation. They will be further discussed in section 7.1.2, with special attention to relevant images from confocal microscopy. Finally, section 7.1.3 introduces the Pearson correlation coefficient.

7.1.1 Cross- and Phase Correlation

The displacements (dx, dy) that map two two-dimensional images $a = a(x, y)$ and $b = b(x, y)$ can be found by minimizing [247]

$$e(dx, dy) = \sum_{x=1}^{n} \sum_{y=1}^{n} \left[a(x, y) - b(x - dx, y - dy)\right]^2 , \tag{7.1}$$

where the sum runs over all n^2 pixels. We assume n to be even. If one expands the expression in the sum, one identifies the cross term

$$cc(dx, dy) = \sum_{x=1}^{n} \sum_{y=1}^{n} a(x, y) b(x - dx, y - dy) . \tag{7.2}$$

The cross-correlation $cc(dx, dy)$ is a scalar quantity and a measure for the similarity between the two images [248].

Equation (7.2) can be evaluated for all possible combinations of (dx, dy) to find the displacement that maximizes $cc(dx, dy)$. This is computationally intensive. Therefore, it is helpful to do the calculation in Fourier space: First, we need the discrete two-dimensional Fourier transforms

$$\mathcal{A} = \mathcal{F}(a)\,, \tag{7.3}$$
$$\mathcal{B} = \mathcal{F}(b) \tag{7.4}$$

of the images a and b. The cross-correlation matrix is then given by

$$\boldsymbol{cc} = \mathcal{F}^{-1}\left(\mathcal{A} \odot \mathcal{B}^*\right)\,, \tag{7.5}$$

where $\odot$ denotes the entrywise product, and $\mathcal{B}^*$ is the complex conjugate of $\mathcal{B}$. The sought after displacements are encoded in the coefficients

$$(cc_{ij}) = \begin{pmatrix} cc_{11} & cc_{12} & \dots & cc_{1n} \\ cc_{21} & \ddots & & c_{2n} \\ \vdots & & \ddots & \vdots \\ cc_{n1} & cc_{n2} & \dots & cc_{nn} \end{pmatrix} \tag{7.6}$$

that contain information on all displacements (dx, dy) for the range $(-n/2+1) < dx < (n/2)$ and $(-n/2+1) < dy < (n/2)$. The exact mapping $(i, j) \to (dx, dx)$ depends on the utilized Fourier transform and programming language.

Fourier transforms are, for instance, implemented in IDL and Matlab, and reasonably fast. Another benefit of a Fourier transform is that it separates amplitude and phase information. Simply put: "The basic notion is that the phase bears topological information about image edges whereas amplitude encodes image intensity" [249]. Thus, for an image containing many colloidal particles, the phase tells us, where the particles are located and the amplitude tells us, how bright they appear.

The expression $\mathcal{A} \odot \mathcal{B}^*$ in equation (7.5) contains both amplitude and phase information. By dividing the term with its absolute value $|\mathcal{A} \odot \mathcal{B}^*|$, one eliminates the amplitude information. This is exactly what is done in the case of the phase correlation. The phase correlation matrix is given by

$$\boldsymbol{pc} = \mathcal{F}^{-1}\left(\frac{\mathcal{A} \odot \mathcal{B}^*}{|\mathcal{A} \odot \mathcal{B}^*|}\right)\,, \tag{7.7}$$

where the expression inside the inverse Fourier transform is also called normalized cross-power spectrum [247]. Again, the information about the displacements (dx, dy) is encoded in the coefficients – this time in the coefficients of $\boldsymbol{pc}$.

7.1.2 Application to Confocal Images

Since homogeneous illumination can be an issue (cf., section 6.1.1), as well as particles moving in- and out-of-focus and thus appearing brighter or darker in different images, amplitude information can readily be rejected. In fact, for a set of images acquired during this thesis, phase correlation is more robust than cross-correlation. This can be seen in figure 7.2, where two raw images are shown together with the cross-correlation ***cc*** and the phase correlation matrix ***pc***. In the case of the phase correlation, the peak is clear and unique – independent of the illumination conditions. Sub-pixel accuracy can be obtained by fitting the peak location by means of a polynomial, a Gaussian or other model function.

Thus, the displacements (dx, dy) between both images can properly be determined with the phase correlation. The cross-correlation is reliable only in the case of homogeneous intensity distribution. Note that we were only interested in the position of the peak and not its value.

7.1.3 Pearson Correlation Coefficient

Sometimes, image correlation is not intended to only find the offset between image pairs, but also to quantify the similarity between two images. In this case, a proper normalization is required. Given two variables $a = (a_1, a_2, \ldots, a_N)$ and $b = (b_1, b_2, \ldots, b_N)$, the Pearson correlation coefficient (PCC) is defined as

$$PCC_{ab} = \frac{\sum_{i=1}^{N} (a_i - \bar{a})(b_i - \bar{b})}{\sqrt{\sum_{i=1}^{N} (a_i - \bar{a})^2} \sqrt{\sum_{i=1}^{N} (b_i - \bar{b})^2}}, \tag{7.8}$$

where $\bar{a}$ and $\bar{b}$ are mean values of a and b, respectively. The Pearson correlation coefficient is bound to the interval $[-1, 1]$, with $PCC_{ab} = 1$ indicating a perfect positive correlation and $PCC_{ab} = -1$ indicating a perfect anti- or negative correlation. In the case of $PCC_{ab} = 0$, no linear correlation between the two variables a and b exists – they are uncorrelated. The Pearson correlation coefficient can be applied to images in which case the sum runs over all pixel-positions of each image. Thus, for two identical images, the PCC is equal to one, that is, $PCC_{aa} = 1$.

The Pearson correlation coefficient is a normalized cross-correlation as inferred from a comparison of equation (7.2) and equation (7.8). The PCC is also a normalized form of the covariance [250] and used in colloidal science [207, 245]. It has been compared with other image correlation criteria and is "highly recommended for practical use" [251].

Fig. 7.2 (a) A raw image and (b) another raw image together with a grayscale representation of the corresponding (e) cross-correlation matrix and (f) phase correlation matrix. In (c) and (d) are intensity-corrected images with corresponding (g) cross- and (h) phase correlation matrices. All images a_i (a-h) are scaled according to $255. * (a_i - \min(a_i))/(\max(a_i) - \min(a_i))$. The peak for phase correlation is much more localized than in the case of the cross-correlation.

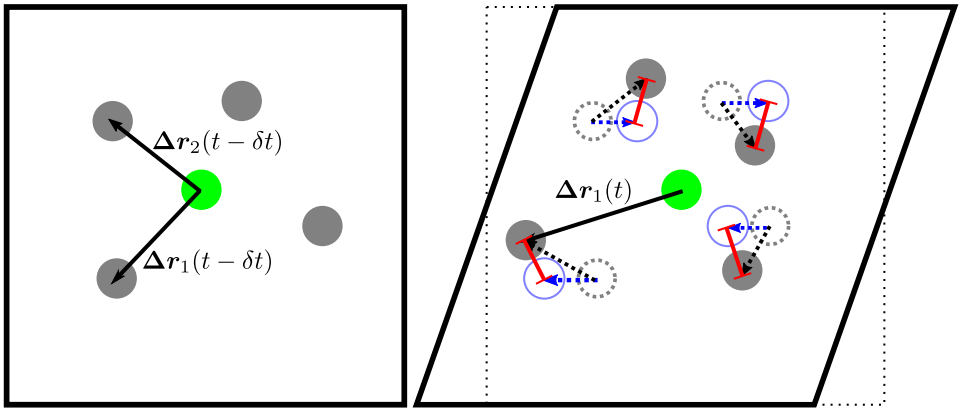

Fig. 7.3 Illustration of local nonaffine motion. A central particle (green) is surrounded by four particles (gray). The left drawing shows a state at time $t - \delta t$. Vectors Δr_i (solid black arrows) connect the central particle with its i surrounding particles. The right drawing shows a state of the same system at a later time t. The four surrounding particles have moved from their previous positions (dashed gray circles) to their current positions (filled gray discs). Their displacements (dashed black arrows) can be split into an affine (dashed blue arrows) and a nonaffine (red line) part. The sum of all nonaffine distances is a measure of the local nonaffine motion.

7.2 Measures of Local Deformation

Rheo-confocal experiments of colloidal particles under shear allow insight into local dynamics. This section will show how this information can be used to quantify the deformation on a single-particle level. Both affine and nonaffine measures will be introduced. Since a nonaffine quantity measures the deviation from affine motion, both quantities are directly linked. First, section 7.2.1 will explain the nonaffine measure D^2_{min} and concurrently establish the basis for the calculation of local shear strains and local shear rates, which are the topic of section 7.2.2.

7.2.1 Local Nonaffine Motion: D2min

Falk and Langer have introduced the quantity D^2_{min} as a measure to quantify local nonaffine deformation [157]. This measure was introduced for amorphous materials and is nowadays used, for instance, in granular flow [252], colloidal glasses [158] or the motion of biological cells [253].

The idea is depicted in figure 7.3: The displacements of the N_b local neighboring particles (gray) around a reference particle (green) are analyzed. The neighboring particles typically do not move in a purely affine way. Nevertheless, the best fit for an affine transformation $\boldsymbol{A}$ can be done. Accordingly, the distances (red) between the real positions and the best-fit positions are calculated. The (squared) sum of

these distances is then the quantity $D^{2*}_{\min}$. Explicitly, the equation reads

$$D^{2*}_{\min}(t, \delta t) = \sum_{n=1}^{N_b} \| \boldsymbol{\Delta r}_n(t) - \boldsymbol{A} \cdot \boldsymbol{\Delta r}_n(t - \delta t) \|^2 \tag{7.9}$$

with the length (Euclidean norm) of a vector $\|\boldsymbol{r}\| = \sqrt{r^x r^x + r^y r^y + r^z r^z}$. The best fit for the affine transformation $\boldsymbol{A}$ is the fit that minimizes $D^2_{\min}$, hence the subscript "min." If the particles would move purely affine, $D^2_{\min}$ would be zero. Rotation, stretching, mirroring or rigid body motion are affine transformations. Any combination of affine transformations is again an affine transformation. Remember that simple shear is a combination of rotation and stretching (figure 1.4). Furthermore, recall the definition of the material deformation gradient tensor $\boldsymbol{F}$ from section 1.1.2. By comparing equation (7.9) with equation (1.3) one can readily identify $\boldsymbol{A} \equiv \boldsymbol{F}$ and the quantity $D^{2*}_{\min} \equiv e(\boldsymbol{F})$ is simply the sum of squared residuals in a least-squares fit.

In practice, $D^{2*}_{\min}$ is obtained from a list of experimental particle coordinates in the following way: First, one finds the coordinates of a reference particle

$$\boldsymbol{r}_0(t) = \begin{pmatrix} r^x_0(t) \\ r^y_0(t) \\ r^z_0(t) \end{pmatrix} \tag{7.10}$$

as well as the coordinates of its neighbors

$$\boldsymbol{r}_n(t) = \begin{pmatrix} r^x_n(t) \\ r^y_n(t) \\ r^z_n(t) \end{pmatrix} , \tag{7.11}$$

where n is used as an index for the N_b neighboring particles and takes values between 1 and N_b.

Next, one needs the set of displacement vectors

$$\boldsymbol{\Delta r}_n(t) = \boldsymbol{r}_n(t) - \boldsymbol{r}_0(t) , \tag{7.12}$$

$$\boldsymbol{\Delta r}_n(t - \delta t) = \boldsymbol{r}_n(t - \delta t) - \boldsymbol{r}_0(t - \delta t) \tag{7.13}$$

between the reference particle and its neighbors. This is equivalent to putting the reference particle into the origin of the coordinate system. Thus, the affine transformation reduces to a linear transformation – no translation is involved anymore. This is consistent with the original work, which states to describe the displacements "by a linear strain field" [157].

The next step is to calculate the two matrices

$$\boldsymbol{X} = \sum_{n=1}^{N} \boldsymbol{\Delta r}_n(t) \cdot \boldsymbol{\Delta r}_n^{\top}(t - \delta t) \tag{7.14}$$

and

$$\boldsymbol{Y} = \sum_{n=1}^{N} \boldsymbol{\Delta r}_n(t-\delta t) \cdot \boldsymbol{\Delta r}_n^{\top}(t-\delta t)\,, \tag{7.15}$$

where $^{\top}$ denotes a transposed vector. Thus, $\boldsymbol{X}$ and $\boldsymbol{Y}$ are 3 by 3 matrices. The affine transformation $\boldsymbol{A}$ that minimizes $D^{2*}_{\min}$ is then obtained by [157]

$$\boldsymbol{A} = \boldsymbol{X} \cdot \boldsymbol{Y}^{-1}\,. \tag{7.16}$$

Finally, $D^{2*}_{\min}$ can be calculated according to equation (7.9). Although not stated in the original paper, it is reasonable to normalize the $D^{2*}_{\min}$-value for each particle by the number of its neighbors, that is,

$$D^2_{\min}(t,\delta t) = \frac{1}{N_b}\sum_{n=1}^{N_b} \|\boldsymbol{\Delta r}_n(t) - \boldsymbol{A} \cdot \boldsymbol{\Delta r}_n(t-\delta t)\|^2\,. \tag{7.17}$$

This normalization has also been done in other work [253]. The quantity might not need to be normalized if always the same number of neighbors is used. For example, some authors using $D^2_{\min}$ took a fixed number of 10 [245] or 12 [254] neighbors. One could also use $D_{\min} = \sqrt{D^2_{\min}}$, but this is avoided for the sake of consistency with the literature.

7.2.2 Local Strains and Shear Rates

A useful way to determine local strains is to use the affine transformation $\boldsymbol{A}$ from the $D^2_{\min}$ calculation (cf., section 7.2.1). In fact, the symmetric part of $\boldsymbol{A}$ has been used to evaluate the local strain tensor or elements thereof [245, 254, 255]. If we take a closer look at the original definition of $D^2_{\min}$, that is, at equation (7.9) and compare it with equation (1.3) to equation (1.5) from the chapter about the strain tensor, then we identify that the local strain tensor $\boldsymbol{\epsilon}$ is actually not the symmetric part of $\boldsymbol{A}$ but the symmetric part of the term $(\boldsymbol{A} - \mathbb{1})$, hence

$$\boldsymbol{\epsilon} = \frac{1}{2}((\boldsymbol{A}-\mathbb{1}) + (\boldsymbol{A}-\mathbb{1})^{\top}) = \frac{1}{2}(\boldsymbol{A}+\boldsymbol{A}^{\top}) - \mathbb{1}\,. \tag{7.18}$$

The local shear strain is thus obtained from the xz-component of the strain tensor (cf., equation (1.10)) as

$$\gamma \equiv \gamma_{xz} = 2\epsilon_{xz}\,. \tag{7.19}$$

Local strains are obtained from the best fit to a linear strain field based on particle positions at t and $t - \delta t$. Accordingly, local shear rates are simply given by

$$\dot{\gamma} = \frac{\gamma}{\delta t}\,. \tag{7.20}$$

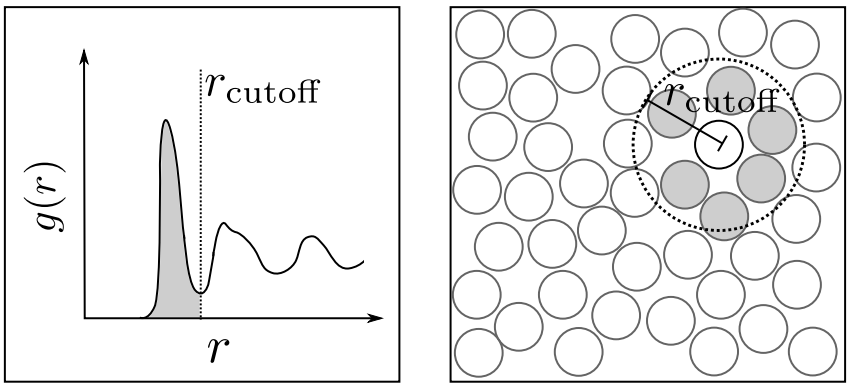

Fig. 7.4 Illustration of neighbors using the cutoff-definition. Neighbors are located in a circle (sphere in 3D) with radius r_{cutoff}, taken from the first minimum of $g(r)$. Small changes in r_{cutoff} can lead to different sets of neighbors.

7.3 Determination of Local Neighbors

Local quantities depend on the local surroundings of a particle. As seen in the previous section (section 7.2), calculations involve the coordinates of neighboring particles. So it is entitled to pose the question: "What is a *neighbor*?" The remainder of this section is organized as follows: In section 7.3.1, three different ways to determine neighbors will be given. Additionally, these definitions are briefly discussed in section 7.3.2. This discussion also includes possibilities to extend the definition of neighbors to binaries and polydisperse systems.

7.3.1 How to Define Neighbors

Intuitively, neighboring particles should be somewhat close to a particle under consideration. This leads to the first definition of a neighbor: A neighboring particle is a particle that is within a given cutoff-distance. If one draws a circle (or a sphere in three-dimensions) with radius r_{cutoff} around the center of a reference particle then all particles within this circle are "neighbors." This is illustrated in figure 7.4. Typically, particles are treated as if they were points, thus the center of a particle has to lie inside the circle. As it is suggested by the dotted line in figure 7.4, the cutoff-radius r_{cutoff} is typically chosen from the position of the first minimum of the pair correlation function $g(r)$.

If particles sit on a perfect lattice, as it is, for instance, the case in a hexagonal crystal, then the number of particles inside a given radius is known a priori. For example, in the case of a close-packed fcc crystal, the smallest distance between pairs of particles is $d = 2R$, where R is the particles' radius. Within that distance, there are 12 particles. Thus, another definition is that a neighbor belongs to the N_b particles that are closer to a reference particle than the rest. Typically, $N_b = 12$.

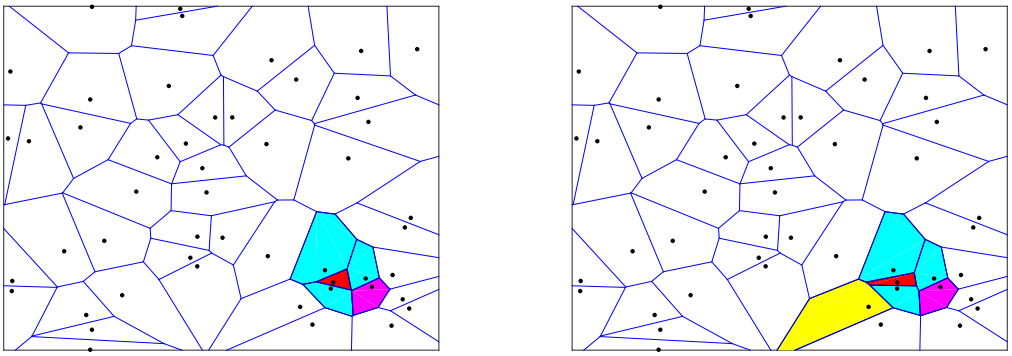

(a) (b)

Fig. 7.5 Illustration of neighbors using the Voronoi criterion. The cells are part of a Voronoi diagram. Particle centers (black dots) are located in cells that are constructed with a Voronoi tessellation. Particles are neighbors if their cells have a shared edge (in 3D: if they share a face). (a) A particle (in the red cell) has three neighbors (in blue cells). The particle in the magenta cell is not a neighbor. (b) A small displacement of two particles has changed the Voronoi diagram and so the neighbors. Another particle (in the yellow cell) has become a neighbor, although it is relatively far away. This leads to a total of 4 neighbors (3x blue, 1x yellow).

Third, a parameter-free definition of neighbors is based on a Voronoi diagram: Given a set of points in space of arbitrary dimension, the Voronoi diagram divides the space without gap into so-called Voronoi cells. Every Voronoi cell contains one point. The space in the Voronoi cell is closer to the point inside the cell than to any other point. By construction, the cells are polygons in 2D and polyhedra in 3D. Two Voronoi diagrams for random sets of points (in 2D) are given in figure 7.5. Under the prevailing circumstances, the points will be particles, and neighboring particles will be particles whose Voronoi cells (in 2D) share an edge (a face in 3D). The number of edges (2D) or faces (3D) of a Voronoi cell is equivalent to the number of neighbors of the particle inside this cell. Thus, in figure 7.5a, the particle in the cell that is highlighted in red has three neighboring particles. Two particles that only share a corner (in 2D) or a vertex (in 3D) are not neighbors. Therefore, the particle in the magenta cell (figure 7.5a) is not considered a neighbor. A marginal change in position (figure 7.5b) can change the neighbors, since, for example, the particle in the yellow cell would now also be considered a neighbor.

7.3.2 Discussion of the Neighbor Definitions

All of the abovementioned definitions are used in colloidal science: The cutoff definition (e.g., [158, 255]), a fixed number of neighbors (e.g., [234, 254]) or neighbors

based on the Voronoi diagram (e.g., [256, 257]) or a combination of more than one definition in the same work (e.g., [245]).

By comparing different work, one should always consider the underlying definition of neighbors. It has been found (for example for the study of bond orientational order parameters) that the definition matters [258]. Difficulties and shortcomings for the case of Voronoi neighbors have been discussed in reference [259].

There are ways to improve the Voronoi definition: One possibility is to consider not only the faces but also the position of the faces with respect to the neighboring particles [260]. Another possibility is to weight the contribution of Voronoi neighbors [258, 259, 261]. In the latter case, one defines and weights neighbors based on the position and size of the corresponding faces. Others distinguish between direct, indirect, degenerate or quasi-direct neighbors [262].

The definitions have advantages and shortcomings: Does a sharp separation by a cutoff-distance do justice to the underlying physics? Do colloidal glasses always have a fixed number of neighbors? Even in the case of a bcc crystal, one might argue that the number of neighbors is either 8 or 14. A fixed number of neighbors can avoid normalization issues (cf., section 7.2.1) while neighbors defined via a cutoff-distance are at least close (which is not necessarily true in the case of the two other definitions). Refinement of the cutoff-definition could involve a weighting-factor: One suggestion is to weight neighbors according to their distance in a way that nearer particles contribute more, while particles farther away add less.

Furthermore, combinations of definitions are possible. For example, one could first select neighbors from the Voronoi diagram and then add the additional restriction of a cutoff radius. This combination of two criteria, as well as the three individual neighbor definitions, are implemented in IDL-routines. If not stated otherwise, the cutoff-criterion is used.

To examine the impact of the neighbor definitions, they need to be compared on the same set of data. To compare them, data from reference [263] is re-analyzed using the cutoff, fixed number and Voronoi method and the obtained results are shown in figure 7.6. In the figure, the ensemble-averaged nonaffine motion $\langle D^2_{\mathrm{min}} \rangle$ of colloidal spheres with diameter $2R$ during a start-up experiment is shown as a function of strain γ. Depending on the underlying definition of a neighbor, quantitatively different results are observed. Luckily, the qualitative trend stays the same and the difference is basically just an offset.

Other quantities can show a stronger dependence on the underlying definition of neighbors. Bond order parameters are a relevant case. Definitions of bond order parameters will be given in section 7.5.2. At the moment, it is sufficient to know that they are used to characterize local structures. Figure 7.7 shows results based on the same set of data but with different definitions of neighbors, to illustrate the impact of neighbors on bond order parameters. Clearly, not only quantitative but also qualitative differences are observed. Using cutoff-neighbors, one finds two main clouds in the $\overline{q}_4 - \overline{w}_4$-plane. One is located around ($\overline{q}_4 = 0.15$, $\overline{w}_4 = 0.13$)

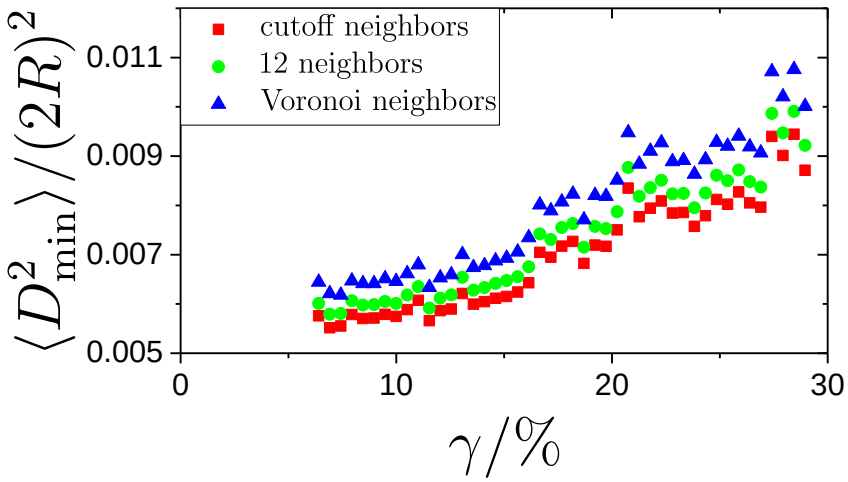

Fig. 7.6 Ensemble-averaged nonaffine motion $\langle D^2_{\mathrm{min}} \rangle / (2R)^2$ as a function of strain for a colloidal glass during start-up of shear. Particle trajectories used for the analysis are identical with those from reference [263]. The quantity $\langle D^2_{\mathrm{min}} \rangle / (2R)^2$ (equation (7.17)) implicitly depends on the underlying definition of neighboring particles. Shown are results based on cutoff neighbors (red squares), a fixed number of 12 neighbors (green circles) and Voronoi neighbors (blue triangles). Further details of the neighbor definitions are given in the text.

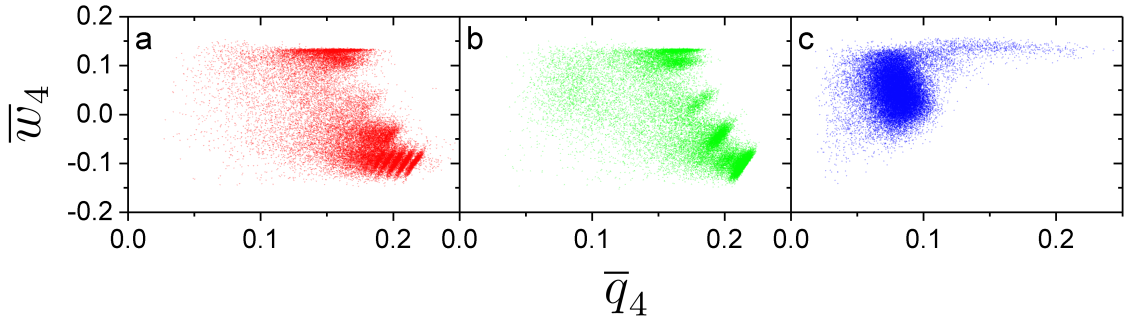

Fig. 7.7 Comparison between the $\overline{q}_4$-$\overline{w}_4$-plane for the same binary system using three different definitions of neighboring particles. The order parameters $\overline{q}_4$ and $\overline{w}_4$ are calculated with (a) cutoff neighbors, (b) a fixed number of 12 neighbors and (c) Voronoi neighbors. Each point corresponds to one particle. The data is part of a measurement from chapter 8. Definitions of the order parameters $\overline{q}_i$ and $\overline{w}_i$ will be given in section 7.5.2.

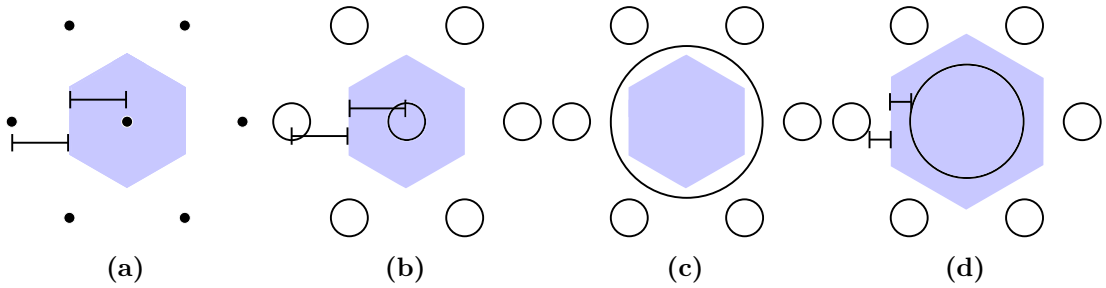

Fig. 7.8 Comparison of different ways to define the local volume (blue) of a central particle. (a) Particles are point objects and each point inside the local (Voronoi) volume is closer to the central particle than to any other one. (b) If all particles have the same finite size, one can use their centers and continue with (a). (c) The use of particle centers can lead to strange results if particles have unequal sizes. (d) The radical Voronoi tessellation splits the space into cells, such that each point inside a cell is closer to the surface of the interior particle than to any other particles' surface.

and another one around (0.19, -0.11). Without going into further detail, the two clouds indicate the existence of hcp and fcc structures. Relatively similar results are obtained using a fixed number of 12 neighbors. Instead, with Voronoi neighbors, only one cloud, centered around (0.08, 0.05), is found. It is, therefore, crucial to state the underlying definition of neighbors used in any calculation.

7.4 Measuring Local Volumes

This section will explain, how local volumes can be determined. While all particles in a perfect mono-crystal occupy the same amount of space, this typically does not hold for heterogeneous systems like colloidal glasses. By preparing a sample of given volume fraction ϕ, one fixes the global number of particles and the overall volume. Using particle coordinates and corresponding particle radii, one can determine a local volume for each individual particle. A natural way to do this is to divide the global volume into small volumes – named cells – that contain only one particle. This can be done by a Voronoi tessellation. The principle of a Voronoi tessellation is illustrated in figure 7.8a and figure 7.8b. In a two-dimensional hexagonal crystal, the Voronoi volume is a hexagon (light blue in the figure). Each edge of the hexagon has the same distance to its interior particle as it has to the corresponding neighboring particle. To be precise, in the "simple" Voronoi construction, the distance is measured from the edge to the *center* of the circle. In this respect, particles are treated as points.

If particles have very different sizes, a possible consequence is that the local Voronoi volume for a very big particle is smaller than its own volume (i.e., smaller than $4\pi R^3/3$ in 3D). This is unphysical (cf., figure 7.8c). Thus, an improved way is

that the edge of a cell is exactly halfway between the *surfaces* of two neighboring particles – this is the *radical* Voronoi tessellation. This definition is suitable for binary or polydisperse systems and reduces to the "simple" Voronoi construction in the case of a monodisperse system. A radical Voronoi cell for a big particle inside symmetrically arranged small particles is shown in figure 7.8d. How to use the "simple" Voronoi construction to find local volumes per particle has been described in a PhD theses by M. C. Jenkins [237, p.158]. Local volumes based on the radical Voronoi tessellation are obtained using voro++ [264].

Regardless of which definition is used to calculate local volumes, the result will always depend on the quality of particle tracking. So, determining local volumes does only make sense if the vast majority of particles are correctly detected. As for any other local measure, extrapolating the information from local volumes to the global system needs the assumption that the local particles are representative of the total system.

7.5 Characterization of Local Structures

This section will describe how to analyze the topology of local structures. From a qualitative point of view, one is, for example, interested in whether particles arrange in an amorphous or an ordered way. Furthermore, one may quantify the degree of order and also distinguish between different crystal structures, like fcc, hcp or bcc structures (cf., section 2.4.2).

In the previous section, it was explained how one can measure local volumes. Since cells from the Voronoi tessellation are convex polyhedra, they can be classified by their number of faces, edges, and vertices. This will be part of section 7.5.1.

The probably most common way to characterize structures invokes the bond order parameters from Steinhardt et al. [265]. Many people quantify the degree of order by a global (i.e., ensemble-averaged) bond order parameter. The necessary equations will be given in section 7.5.2 together with an improved version by Lechner and Dellago [266]. For further reading, references [260, 267, 268] are recommended.

7.5.1 Identification of Local Polyhedra

As introduced in section 7.4, the Voronoi tessellation divides the total space into convex polyhedra. The surface of a convex polyhedron is classified via Euler's polyhedron formula, namely,

$$N_v - N_e + N_f = 2\,, \tag{7.21}$$

where N_v, N_e, and N_f are the numbers of vertices, edges, and faces, respectively.

Some possible combinations are given in table 7.1. In the last column of the table, the name of the corresponding *dual* or *reciprocal polyhedron* is given. If a

Polyhedron	N_f	N_e	N_v	Dual
Cube (sc)	6	12	8	Octahedron
Regular dodecahedron*	12	30	20	Regular Icosahedron
Rhombic dodecahedron (fcc)	12	24	14	Cuboctahedron
Trapezo-rhombic dodecahedron (hcp)	12	24	14	Triangular orthobicupola
Truncated octahedron (bcc)	14	36	24	Tetrakis Hexahedron
Tetrakis Hexahedron	24	36	14	Truncated octahedron
Triangular orthobicupola	14	24	12	Trapezo-rhombic dodecahedron
Cuboctahedron	14	24	12	Rhombic dodecahedron
Regular Icosahedron	20	30	12	Regular dodecahedron
Octahedron	8	12	6	Cube

Tab. 7.1 Some relevant polyhedra with their number of faces N_f, edges N_e, and vertices N_v. Faces, edges, and vertices are interrelated by equation (7.21). If a polyhedron has N_f faces and N_v vertices, its dual (or reciprocal polyhedron) has N_v faces and N_f vertices. *Interestingly, a polyhedron with the tuple ($N_f = 12$, $N_e = 30$, $N_v = 20$) is sometimes referred to as an icosahedron (e.g., [269, tab. 1]). In fact, a ($N_f = 12$, $N_e = 30$, $N_v = 20$)-polyhedron is not an icosahedron but a regular dodecahedron. The icosahedron is the *dual* polyhedron of the regular dodecahedron.

polyhedron has N_f faces and N_v vertices, its dual has N_v faces and N_f vertices (cf., [270, p.157]). The relation between a polyhedron and its dual is illustrated in figure 7.9 for the case of a single cubic (sc) lattice. In this case, the cube corresponds to the Voronoi cell of one particle. The cube contains one and only one particle. Instead, the octahedron is essentially obtained by connecting all (Voronoi) neighbors of a given particle. Thus, the number of vertices of the cuboctahedron is equal to the number of (Voronoi) neighbors. In general, if a Voronoi polyhedron has N_f faces, N_e edges, and N_v vertices, its dual has N_v faces, N_e edges, and N_f vertices.

The remaining polyhedra from table 7.1 are visualized in figure 7.10. The polyhedra that belong to crystal structures are all space-filling. Instead, the regular icosahedron does not fill space. Nevertheless, all these polyhedra have high symmetry.

What happens in the case of a thermal system, where the particle centers are fluctuating? Are the polyhedra robust against thermal noise? The answer is no [259, 260]. This is exemplified in figure 7.11. In an ideal fcc crystal (figure 7.11a), all particles are exactly on their lattice positions (cf., figure 7.11c), and the polyhedron analysis finds rhombic dodecahedra with 100% accuracy. In a thermal fcc crystal (figure 7.11b), where noise is added to the particle position (cf., figure 7.11d), no (!) polyhedron with 12 faces, 24 edges and 14 vertices is found. Simply speaking, polyhedra of a thermal system are dented and have additional edges and faces.

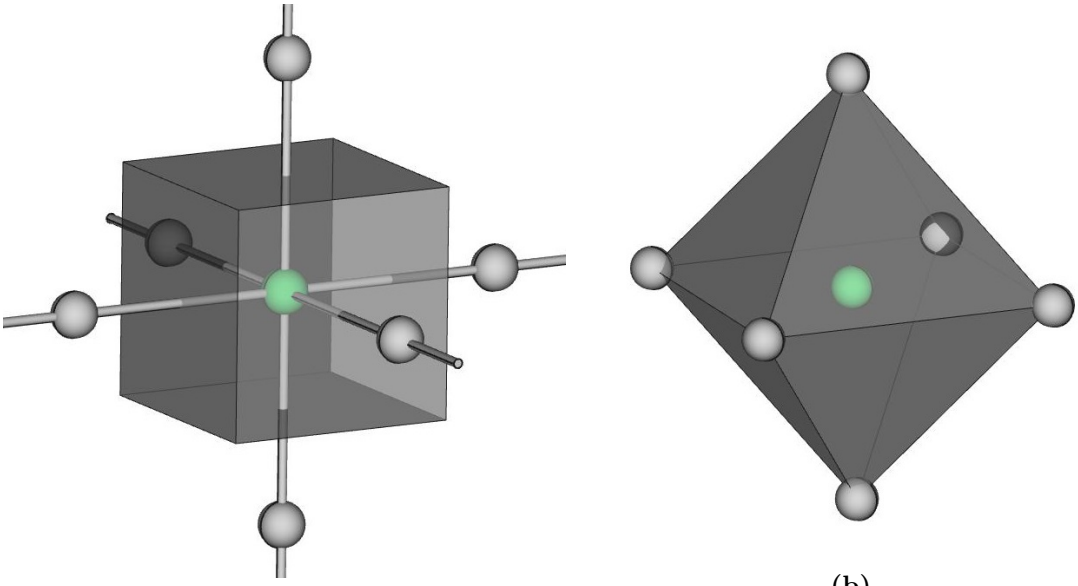

Fig. 7.9 (a) A cube ($N_f = 6$, $N_e = 12$, $N_v = 8$) and (b) its dual, an octahedron $(8, 12, 6)$.

This is nicely illustrated in figure 1 of reference [259] for corresponding sc and fcc polyhedra.

Nevertheless, not all structures are prone to noise. A bcc structure is way more robust, as shown in figure 7.12.

7.5.2 Local Order Parameters

The structure (and hence also degree of crystallization) is typically quantified using local bond parameters, also known as Steinhardt order parameters [265]. Since the characterization of local structures is based on the position of neighboring particles, it will depend on the underlying definition of a neighbor (as can be seen in figure 7.7 or in reference [258]). Often, bond order parameters are calculated with cutoff-neighbors (cf., [265, 266]). In the following, it will be implicitly assumed that "appropriate" neighbors are used.

The local order parameters are based on the complex vectors

$$q_{lm}(k) = \frac{1}{N_b(k)} \sum_{j=1}^{N_b(k)} Y_{lm}(\vec{r}_{kj}) \tag{7.22}$$

with the spherical harmonics Y_{lm}, where l is a free integer parameter and m is running in steps of one from $-l$ to $+l$. The vector $\vec{r}_{kj}$ points from particle k to particle j. The summation runs over all N_b neighbors of particle k. The averaged

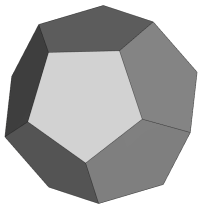

(a) Regular dodecahedron (12,30,20)

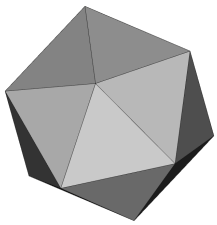

(b) Regular icosahedron (20,30,12)

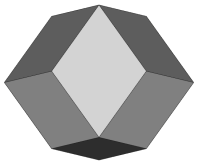

(c) Rhombic dodecahedron (12,24,14)

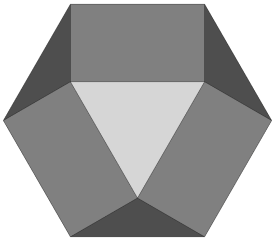

(d) Cuboctahedron (14,24,12)

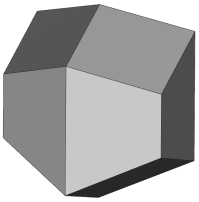

(e) Trapezo-rhombic dodecahedron (12,24,14)

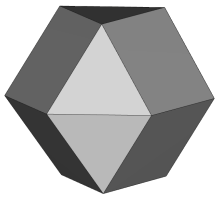

(f) Triangular orthobicupola (14,24,12)

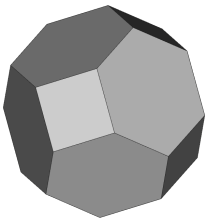

(g) Truncated octahedron (14,36,24)

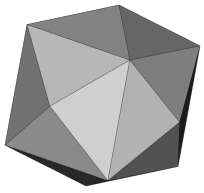

(h) Tetrakis hexahedron (24,36,14)

Fig. 7.10 Illustration of polyhedra. Names, as well as the number of faces, edges, and vertices, are given in the respective captions.

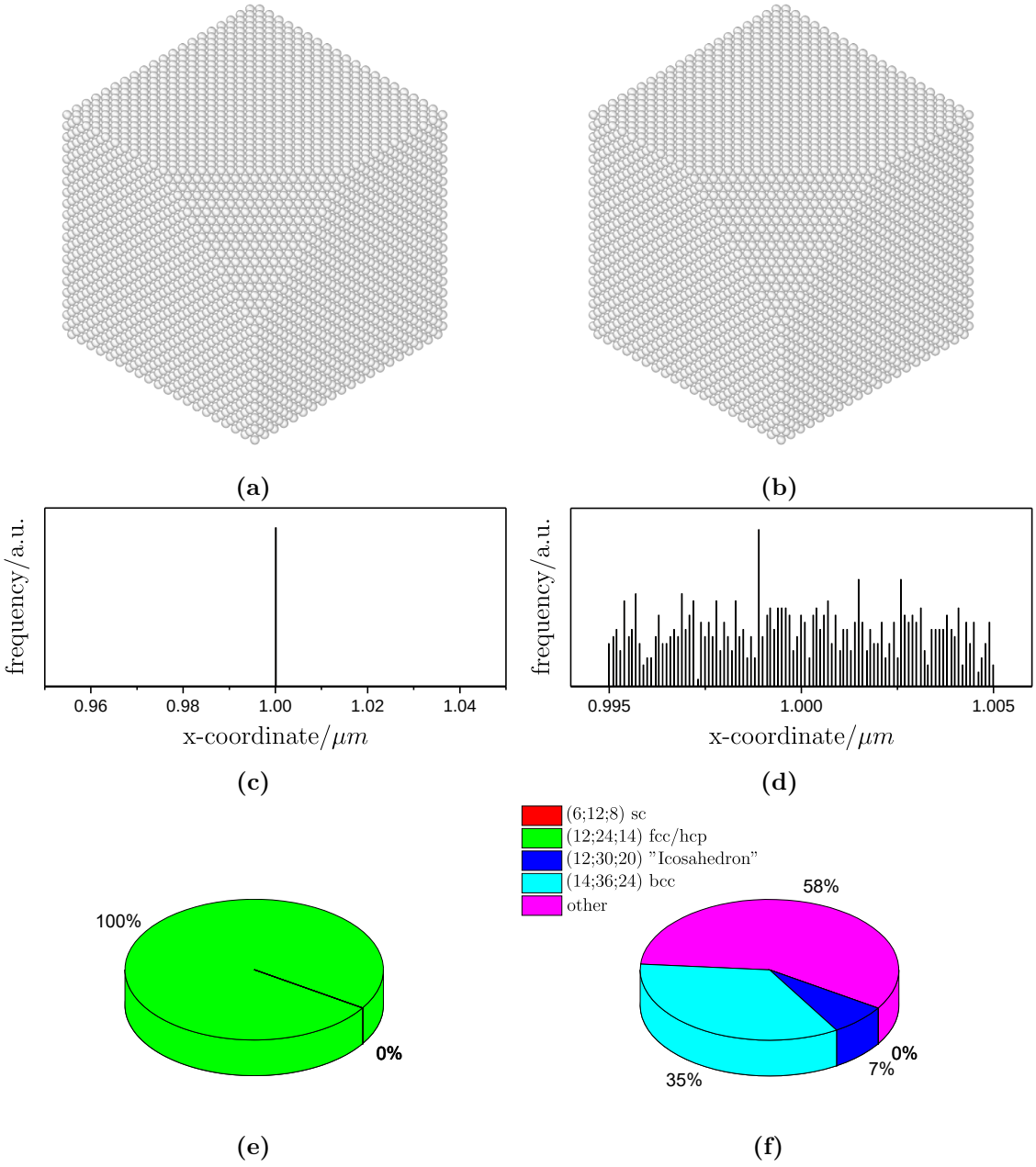

Fig. 7.11 Comparison of (a) an ideal fcc crystal and (b) an fcc crystal in which uniform noise is added to the particle positions. (The difference is not visible by eye.) Each cube is cut in the (111)-direction in order to show the six-fold symmetry. Histograms are intended to indicate that the particles are located (c) exactly or (d) close to their grid points. Results based on a Voronoi calculation are shown for (e) the ideal fcc crystal and (f) the "Brownian" fcc crystal. A small distortion of particle positions has dramatic effects on the shape of the individual Voronoi cells. The numbers in brackets are faces, edges, and vertices. "Other" refers to polyhedra not listed in table 7.1.

(a) ideal bcc crystal **(b)** bcc crystal with noise

Fig. 7.12 Impact of small lattice distortions on a bcc crystal. In contrast to the fcc-crystal shown before (figure 7.11), the Voronoi polyhedra for the bcc structure are much more robust against small distortions.

(local) bond order parameter according to Lechner and Dellago [266] is[1]

$$\overline{q}_l(i) = \sqrt{\frac{4\pi}{2l+1} \sum_{m=-l}^{l} |\overline{q}_{lm}(i)|^2}\,, \tag{7.23}$$

where

$$\overline{q}_{lm}(i) = \frac{1}{N_b(i)} \sum_{k=0}^{N_b(i)} q_{lm}(k)\,. \tag{7.24}$$

The sum in equation (7.24) runs over all $N_b(i)$ neighbors of particle i and additionally includes particle i itself. One can calculate a global order parameter

$$\langle \overline{q}_l \rangle \equiv \langle \overline{q}_l(i) \rangle_i \tag{7.25}$$

as an ensemble average of all local order parameters. Important values of l are 4 and 6. A value of $\langle \overline{q}_6 \rangle \approx 0.3 - 0.33$ can be regarded as a threshold to separate liquid and crystal structures [266]. Crystal structures themselves can be distinguished, for instance, by the combination of $\overline{q}_6(i)$ and $\overline{q}_4(i)$.

Lechner and Dellago also use the averaged order parameter $\overline{w}_l$. The equation for this averaged version reads

$$\overline{w}_l(i) = \frac{\displaystyle\sum_{m_1+m_2+m_3=0} \begin{pmatrix} l & l & l \\ m_1 & m_2 & m_3 \end{pmatrix} \overline{q}_{lm_1}(i)\overline{q}_{lm_2}(i)\overline{q}_{lm_3}(i)}{\left(\displaystyle\sum_{m=-l}^{l} |\overline{q}_{lm}(i)|^2 \right)^{3/2}}\,, \tag{7.26}$$

[1] The classical Steinhardt order parameter q_l is recovered by setting $\overline{q}_{lm}(i) = q_{lm}(i)$ in the right-hand side of equation (7.23).

	q_2	q_4	q_6	q_7	q_8	w_4	w_6	w_8	w_{10}
sc	0	0.764	0.354	0	0.718	0.159	0.013	0.058	0.090
bcc^1	0	0.509	0.629	0	0.213				
bcc^2	0	0.036	0.511	0	0.429	0.159	0.013	-0.058	-0.080
fcc	0	0.190	0.575	0	0.404	-0.159	-0.013	0.058	-0.090
hcp	0	0.097	0.484	0.311	0.317	0.134	-0.012	0.051	-0.080
icos	0	0	0.663	0	0	0	-0.170	0	-0.094

Tab. 7.2 Selected values of (non-averaged) order parameters q_l and w_l, taken from references [258, 265]. In the case of the bcc crystal, values are given for the closest eight (bcc^1) and fourteen neighbors (bcc^2), respectively. Note that while all q_l are positive, the w_l can be positive or negative.

where

$$\begin{pmatrix} l & l & l \\ m_1 & m_2 & m_3 \end{pmatrix} \tag{7.27}$$

are Wigner 3j symbols. They are calculated using a lengthy expression, first derived by Racah [271, 272] and shown in an explicit form in the book by Landau and Lifshitz [273, p.405]. Again, the non-averaged order parameter w_l is recovered if one replaces the $\overline{q}_{lm}$ by q_{lm} in equation (7.26). Selected values for q_l and w_l are listed in table 7.2. Perfectly symmetric structures have a vanishing q_2 value. This can also be used to distinguish ordered from disordered structures [258]. The parameter q_6, which is often used to quantify order, has its highest value for an icosahedral structure. As can be seen in the case of the bcc crystal, it makes a difference, whether the closest eight or the closest fourteen neighbors are used. Generally speaking, the underlying neighbor definition can affect the numbers. Still, a suitable set of bond order parameters is relatively robust in distinguishing different structures.

Part III

Experiments

8

Structure of Binary Mixtures under Shear: Hand in Hand or Topsy-Turvy?

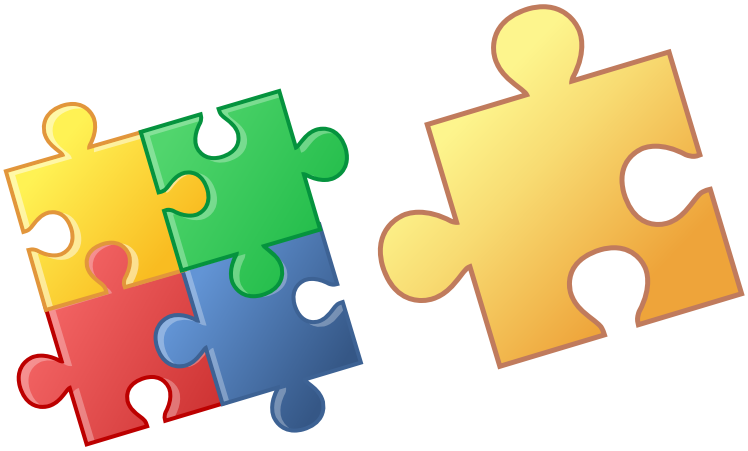

8.1 Abstract

Colloidal hard spheres are expected to crystallize at high volume fractions (i.e., $\phi > 0.545$). However, if the system is polydisperse, then crystallization can be suppressed. In this work, we study crystallization under shear. To mimic polydispersity, we investigate binary suspensions of various size ratios (i.e., $0.65 \leq \alpha \leq 0.94$). Confocal microscopy is used to obtain structures on a single-particle level. In the quiescent state, we observe ordering for large size ratios (i.e., $\alpha \gtrsim 0.91$). Under oscillatory shear, this regime extends to $\alpha \gtrsim 0.85$, corresponding to a critical polydispersity of $\delta_c \approx 9\%$. For samples with liquid-crystal-coexistence, we separately study the amorphous and the ordered part and find a larger number of bigger spheres in the crystalline regions. We link the crystallization ability to local packing constraints in terms of nearest neighbors. The results are consistent with previous findings on colloidal crystallization and in agreement with the empirical Hume-Rothery size factor for metallic alloys.

8.2 Introduction

Colloidal hard spheres are a widely used model system with a simple interaction potential and can mimic atoms, rare gasses, and metallic alloys. The pairwise interaction between two hard spheres is infinite at contact and zero else. Due to the hard-sphere interaction, the temperature does not play a role, and in terms of the free energy $F_{\mathrm{H}} = E - TS$, the phase behavior is solely driven by entropy. The only control parameter in single-component systems is the packing fraction $\phi = V_{\mathrm{spheres}}/V_{\mathrm{total}}$, which relates the volume of all spheres to the total volume.

The phase behavior of colloidal single-component hard spheres has been studied by Pusey and van Megen [70]. They find a fluid phase for low volume fractions (i.e., $0 \leq \phi < 0.454$), a liquid-solid coexistence region at intermediate volume fractions (i.e., $0.454 \leq \phi < 0.545$) and a crystalline region for moderately high volume fractions (i.e., $\phi \geq 0.545$). As the glass transition (i.e., $\phi_g \approx 0.58$) is approached, particle motion gets frustrated and the system forms a nonequilibrium glass.

Colloidal spheres with a nominal radius R typically have a finite size distribution $P(R)$. This is quantified in terms of the polydispersity $\delta = \mathrm{SD}/\overline{R}$, which is the standard deviation of the size distribution divided by its mean value. Polydispersity has an important impact on the phase behavior of hard spheres [88–93]. Especially, polydispersity impedes crystallization. Geometrical arguments based on a Lindemann melting criterion estimate a critical polydispersity between 6-12% [99]. Previous work on equilibrium hard spheres states a terminal polydispersity (above which crystallization is suppressed) to be around 5%, 5.7% or 7%, respectively [90, 94, 96, 274]. If fractionation is allowed then samples with polydispersities of 12%, 14% and more can form coexisting liquids and crystals [87, 90]. We will make use of the fact that the equilibrium phase behavior of polydisperse colloids can be mapped to an equivalent binary mixture based on the first moments of the size distribution [102]. Therefore, we investigate binary mixtures of different size ratios to reveal the impact of polydispersity on crystallization.

Binary materials are the simplest multi-component systems. Compared to one-component systems, the introduction of a second species increases the number of free parameters. Accordingly, additional parameters are the size ratio $\alpha = R_s/R_b$, and the relative volume fraction of big spheres $X = V_b/(V_s + V_b)$, where the subscripts s and b refer to the smaller and bigger species, respectively.

Binary materials with industrial relevance are, for example, metallic alloys. For binary metallic alloys, Barrat et al. [104] used density-functional theory to establish three different phase-diagrams for size ratios close to unity: The first one is the *spindle* phase diagram, where the two components are miscible in both the fluid and crystal phase. In this case, both components are fully miscible, but the crystal phase has a higher fraction of large spheres. The second one is the *azeotropic* phase diagram. There, the two components are not miscible in all proportions and details depend on the composition X. In the third phase diagram, the *eutectic* one, a stable

crystal is only formed by fractionation. These three phases are typically found in the range $0.85 < \alpha < 1$ [104, 109–112]. Barrat et al. state that it is impossible to obtain a mechanically stable crystal below $\alpha = 0.85$ [104]. This is consistent with experimental results [275]. Denton and Ashcroft find similar values for the eutectic phase using a density-functional theory and predict a disordered fcc crystal to be the most stable phase in the region $0.76 < \alpha < 1$ [110]. A crystal that is composed of two species can have various internal structures. In the case of the random ordered substitutional alloy, there exists an empirical rule in terms of the size difference: According to the first Hume-Rothery rule, metallic alloys can form crystalline structures, as long as the difference in diameter between the two atoms is less than 14% [117].

This empirical finding is supported by various techniques. For instance, vapor quenching of binary metallic alloys (e.g., Co-Cu, Cu-Ag, Co-Ag, Cu-Mg, Au-Mg, Cu-Au) creates an amorphous structure for size differences larger than 10% [276]. Millimeter-sized hard spheres have been used to model 2D alloys [277], where amorphous structures over a wide range of compositions are found for size differences around 25%. Numerical simulations typically use systems with $\alpha = 0.71$ to prevent crystallization [138, 139, 278]. The latter is in agreement with an experimental study on binary mixtures of PMMA spheres, where no crystalline structure was found for $\alpha = 0.72$, except for scenarios where the mixture consisted of mainly large or small spheres [98]. Metastable single cubic structures were observed for $\alpha = 0.736$ [279]. Further relevant literature including binary mixtures with similar amounts of large and small spheres and size ratios in the range $0.5 < \alpha < 1$ and below can be found elsewhere [105, 107]. Binary mixtures with still larger difference in the radii between the two components have been studied in experiments [113] and theory [114], but are beyond the scope of this letter. In two dimensions, numerical studies analyzed disorder as a function of size ratio [280], or mapped the jamming transition as a function of size and number ratio [281].

Structural ordering is also studied under external constraints: For instance, structural ordering of hard and soft spheres is observed by experiments and simulations under steady [239, 282–284] and oscillatory shear [228, 282, 285–287]. Strain amplitudes around 40% are useful for (macroscopic) crystal formation of soft spherical micelles [286]. With PMMA-spheres, strain amplitudes around 100% are found to crystallize previously fluid-like samples [282]. Experiments on a two-dimensional system of soft colloids with intermediate volume fraction find that small oscillatory strains lead to large defect-free crystals [257]. Oscillation frequencies should be in the order of one [282, 286]. As an application, flow can be used to align photonic crystals of colloids [288]. While flow can be used to form structures, also the opposite is possible, that is, shear above a critical stress can melt crystals [289].

The ability to design crystalline or amorphous solids is crucial for material scientists since their mechanical properties differ. For example, hitting a golf ball with a golf club from amorphous metal yields higher distances than with a crystalline

metal because the amorphous club deforms less and hence transfers the momentum with fewer losses.

In this work, we investigate the structure of binary mixtures of hard-sphere-like colloidal particles under shear. Due to their sizes, colloids can be observed by light microscopy and their dynamics are slow enough to be followed in experiments. Structural ordering has previously been inferred experimentally by light [282], x-ray [286, 290] or neutron scattering [286, 291, 292] as well as using microscopic techniques [239, 289]. Using confocal microscopy, three-dimensional images can be obtained on a single-particle level. One advantage of confocal microscopy as compared to scattering techniques is that local inhomogeneities can be observed more easily.

The goal is to experimentally find the transition between crystallizing and non-crystallizing samples under nonequilibrium conditions, that is, under shear. This shall shed light on the role of the size ratio (or equivalently, the polydispersity) in order to be able to design materials with a priori knowledge about their ability to crystallize.

8.3 Materials and Methods

The colloidal model system consists of poly(methyl methacrylate) (PMMA) spheres stabilized by poly(12-hydroxy-stearic acid) (PHS) [60], dispersed in a solvent of *cis*-decahydronaphthalene (*cis*-decalin) and cycloheptyl bromide (CHB7), which almost matches both the density and the refractive index of PMMA. In CHB7, PMMA particles acquire a charge [51, 52], especially, if they are locked [61]. Our particles are locked and labeled with rhodamine-B, where also rhodamine is known to slightly charge particles [62]. In order to screen charges, we add a concentration of $c = 4\,\mathrm{mmol}$ of the salt tetrabutylammonium chloride (TBAC) [51].

Particle radii of the single components are obtained from electron microscopy images (SEM) in the dry state and averaged over at least 50 particles. As an example, one SEM-image is given in figure 8.1. In order to obtain "true" sizes, the sizes from SEM may be increased by up to 25% to incorporate for swelling [209]. We anticipate uncertainties in the determination of *absolute* sizes but stick to the estimates from SEM since we are currently interested in size *ratios*. Corresponding sizes and size ratios of the studied samples are listed in table 8.1.

The volume fractions of the one-component batches are set by centrifuging the samples and assuming a random close packing, $\phi_{\mathrm{RCP}} = 0.65$ [91]. Binary mixtures are prepared by mixing two one-component batches at intermediate volume fractions of $\phi = 0.4$. If not stated otherwise, the binary mixtures contain the same volume of bigger and smaller spheres (i.e., $X = 0.5$). A total volume fraction of $\phi = 0.58$ for each binary-mixture is then set by subsequent centrifugation and dilution from random close packing. The random close packing of the binaries is estimated from jamming packing fractions of binary hard-sphere mixtures [86, 293]. For size ratios

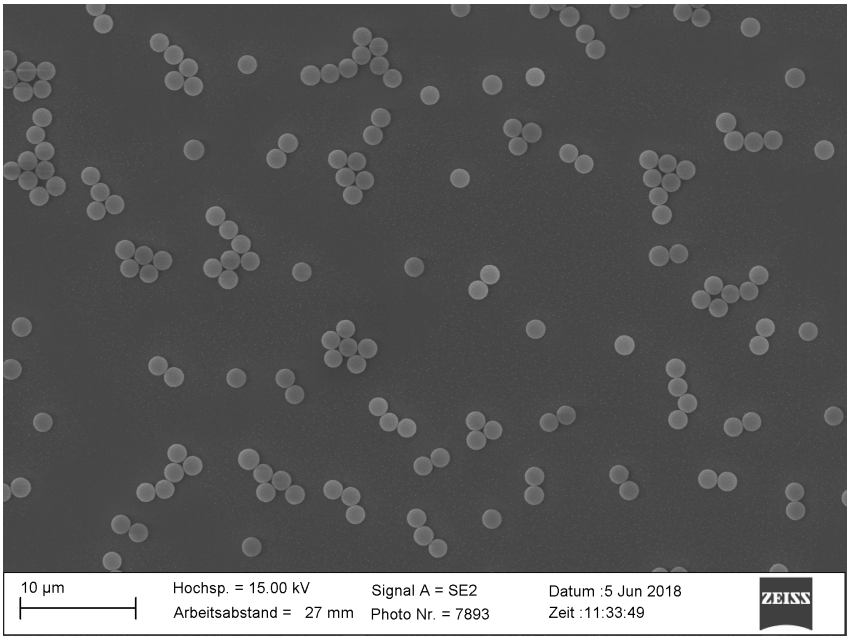

Fig. 8.1 SEM-image of a one-component batch of particles with a mean radius of $R = 902\,\mathrm{nm}$. The image is taken at the Center of Advanced Imaging (CAi) at HHU Düsseldorf.

$R_s/\,\mathrm{nm}$	786	1104	786	902	835	902	786	835	786
$R_b/\,\mathrm{nm}$	835	1215	902	1104	1104	1215	1104	1215	1215
α	0.94	0.91	0.87	0.82	0.76	0.74	0.71	0.69	0.65
δ_α	0.03	0.05	0.07	0.10	0.13	0.14	0.16	0.18	0.20
$\delta_{\mathrm{conf.}}$	0.06	0.06	0.09	0.15	0.18	0.19	0.23	0.21	0.28

Tab. 8.1 Summary of the prepared samples with $X = 0.5$. Shown are radii R_i, size ratios $\alpha = R_a/R_b$ and polydispersities δ_i. Here, δ_α is a theoretical polydispersity that is calculated for an ideal binary system with size ratio α, whose size distribution consists of two delta peaks (cf., [123]). The experimentally obtained polydispersity $\delta_{\mathrm{conf.}}$ is based on size distributions of the binary mixtures as obtained from feature localization with confocal microscopy.

$0.71 \leq \alpha \leq 1$, the jamming packing fractions are almost identical [86, 293], and we thus use $\phi_{\mathrm{RCP}} = 0.65$ for all our mixtures.

Shear is applied by means of a home-build shear cell (cf., section 4.1). Our gap height is $h = 131\,\mathrm{nm}$. Scratched coverslips act as the top and bottom plates, and the surface roughness prevents wall slip, as verified with confocal microscopy.

We divide the shear protocol into four steps: After loading, the sample is left undisturbed to equilibrate for 10 minutes (step 1). The first application of shear is then performed by means of a dynamic strain sweep (DSS), at a frequency of $f = 0.7\,\mathrm{Hz}$, and covers strains from $\gamma_0 = 10\%$ to $\gamma_0 = 84\%$ (step 2). We then fix the strain amplitude $\gamma_0 = 84\%$ and shear the system at $f = 0.2\,\mathrm{Hz}$ for 200 oscillations (step 3). A subsequent inverse DSS ($\gamma_0 = 84\%$ to $\gamma_0 = 10\%$ at $f = 0.7\,\mathrm{Hz}$) is used to anneal the structure (step 4). *After* each step, shear is stopped for a short time (i.e., $\sim 3\,\mathrm{min}$) to record 3D-images. With that, we are able to follow the structural evolution of the system.

Image stacks from $z = 0\,\mu\mathrm{m}$ to $z = 30\,\mu\mathrm{m}$ inside the sample are recorded with a Nikon A1 confocal, which is equipped with an oil-immersion objective (Nikon, Plan Apo 100x NA = 1.4) and a solid-state laser ($\lambda = 561\,\mathrm{nm}$). Individual images contain 512×512 pixels corresponding to $64\,\mu\mathrm{m} \times 64\,\mu\mathrm{m}$ for $\alpha = 0.91$ and $42\,\mu\mathrm{m} \times 42\,\mu\mathrm{m}$ for all other mixtures.

Particle tracking is performed using the size-sensitive algorithm by Leomach and Tanaka [209]. Structural analysis includes the order parameter $\overline{q}_6 \equiv \overline{q}_6(i)$ (equation (7.23),[266]), calculated for each particle i, as well as the ensemble-averaged version $\langle \overline{q}_l \rangle \equiv \langle \overline{q}_l(i) \rangle_i$ (cf., section 7.5.2). Both quantities are based on the Steinhardt order parameters [265], and the calculation incorporates the positions of neighboring particles. We follow previous approaches and define neighbors with a distance threshold (cf., [265, 266]). For each mixture, thresholds are taken from the first major minimum of the respective pair correlation function. Results are cross-checked with Voronoi neighbors as well as a fixed number of twelve neighbors (cf., section 7.3). While the numbers of the $\overline{q}_6$-values, in fact, shift to smaller or larger values, qualitative trends (on which we will mainly focus in section 8.4) are not affected. By analyzing only particles that are located at least $3\,\mu\mathrm{m}$ away from the boundaries of the confocal z-stack, we reduce possible edge and wall effects. The averaged third-order bond order parameter $\overline{w}_4$ (equation (7.26)) is also calculated [266]. A radical Voronoi tessellation, for the calculation of contact numbers, is performed with voro++ [264]. The radical Voronoi tessellation calculates a polyhedron for every particle, where the space inside the polyhedron is closer to the surface of the interior particle than to any other particle's surface. Renderings are prepared using Ovito [243].

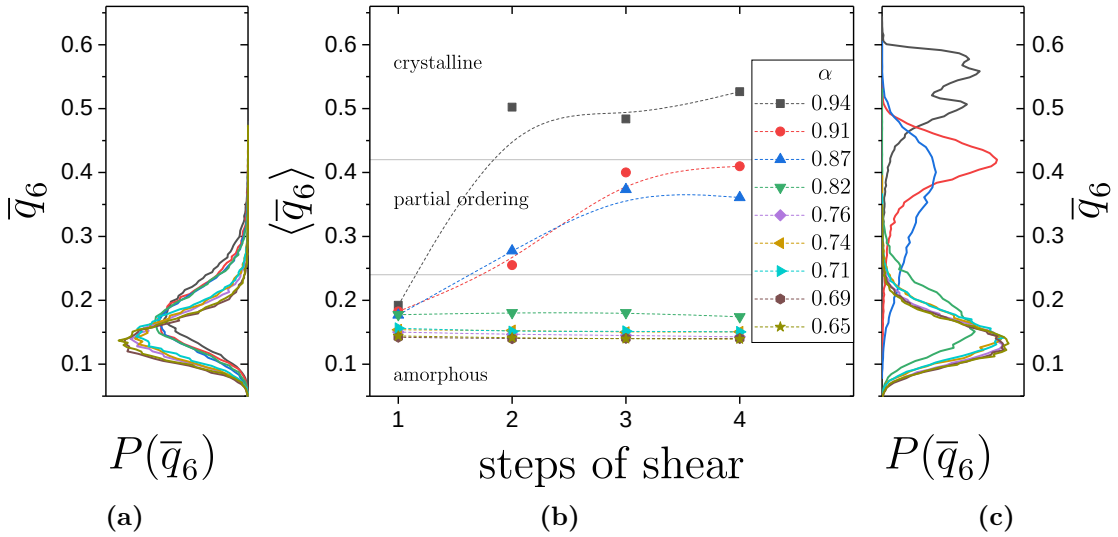

Fig. 8.2 (a) Full distributions of $\overline{q}_6$ before any application of shear (i.e., step 1). (b) Evolution of the ensemble-averaged structural order parameter $\langle \overline{q}_6 \rangle$ for the four steps of shear. Dashed lines are guides to the eye. Horizontal solid lines indicate qualitative findings as obtained by inspection of raw images. (c) Full distributions of $\overline{q}_6$ at the end of the experiment (i.e., step 4). The four steps of shear are defined in the text. Sizes ratios α are given in the legend. All mixtures have a symmetric composition with $X = 0.5$.

8.4 Results

We first check whether samples crystallize without shear. After a time period of three weeks, the $\alpha = 0.94$ sample shows full and the $\alpha = 0.91$ sample partial crystallization. During the same amount of time, the $\alpha = 0.87$ sample shows some wetting at the surface but does not exhibit any crystalline regions in the bulk. Accordingly, samples with $\alpha < 0.87$ are not expected to crystallize either.

We now include shear: Figure 8.2 shows the main findings that can be grouped as follows: All mixtures are amorphous after loading and before the application of shear (i.e., step 1), as can be inferred, for example, from the evolution of the ensemble-averaged structure order parameter as well as the initial distributions of individual q_6-values. For samples with small size ratios, that is, for $0.65 \leq \alpha \leq 0.82$, nothing changes upon shear. They stay amorphous during all four steps of our protocol. In contrast, samples with size ratios $\alpha \geq 0.87$ (partially) crystallize, as quantified by an increase of the $\langle \overline{q}_6 \rangle$-values under shear (cf., figure 8.2b).

For the sake of clarity, we will now focus on the four samples with size ratios 0.71, 0.82, 0.87 and 0.94. We choose these four representative samples because they include the one with the most dominant ordering (i.e., $\alpha = 0.94$), the one with the smallest size ratio that still shows ordering under shear (i.e., $\alpha = 0.87$), the sample

with the highest size ratio that stays amorphous under shear (i.e., $\alpha = 0.82$), as well as a sample that is far away from any crystallization (i.e., $\alpha = 0.71$).

We can take a direct look at the corresponding structures. Renderings of these four mixtures before (i.e., step 1) and after shear (i.e., step 4) are shown in figure 8.3. As can be seen, the $\alpha = 0.71$ and $\alpha = 0.82$-mixtures are amorphous in both cases.

In contrast, the $\alpha = 0.94$ sample is amorphous before shear, but crystalline afterward. In the latter, the stacking is a random mixture of hcp (ABABAB) and fcc (ABCABCABC). Both stacking orders are distinguished using the second-order bond orientational order parameter $\overline{w}_4$, where the hcp structure has positive and the fcc structure has negative values, respectively [266] (data not shown here). As can be seen in the rendering, the crystalline structure is interrupted by point- and line-defects. Significant signatures of single cubic and body-centered crystals, as well as icosahedral structures, are not found.

Interestingly, the $\alpha = 0.87$ mixture has coexisting amorphous and crystalline regions after shear. This enables us to investigate these structural differences in more detail. To do so, we focus on extremely amorphous (i.e., $\overline{q}_6 < 0.23$) and highly crystalline (i.e., $\overline{q}_6 > 0.45$) regions of this sample. Threshold values are chosen such that each subpopulation corresponds to 10% of the total population. To account for possible inhomogeneities in the distribution of bigger and smaller particles, we plot histograms of particle sizes in figure 8.4. Clearly, crystalline regions have a larger amount of bigger particles as compared to both the total and the amorphous part of the sample.

In order to further reveal the impact of the particle size distribution on the global structure, we analyze the local topology on a single-particle level by considering the total number of nearest neighbors around each particle. Here, neighboring particles are defined from the radical Voronoi tessellation (where the total number of neighbors corresponds to the total number of faces of a given polyhedron). The histograms of radical Voronoi contact numbers N_c are shown in figure 8.5.

For the two binary mixtures that show (partial) crystallization (i.e., $\alpha = 0.94$ and $\alpha = 0.87$), the total radical Voronoi contact distribution is unimodal and symmetric. The histograms are further subdivided into big and small spheres. In both cases, bigger spheres have a higher number of contacts than the smaller spheres. The mean values are $\langle N_c \rangle_{\text{small}} = 13.6$ and $\langle N_c \rangle_{\text{big}} = 14.5$ for $\alpha = 0.94$, and $\langle N_c \rangle_{\text{small}} = 13.6$ and $\langle N_c \rangle_{\text{big}} = 14.8$ for $\alpha = 0.87$. In the case of the $\alpha = 0.82$ sample, the individual histograms for small and big particles are now well distinct with mean values of $\langle N_c \rangle_{\text{small}} = 13.2$ and $\langle N_c \rangle_{\text{big}} = 15.7$, respectively. Additionally, the total distribution is broader and asymmetric. For $\alpha = 0.71$, the contact histogram is bimodal and the mean values of the big and small species are well separated.

For samples close to the crystal-amorphous transition (i.e., $\alpha \approx 0.87$), we also study different compositions, that is, we repeat the experiments with $X = 0.2$ and $X = 0.8$. The results after shear (i.e., step 4) are shown in figure 8.6. Asymmetric mixtures with a more dominant amount of small spheres (i.e., $X = 0.2$) or big

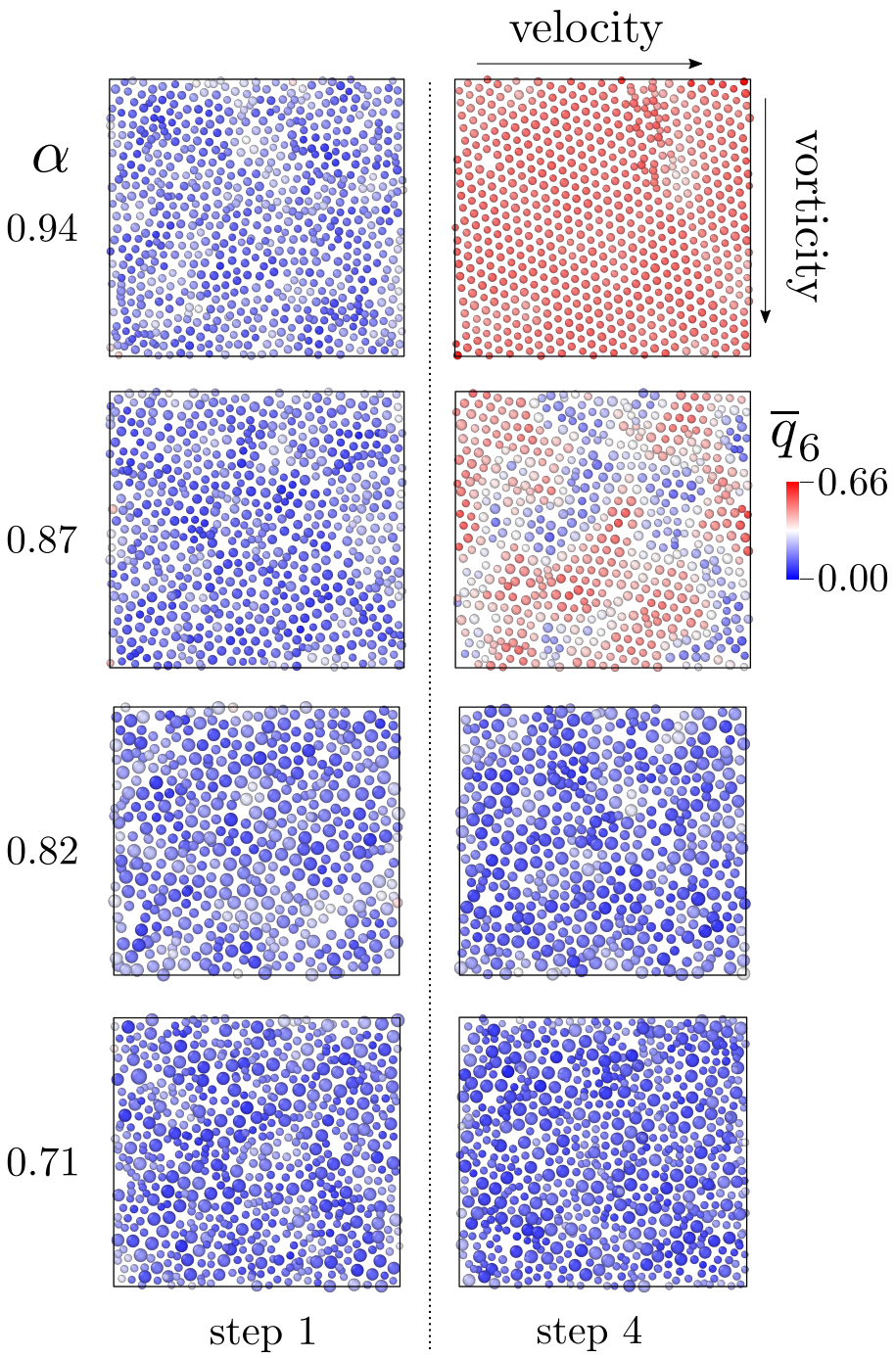

Fig. 8.3 Renderings of the samples with (from top to bottom) $\alpha = 0.94$, $\alpha = 0.87$, $\alpha = 0.82$, $\alpha = 0.71$ before (left) and after shear (right). Particles are drawn according to their size and marked blue for a liquid state ($\overline{q}_6 < 0.33$) and red for a crystal state ($\overline{q}_6 > 0.33$). Directions of shear as indicated.

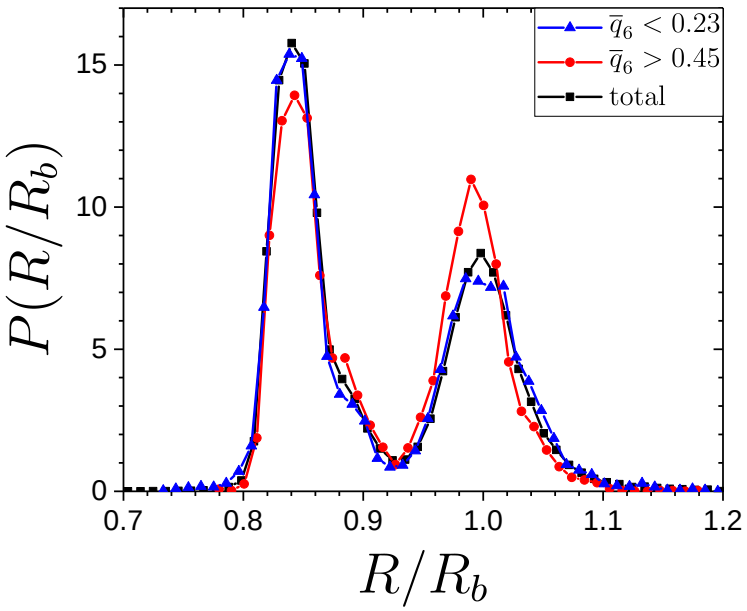

Fig. 8.4 Histogram of particle sizes for the $\alpha = 0.87$ sample after shear (i.e., step 4) for very crystalline particles $\overline{q_6} > 0.45$ (red), very amorphous particles $\overline{q_6} < 0.23$ (blue), and the total population (black).

spheres (i.e., $X = 0.8$) yield a higher $\langle \overline{q}_6 \rangle$-values, indicating a more ordered sample. For the given set of data, the change of $\langle \overline{q}_6 \rangle$ is relatively small, that it, the overall structure is not changed a lot. Samples that show (partial) crystallization at $X = 0.5$, still show (partial) crystallization at the other compositions. The only difference is that crystallization is more pronounced in the asymmetric mixtures. For $X = 0.2$ and $X = 0.8$, we find large areas that consist of essentially one component. In the mono-component case (i.e., $X = 0$ or $X = 1$), a full crystal is expected for all particle sizes.

As with different compositions, we also check a couple of different volume fractions and we have indications that the ability to crystallize is affected by ϕ. For instance, the $\alpha = 0.87$ sample, which shows (partial) ordering at $\phi = 0.58$, stays amorphous at $\phi = 0.61$.

8.5 Discussion

For studies of noncrystallizing systems, binaries with a size ratio of 1:1.4 (i.e., $\alpha = 0.71$) are frequently used [138, 187, 294]. This is supported by our experiments: We find that the limiting size ratio, which separates binary mixtures that can crystallize from those that cannot, is in the range $0.82 < \alpha < 0.87$. Our critical size ratio thus corresponds to a critical polydispersity of $8\% \lesssim \delta \lesssim 10\%$ and is, therefore,

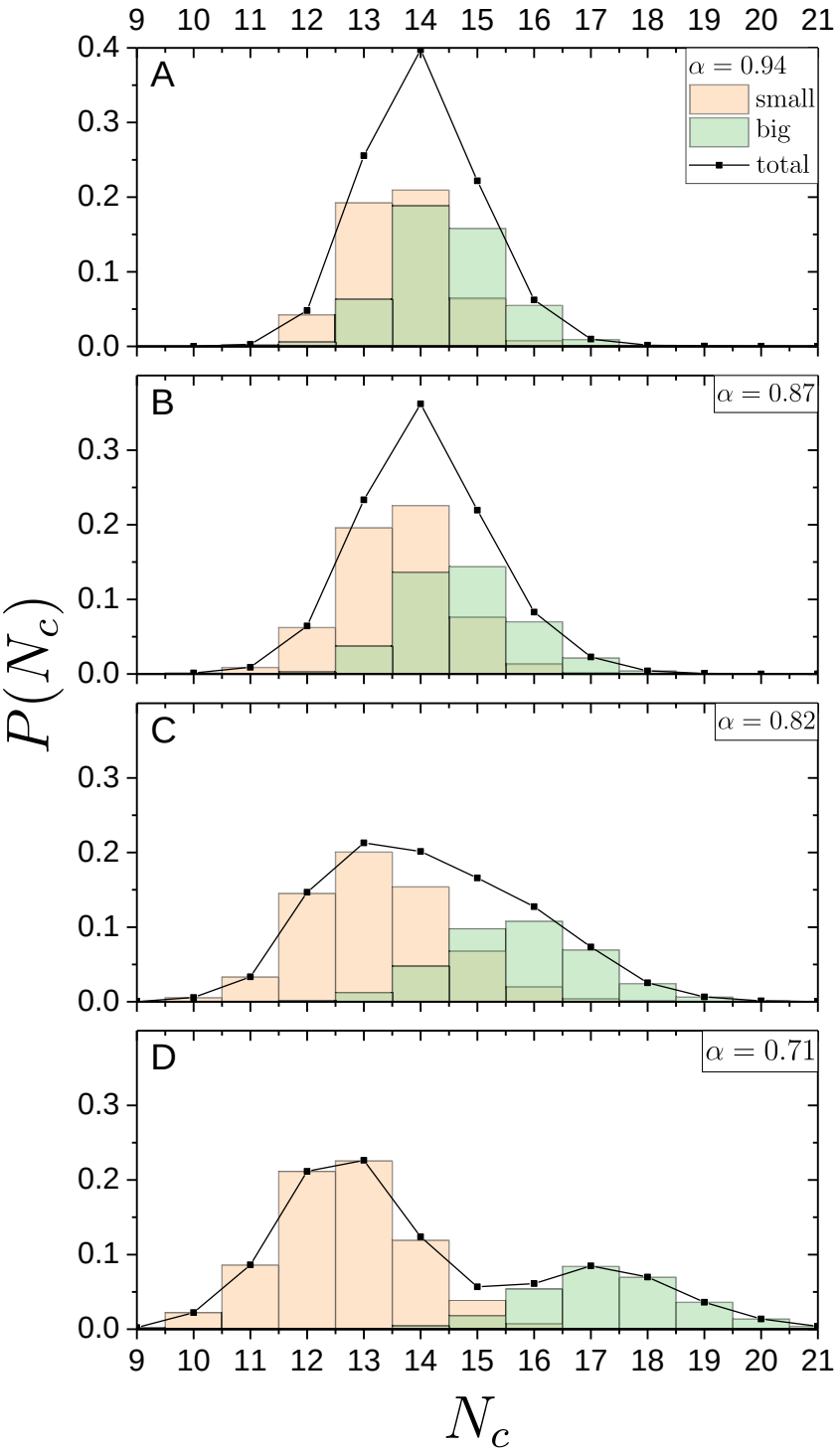

Fig. 8.5 Radical Voronoi contact number per species for (from top to bottom) $\alpha = 0.94$, $\alpha = 0.87$, $\alpha = 0.82$, $\alpha = 0.71$ after shear (step 4). Data are shown for smaller spheres (orange), larger spheres (green), and all spheres (black).

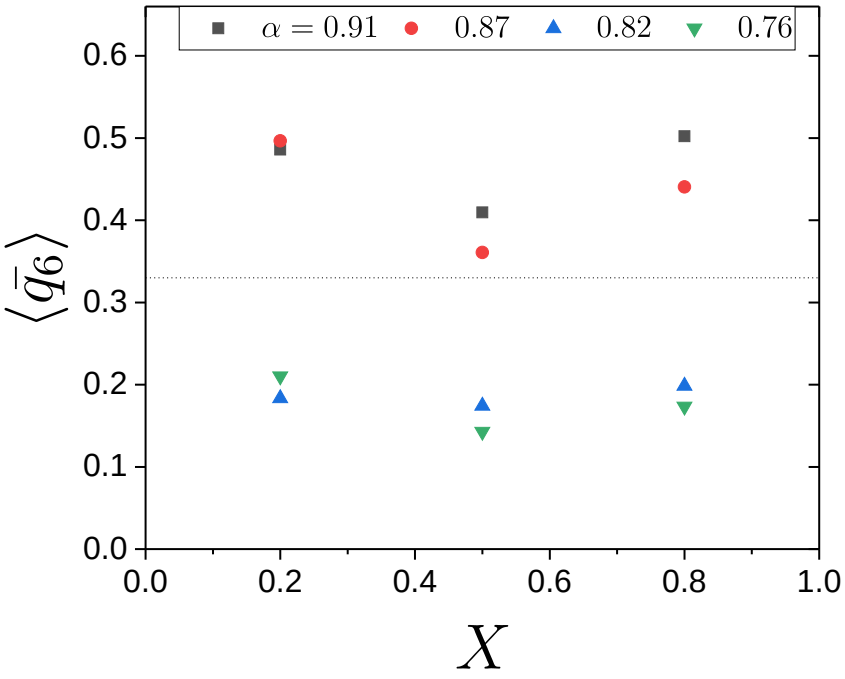

Fig. 8.6 Ensemble-averaged order parameter $\langle \bar{q}_6 \rangle$ as a function of composition X for $\phi = 0.58$. Size ratios α are indicated in the legend.

in good agreement with previous theoretical work on equilibrium systems [90].

In mixtures that show crystallization, we observe randomly close-packed structures, in perfect agreement with previous work [83, 285]. The orientation of the crystals is expected to depend on the strain amplitude [228, 285]. We do not observe any preferred orientation for all of our crystallizing samples. This might be related to our shear protocol, which incorporated both high ($\gamma_0 > 50\%$) and low strains ($\gamma_0 < 50\%$).

In terms of composition, we observe that symmetric mixtures are best suited to prevent crystallization (cf., figure 8.6). This is in qualitative agreement with simulations on binary colloids [295], theory [296, 297], and results from metallic alloys [276].

Fractionation (or demixing) is predicted for polydisperse samples at equilibrium [93, 298, 299]. We do not observe fractionation in our experimental time window. Also, the formation of more complex crystal structures, like $A_m B_n$ with m and $n > 1$, is not found in our experiments. Nevertheless, the mixtures could fractionate on much longer time scales.

We observe a liquid-crystal coexistence for $\alpha = 0.87$. The crystalline part contains a larger number of bigger spheres than the liquid, in agreement with previous results [83, 90, 295]. Williams et al. state that crystallites in an $\alpha = 0.90$ mixture form in places where the composition is favorable, and that crystallization should

be considerable slower below $\alpha = 0.90$ [295]. Similarly, it has been found that small particles are expelled from crystallites [209] and that crystals consist of predominantly big spheres [95]. This is also in agreement with the spindle type phase diagram for size ratios close to unity [104, 110].

In previous work, it has been found that larger impurities, that is, bigger particles, have a more disruptive influence on a lattice than smaller ones [104, 277]. Along these lines, Martin et al. find that a size distribution that is skewed to smaller sizes decreases crystallization by an order of magnitude [275]. This can be understood with the help of a Gedankenexperiment: Let us assume a close-packed crystal consisting of identical spheres. Replacing a spherical particle of the crystal with a smaller one is certainly less destructive than replacing it with a bigger particle, especially, if the diameter of the bigger particle is larger than the lattice spacing. From our findings, we conclude that few big particles can indeed destroy a mono-crystal, but a few crystallites of small spheres may persist.

Similarly to inhomogeneities in the distribution of particle sizes, there are possibly density inhomogeneities. For instance, it has been reported that shear-induced crystal structures within a glass create additional free volume [300]. The general agreement is that the crystalline phases have a higher volume fraction than the liquid phase of the same sample [90, 95, 104, 296, 301]. Uncertainties in the experimental determination of particle sizes [64] do not allow us to further contribute to this issue.

Exploitable results are instead obtained by counting the number of neighboring particles. The distribution of radical Voronoi contact numbers for the mixture with $\alpha = 0.94$ exhibits a peak around $N_c = 14$, which is in good agreement with Voronoi contact numbers of a concentrated one-component glass [256]. Note, that we would find a maximum of 12 instead of 14 nearest neighbors if we would consider neighbors from a cutoff distance that is taken from the first minimum of the pair correlation function (data not shown). Using the terminology of Bernal, Voronoi contacts are geometrical neighbors, while the particles within the first shell of the pair correlation function are physical neighbors [302]. Our results of the number of neighbors are also consistent with the picture described by Egami for the stability of metallic alloys [303] as well as theoretical considerations on parking numbers [304]. A higher contact number for larger as compared to smaller spheres is also reported in reference [293].

To correlate the number of neighbors with the ability to crystallize, we propose a qualitative picture that has already been noted by Smithline and Haymet [305]. Their idea is that for a size ratio far enough from unity, it becomes geometrically more and more difficult packing the same number of neighbors around each sphere. This qualitative difference between bigger and smaller particles is reasonable since bigger particles have a larger surface area than smaller ones and thus have, on average, more contacts.

Finally, crystallization depends on the volume fraction. For instance, increasing the volume fraction avoids crystallization [275] (cf., section 2.4.3). Preliminary

results on the $\alpha = 0.87$ mixture support this: While it shows (partial) ordering under shear at $\phi = 0.58$, it does not show ordering at $\phi = 0.61$. A kinetic argument is that particle rearrangements get more tricky above the glass transition. Additionally, the maximum packing fraction for ordered structures decreases as a function of polydispersity [87]. For $\delta \approx 12\%$, the maximum packing fraction is the same for ordered and disordered systems [87]. Thus, for a given volume fraction and size ratio, it may no longer be desirable to form crystals.

8.6 Conclusion

We investigated binary mixtures in the vicinity of the colloidal glass transition under oscillatory shear and determined the microscopic structure of the mixtures with confocal microscopy. For $\phi = 0.58$, we have identified three different regimes in the size ratio range $0.65 \leq \alpha \leq 0.94$. For size ratios close to unity (i.e., $0.91 \lesssim \alpha \lesssim 1$), the mixtures form random close-packed crystals in the quiescent state as well as under shear. For $0.83 \lesssim \alpha \lesssim 0.91$, crystal nuclei are only observed under shear and details depend on the size ratio and composition. Asymmetric compositions show higher $\langle \overline{q}_6 \rangle$-values than symmetric mixtures. For size ratios $\alpha \lesssim 0.83$, no crystalline regions are observed at any instant. We believe that mixtures can form substitutional crystals if the individual particles are similar enough such that both bigger and smaller spheres can have an equal number of contacts. In a random hexagonal close packing, the nominal number of neighbors is 12. For size ratios $\alpha \lesssim 0.91$, the surface area of the small particles is too small to keep contact with 12 neighbors, while bigger particles can have many more contacts. As a consequence, any formation of simple hexagonal structures is suppressed. Future studies could extend the range of volume fractions or vary the shape of the size distribution of the particles.

Acknowledgments

The Center for Advanced Imaging (CAi) is acknowledged for the SEM images.

9

Colloids under Large Amplitude Oscillatory Shear: You Spin Me Round

9.1 Abstract

Yielding and flow of colloidal hard spheres ($0.57 \leq \phi \leq 0.65$) is studied under large amplitude oscillatory shear (LAOS). Rheologically, the transition from elastic to viscous behavior is investigated in terms of Fourier rheology, Lissajous–Bowditch figures, and an elastic-viscous stress decomposition. Microscopically, the response of the system is analyzed in the framework of reversible and irreversible particle motions, based on stroboscopic and continuous imaging. In the linear viscoelastic regime, particle motions are found to be almost fully reversible. For strain amplitudes above the yield strain, particle motions get increasingly decorrelated with both an increasing number of shear cycles and an increasing strain amplitude. Furthermore, the system is found to shear thicken around the yield strain, which is located between $\gamma_0 \approx 2\%$ (for $\phi = 0.65$) and $\gamma_0 \lesssim 20\%$ (for $\phi = 0.57$).

9.2 Introduction

Large amplitude oscillatory shear (LAOS) has attracted interest in colloidal rheology since it probes the nonlinear response and is supposed to give a deeper understanding of the material properties. In oscillatory measurements, both strain amplitude and oscillation frequency can be varied independently. Regimes of linear viscoelasticity (cf., section 1.2) and nonlinear viscoelasticity (cf., section 1.3) are accessible depending on the choice of amplitude and frequency. One advantage of LAOS is that it disentangles strain and frequency dependence, which otherwise are typically coupled under nonequilibrium conditions. LAOS experiments, including dynamic strain sweeps (DSS), are standard tests in almost any rheological study and there is a need for a deeper understanding, particularly with regard to complex viscoelastic materials [16].

Colloidal glasses are an important example of viscoelastic materials and have similarities to other industrially relevant systems such as, for instance, metallic glasses. General microscopic and macroscopic properties of colloidal glasses have been studied in detail (cf., section 2.5.3 and section 2.5.4). Due to their size, colloidal glasses can be observed with a microscope and their dynamics are slow enough to be followed with time. The equilibrium phase behavior of colloidal hard spheres is driven purely by entropy (cf., section 2.4.1), where the relevant quantity is the volume fraction $\phi = (N\frac{4}{3}\pi R^3)/V_{\text{total}}$, which relates the volume occupied by all N spheres to the total volume. Around $\phi_g \approx 0.58$, colloids exhibit a glass transition (cf., section 2.5.2). The glass transition and the random close packing both depend on the polydispersity (cf., section 2.4.3). The maximum packing fraction for monodisperse hard spheres is reached at $\phi_{\text{max}} = 0.74$. Above the glass transition, particles are kinetically arrested. They are trapped in cages formed by their neighbors (cf., section 2.5.3). Shear can break these cages. Accordingly, colloidal glasses show viscoelastic behavior when subjected to shear. Colloidal glasses behave solid-like at small strains and are liquefied at high strains, giving rise to a solid-to-liquid transition. Similarly, a transition from reversible to irreversible particle motion is observed. Shear can also induce order, which can be avoided with high enough polydispersities (cf., chapter 8). Experiments have been performed at various volume fractions, including $\phi = 0.1 - 0.4$ [306], $\phi = 0.17 - 0.44$ [307], $\phi = 0.51 - 0.57$ [245] and $\phi = 0.58 - 0.67$ [30, 214, 308]. Glasses under oscillatory shear are also studied by simulations including relatively low [307] and high volume fractions [309].

Many experiments involve shear cells [30, 214, 218, 245, 307, 308, 310] in combination with microscopy [218, 245, 307] or scattering techniques [30, 214, 308, 310]. In these experiments, shear is applied by two parallel plates and strain amplitudes are typically restricted to strains below 100%. Couette cells are also used as well as oscillatory channel flow [311]. Complementary to microscopic techniques, also pure rheology experiments are conducted with glasses under LAOS [16, 166]. Previous work has suggested combining rheology and confocal microscopy to shed light on

the flow of colloidal glasses under shear [30]. If both microscopic and rheological data is presented in one study, then they are usually measured individually (cf., e.g., [30, 218]).

The typical number of oscillation cycles is relatively small in experiments. Microscopic analysis is based on dynamics after one [218], up to three [245], sixteen [310], or at least 21 cycles [308]. Higher numbers of oscillations are studied by simulations, reaching up to 100 [307] or more than 1000 cycles [309].

We can extract the following landmark observations from previous studies: Diffusion increases with increasing shear rates [311]. While dilute samples follow reversible motions for small shear strains, there is a "transition to chaos" for larger strains as confirmed by experiments and theory [306, 309]. In this respect, chaos refers to irreversible particle motions. While details depend on the initial configuration of the system, averaged values are independent of the initial state [309].

Reversibility is understood in the view of "cage elasticity" [30]: Cages, formed by surrounding particles, can deform elastically until a finite yield strain (sometimes also called characteristic or critical strain). Only above the yield strain, cages break up and the local neighborhood of a particle changes. Shear-induced rearrangements under oscillatory shear are localized and spatially heterogeneous [218, 245, 310], consistent with findings under steady shear [182]. While Hébraud et al. state that the fractions of mobile and immobile particles stays constant [310], Knowlton et al. argue that they change with time [218]. Nevertheless, even for strain amplitudes of $\gamma_0 = 12\%$, a small fraction of particles shows essentially reversible motion after one cycle of shear [310]. Along these lines, cage elasticity is found to exist even in the fluidized regime. Under large shear, cages break up and reform continuously, leading to a finite elasticity – even for large strains [16, 312].

It is attempted to quantify the transition from elastic/solid/reversible to viscous/liquid/chaotic behavior by a characteristic shear strain γ_c. From a rheological perspective, a static yield strain can be extracted from start-up experiments. Under oscillatory shear, a dynamical yield strain is typically defined as the cross-over strain, where the elastic and viscous moduli are equal ($G^{'} = G^{''}$). From a microscopic point of view, definitions of yield strains are based on decays of correlation functions or the nature of individual particle motions. Characteristic values from macroscopic (rheology) and microscopic (e.g., scattering) techniques for concentrated samples ($\phi \approx 60\%$) yield values that are somewhere between $\gamma_c = 6 - 20\%$ [30, 218, 309]. The yield strain depends explicitly [218, 307] or implicitly [310] on the volume fraction. For instance, yield strains for dilute samples ($\phi = 10\%$) are found to be much higher ($\gtrsim 1000\%$) [306]. The microscopic yield strain is smaller than the rheological cross-over strain [218]. Finally, the yielding transition is found to be smooth in rheology but sharp with respect to microscopic mobility [218].

This study will focus on colloidal glasses around and above the colloidal glass transition. As a special feature, the sample will be probed *simultaneously* by rheology and confocal microscopy. Therefore, observations from rheology and microscopy

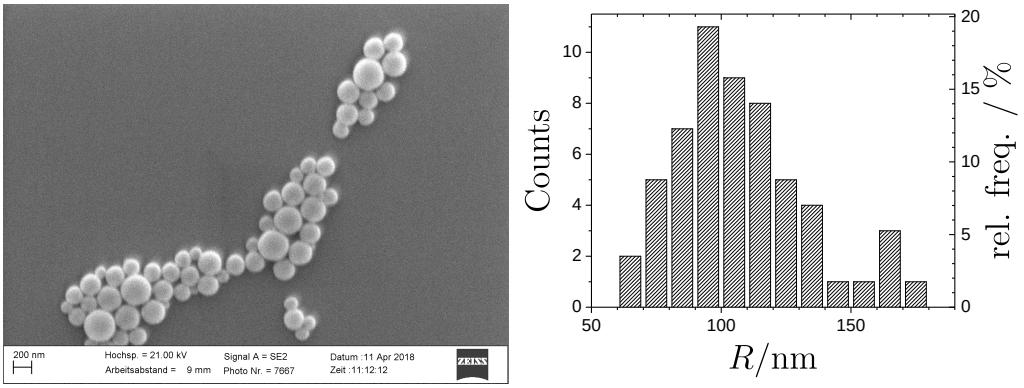

(a) **(b)**

Fig. 9.1 (a) Image of dried "ASM 126"-particles as obtained with electron microscopy in the Center for Advanced Imaging (CAi) at HHU Düsseldorf. (b) Corresponding histogram of particle radii. The mean value is $R = 108\,\text{nm}$, and the polydispersity is $\delta_{ASM126} = 23.6\%$. It is expected that particles are bigger if dispersed in a liquid than in the dried state. Dynamic light scattering experiments on particles from the same batch yield an average radius of 157 nm. The value $R = 157\,\text{nm}$ is later on used for scaling purposes.

actually are based on the same sample under the same conditions. Fundamental assumptions based on velocity profiles or wall slip are checked directly. Furthermore, by using Fourier series, phase shift angles, shear thinning and thickening parameters, as well as confocal particle motions, we try to provide a comprehensive rheological and microscopic picture.

9.3 Materials and Methods

Experiments are performed with spherical PMMA-particles (cf., section 2.3). Particles are taken from the batch "ASM 126," synthesized by A. B. Schofield. Figure 9.1a shows a scanning electron microscopy image (SEM-image) taken at CAi (HHU Düsseldorf), together with the size distribution of particles as determined from that image. The SEM-image shows dry particles. During experiments, particles are dispersed in a refractive index matching mixture of *cis*-decahydronaphthalene (*cis*-decalin) and tetrahydronaphthalene (tetralin). This solvent mixture has been used before [31, 107, 127, 282, 313, 314] and is expected to provide the hard-sphere behavior of PMMA spheres [128, 240]. The mean radius of the "ASM 126"-particles, dispersed in Octadecene, is $R = 157\,\text{nm}$, as determined by A. Pamvouxoglou using static light scattering (SLS). The "ASM 126"-particles are not fluorescent. "Bigger" particles – dyed with rhodamine B – are added (i.e., 1% (V/V)) and act as tracers. The tracer particles are taken from the batch "Rhodamine 47.1%," synthesized by M. A. Escobedo Sánchez and J. P. Segovia Gutiérrez. The radius of the tracers is

ϕ/ϕ_m	0.83	0.86	0.89	0.92	0.95
ϕ	0.57	0.59	0.61	0.63	0.65

Tab. 9.1 Relative ϕ/ϕ_m and absolute volume fractions ϕ of the samples. Samples are prepared using relative volume fractions. Absolute volume fractions are obtained by multiplication with the volume fraction after sedimentation, that is, with $\phi_m = 0.687$. More details in the text.

$R_{\text{tracer}} = 795\,\text{nm}$, as determined by confocal microscopy.

Five different volume fractions of the combined system are achieved by diluting a sediment of particles after centrifugation at 1490 g. A priori, it is not trivial to know the volume fraction ϕ_m of the sediment. Thus, reduced volume fractions ϕ/ϕ_m are reported to handle the uncertainty of absolute volume fractions. It is typically assumed that the volume fraction of the sediment ϕ_m is equal to the random close packing, that is, $\phi_m = \phi_{RCP}$. From the polydispersity $\delta = 23.6\%$ (cf., figure 9.1), a random close packing close to $\phi = 0.68$ or $\phi = 0.69$ is expected [91]. It will turn out that a packing of $\phi_m = 0.687$ fits the rheological data quite well (cf., figure 9.4), in perfect agreement with the assumption based on the polydispersity. The high polydispersity furthermore ensures that results are not affected by any shear-induced ordering. Relative and absolute volume fractions of the probed samples are given in table 9.1.

Measurements are performed with the rheo-confocal setup (cf., section 4.2). The rheometer and confocal microscope are synchronized electronically, and image acquisition is triggered depending on the rheological tests. The stress-controlled rheometer (Anton Paar 302, WESP) is equipped with a cone-plate geometry (Anton Paar, CP25-2/S, SN36375). The cone is sandblasted and has a diameter of $d = 24.9826\,\text{mm}$, an angle of $\beta = 2.001°$ and a truncation gap of $h = 106\,\mu\text{m}$. A coverslip (diameter: 50 mm, nominal thickness: 0.17 mm) acts as a bottom plate. The coverslip is scratched with sandpaper to reduce wall slip. Measurements are performed at $T = 20.5\,°\text{C}$ and a solvent trap filled with *cis*-decalin is used to prevent solvent evaporation.

In the case of oscillatory shear, a sinusoidal strain $\gamma(t) = \gamma_0 \sin(\omega t)$ is applied and the full waveform of the stress signal is recorded. For measurements with simultaneous stroboscopic confocal imaging, an oscillation cycle is discretized by 128 points and the tests are designed such that an electronic trigger signal is sent to the confocal unit at predefined points of the shear cycle. In either case, a strain range from 0.5% up to 500% is covered.

The oscillation frequency is chosen according to the following constraints: The frequency should be high to minimize the overall duration of the experiment due to sedimentation and evaporation issues. On the other hand, it should be reasonably small, such that any uncertainties from the triggering only result in small uncer-

job name	γ_0 or γ	ω/f or $\dot{\gamma}$	duration	confocal
sample at rest	0%	$0\,\mathrm{s}^{-1}$	483 s	✓
RJ (first part)	200%	1 Hz	60 s	
RJ (second part)	2%	1 Hz	120 s	
DFS 1%	1%	100-0.01 rad/s	3416 s	
DFS 2%	2%	100-0.03 rad/s	1108 s	
DSS 0.1 Hz	0.5-500%	0.1 Hz	1240 s	✓
DSS 1 rad/s	0.5-500%	1 rad/s	1953 s	
waveform	various	0.1 Hz	$15 \cdot 100$ s	✓
start-up $1\,\mathrm{s}^{-1}$	0-50000%	$1\,\mathrm{s}^{-1}$	500 s	✓
start-up $0.2\,\mathrm{s}^{-1}$	0-10000%	$0.2\,\mathrm{s}^{-1}$	500 s	✓
flowcurve		10-0.002 s^{-1}	1574 s	

Tab. 9.2 Details of the utilized rheological tests. The first column contains the code-name of each test. Column two, three, and four contain the applied strain range or strain amplitude, the oscillation frequency or shear rate, and the total duration of each test. No shear is applied during the test "sample at rest." The rejuvenation procedure ("RJ") is a combination of two tests and, therefore, split into two parts. Further tests include a dynamic frequency sweep (DFS), a dynamic strain sweeps (DSS), start-up experiments (start-up), and a flowcurve (flowcurve). The "waveform" stands for the application of a discretized sinusoidal strain. This test is performed at various strain amplitudes, explicitly at $\gamma_0 = 0.632\%$, 1%, 1.59%, 2.52%, 3.99%, 6.32%, 10%, 15.9%, 25.2%, 39.9%, 63.2%, 100%, 159%, 252%, and 399%. The actual running sequence of the tests is given in table 9.4.

tainties in units of strain. Similar to diffusing wave spectroscopy (DWS) – where the width of the echos scale with the inverse shear rate [310] – the time window to capture the same point of strain during a cycle decreases with increasing oscillation frequency. Also, it takes a finite time to capture one image as well as to wait for and process the trigger signal. Finally, for continuous image acquisition, the strain rate amplitude $\dot{\gamma}_0 = \omega\gamma_0$ needs to be small enough to allow for particle tracking. For oscillatory shear with simultaneous confocal microscopy, a relatively low frequency of $f = \omega/2\pi = 0.1\,\mathrm{Hz}$ is chosen, resulting in a Péclet number of $\mathrm{Pe}_\omega = \omega\tau_\mathrm{B} = 0.034$. If not stated otherwise, rheological values are obtained directly from the RheoCompass Software (Anton Paar GmbH). More details of the rheological tests are given in table 9.2.

Simultaneous confocal data is recorded with a confocal scan head (Visitech, VTEye) mounted on an inverted microscope (Nikon, Eclipse Ti) equipped with an oil-immersion objective (Nikon, Plan Fluor, NA=1.3, 100x; immersion oil: type HF, viscosity: 700cSt, Cat. No. 16245). The objective is focused on an area located in a radial distance of $r = 10\,\mathrm{mm}$ away from the center of the cone to avoid edge effects.

At this radial distance, the gap height is $h = r\tan(\beta) = 350\,\mu m$, such that there are around 1100 (small) particles are filling the gap. Z-Stacks can be acquired until a height of 100 µm. The height is limited by the range of the piezo as well as the working distance of the objective. If not stated otherwise, images are recorded in a height of 50 µm above the bottom plate to avoid boundary affects while at the same time maintaining good image quality. Two-dimensional image series are recorded, where a single image contains 512×512 pixels and covers an area of $51 \times 54\,\mu m^2$.

For specific oscillatory tests, the confocal image acquisition is triggered to capture images at predefined points during an oscillation cycle (as stated before). In that case, several stroboscopic movies are recorded with one frame per cycle. One predefined point is, for instance, at the maximum positive strain. Having a total of 10 cycles then yields a movie with 10 frames, where each frame images the sample at $\gamma = +\gamma_0$. The images of these stroboscopic echo-style experiments are analyzed using the Pearson correlation coefficient (PCC) (cf., section 7.1.3). We define

$$PCC(\tau) \equiv \langle PCC(a(t), a(t+\tau)) \rangle_t \,, \tag{9.1}$$

where the images a are taken at times t and $t + \tau$, respectively. The average is taken over all times (i.e., over all available images), and lag times τ will later be given in multiples of the oscillation period t_p. The use of the Pearson correlation coefficient is motivated by the following consideration: If particles move in or out of focus, their apparent intensity will change. Thus, a normalized cross-correlation – as it is the case for PCC – is used instead of a phase correlation, where knowledge of the intensity would be lost (cf., section 7.1.2). To allow for uncertainties in the triggering process, equation (9.1) is not performed directly on the raw images. An additional step is inserted before: Raw images are first preprocessed to remove any global offset between them. This is done in conjunction with the IDL routine `correl_images.pro`, which is available online [315]. Only then, these preprocessed images are correlated using equation (9.1).

Apart from stroboscopic imaging, images are sometimes also recorded continuously with a frame rate of 10 or 50 frames per second (fps). Details are given in table 9.3.

Before starting a series of measurements, the following actions are taken: The rheometer is calibrated by means of a motor adjustment and instrument inertia calibration using the RheoCompass software. Samples are put in a vortex mixer for 15 minutes to homogenize the sample. Since the mixer produces heat, the samples are afterward cooled down in a fridge at $T = 10\,°C$ for 10 minutes and subsequently placed next to the rheo-confocal setup for one hour at $T = 20.5\,°C$ to equilibrate. Samples with $\phi/\phi_m = 0.95$, $\phi/\phi_m = 0.92$, and $\phi/\phi_m = 0.89$ are loaded with a spatula, while samples with $\phi/\phi_m = 0.86$ and $\phi/\phi_m = 0.83$ can be poured directly from the vial. After loading, samples are sealed and stored in a fridge at $T = 10\,°C$.

The full sequence of executed tests is given in table 9.4. Sometimes, images have to be exported and consequently deleted from the memory before another set of

job name	z/ µm	images	fps	trigger	τ_w/ s	iteration
sample at rest	0-75	15x418	50	✓	60	1
DSS 0.1 Hz	50	1950 per γ_0	50	✓	0	1 per γ_0
waveform	50	2 per cycle		✓	0	10 per γ_0
start-up $1\,s^{-1}$	0-100	500	50	✓	60	2
start-up $0.2\,s^{-1}$	0-100	100	10	✓	60	2

Tab. 9.3 Summary of the confocal parameters for tests with simultaneous confocal imaging. All images are recorded in a radial distance of 10 mm with respect to the center of the cone. The first column contains the code names of the tests. Identical code names with table 9.2 indicate that these tests are simultaneously measured with rheology and confocal microscopy. Column two reveals the height z, in which the images are taken. For the start-up experiments, images are acquired between $z = 0\,\mu m$ and $z = 100\,\mu m$ in steps of $z_{step} = 10\,\mu m$. A waiting time of five seconds is inserted after each piezo move. Column three and four show the number of recorded images and the frame rate, respectively. In all cases, image acquisition is triggered externally by the RheoCompass Software as indicated in column five. Images are either taken directly at the start of the test ($\tau_w = 0\,s$) or with a delay ($\tau_w = 60\,s$). Finally, the last column shows how many loops are executed during the same test.

images can be captured. This constraint results from the VoxCell software that controls the confocal microscope. The sequence of tests accounts for this. Confocal images are only taken during "high-priority" tests so that confocal images can be exported while "low-priority" points are measured with the rheometer alone. The total experiment (full job list) lasts about four hours. All tests are repeated once and results are found to be reproducible. For the sake of clarity, sometimes only data of one experiment will be presented.

9.4 Results

This section is organized as follows: First, standard rheological tests characterizing the sample will be shown. In this context, confocal microscopy will reveal velocity profiles under steady shear. Afterward, the focus will be largely on oscillatory tests, especially on a dynamic strain sweep (DSS) at $f = 0.1\,Hz$. The results will be first analyzed using different rheological methods. Insights from stroboscopic confocal imaging then add to the rheological findings. Individual results are discussed directly in this section. A general comparison of the results from this work with previous literature will be part of the discussion in section 9.5.

Let us first have a look at the sample before any application of shear. Figure 9.2 shows a 3D-reconstruction as obtained from confocal microscopy. Only the tracer

number	job name
1	sample at rest
2	RJ (“Rejuvenation”)
3	DFS 2%
4	RJ
5	DSS 0.1 Hz
6	RJ
7	DSS 1 rad/s
8	RJ
9-23	waveform(s)
24	RJ
25	flowcurve
26	RJ
27	DFS 1%
28	RJ
29	sample at rest
30	RJ
31	start-up $1\,\mathrm{s}^{-1}$
32	RJ
33	start-up $0.2\,\mathrm{s}^{-1}$

Tab. 9.4 Running sequence of all executed tests. Details of the tests are given in table 9.2 and table 9.3, respectively. The duration of the entire job list is roughly four hours. The test with number 33 has been added later and is not included in the measurements of the $\phi/\phi_m = 0.95$ sample.

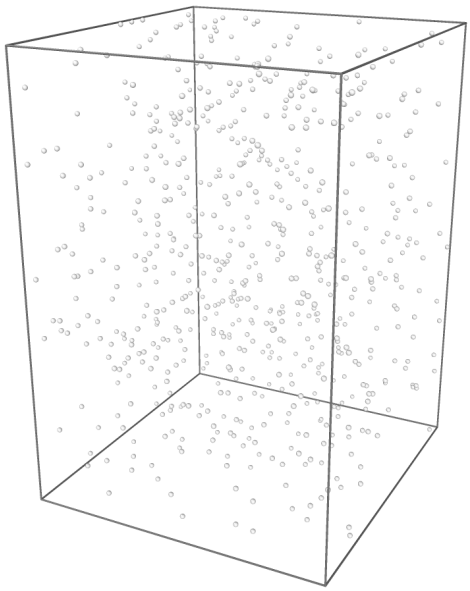

Fig. 9.2 Reconstruction of 664 tracer particles. The volume has a dimension of 51 µm × 54 µm × 74 µm. Particles are drawn with half of their real size. Data is obtained from the $\phi/\phi_m = 0.86$ sample during job #1.

particles are visible. The rest of the sample is not fluorescent and, therefore, not detected. Nevertheless, three observations can be made: First, the distribution of tracers is homogeneous. This is reassuring. It confirms that mixing the sample with the vortex mixer creates homogeneous samples. Second, the number of tracer particles gives a relative volume fraction of the tracer particles of approximately 1%. This is consistent with sample preparation. Third, no sedimentation of tracer particles is observed over time. These three observations are also confirmed by confocal imaging at the very end of a measurement (data not shown here).

From a rheological point of view, the sample is first characterized by means of a dynamic strain sweep (DFS), given in figure 9.3: The viscous moduli show a minimum around $\mathrm{Pe} \lesssim 0.01$, which corresponds to a characteristic time of $\tau_\beta \gtrsim 30\,\mathrm{s}$ (cf., section 2.5.4). A potential peak at smaller frequencies is outside the experimental window. The elastic moduli are almost independent of the oscillation frequency and always larger than their viscous counterparts. Samples of all volume fractions thus behave solid-like in the applied range of frequencies. A relation between the elastic moduli and the volume fraction for hard spheres has been established by Koumakis et al. [220]. Their empirical model can be compared with data from this work. This is done in figure 9.4. Reasonable agreement is obtained, if one sets $\phi_m = 0.687$ for all scaled volume fractions ϕ/ϕ_m. This is consistent with the estimate of the random close packing based on the polydispersity of the samples [91].

Further characterization of the sample is done by means of a flowcurve. Scaled

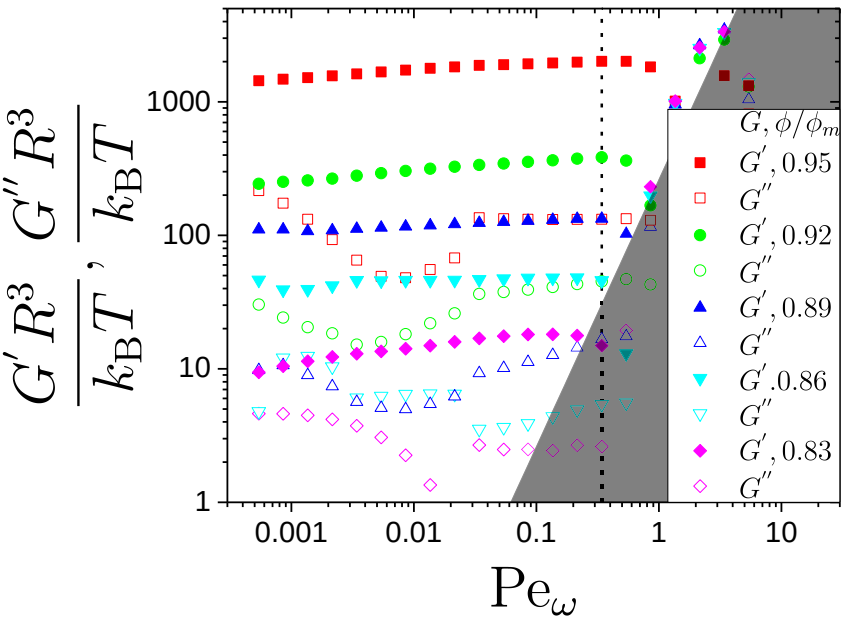

Fig. 9.3 DFS at $\gamma_0 = 1\%$. The dashed line is at $\mathrm{Pe}_\omega = 0.34$ (cf., figure 9.4). The gray area shows the region, where the instrument inertia equals the inertia of the sample (cf., equation (1.46)).

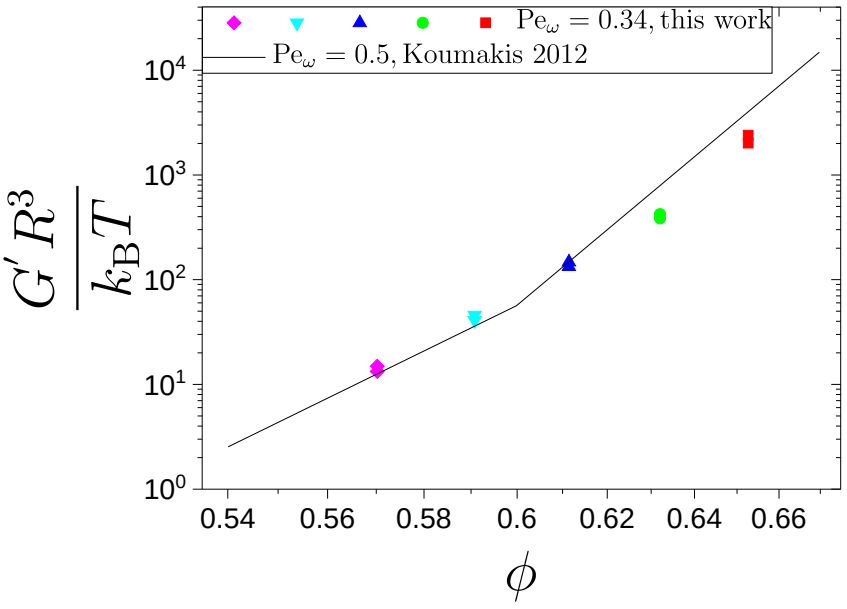

Fig. 9.4 Scaled elastic moduli $G' R^3/k_\mathrm{B}T$ at $\mathrm{Pe}_\omega = 0.34$ as a function of absolute volume fraction ϕ. For each volume fraction data points from two independent experiments are plotted. They overlap almost completely. Symbol colors and shapes correspond to those in figure 9.3. The absolute volume fractions ϕ are obtained from relative volume fractions ϕ/ϕ_m by setting $\phi_m = 0.687$. The solid line is taken from reference [220].

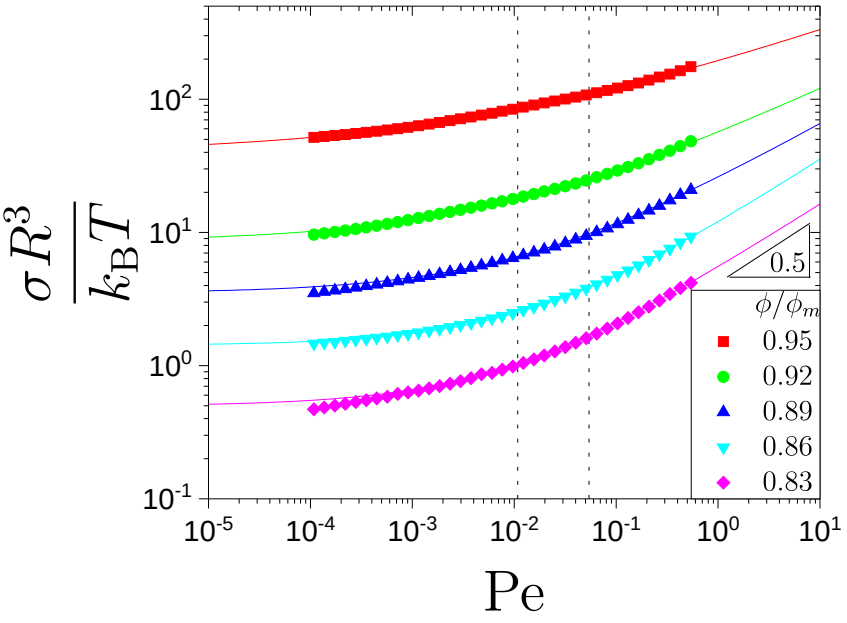

Fig. 9.5 Flowcurves with scaled stresses as a function of Péclet number for all volume fractions as indicated in the legend. Lines are fits to the Herschel-Bulkley law (equation (1.18)). Vertical dashed lines are located at Pe = 0.011 and Pe = 0.054.

shear stresses over a wide Péclet range are shown in figure 9.5, together with fits according to the Herschel-Bulkley law (cf., equation (1.18)). The Herschel-Bulkley law fits the data well, indicating hard-sphere-like behavior. The fits give yield stress values of $\sigma_y R^3/(k_B T) \in [0.50, 1.4, 3.5, 8.5, 39]$. The flow index is $\upsilon = 0.50$ for both $\phi/\phi_m = 0.83$ and $\phi/\phi_m = 0.86$, in agreement with previous work [12]. For the higher volume fractions, the flow index deviates from the value 0.5 (i.e., $\upsilon(\phi/\phi_m = 0.89) = 0.44$, $\upsilon(0.92) = 0.36$, $\upsilon(0.95) = 0.28$).

To investigate the flow in greater detail, transient start-up tests are performed at $\dot{\gamma} = 0.2\,\mathrm{s}^{-1}$ and $1\,\mathrm{s}^{-1}$, corresponding to Pe = 0.011 and Pe = 0.054. The results are given in figure 9.6. The data for short times ($t \lesssim 0.5\,\mathrm{s}$) is very scattered and, for the sake of clarity, only shown for one volume fraction. Remember that the rheometer is stress-controlled and the application of a constant shear rate works via an iterative process. This may make it difficult to determine a yield strain from this steady shear experiments. If we consider the $\phi/\phi_m = 0.92$ sample at $\dot{\gamma} = 0.2\,\mathrm{s}^{-1}$, the peak of the stress overshoot could be located around $\gamma \approx 15\%$. The position of the peak of the stress overshoot is expected to increase with increasing Péclet [220]. Figure 9.6a and figure 9.6b include a time axis to show the time window where confocal images are taken. The time windows are in both cases well in the rheological steady-state regime where the shear stress does not change with time.

Confocal images are taken in different heights (cf., table 9.3) and the corre-

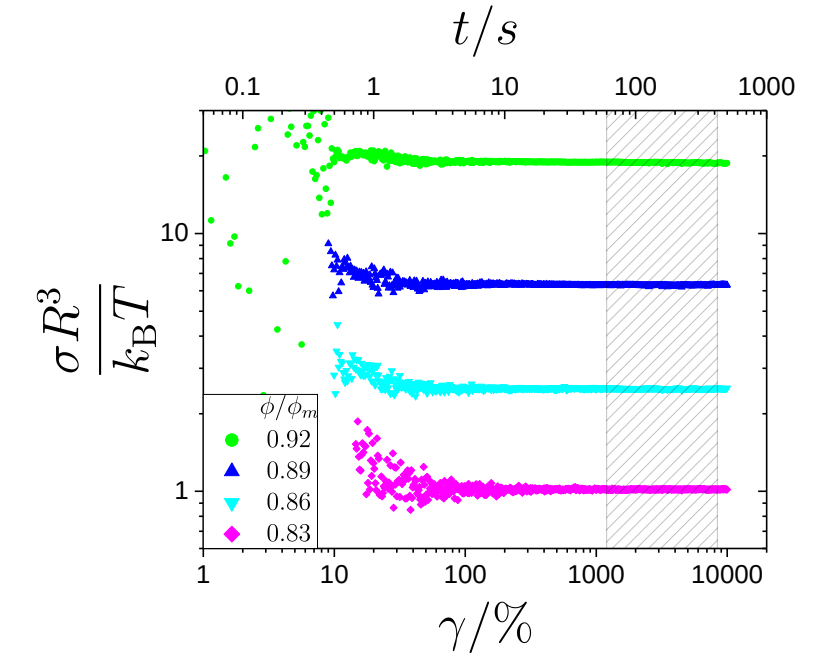

(a)

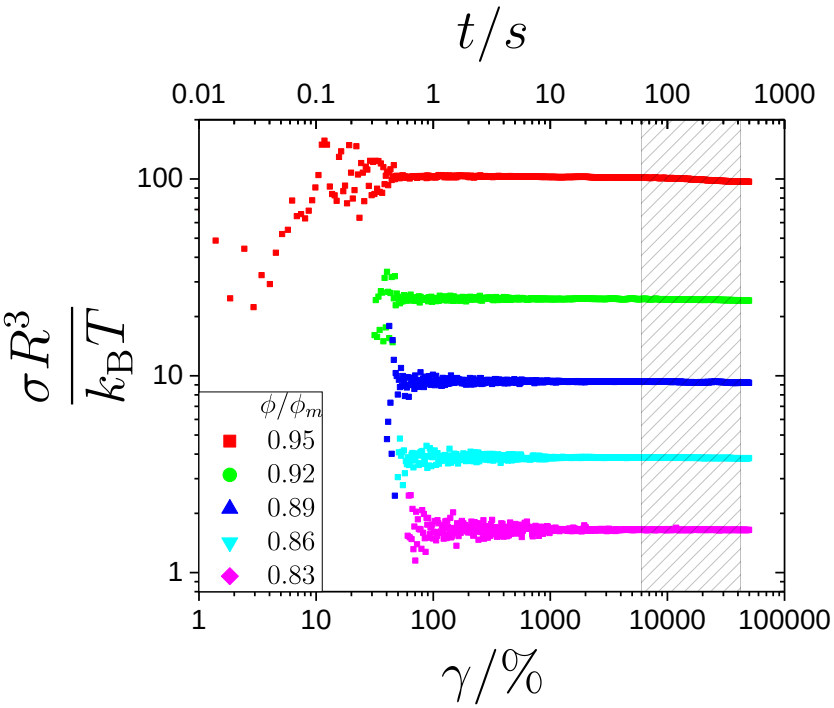

(b)

Fig. 9.6 Start-up tests at (a) $\dot{\gamma} = 0.2\,\mathrm{s}^{-1}$ and (b) $1\,\mathrm{s}^{-1}$. Data at small times ($t \lesssim 1\,\mathrm{s}$) is scattered and not shown for clarity. The gray shaded areas indicate regions with simultaneous image acquisition.

sponding shear-profiles are shown in figure 9.7. In all cases, a linear shear profile is observed, with considerable slip for higher volume fractions. The agreement of the $\phi/\phi_m = 0.83$ sample with the "ideal" Newtonian velocity profile is astonishing. These velocity profiles contain valuable information that should be kept in mind for the interpretation of the previous and upcoming rheological and confocal data.

Is there a link between the shear profiles under steady and the behavior under oscillatory shear? To test this, tracer motions in a height of $z = 50\,\mu\text{m}$ are analyzed during the dynamic strain sweep at $f = 0.1\,\text{Hz}$. For simplicity, we will first focus on a fixed macroscopically applied strain amplitude, namely, $\gamma_0 = 159\%$. This macroscopic strain amplitude is chosen on purpose: The macroscopic amplitude of the shear rate under these conditions is $\dot{\gamma}_0 = 2\pi f \gamma_0 = 1\,\text{s}^{-1}$, and, therefore, comparable one of to the conditions under steady shear (cf., figure 9.7b). The motion of particles is obtained from particle tracking. At these relatively high strains, particles leave the field of view (FOV) but there is always a finite number of particles inside the FOV that can be tracked. From all particle trajectories, ensemble-averaged displacements and velocities are calculated. Selected results are shown in figure 9.8 for volume fractions $\phi/\phi_m = 0.83$ and $\phi/\phi_m = 0.92$. First of all, the confocal motions are well fitted by the sine function

$$\Delta x^{\text{conf}} = o_0 + \Delta x_0^{\text{conf}} \sin(2\pi f^{\text{conf}} t + \psi)\,. \tag{9.2}$$

The amplitude of the "confocal displacements" Δx_0^{conf} can be compared with the maximum displacement $\Delta x_0 = \gamma_0 z^{\text{conf}}$ that is expected in the case of a linear velocity profile without slip. Here, γ_0 is the applied macroscopic strain amplitude and z^{conf} the height, where the tracers are tracked. For $\phi/\phi_m = 0.83$, the agreement between the measured and "ideal" motion is again astonishing. The confocal displacement amplitude $\Delta x_0^{\text{conf}} = 78.8\,\mu\text{m}$ is very close to the expected displacement amplitude of $\Delta x_0 = 79.5\,\mu\text{m}$. For the same externally applied stain, particle displacements in the case of $\phi/\phi_m = 0.92$ are larger than expected. A fit to the data yields a displacement amplitude of $\Delta x_0^{\text{conf}} = 104\,\mu\text{m}$, being 1.3 times larger than expected. This deviation is reasonably close to the corresponding case under steady shear (cf., figure 9.7b), where the tracer velocity in a height of $z = 50\,\mu\text{m}$ is 1.4 times higher than expected for a linear profile without slip. Accordingly, fitting the motion of tracer particles under oscillatory shear can elucidate wall slip. Let us examine in more detail the deviation between the observed displacement amplitude Δx_0^{conf} and expected displacement amplitude Δx_0. We define the relative error

$$Err(\Delta x_0^{\text{conf}}) = \frac{\Delta x_0^{\text{conf}} - \Delta x_0}{\Delta x_0}\,. \tag{9.3}$$

Results over a wide range of strain amplitudes are summarized in figure 9.9, where we show deviations of displacements $Err(\Delta x_0^{\text{conf}})$ and frequencies

$$Err(f^{\text{conf}}) = (f^{\text{conf}} - f)/f\,. \tag{9.4}$$

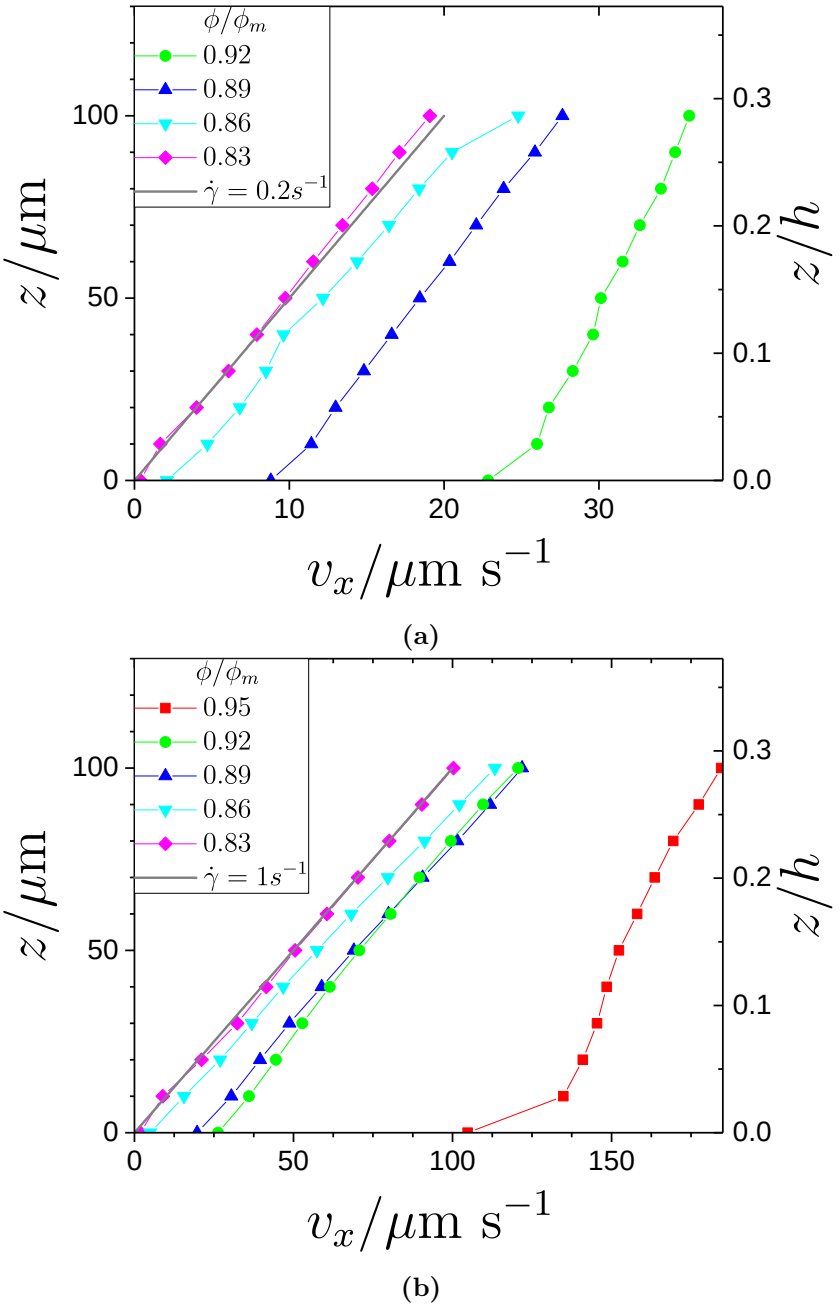

Fig. 9.7 Velocity profiles at (a) $\dot{\gamma} = 0.2\,\mathrm{s}^{-1}$ and (b) $\dot{\gamma} = 1\,\mathrm{s}^{-1}$. Corresponding images are acquired in the rheological steady state (cf., figure 9.6). The right axis shows heights with respect to the gap height h. Volume fractions as indicated in the legend. Solid gray lines represent a Newtonian velocity profile with $v_x = \dot{\gamma} z$.

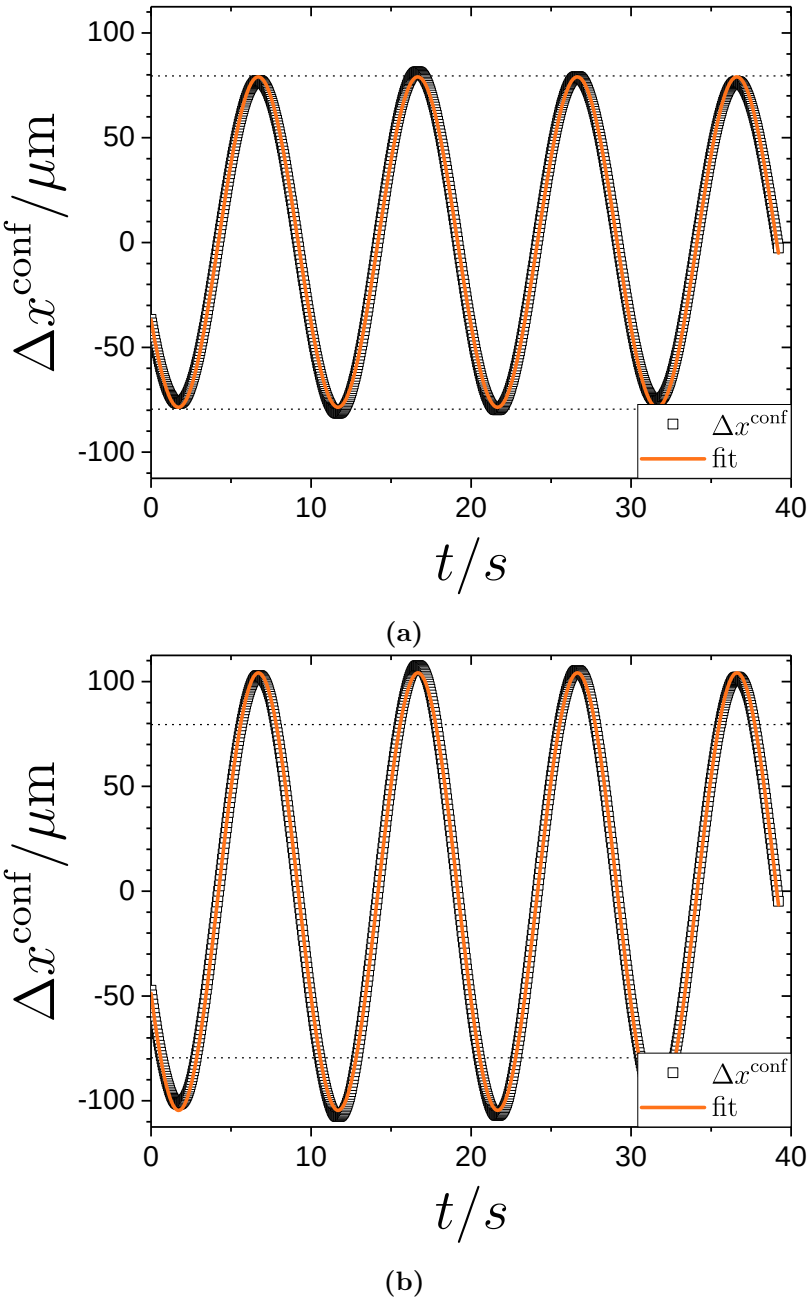

Fig. 9.8 Time-dependent local displacements $\Delta x^{\mathrm{conf}}(t)$ as obtained from confocal microscopy in a height of $z^{\mathrm{conf}} = 50\,\mu\mathrm{m}$ for (a) $\phi/\phi_m = 0.83$ and (b) $\phi/\phi_m = 0.92$. In both cases, macroscopic shear is applied at a strain amplitude of $\gamma_0 = 159\%$. Thus, the "ideal" displacement amplitude is expected to be at $\Delta x_0 = \gamma_0 z^{\mathrm{conf}} = 79.5\,\mu\mathrm{m}$, as indicated by the dotted lines. Fitting the data with a sine function ($\Delta x^{\mathrm{conf}} = o_0 + \Delta x_0^{\mathrm{conf}} \sin(2\pi f^{\mathrm{conf}} t + \psi)$) yields amplitudes of $\Delta x_0^{\mathrm{conf}} = 78.8\,\mu\mathrm{m}$ and $\Delta x_0^{\mathrm{conf}} = 104\,\mu\mathrm{m}$ for $\phi/\phi_m = 0.83$ and $\phi/\phi_m = 0.92$, respectively. In both cases, the fitted frequency is identical with the applied frequency (i.e., $f^{\mathrm{conf}} = f = 0.1\,\mathrm{Hz}$).

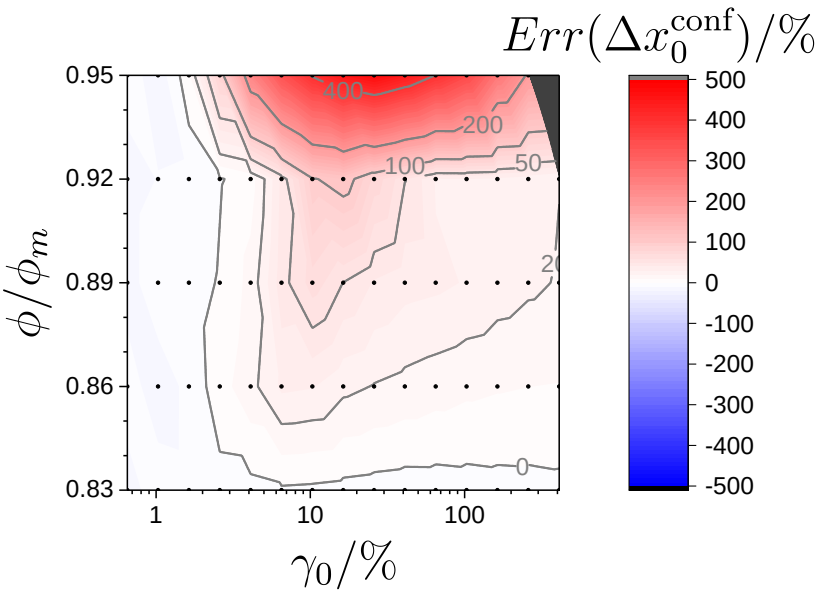

(a)

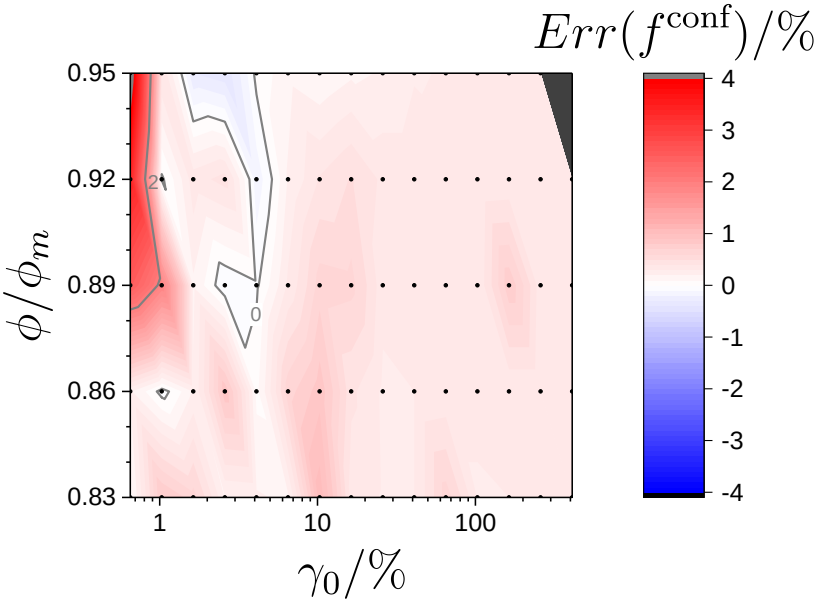

(b)

Fig. 9.9 Maps with (a) local deviations of displacement amplitudes $Err(\Delta x_0^{\mathrm{conf}})$ and (b) local deviations of oscillation frequencies $Err(f^{\mathrm{conf}})$ for all volume fractions. Definitions of the quantities are given in the text. Stain amplitudes γ_0 on the x-axis are macroscopic values as applied by the rheometer. The macroscopic applied frequency is $f = 0.1\,\mathrm{Hz}$. The figures contain interpolated results, and points inside the figure mark the underlying data points from confocal microscopy. Positive values are colored red and negative ones blue. Values close to zero are drawn in white. The top right area (dark gray) does not contain data due to the limitations of particle tracking.

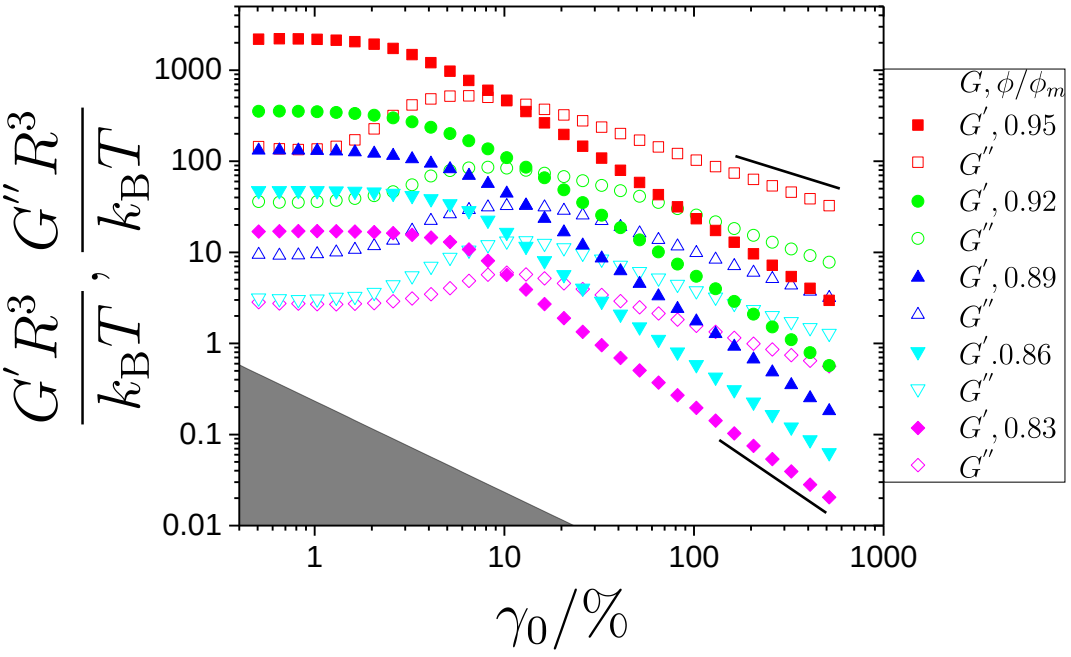

Fig. 9.10 DSS at $f = 0.1\,\mathrm{Hz}$. The gray area corresponds to the region below minimum torque (cf., equation (1.43)). Lines show apparent slopes of -0.65 and -1.4, respectively.

From the discussion before, strain deviations can be interpreted as indications for wall slip. Displacement deviations are negligible (i.e., $Err(\Delta x_0^{\mathrm{conf}} \approx 0)$ for $\phi/\phi_m \approx 0.83$ or $\gamma \lesssim 2\%$. They seem to increase around $\gamma = 10\%$ but definitely grow enormously for $\phi/\phi_m \gtrsim 0.92$. The latter is consistent with the observation of wall slip under steady shear (cf., figure 9.7).

We can now turn to the fitted oscillation frequencies f^{conf}. It seems far-fetched that wall slip will affect the oscillation frequency. This assumption is consistent with figure 9.9b, where the frequency deviations $Err(f^{\mathrm{conf}})$ are shown as a function of volume fraction and strain amplitude. The deviations are relatively small ($Err(f^{\mathrm{conf}}) < 4\%$). Notable deviations are only observed for very small strains ($\gamma \lesssim 1\%$). At vanishing strain amplitudes, the motions of the tracers are so small that they can hardly be detected with particle tracking. Thus, the deviations at small strains are – at least to some extent – limited by the resolution of the microscope and the accuracy of particle tracking.

Now that we have examined the motion of tracer particles under oscillatory shear, we will once more take a look at the rheological data. The response to a DSS at $f = 0.1\,\mathrm{Hz}$ is shown in figure 9.10 for all probed volume fractions. All samples show the characteristics of a weak strain overshoot (cf., figure 1.7). Interestingly, the macroscopic rheological response seems not to be affected by slip. The following is observed: For small strains, both the elastic and viscous moduli are independent of strain. This is the linear regime (LVE). In the LVE, all storage moduli G' are

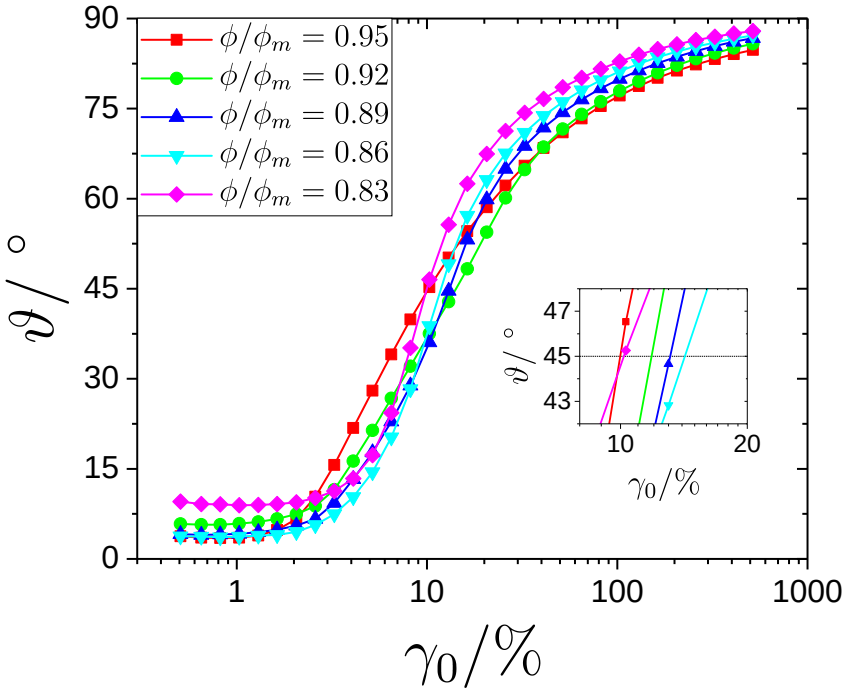

Fig. 9.11 Phase angle $\vartheta = \arctan(G''/G')$ for the same data as in figure 9.10. Inset shows a magnified area around $\vartheta = 45°$ (i.e., where $G' = G''$). Volume fractions are indicated in the legend.

greater than their viscous counterparts. Above $\gamma_0 \approx 2\%$, the LVE ends and G' starts to decrease. At the same time the viscous moduli G'' increase. They develop a peak at around $\gamma_0 \approx 10\%$ and decrease afterward. The elastic and viscous moduli roughly cross at the peak of G''. For high strains, the ratio of the slopes of G' and G'' in the log-log representation is close to 2, as expected [316].

Elastic and viscous moduli are related via $G' = G'' \tan(\vartheta)$. The phase angle shift ϑ is plotted as a function of strain in figure 9.11. Almost pure elastic ($\vartheta = 0°$) and viscous behavior ($\vartheta = 90°$) is observed for small and large strains, respectively. A closer look reveals that there is some viscous dissipation (i.e., $\vartheta > 0$) also in the above defined linear regime, especially for $\phi/\phi_m = 0.83$. In terms of the phase angle shift ϑ, the transition from the solid-like to liquid-like behavior is smooth. A phase shift angle of $\vartheta = 45°$ corresponds to the crossing of moduli. From the inset of figure 9.11, the crossings can be read off at $\gamma_0 = [10\%, 12\%, 13\%, 14\%, 10\%]$ for $\phi/\phi_m = [0.83, 0.86, 0.89, 0.92, 0.95]$, respectively.

Another way to interpret the dynamic strain sweep from figure 9.10 is to use Fourier rheology (cf., section 1.4.2). The normalized 3rd and 5th harmonics of the stress response are presented in figure 9.12. One can make the following observations: The 3rd and 5th harmonic increase with increasing strain. At $\gamma_0 = 15\%$, the

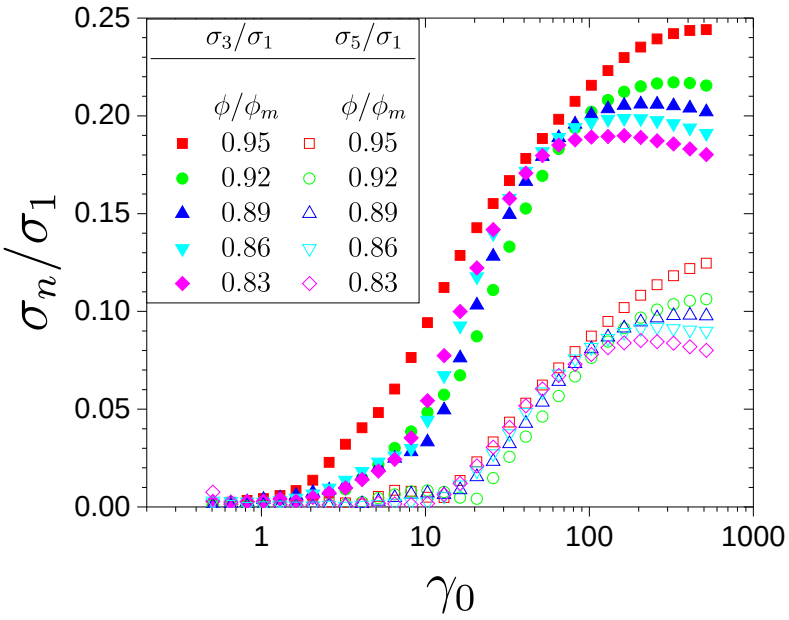

Fig. 9.12 Dependence of the 3rd (filled symbols) and 5th (open symbols) stress harmonic as a function of strain amplitude for the same data as in figure 9.10. Stress harmonics are normalized by the fundamental component σ_1. Data for different volume fractions are color-coded as indicated in the legend.

ratio σ_3/σ_1 is already equal to 0.1 and reaches up to 0.20 or 0.25 for high strains ($\gamma_0 \approx 200\%$). The higher harmonics σ_5/σ_1 show the same trend, but smaller in magnitude and shifted to higher strains. It is remarkable that the $\phi/\phi_m = 0.95$ sample has significantly higher values for the 3rd harmonic for strains between 2% and 20%. Generally speaking, significant contributions of higher harmonics indicate that the stress response deviates from a simple sinusoidal response.

This can also be inferred from the full (normalized) waveform of the stress response. Lissajous-Bowditch curves are shown in figure 9.13 for $\gamma_0 \in [1\%, 10\%, 20\%, 100\%]$ and for all volume fractions. All curves have been normalized by the maximum stress value, such that the values of the curves are constrained to the interval $[-1, 1]$. Let us first take a look at the curves of the total stress (left column) with ascending strain amplitudes. The curves should be traced clockwise. At $\gamma_0 = 1\%$, the curves are close to a straight line through the origin. The enclosed area in the σ-γ-representation is small, corresponding to almost no mechanical dissipation (cf., equation (1.25)). The dissipation seems to be largest for the smallest volume fraction. With increasing strain, the enclosed area and the mechanical dissipation increases for all volume fractions. By further increasing γ_0, the curves develop a more and more rectangular shape but stay smooth. Only for $\phi/\phi_m = 0.83$ and $\gamma_0 = 100\%$, there might be a small stress overshoot after strain reversal. Apart from that, all volume fractions

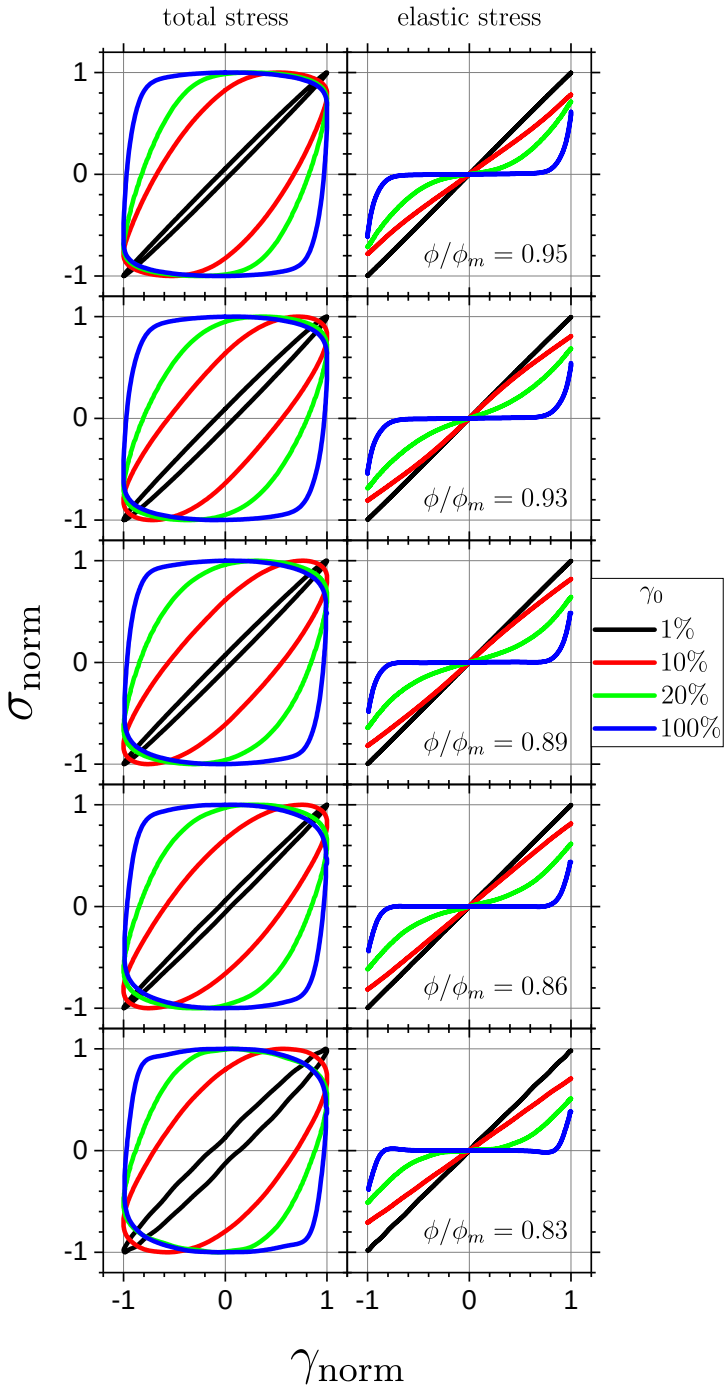

Fig. 9.13 Normalized (elastic) Lissajous-Bowditch curves (stress vs. strain) for selected strain amplitudes (i.e., $\gamma_0 \in [1\%, 10\%, 20\%, 100\%]$) as indicated in the legend. Each row corresponds to one volume fraction. The left column shows the total stress response (to be read clockwise), and the right column the elastic stress component according to equation (1.28). Normalization is done with respect to the maximum value per cycle.

have very similar Lissajous-Bowditch curves for a given γ_0.

This similarity is also reflected in the elastic stress component, which is shown in the right column of figure 9.13. The elastic stresses are calculated according to equation (1.28) and normalized in the same way as the total stress, that is, by the maximum total stress value per cycle. In the σ-γ-representation, the elastic stresses are represented by lines and the enclosed area is zero. This is expected because the elastic stresses are lines by definition (cf., section 1.4.2). At $\gamma_0 = 1\%$, the lines are straight and pass through the origin. This corresponds to an ideal solid, fulfilling hooks law. The situation changes when we increase the strain amplitude γ_0: First of all, the lines do not reach $\sigma_{\text{norm}} = \pm 1$. Thus, there has to be a considerable viscous contribution and the samples behave only partially elastic. Furthermore, the lines are not straight anymore, and one can make an interesting observation with respect to the curvature of the lines: Let us take a look at the first quadrant (positive values of γ and σ_{elastic}). While for $\gamma_0 = 10\%$, the second derivative $d^2\sigma_{\text{elastic}}/d\gamma^2$ is negative, it is positive for $\gamma_0 = 20\%$ and $\gamma_0 = 100\%$. Thus, the intra-cycle elastic stress response is reminiscent of strain softening for $\gamma_0 = 10\%$ and of strain stiffening for $\gamma_0 = 20\%$ and $\gamma_0 = 100\%$. For $\gamma_0 = 100\%$, there is a considerable elastic stress contribution only at $\gamma = \pm\gamma_0$, where the shear rate is lowest.

A complementary way to analyze the LAOS response is to look at the stress as a function of shear rate. Corresponding curves are given in figure 9.14. As before, the total stress is presented in the left column and the viscous stress is now shown in the right column. In neither case is there a dependence on the studied volume fractions for a given γ_0. For $\gamma_0 = 1\%$, the curves of the (normalized) total stresses in the σ-$\dot{\gamma}$-representation are essentially equal to a circle, corresponding to a perfectly elastic response. With increasing strain amplitude, the curves get more and more asymmetric. One may think of grabbing the curves at their top-right and bottom-left position and pulling them to $[-1, -1]$ and $[1, 1]$. A straight line from $[-1, -1]$ to $[1, 1]$ would correspond to an ideal fluid. This is not observed here. Instead, the curves (to be read counterclockwise) show hysteresis.

In the right column of figure 9.14, the total stress is decomposed into viscous stress according to equation (1.29). Viscous stresses are normalized in the same way as the total stress, that is, by the maximum total stress value per cycle. One can observe the following: All lines cross in the origin. For $\gamma_0 = 1\%$, the line is very close to zero for all values of $\dot{\gamma}_{\text{norm}}$, meaning that there is a vanishing viscous contribution during one oscillation cycle. This is consistent with figure 9.13, where an almost ideal elastic behavior is observed at this small strain amplitude. Higher strain amplitudes, instead, lead to higher (normalized) viscous stresses. Furthermore, the viscous stresses are not linear anymore. The lines are curved and their curvature depends on strain. Let us examine again the first quadrant: While the second derivative $d^2\sigma_{\text{elastic}}/d\dot{\gamma}^2$ is positive in the case of $\gamma_0 = 10\%$ and $\gamma_0 = 20\%$, it is negative for $\gamma_0 = 100\%$. This can be interpreted as intra-cycle shear thickening and thinning, respectively.

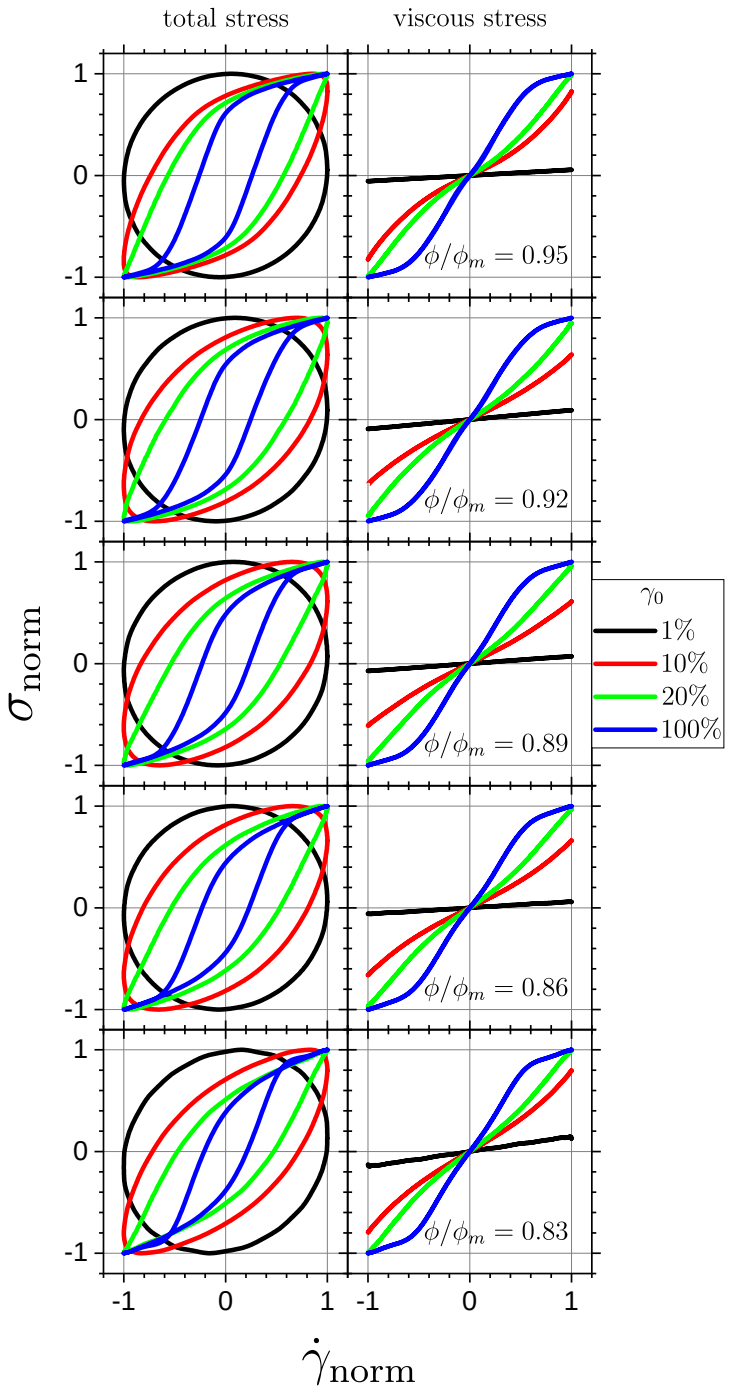

Fig. 9.14 Normalized (viscous) Lissajous-Bowditch curves (stress vs. shear rate) for selected strain amplitudes $\gamma_0 \in [1\%, 10\%, 20\%, 100\%]$ as indicated in the legend. Each row corresponds to one volume fraction. The left column shows the total stress response (to be read counterclockwise), and the right column the viscous stress component according to equation (1.29). Normalization is done with respect to the maximum value per cycle.

One can quantify the amount of shear thickening following Ewoldt at al.[25] (cf., section 1.4.2). The dimensionless strain-stiffening ratio $\widetilde{S}$ (equation (1.35)) and the shear-thickening ratio $\widetilde{T}$ (equation (1.36)) are shown in figure 9.15. Recall that $\widetilde{S} > 0$ ($\widetilde{T} > 0$) resembles strain stiffening (shear thickening) and $\widetilde{S} < 0$ ($\widetilde{T} < 0$) describes intra-cycle strain softening (shear thinning). The color scale is chosen such that red is positive and blue is negative. Let us first examine the strain-stiffening ratio $\widetilde{S}$, shown in figure 9.15a: We may follow the evolution of $\widetilde{S}$ from small to large strains. Starting with a linear elastic response (i.e., $\widetilde{S} \approx 0$), the system undergoes strain softening in a small range around $\gamma_0 \approx 7\%$, which is followed by a strain stiffening regime above $\gamma_0 \gtrsim 20\%$. The three regimes (initial elastic response, strain softening, strain stiffening) show only little dependence on the volume fraction.

Three regimes can also be identified with respect to the shear-thickening ratio $\widetilde{T}$, shown in figure 9.15b: For small strains ($\gamma_0 \lesssim 2 - 3\%$), there is an (approximately) ideal viscous behavior with a tendency to shear thinning ($\widetilde{T} \lesssim 0$) . Shear thickening is observed around $\gamma_0 = 15\%$ and the extent of this region depends on the volume fraction. The shear thickening regime is more pronounced for the highest volume fraction. Above $\gamma_0 \gtrsim 100\%$, shear thinning is observed again. The amount of shear thinning then increases with increasing strain for all volume fractions. Shear thinning at high strains is consistent with shear thinning at high Péclets in the previously shown flowcurves. The thickening/thinning regimes are also consistent with experimental results on hard spheres under oscillatory shear [317].

We may now switch from the analysis based on rheology to the analysis of the confocal data. To this end, results from the "echo-style"-analysis will be presented. During oscillation cycles, images ("echos") are taken at $\gamma = \pm\gamma_0$. These points are particularly suitable since the instantaneous shear rate is zero. The process of the system under shear is quantified by image correlation as described earlier (cf., section 9.3 and equation (9.1)). Pearson correlation coefficients $PCC(\tau)$ for different delay times τ are given in figure 9.16 for positions at maximum strain per cycle (i.e., $\gamma = +\gamma_0$) and minimum strain per cycle (i.e., $\gamma = -\gamma_0$). In the figure, the volume fractions are increasing from bottom to top. At first sight, the correlation functions decay faster with increasing γ_0. For high strain amplitudes, the correlation functions decrease to zero after two to three cycles. This suggests that at these high strains, the sample is fully liquefied and has lost its memory.

An inspection of the raw images reveals that the decay of the (image) correlations does not only result from particle rearrangements but also from offsets between images. This is illustrated with a rather extreme example in figure 9.17, where raw images are shown for $\phi/\phi_m = 0.86$ and $\gamma_0 \in [1\%, 250\%]$. The contrast of the images is enhanced and the gray levels are inverted such that tracer particles appear dark on a bright background. Successive images are arranged from bottom to top and correspond to the first, fifth and ninth oscillation cycle. The three images for $\gamma_0 = 1\%$ (figure 9.17a) are essentially identical. This is consistent with the corresponding correlations functions in figure 9.16 that are between 0.9 and 1 (note

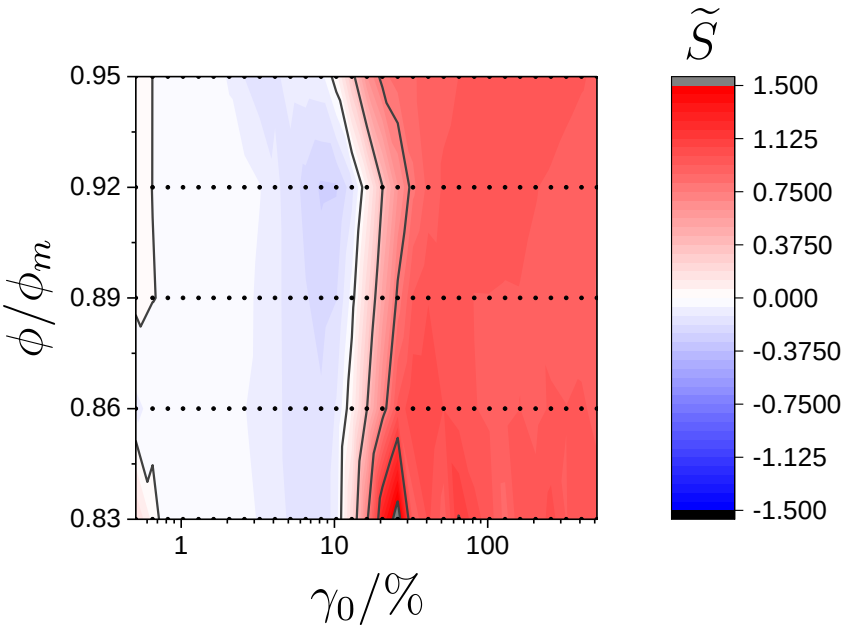

(a)

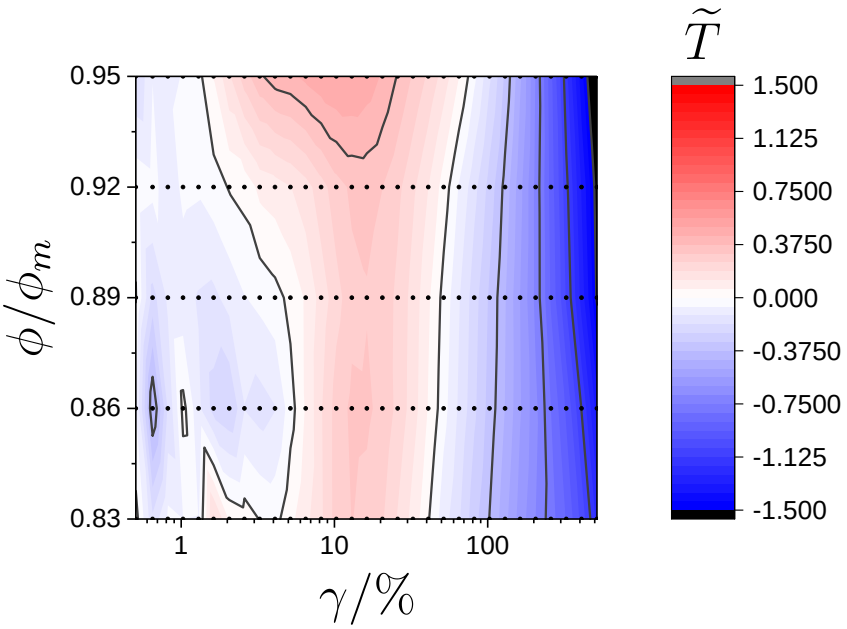

(b)

Fig. 9.15 Two maps that show (a) the strain-stiffening ratio $\widetilde{S}$ and (b) the shear-thickening ratio $\widetilde{T}$ as a function of the strain amplitude γ_0 and the scaled volume fraction ϕ/ϕ_m. The parameters $\widetilde{S}$ and $\widetilde{T}$ are calculated according to equation (1.35) and equation (1.36), respectively. Data points are based on the same DSS (at $f = 0.1\,\mathrm{Hz}$) as in figure 9.10.

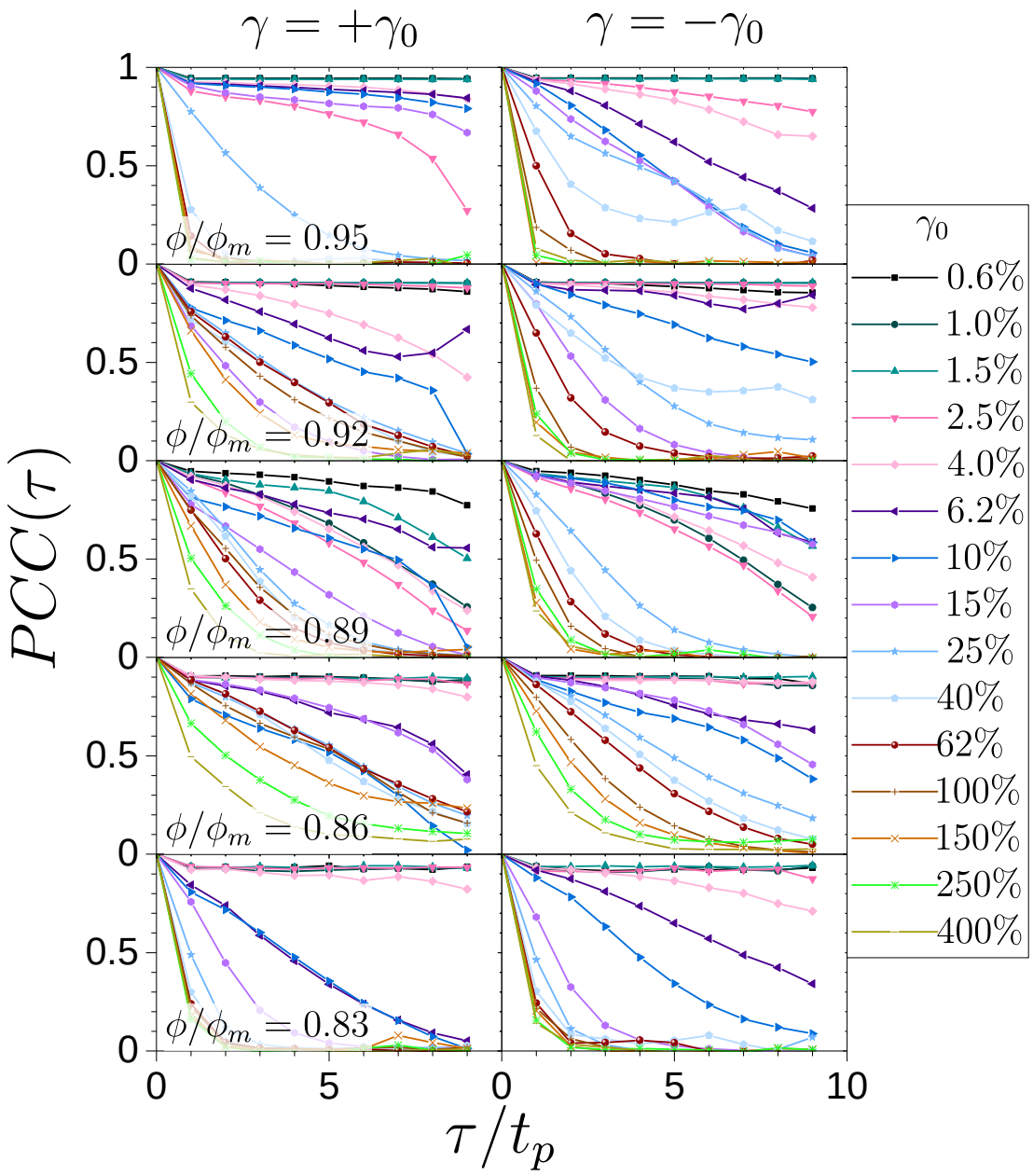

Fig. 9.16 Set of echo style confocal analysis based on raw images taken at $\gamma = \pm\gamma_0$ (left and right column, respectively) during oscillatory shear for samples with (from top to bottom) $\phi/\phi_m = 0.95$, $\phi/\phi_m = 0.92$, $\phi/\phi_m = 0.89$, $\phi/\phi_m = 0.86$, and $\phi/\phi_m = 0.83$. Data is based on jobs #9-23 (cf., table 9.4). Further details in the text.

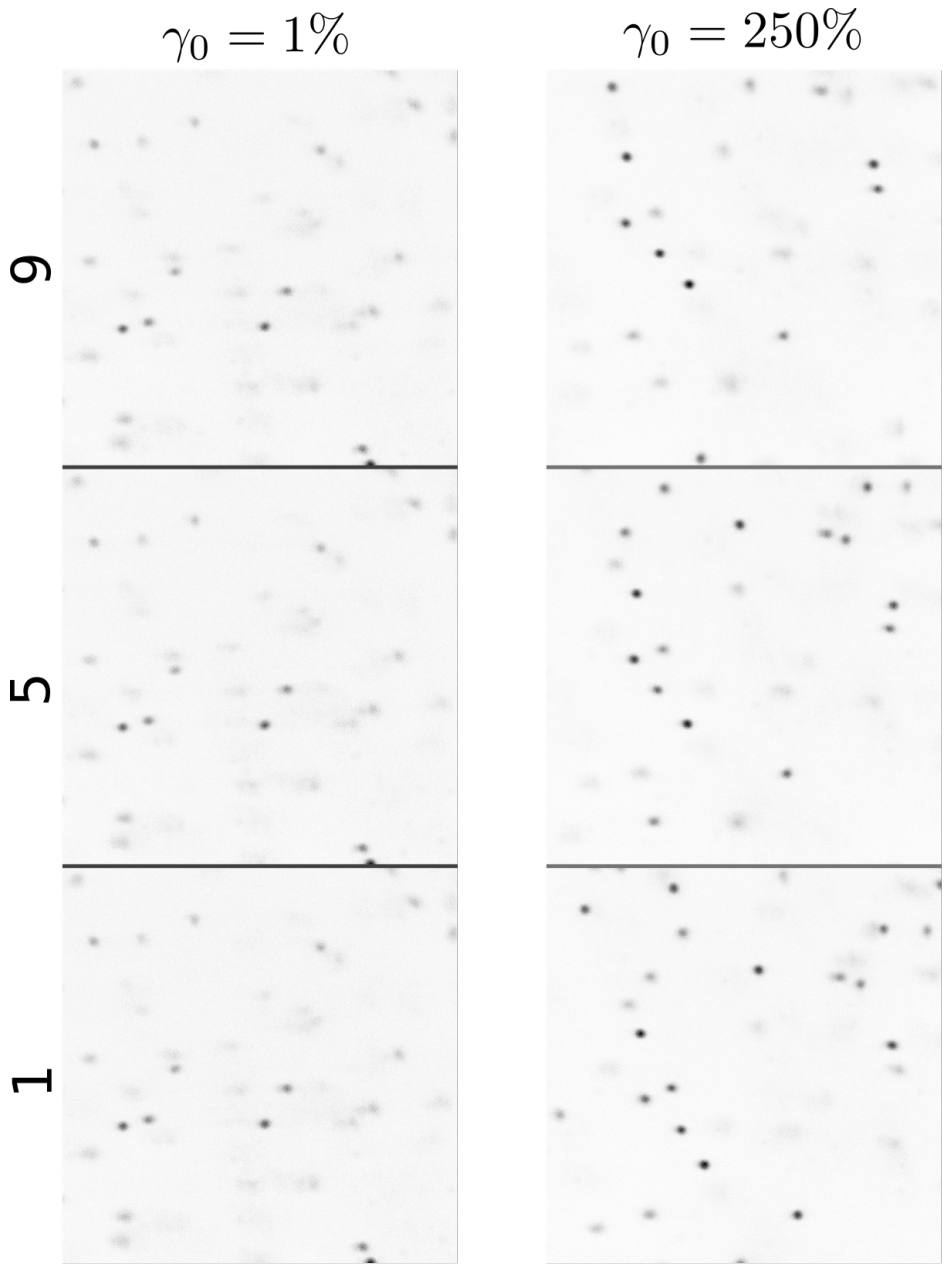

Fig. 9.17 Example set of confocal images used for the echo-style analysis. Shown are the 1st, 5th, and 9th image of an image series taken at maximum strain during oscillatory shear with strain amplitude (a) $\gamma_0 = 1\%$ and (b) $\gamma_0 = 250\%$. Presented data is from the $\phi/\phi_m = 0.86$ sample. The figure contains images with the following modifications: gray levels are inverted, and contrast is enhanced.

that the values are partially hidden behind other data points). When one looks at the images for $\gamma_0 = 250\%$ (figure 9.17b) and calculates the Pearson correlation coefficient for the top and bottom image (which are separated by 8 oscillation cycles), the result is roughly $PCC(8\,t_p) = 0.1$. A correlation value so close to zero intuitively suggests that the images look very different. But one may argue that the images for $\gamma_0 = 250\%$ are in fact not that different: There are a few repeating patterns. The tracer particles (dark points) in total move upwards (from image 1 to 9), but their relative positions do not change dramatically. Similar observations are also observed for other image series. Besides, tracer particles are also found to (collectively) move to the right, left or any other direction. Between some images, the offset might be only a few pixels, in others, the global offset can be as large as a few tens of pixels.

One, therefore, might try to distinguish two phenomena: One phenomenon is that the decay of the echos stems from a global or collective translation of (all) particles in the field of view. This could be related to slip, imprecision of the experimental setup or any additional, non-reversible motion. This is different from decays due to *relative* particle motions. To separate the two phenomena, one can attempt to reject the global translation and only analyze changes in relative positions of tracer particles. Therefore, global offsets are removed from the raw images in an additional step. This can be interpreted as going from the laboratory reference frame to a local sample reference frame.

Corresponding reshifted images of the sample are shown in figure 9.18, again for $\phi/\phi_m = 0.86$ and $\gamma_0 \in [1\%, 250\%]$. By construction, there is hardly any total tracer movement (i.e., $\sum_{\text{tracers}} \delta\vec{r} \approx 0$) and the images appear "more similar." This is especially the case for $\gamma_0 = 250\%$ (cf., figure 9.18b). Only minor changes visible. For instance, a particle that is not present in the 1st image appears in the 5th and 9th image. Particles also wiggle around their positions. This is not easy to see from the three images, but the reader may believe that the wiggling movements can be readily ascertained in a movie. The wiggling movements are stronger for $\gamma_0 = 250\%$ than for $\gamma_0 = 1\%$.

We can now compare the previous results from the echo-style analysis (figure 9.16) with the analysis based on images where the decay can only be caused by *relative* motions. These correlation functions based on the images in the sample-reference-frame are given in figure 9.19. A first remark is that it is not possible to unambiguously remove a global offset in all cases. Therefore, some data at high strains are missing – especially for the highest volume fraction ($\phi/\phi_m = 0.95$). Apart from that, the decays are similar for all volume fractions. For small strains (i.e., $\gamma_0 \lesssim 10\%$), the correlation functions now have values between 0.9 and 1 and are almost independent of τ in the studied time window. At intermediate strains (e.g., $\gamma_0 = 25\%$, (light blue line with filled stars)), the correlation functions decay with increasing lag time. And for the highest strains ($\gamma_0 \gtrsim 100\%$), the $PCC(\tau)$-values decrease significantly. In all cases (i.e., for all volume fractions and strain amplitudes), there is a decay from $\tau/t_p = 0$ to $\tau/t_p = 1$. This can be explained by considering the steps that were

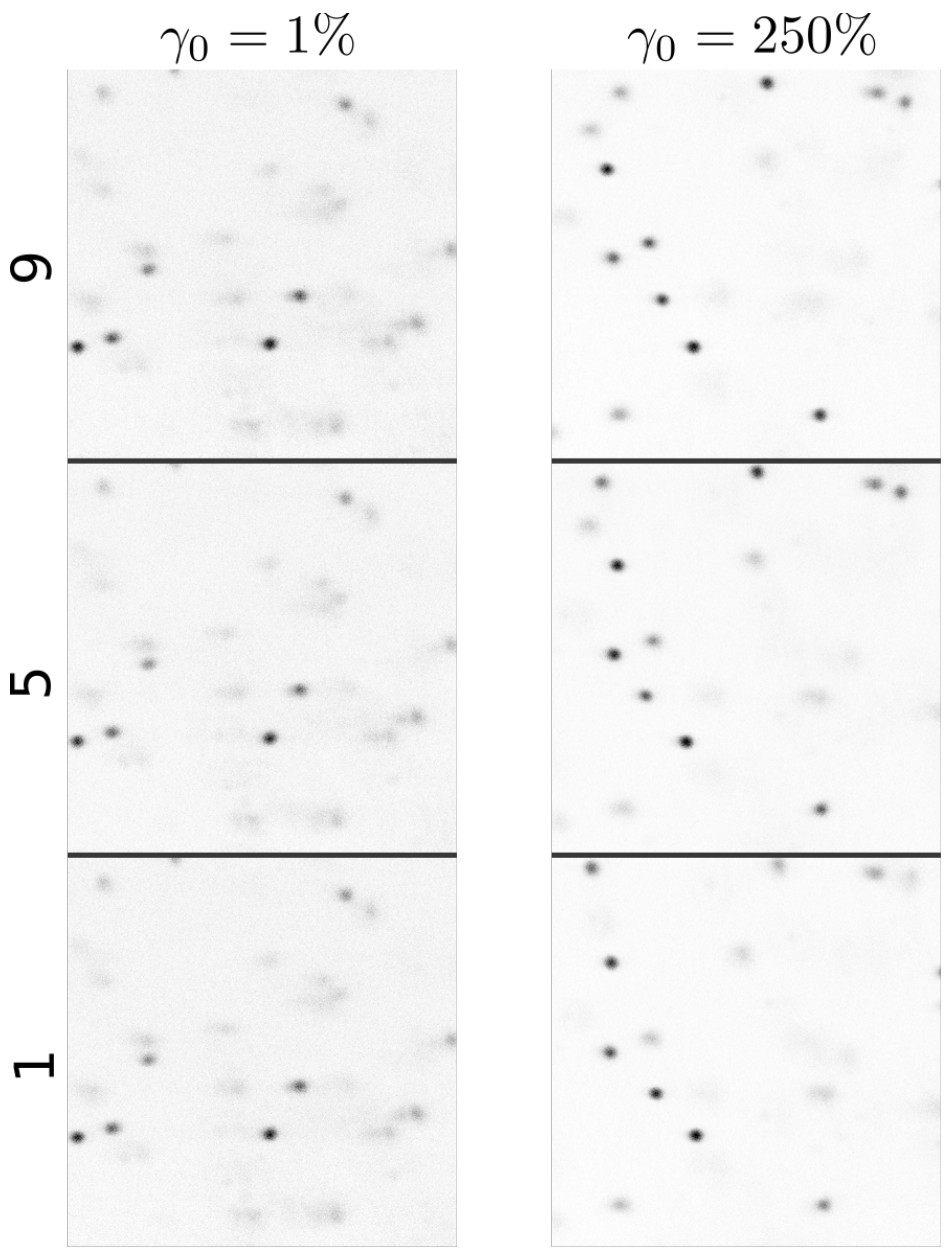

Fig. 9.18 Example set of reshifted confocal images used for the corrected echo-style analysis. These reshifted images are based on the same data as the images in figure 9.17. Due to reshifting, the size of individual images is reduced to 372×372 pixels, corresponding to $25\,\mu m \times 25\,\mu m$. The figure contains post-processed images with inverted gray levels and enhanced contrast.

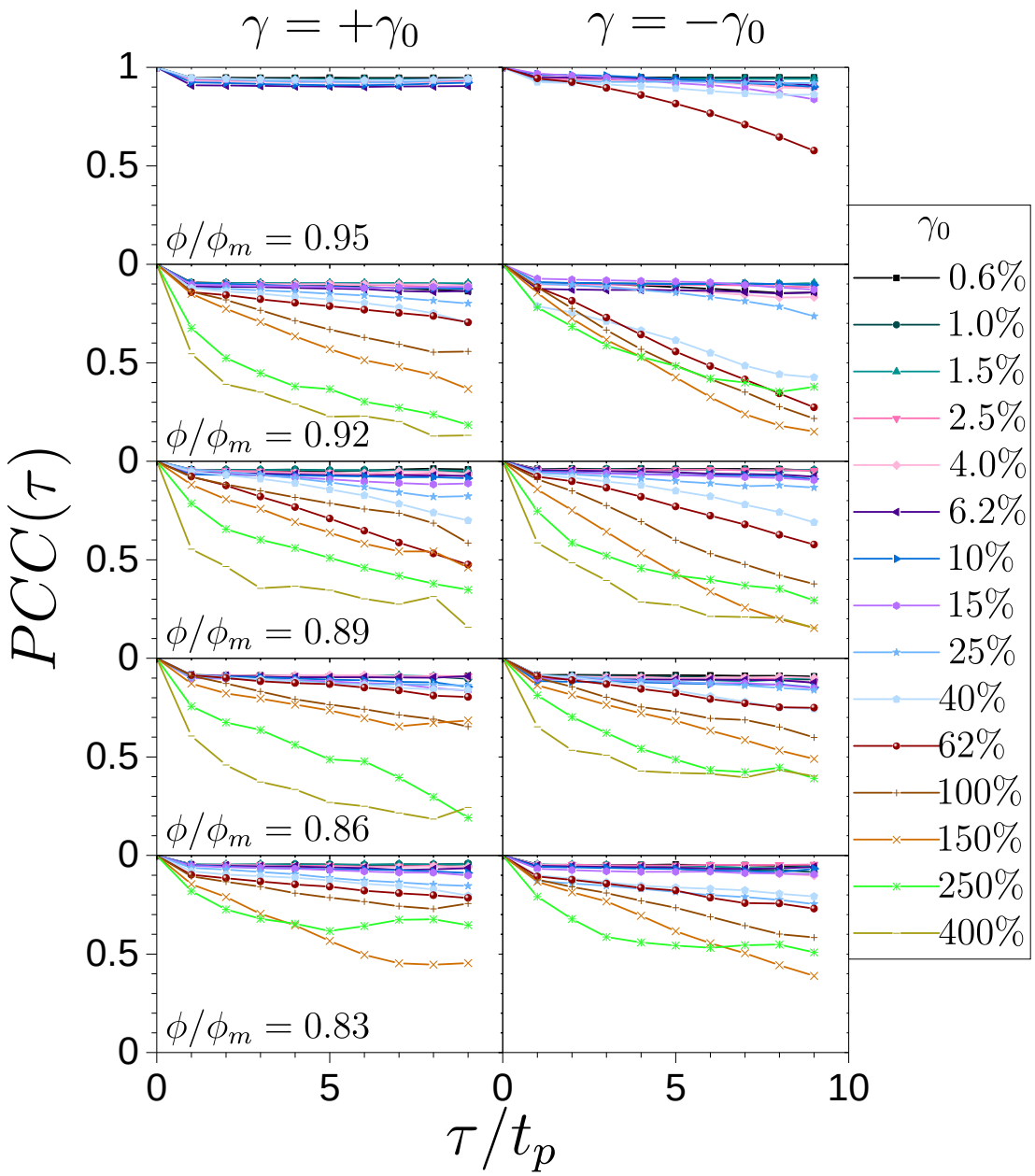

Fig. 9.19 Set of echo-style confocal analysis based on reshifted images taken at $\gamma = \pm\gamma_0$ (left and right column, respectively) during oscillatory shear for samples with (from top to bottom) $\phi/\phi_m = 0.95$, $\phi/\phi_m = 0.92$, $\phi/\phi_m = 0.89$, $\phi/\phi_m = 0.86$, and $\phi/\phi_m = 0.83$. Data is taken from jobs #9-23 (cf., table 9.4). At first sight, it seems that correlation functions show no decay for $\phi/\phi_m = 0.95$. This is misleading: A lot of data for higher strains is missing because global offsets could not be identified in a unique way.

taken to calculate the correlation functions: In the image processing step that leads from figure 9.17 to figure 9.18, images are reshifted by integer pixel numbers. Global offsets are, therefore, only removed up to an accuracy of about one pixel or 100 nm, respectively. What is the consequence of that? If one takes two *identical* images and computes the Pearson correlation coefficient, the result is 1.0. Shifting one of the two *identical* images by one pixel reduces the correlation coefficient down to about 0.95. A shift by two pixels causes a reduction to 0.9. This makes it very plausible that the initial decay is caused by the limited accuracy. Comparable studies based on light scattering find values of 0.8 for small lag times and have been normalized [30, 308]. From the data in figure 9.19, one may suggest that irreversible particle rearrangements occur above $\gamma_0 \approx 10 - 40\%$. Furthermore, a decay close to zero is only observed in the cases of the highest studied strain amplitude $\gamma_0 = 400\%$ and the maximum delay time $\tau/t_p = 9$.

To elucidate the strain dependence in more detail, we will consider a fixed delay time τ and plot the correlation values as a function of strain amplitude γ_0. This is done in figure 9.20 for fixed delay times $\tau/t_p = 2$ (figure 9.20a) and $\tau/t_p = 9$ (figure 9.20b). In both cases, the values have been normalized by the correlation value at $\tau/t_p = 1$. Normalization by a point with $\tau > 0$ has also been done in previous studies [218]. Data points in figure 9.20 are obtained by averaging results from $\gamma = +\gamma_0$ and $\gamma = -\gamma_0$ at the same ϕ/ϕ_m, and also incorporate repeated measurements. As before, data may not be available for the highest strain amplitudes ($\gamma_0 \gtrsim 70\%$). The following is observed: For $\gamma_0 \lesssim 10\%$, the normalized correlation values are identical to 1 within experimental uncertainties. This suggests that particles do not change their relative positions in this strain regime.

Following previous work [30], we define a characteristic strain γ_c^{conf} from the position where the normalized correlation function first drops significantly below unity, and use a threshold value of 0.95. From the confocal analysis in figure 9.20, we can identify a yield strain at $\gamma_c^{\mathrm{conf}} \approx 10\% - 20\%$. Above $\gamma_0 \gtrsim 10\%$, the correlations start to decay. The decays are already for $PCC(2\,t_p)/PCC(1\,t_p)$ and consequently also for $PCC(9\,t_p)/PCC(1\,t_p)$. In the latter case, the decays are more pronounced, which suggests that irreversible particle motions accumulate over many shear cycles. This implies that the rearrangements are not limited to a finite fraction of particles. Rather, the fraction of rearranging particles grows or different particles contribute to the rearrangements during different shear cycles.

Let us have a closer look at figure 9.20b in the regime $\gamma_0 \in [0.5, 70\%]$, where data for all volume fractions is available. The correlations functions decay faster with increasing volume fraction. A possible interpretation is that in a dilute system, particles have more free space to move. With increasing volume fractions, particle motions seem to become increasingly irreversible. Thus, one can argue that the yield strain γ_c^{conf} shifts to smaller values with increasing volume fraction.

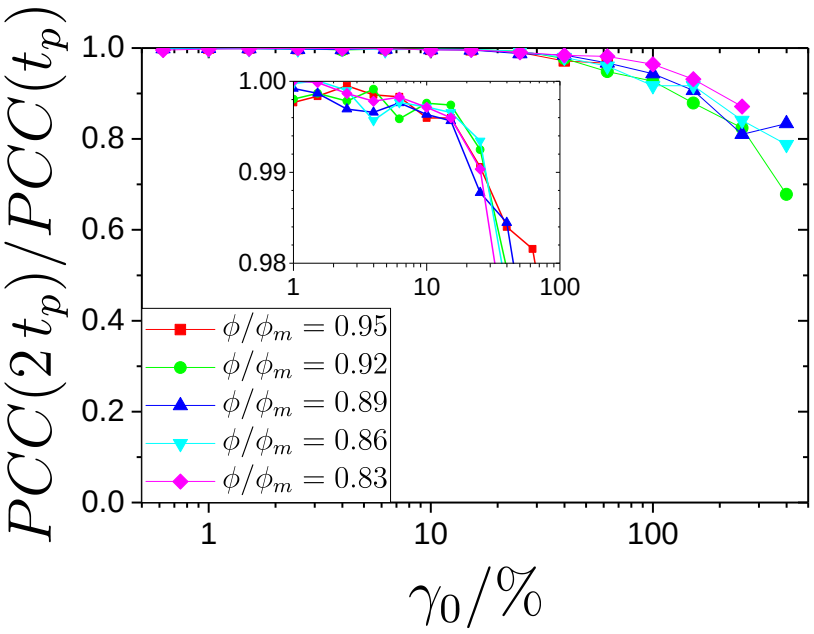

(a)

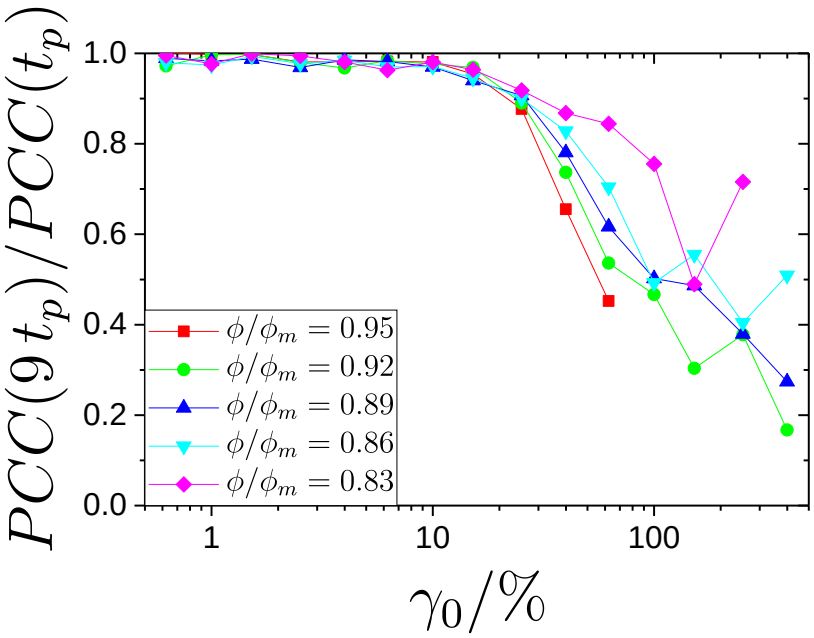

(b)

Fig. 9.20 Dependence of (a) $PPC(2\,t_p)/PPC(1\,t_p)$ and (b) $PPC(9\,t_p)/PPC(1\,t_p)$ as a function of strain amplitude γ_0 for all volume fractions. In other words, shown are correlation values for echos after (a) two and (b) nine cycles of shear that are normalized with the correlation value after one cycle. The presented data points are averages based on figure 9.19 as well as a repeated set of experiments. Furthermore, each point is an average from values obtained at maximum and minimum strain (i.e., at $\gamma = \pm\gamma_0$).

9.5 Discussion

Individual results from the last chapter have been discussed on the spot. This section is meant to discuss the findings in a more general context and to compare them with previous work.

Flow and turbulence of a fluid in a cone and plate geometry have been investigated in conjunction with a single parameter $\widetilde{R}$ (cf., section 1.5.2.3, equation (1.47)). The parameter compares centrifugal to viscous forces. Laminar flow of a fluid is found for $\widetilde{R} < 0.5$ and turbulence for $\widetilde{R} \gtrsim 4$ [34]. Parameters of this work (radial distance $r = 0.01\,\mathrm{m}$, maximum angular velocity $\dot{\Theta} = 0.11\,\mathrm{rad/s}$, cone angle $\beta = 0.035\,\mathrm{rad}$, density $\rho = 1200\,\mathrm{kg/m^3}$) result in $\widetilde{R} = 0.0005$, if we use the viscosity of the dispersion medium ($\eta_0 = 0.003\,\mathrm{Pas}$). Thus, any turbulent, chaotic and irreversible flow should originate from the presence of the colloidal spheres – especially at high volume fractions.

Regarding the volume fraction, results from this work are self-consistent: The flow behavior upon loading (possibility of pouring the sample vs. necessity of loading with a spatula, (cf., section 9.3)) is in qualitative agreement with the assumption of the random close packing based on the polydispersity (cf., section 9.3) and the trends of the elastic moduli (cf., figure 9.4). For a comparison with literature, it is convenient to now convert the relative volume fractions $\phi/\phi_m \in [0.83, 0.86, 0.89, 0.92, 0.95]$ to absolute volume fractions $\phi \in [0.57, 0.59, 0.61, 0.63, 0.65]$ using $\phi_m = 0.687$.

We interpret the deviations between measured and expected particle displacements (cf., figure 9.9a) as signatures of wall slip. Wall slip is an unwanted effect and adds a bias to the results. One has to, therefore, handle the results of this work for $\phi \gtrsim 0.61$ with care. Nevertheless, it is reassuring that wall slip can be identified concordantly under steady (cf., figure 9.7) and oscillatory shear (cf., figure 9.9). Slip might even explain the unexpected small exponent in the Herschel-Bulkley fit for $\phi \gtrsim 0.61$. The standard flow index in the Herschel-Bulkley fit for hard spheres is around $\upsilon = 0.5$ [12], indicating shear thinning [11]. Shear thinning is also found during our large amplitude oscillatory shear (cf., figure 9.15b).

Knowledge of slip from microscopic observation can be used to correct for slip in macroscopic rheology. If a sample slips, it is sheared less then expected. For oscillatory shear, ideal γ_0 and true strain amplitudes γ_0^{true} for the case of slip are illustrated in figure 9.21. We identify the true strain as

$$\gamma_0^{\mathrm{true}} = \frac{\Delta x_0^{\mathrm{true}}}{h}\,, \tag{9.5}$$

where $\Delta x_0^{\mathrm{true}}$ is the relative displacement of the sample over the gap with height h. Using quantities that are directly available we can rewrite equation (9.5) as

$$\gamma_0^{\mathrm{true}} = \tan(\theta_0^{\mathrm{true}}) = \frac{\gamma_0 h - \Delta x_0^{\mathrm{conf}}}{h - z^{\mathrm{conf}}}\,, \tag{9.6}$$

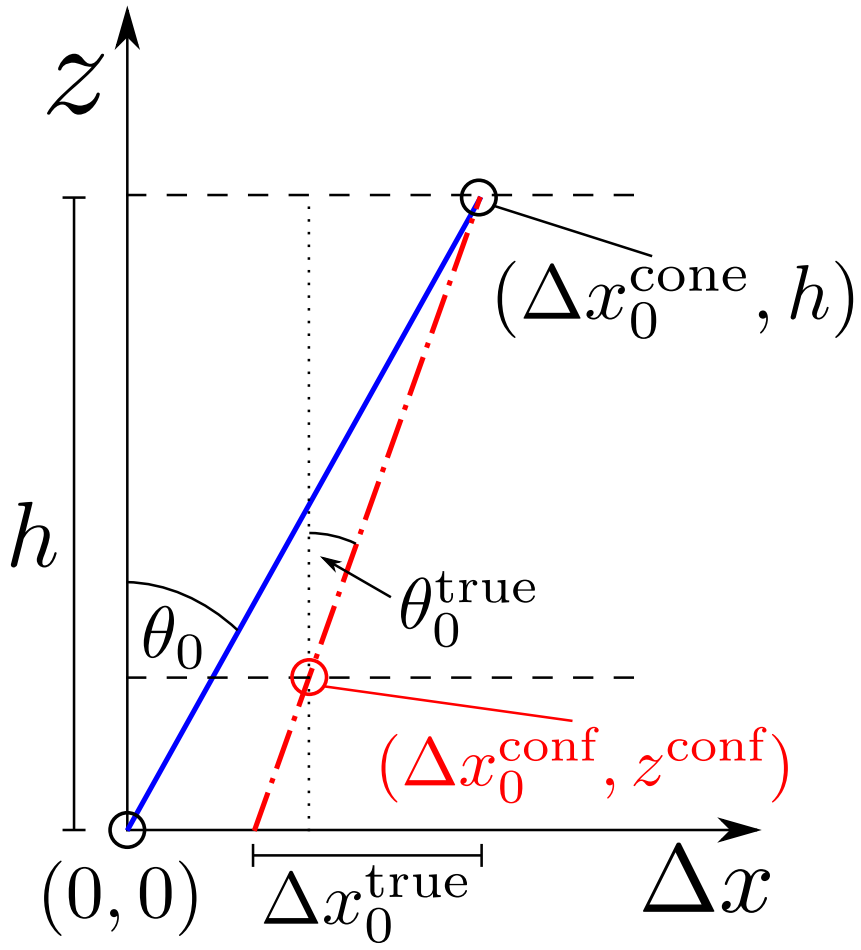

Fig. 9.21 Illustration of the calculation of the "true" strain. Axis show gradient positions z versus the displacement in velocity-direction Δx. Under no-slip conditions, the strain amplitude is $\gamma_0 = \tan(\theta_0) = \Delta x_{0,\text{cone}}/h$, where $\Delta x_{0,\text{cone}}$ is the corresponding displacement of the cone and h the corresponding gap height. With slip, the sample is sheared less. We assume that slip takes place only at the bottom plate (at $z = 0$) but not at the top (at $z = h$). We furthermore assume linear profiles. Microscopic knowledge is given at $z = z^{\text{conf}}$ The "true" strain (amplitude) is $\gamma_0^{\text{true}} = \tan(\theta_0^{\text{true}}) = (\Delta x_0^{\text{cone}} - \Delta x_0^{\text{conf}})/(h - z^{\text{conf}})$. If the sample would also slip at the top, then the true strain would be even smaller.

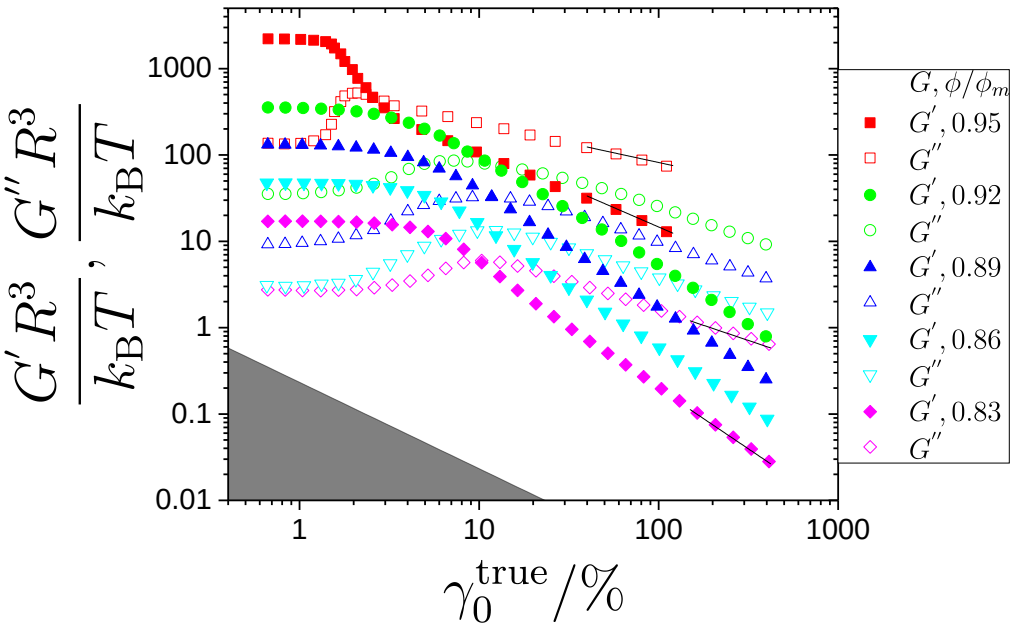

Fig. 9.22 Same DSS as in figure 9.10 but now with γ_0^{true} instead of γ_0 (i.e., strain amplitudes are corrected for slip). Lines show apparent slopes of -0.45 and -0.9, and -0.7 and -1.4, respectively.

where γ_0 is the applied strain amplitude and Δx_0^{conf} the measured displacement amplitude at height z^{conf}. If we rewrite the expression in terms of $Err(\Delta x_0^{\text{conf}})$ (equation (9.3)) we obtain

$$\gamma_0^{\text{true}} = \gamma_0 \frac{h - z^{\text{conf}}(1 + Err(x_0^{\text{conf}}))}{h - z^{\text{conf}}}, \tag{9.7}$$

and see that the true strains are smaller than the applied strains since $Err(\Delta x_0^{\text{conf}})$ is almost always positive (cf., figure 9.9a).

We can use equation (9.7) to correct the previously shown rheological results. For example, most values of storage and loss moduli during a DSS as shown in figure 9.10 actually correspond to smaller values of strain. Corrected results are now presented in figure 9.22. For the $\phi/\phi_m = 0.95$ sample, major differences are revealed. We may recall that in the uncorrected case both moduli cross around 10% strain. Including the slip-correction, the linear regime of the $\phi/\phi_m = 0.95$ sample is shifted to much smaller values of strain and the elastic and viscous moduli already cross at $\gamma_0^{\text{true}} = 2 - 3\%$ (!). The corrected results for the other samples are also located at (slightly) smaller strains, but differences to the non-corrected case (cf., figure 9.22 and figure 9.10) are hardly visible by eye.

Similarly, we can correct for the impact of slip in the analysis of confocal echos. This is done in figure 9.23. The figure shows the normalized correlation between echos that are separated by nine cycles of shear (i.e., $PPC(9\,t_p)/PPC(1\,t_p)$) as a function of true

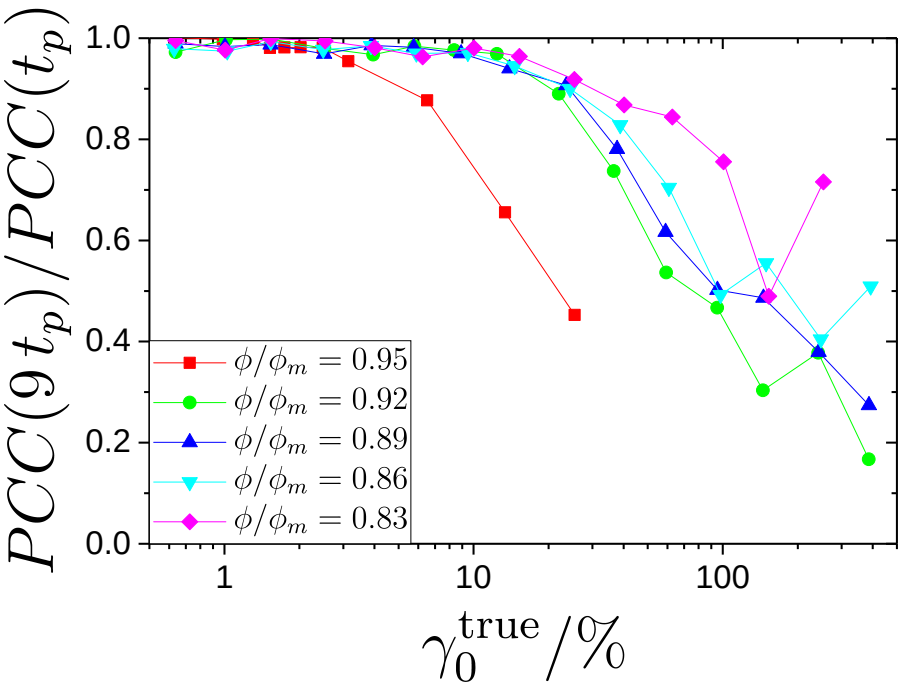

Fig. 9.23 Dependence of $PPC(9\,t_p)/PPC(1\,t_p)$ as a function of γ_0^{true}. Despite the correction for slip, the figure contains the same data as in figure 9.20b.

strain γ_0^{true}. It is expected that echos from samples with higher volume fraction decay even faster if plotted against γ_0^{true}. This is indeed the case. We observe that echos decay faster with increasing volume fraction but the difference between $\phi/\phi_m = 0.95$ and the other volume fractions becomes more obvious. For example, at $\gamma_0^{\text{true}} = 10\%$, the values of $PPC(9\,t_p)/PPC(1\,t_p)$ are close to 1 for $\phi/\phi_m \in [0.83, 0.86, 0.89, 0.92]$, but decreased already down to about 0.7 for the $\phi/\phi_m = 0.95$ sample. We may recognize that there is a range of strains ($2\% \lesssim \gamma_0^{\text{true}} \lesssim 10\%$) where moderately concentrated colloidal suspensions still behave elastic, while highly concentrated ones already show viscous signatures.

This leads us to the discussion of yielding phenomena. There are a number of ways to define characteristic yield strains. In terms of rheology, it is common to use the value of the strain amplitude in a dynamic strain sweep where G' and G'' cross, or the position where G'' exhibits a maximum. Another estimate of a characteristic strain γ_c can be obtained by equating the mechanical energy $G'{\gamma_c}^2R^3$ to the thermal energy k_BT [310]. This estimate will be tested using the elastic moduli from figure 9.4. Estimates for the yield strain, based on rheological data from this work using the three abovementioned methods, are given in figure 9.24. We will compare these results with estimates from the confocal echos as well as with literature data. Relevant work has been done, for instance, by Petekidis et al. [30, 308]. They have studied yielding of hard-sphere glasses (PMMA, $R = 183\,\text{nm}$) of

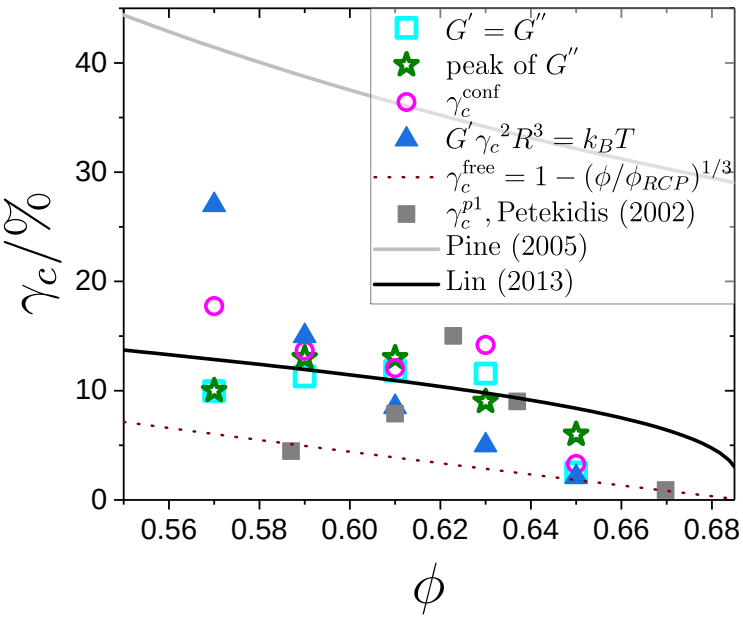

Fig. 9.24 Dependence of the yield strain as a function of absolute volume fraction. Yield strains are defined from the slip-corrected DSS (figure 9.22) as strains where G' and G'' cross (open squares), and where G'' exhibits a peak (open stars). The critical strains γ_c^{conf} are taken from figure 9.23 as values where $PPC(9\,t_p)/PPC(1\,t_p)$ drops below a threshold of 0.95. Solid triangles show critical strains obtained from a comparison of energies [310], for data of this work. The dotted line is based on an estimate of free volume [308] using $\phi_{RCP} = 0.687$. Additional literature values (solid squares, solid gray line, solid black line) from references [306–308] are included for comparison. Further details in the text.

similar volume fractions and analyzed the relative decays of light scattering echos as a function of strain. Two different characteristic strains were defined: One (i.e., γ_c^{p1}), where the echos first drop and another one, where the echos disappeared completely. For volume fractions $\phi = 0.587$ and $\phi = 0.61$ they find that Brownian motion plays a significant role in the decay of the echos. Their values of γ_c^{p1} are also shown in figure 9.24.

The onset of irreversibility of sheared PMMA-suspensions ($R = 115\,\mathrm{nm}$) has also been studied at lower volume fractions (i.e., $0.1 < \phi < 0.4$) by Pine et al. [306]. They fitted threshold strains as a function of volume fraction with the equation $\gamma_{\mathrm{threshold}} = 0.14\,\phi^{-1.93}$. Lin et al. analyzed the structure of hard spheres (silica particles, $R = 490\,\mathrm{nm}$, $\phi = 0.17 - 0.44$) under shear with confocal microscopy. To this end, they fitted a cutoff strain amplitude with the relation $\gamma_c \propto (\frac{\phi_{RCP} - \phi}{\phi})^{1/3}$ [307]. The constant of proportionality can be extracted from their data and is about 0.218. The fits of Pine and Lin can thus be compared with findings from this work and they are both included in figure 9.24, together with the other estimates. Figure 9.24 also includes a line following $\gamma_c^{\mathrm{free}} = 1 - (\phi/\phi_{RCP})^{1/3}$. This is related to

the free space between two hard particles as a function of volume fraction [308].

From the comparison of yield strains in figure 9.24, we see that the critical strain that is related to the free space between particles serves as a lower limit. All other estimates of characteristic strains lie essentially above the line of γ_c^{free}. The fact that other measures of the critical strain result in larger values has led to the picture of "cage elasticity" [308]. Even though particles should collide above γ_c^{free}, they seem to retain their relative positions after one or more cycles of shear. Most estimates for critical strains lie in the range between strains of 5% and 15%, which is in good agreement with the estimate from the confocal echo analysis of this work. The fit by Pine et al. is an outlier. Fair enough, it was used to fit (much) smaller volume fractions. Approaching ϕ_{RCP}, most estimates suggest that the critical strain goes to zero. This can be inferred from the fit by Lin, the data of Petekidis, and the trend of the critical strain from the equalization of mechanical and thermal energy. The situation between the glass transition and random close packing (i.e., $\phi = 0.57 - 0.64$) is not that clear. While some estimates show a monotonic decrease as a function of volume fraction, other estimates show local peaks (e.g., at $\phi \approx 0.62$). Generally speaking, the critical strain depends on the volume fraction, as also found in other systems like oil in water emulsions [218].

It has been observed before that critical strains γ_c from a microscopic perspective are close to but not identical to a (macroscopic) yield strain [318]. In reference [318], the characteristic microscopic strain is found to be slightly lower than the rheological yield strain. Apparently, it seems quite difficult to define a characteristic microscopic strain. For example, irreversible rearrangements are observed for the small strain amplitudes down to $\gamma_0 = 1\%$ [310] and large exponential tails are found in the distribution of particle displacements at small strains [245]. Actually, also macroscopic rheology from this work reveals some viscous contribution at small strain (cf., figure 9.11). So one might pose the question differently. To elucidate the effect of shear, one might not ask "when will trajectories become irreversible?" but rather "when will trajectories become more irreversible than without shear?" The combination of slow dynamics in glasses combined with external shear and the possibility of aging are driving complexity upwards. (Shear-induced) spatial heterogeneities do not make it easier either [218, 245, 310]. The same system of particles may have a fraction of mobile and a fraction of immobile particles. Observation time can also play a crucial role. Many microscopic studies are limited to a small number of oscillation cycles, while rheology or simulations can average over many more cycles.

This work covers delay times up to nine cycles and may, therefore, contribute to the controversial discussion of whether the fraction of mobile and immobile particles changes with time [218] or not [310]. A constant fraction of immobile particles would contribute to a finite and time-independent correlation coefficient. We observe that the correlation coefficients decay more and more with increasing delay times (cf., figure 9.19 and figure 9.20). This suggests that the fraction of mobile and immobile

particles indeed changes with time.

When analyzing spatially heterogeneous samples, one has to make sure that results from a subset of particles are representative of the total system. This calls for a critical opinion upon the use of two-dimensional confocal microscopy images. By construction, confocal microscopy only images a thin layer. Nevertheless, linear velocity profiles are found and thus particles all over the gap are subjected to the same local shear rate. The gap is large enough to avoid confinement effects, which could be present in other work [307]. Images of this work used to evaluate microscopic motions contain about 10 tracer particles (cf., figure 9.18) and a few thousand (hidden) small particles. The physics should be dominated by the small spheres and not by the tracer particles. At the present moment, it is, therefore, reasonable to assume that the confocal results are representative of the whole system.

Experimental studies using scattering techniques are superior to microscopy techniques when it comes to statistics. By varying the scattering angle, light scattering can also probe different length scales. They, therefore, take up an important position. Real-space confocal movies can relatively easily be used to distinguish linear and nonlinear shear profile and to reveal the existence of wall slip. If this information is not available directly, one has to be very careful with the corresponding assumptions.

9.6 Conclusion

The flow of colloidal hard-sphere glasses was analyzed under oscillatory shear by means of simultaneous rheology and confocal microscopy. Experiments cover a large strain range with strain amplitudes from $\gamma_0 = 0.5\%$ up to $\gamma_0 = 500\%$. Large strains are accessible due to the use of a rotational rheometer that is coupled to a fast scanning confocal microscope. The experimental setup allows measuring macroscopic rheological properties on the same sample that is simultaneously imaged with the microscope. Samples of different volume fractions were first characterized using standard rheological tests. Results from a dynamic frequency sweep and a flowcurve are essentially consistent with the literature on hard spheres. Confocal observations elucidated wall slip for higher volume fractions and accordingly, strain values were corrected. Despite slip, a linear shear profile is observed for all samples.

With the help of LAOS experiments, strain stiffening and shear thickening regimes are identified as a function of volume fraction and strain. Shear thickening is found to occur during yielding.

Estimates for yield strains are obtained from rheology and confocal echos and compared with previous work. Confocal microscopy is used to distinguish between collective and relative motion of tracer particles. Characteristic yield strains are found around 10% strain. Particle motions are essentially reversible below the yield strain. Above yielding, the amount of irreversibility increases both with increasing strain and lag time. We may conclude with the following picture: Yielding of hard

spheres is a smooth transition from a solid-like to a liquid-like state. A single-valued critical strain might be an oversimplification. The scattering of the yield strain data (cf., figure 9.24) indicates that there is, in fact, a finite region of strains where the yielding process takes place. During yielding, some particles undergo irreversible motions. This fraction of non-elastic, mobile or "super-mobile" [218] particles increases, until, at some point, essentially all particles experience irreversible motions. Future rheological measurements could systematically vary the number of cycles contributing to quantities like the elastic or viscous moduli. A related question is whether echos (or correlation coefficients) will eventually decay to zero for strains just above yielding and for sufficiently long times, and this could be answered in future investigations.

A similar question involves the dependence on the oscillation frequency: Observations of yielding and flow under LAOS may differ due to differently used oscillation frequencies. Some experimental particle diffusion coefficients are found to be rather independent of the oscillation frequency [306]. In contrast, frequency dependence is found by Poulos et al. [166]: The frequency dependence is found to be different above and below the glass transition. Below ϕ_g, the amount of irreversibility increases with increasing frequency, above ϕ_g, the opposite trend is observed. Additionally Poulos et al. find that measurements with conventional rheometers at moderate frequencies $\omega > 5\,\mathrm{rad/s}$ can be biased by instrumental effects [166]. Experimental studies at high frequencies, therefore, require sophisticated machines.

Finally, confocal imaging is ideal to probe the microscopic dynamics at different z-heights (i.e., at different positions within the gap). Future studies could perform experiments at different heights to clarify whether the observed physics is height-dependent or not.

Acknowledgments

The Center for Advanced Imaging (CAi) is acknowledged for the SEM image, A. Pamvouxoglou for the SLS measurement, and G. Petekidis for helpful discussion.

10

Transient Start-Up Tests: Bend It like Beckham

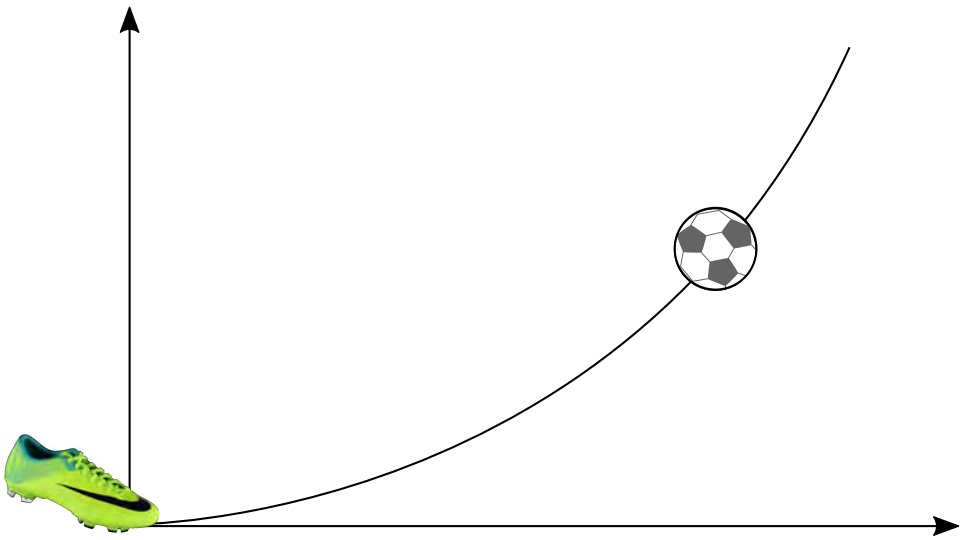

10.1 Abstract

Transient dynamics of hard-sphere-like colloidal suspensions in the vicinity of the glass transition are investigated during start-up shear at low Péclet numbers. Using a rheo-confocal setup, we shed light on the evolution of mesoscopic velocity profiles while simultaneously monitoring the overall stress-strain response. We find that microscopic dynamics depend on parameters such as volume fraction, gap height, particle size, and experimental protocol. In particular, one sample exhibits time-dependent and highly nonlinear velocity profiles. These transient nonlinear responses are furthermore reflected in local quantities such as nonaffine motions and mean squared displacements. We phenomenologically establish a link between the evolution of mesoscopic shear profiles on the one hand and microscopic dynamics on a single-particle level on the other hand. The origin of the nonlinearity remains to be understood. Possible explanations are related to yield stress, aging, and size effects.

10.2 Introduction

The flow of soft matter is ubiquitous in daily life, ranging from squeezing of toothpaste and the handling of paints to flow of blood cells inside the human body. Understanding and tuning the flow of soft materials is a long-standing problem and tackled by experiments [64, 135, 136, 164, 190, 215, 319], theory [320–323], and simulations [324–326].

In order to understand the underlying physics, particular interest has emerged in the investigation of hard spheres. The popularity of the hard-sphere model system stems from its – in principle – simple interaction potential that is infinite at contact and zero else. The only control parameter is the volume fraction $\phi = V_{\text{spheres}}/V_{\text{total}}$, relating the volume of all spheres to the total volume. Hard spheres can be experimentally realized with colloidal suspensions (cf., section 2.3). Due to their size, colloids are observable with visible light, making them ideal candidates for studies on a single-particle level.

The equilibrium phase behavior has been experimentally studied by Pusey and van Megen [65] (cf., section 2.4.1). The so-called glass transition (cf., section 2.5.2) is located around $\phi_g \approx 0.58$ and reflected in an increase of the viscosity (cf., section 2.5.4). The microscopic picture is that for volume fractions $\phi > \phi_g$, particles are trapped in cages formed by their neighbors and motion gets frustrated. Colloidal glasses have amorphous structures like fluids but behave mechanically more similar to solids. This means that structural quantities cannot be solely responsible for the mechanical properties of glasses, and dynamical quantities have to be important. Indeed, dynamical quantities differ between liquids and glasses (cf., section 2.5.3), and they could be the key to a complete understanding of the physics of glasses.

Transient dynamics of colloidal glasses during start-up shear have been studied extensively [168, 169, 263, 327]. Experimental observations reveal that particles undergo different kinds of rearrangements depending on the applied strain. The deformation is reversible for low strains. By further increasing the strain, particles experience irreversible changes in structure and dynamics. Under shear, the behavior thus changes from elastic to plastic deformation and eventually the systems flows [255, 308, 327]. Rheological experiments reveal that the stress overshoot is related to the cage deformation and yielding of the system [168, 215, 220, 327]. Recent studies find super-diffusion at strains similar to the strains at which the stress overshoot occurs [168].

Dynamics of glassy systems are in general heterogeneous and much interest is related to so-called dynamical heterogeneities. For instance, some groups suggests that the onset of yielding is related to a percolation transition and plastic deformation zones [133, 188, 231, 245, 328, 329]. Heterogeneities occur on the scale of a few particles as well as on larger length scales. Heterogeneous flow is expressed in nonlinear shear profiles and has been related to non-monotonic flow curves [330] or a plateau region within a flow curve [331]. Shear bands (cf., section 2.5.4.2) are

	$R/\,\mathrm{nm}$	$\delta/\%$	dye	tracer particles
Batch A	178	18	–	1% (v/v), $R \approx 795\,\mathrm{nm}$
Batch B	780	8	Rhodamine B	–

Tab. 10.1 Summary of sample parameters. Specified is the mean radius R, the polydispersity δ, the fluorescent dye, and details of any existing tracer particles.

usually expected for stresses below the yield stress (cf., e.g., [176]) or, alternatively, below a critical shear rate [187, 331].

This chapter deals with the dynamics of concentrated ($\phi \approx \phi_g$) hard-sphere-like colloidal suspensions during start-up shear. The investigated Péclet number (equation (2.22)) is below unity ($\mathrm{Pe} \approx 0.016$) meaning that Brownian dynamics are expected to dominate over shear. Using two different samples we study and compare macroscopic rheology with mesoscopic velocity profiles and microscopic dynamics. We will show that shear profiles are directly linked to local properties – even for transient non-uniform flows.

10.3 Materials and Methods

We investigate dispersions of polymethylmethacrylate (PMMA) hard-sphere-like particles with volume fractions $\phi_1 = 0.57$ and $\phi_2 = 0.61$, that is, in the vicinity of the colloidal glass transition [65, 70]. The samples contain either smaller spheres ("batch A") with a mean radius of $R_A = 178\,\mathrm{nm}$ or larger spheres ("batch B") with a mean diameter of $R_B = 780\,\mathrm{nm}$. A summary of sample properties is provided in table 10.1.

Size and polydispersity of non-dyed particles of Batch A are estimated with dynamic light scattering and the corresponding correlation function is shown in figure 10.1. Fluorescently labeled tracer particles are added afterward (1% (V/V)) to allow for confocal imaging.

Batch B contains only dyed particles and we assume a mean radius of $R_B = 780\,\mathrm{nm}$. An upper limit for the mean particle radius is taken from the first peak of the pair correlation function located at $2R_{B,\mathrm{max}} = 2 \cdot 820\,\mathrm{nm}$ (not shown here). A lower limit is estimated from electron microscopy (SEM) images. A corresponding SEM image of batch B is shown in figure 10.2 together with a size distribution as obtained from multiple SEM images. The distribution is bimodal with a mean value of 725 nm and an overall polydispersity of $\delta_B = 8\%$. Particles for the SEM micrographs are prepared in a dried state, which means that sizes are smaller than if particles were dispersed in a liquid.

In the experiments, particles of both batch A and batch B are dispersed in a mixture of *cis*-decalin and cycloheptyl bromide, matching closely both the refractive

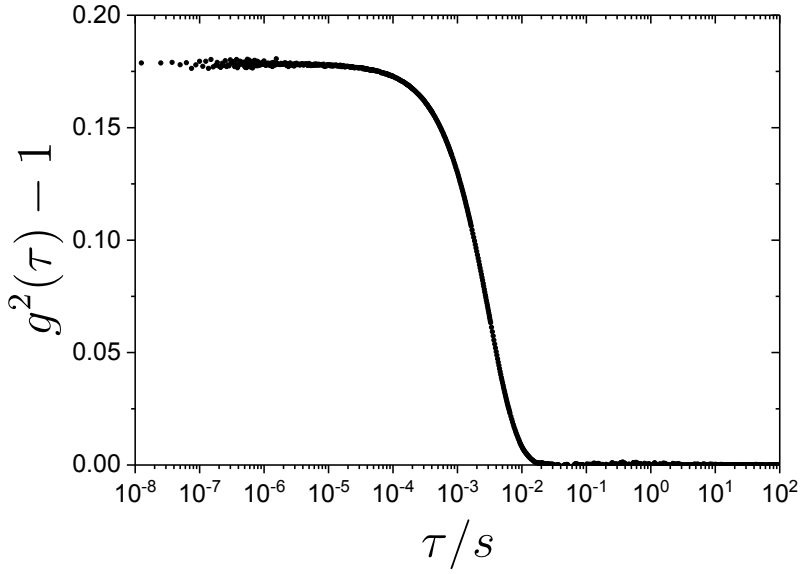

Fig. 10.1 Correlation function for batch A as obtained from dynamic light scattering at an angle of $\theta = 90°$. Based on this data, the cumulant analysis from the 3D LS Spectrometer Software (LS Instruments) yields a hydrodynamic radius of $R_A = 178\,\text{nm}$ and a polydispersity of $\delta_A = 18\%$.

index and the density of the particles. The addition of 4 mmol of the salt tetrabutyl ammonium chloride (TBAC) screens residual charges. Volume fractions are set by a dilution from random close packing after sedimentation, which is assumed to be at $\phi_{A,RCP} = 0.67$ and $\phi_{B,RCP} = 0.66$, respectively [91].

Simultaneous rheology and confocal microscopy experiments are performed with the rheo-confocal setup (cf., section 4.2). The rheo-confocal setup consists of a stress-controlled rheometer (Anton Paar, MCR302 WESP) mounted on an inverted microscope (Nikon, Eclipse Ti-U) that itself is connected to a confocal unit (Visitech, VTEye). We use an oil-immersion objective (Nikon, Plan Fluor 100x, NA = 1.30) with a working distance of 200 µm (cf., figure 4.2). Rheological properties of batch A are measured with a sandblasted cone-plate geometry (Anton Paar, CP25-2/S, SN36375, $d = 24.9826\,\text{mm}$, $\beta = 2.001°$). The larger spheres (batch B) need larger cones to produce enough torque. If not stated otherwise then shear in the case of batch B is applied with a home-build cone-plate geometry ($d = 40.1\,\text{mm}$, $\beta = 3.03°$) with a roughened surface. In any case, a serrated glass bottom-plate ($d = 50\,\text{mm}$, thickness #1.5 (0.16-0.19 mm)) prevents slip as verified by confocal microscopy. A solvent trap filled with *cis*-decalin is used to prevent evaporation.

To make sure that rheological results are not affected by the customized set-up, start-up tests with batch A are additionally carried out with a strain-controlled rheometer (TA, ARES G2) that is equipped with a stainless steel cone-plate geometry

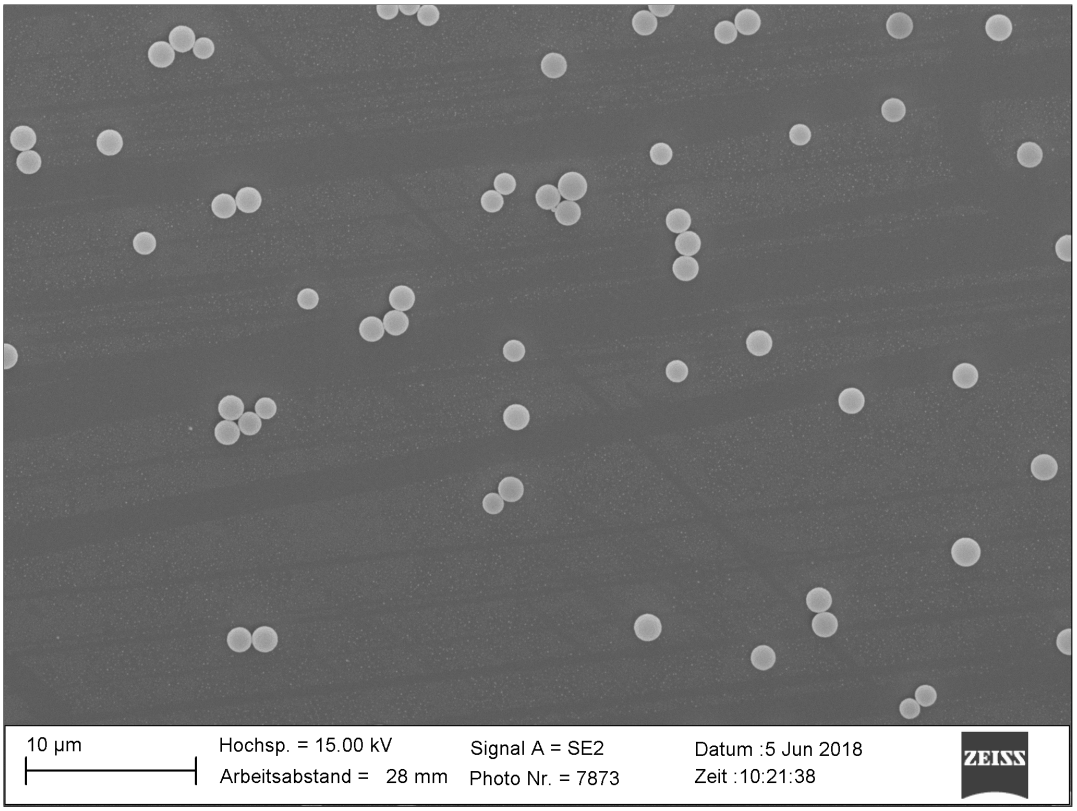

(a)

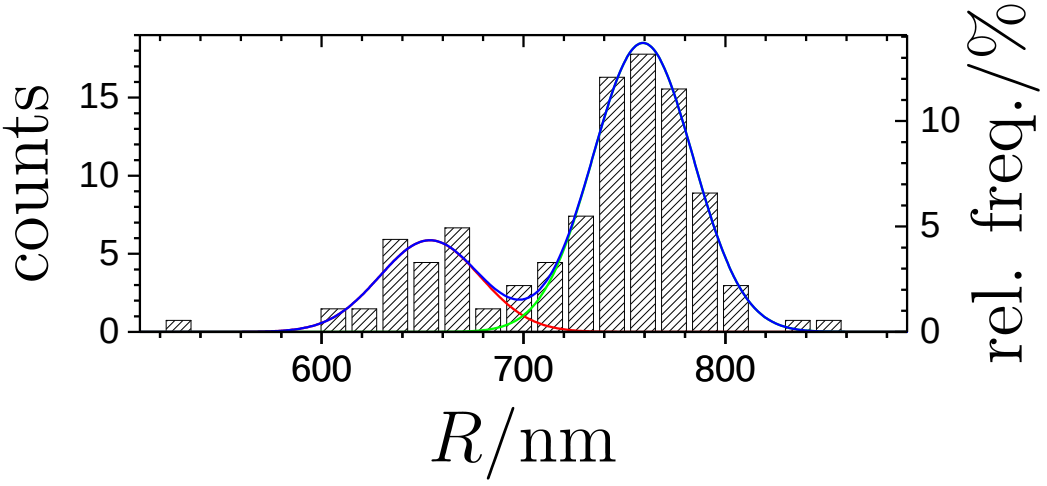

(b)

Fig. 10.2 (a) SEM image of batch B. (b) Histogram of particle radii as obtained from several SEM images.

($d = 50\,\mathrm{mm}$, $\beta = 1.16°$). All experiments are performed at $\mathrm{Pe} = \dot{\gamma}\tau_B = 0.016$, that is, at $\dot{\gamma} = 0.2\,\mathrm{s}^{-1}$ for batch A and at $\dot{\gamma} = 0.0025\,\mathrm{s}^{-1}$ for batch B. Loading and history effects are reduced by means of a rejuvenation procedure. If not stated otherwise, the following rejuvenation procedure (RJ) is executed before starting each measurement: An inverse strain sweep with amplitudes from $\gamma_0 = 150\%$ to $\gamma_0 = 1\%$ at a frequency of $\omega = 1\,\mathrm{rad/s}$, followed by a waiting time with a duration of $185\tau_B$ at zero stress.

Local velocities are determined at various heights (i.e., $0 \leq z \leq 100\,\mu\mathrm{m}$) throughout the gap. For high rates (i.e., $\dot{\gamma} = 0.2\,\mathrm{s}^{-1}$), images of 512×512 pixels, corresponding to $49{\times}49\,\mu\mathrm{m}^2$, are acquired in $\Delta t_{2\mathrm{D}} = 0.02\,\mathrm{s}$. Single data points for the velocity profiles are obtained from independent start-up tests (one for each z-height). For each height, velocities are calculated with particle tracking of tracer particles for strains between $100\% \leq \gamma \leq 900\%$ and based on image-series with more than 2000 images.

For low rates (i.e., $\dot{\gamma} = 0.0025\,\mathrm{s}^{-1}$), image stacks of 512×512×101 pixels, corresponding to $49{\times}49{\times}75\,\mu\mathrm{m}^3$, and are captured within $\Delta t_{3\mathrm{D}} = 2.0\,\mathrm{s}$. To avoid disturbances due to the scanning of large heights, we move the piezo with the same speed up and down and add a time delay. Consecutive image stacks are separated by 7.2 s and analyzed with image velocimetry. Additional image stacks of 512×512×57 pixels or $31{\times}31{\times}10\,\mu\mathrm{m}^3$ (with the intermediate magnification knob on the microscope set to 1.5x instead of 1.0x) are acquired within time periods of $\Delta t_{3\mathrm{D}} = 1.1\,\mathrm{s}$ to extract ∼2500 particle coordinates using standard routines [203] that are extended for flowing systems ([207], cf., section 6.2). Once more, we lower the piezo with a finite speed after image acquisition such that consecutive image stacks are separated by 1.8 s. These image stacks correspond to regions of the sample that are 15-25 µm away from the bottom wall. All images are collected in a radial distance of $r = 10\,\mathrm{mm}$ with respect to the center of the cone.

Single-particle dynamics are quantified by local nonaffine motions D^2_{min} (equation (7.17)) and local shear rates $\dot{\gamma}_{\mathrm{local}}$ (equation (7.20)) (cf., section 7.2). For $D^2_{\mathrm{min}} = D^2_{\mathrm{min}}(t, \delta t)$ we use a fixed time interval $\delta t = 9.0\,\mathrm{s} = 1.4\tau_B$. We also utilize mean squared displacements (MSDs), which we calculate in the moving reference frame and with respect to the vorticity direction, that is,

$$\left\langle \Delta y^2(\tau, t_w) \right\rangle = \left\langle \left(y_n(t_w + \tau) - y_n(t_w)\right)^2 \right\rangle_n , \tag{10.1}$$

where y_n is the y-position of particle n. The quantity $\langle \Delta y^2(\tau, t_w) \rangle$ is an ensemble average but it is not averaged over delay times τ. The waiting time t_w defines the elapsed time with respect to the start of the experiment and shear is applied for $t_w \geq 0$.

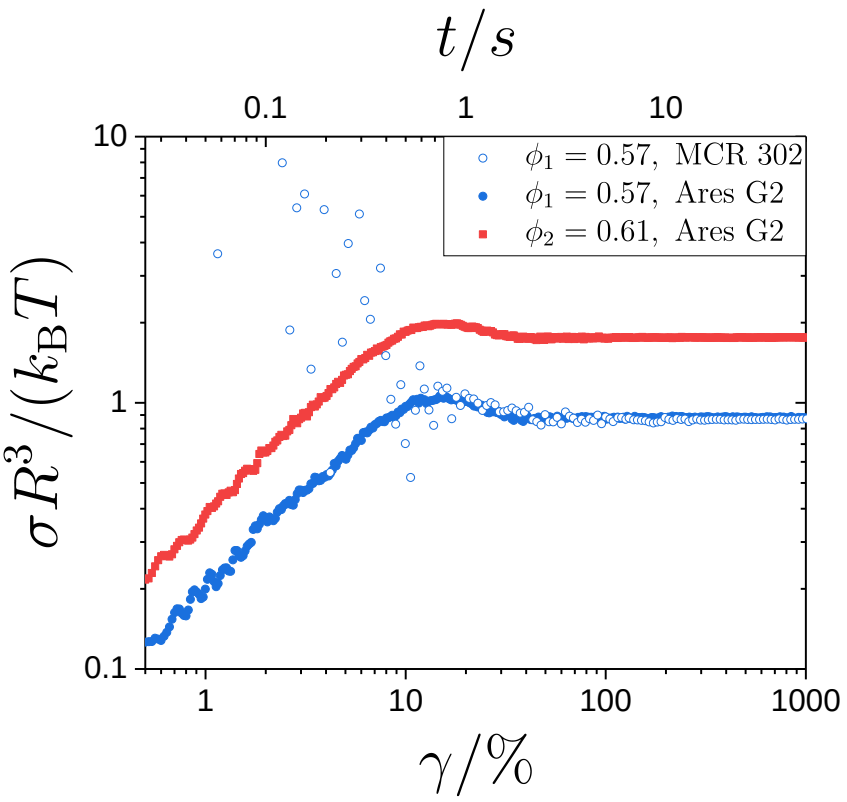

Fig. 10.3 Start-up tests ($\dot{\gamma} = 0.2\,\mathrm{s}^{-1}$ or $\mathrm{Pe} = 0.016$) of batch A at $\phi_1 = 0.57$ (open and filled blue circles) and $\phi_2 = 0.61$ (filled red squares). Measurements are performed with a stress-controlled rheometer (Anton Paar, MCR302) and a strain-controlled rheometer (TA Instruments, ARESG2) as indicated in the legend. Both rheometers are equipped with cone-plate geometries. The ARES G2 is superior in short times.

10.4 Results

This chapter is organized as follows: First, we will focus on batch A. To this end, we examine the rheological response to a start-up experiment and reveal corresponding shear profiles by means of confocal microscopy. Then we take effort to reproduce the experiments with batch B. Since batch B consists of bigger spheres – where overall dynamics are slower and particles can be tracked in three dimensions – we aim to get better insights into the single-particle dynamics. We will once more take a look at mesoscopic velocity profiles and complement them with local quantities such as nonaffine motions and mean squared displacements.

Figure 10.3 shows a typical response of batch A to a start-up experiment at Pe = 0.016. Data is collected with the strain-controlled ARES G2 as well as the stress-controlled MCR302, and the results collapse reasonably well. The only

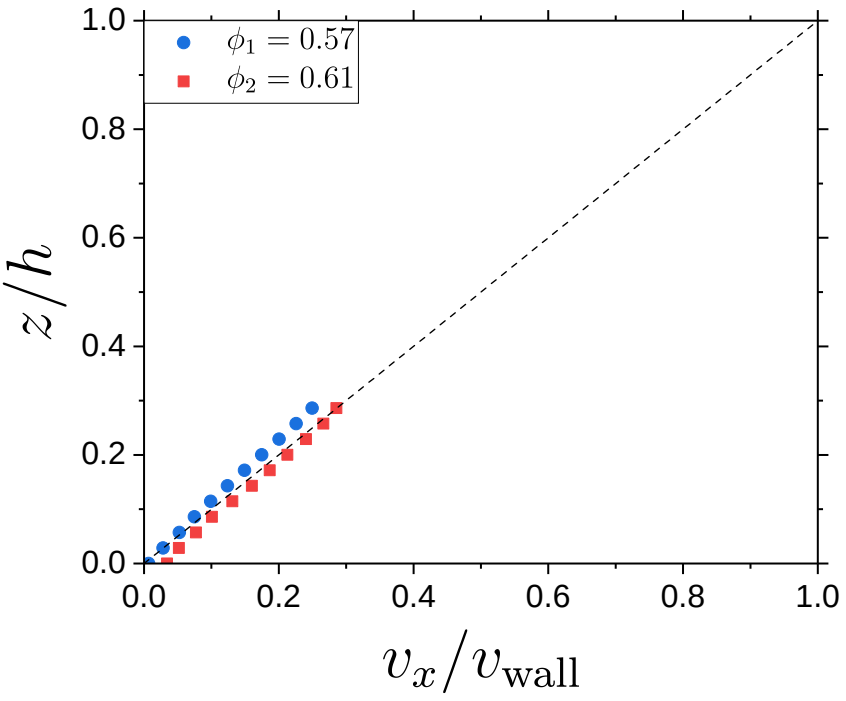

Fig. 10.4 Steady-state velocity profiles of batch A at Pe = 0.016 for $\phi_1 = 0.57$ (blue circles) and $\phi_2 = 0.61$ (red squares). The dashed line indicates an ideal Newtonian velocity profile.

striking difference is that the values at low strains are noisy in the case of the rheo-confocal setup. Recall that the Anton Paar MCR302 WESP rheometer is stress-controlled and performs strain-controlled measurements with a feedback-loop. In this specific configuration (i.e., for $\dot{\gamma} = 0.2\,\mathrm{s}^{-1}$) it takes up to one second to set up a constant shear rate, which corresponds to up to 20% strain.

Corresponding velocity profiles are shown in figure 10.4. Linear velocity profiles are found for batch A for both $\phi_1 = 0.57$ and $\phi_2 = 0.61$. The velocity profiles essentially match the ideal "Newtonian" velocity profile (i.e., $v_x = \dot{\gamma} z$, dotted black line in the figure) as expected for simple shear (cf., figure 1.6).

With batch A, dynamics are only accessible indirectly from the motion of the tracer particles. This shortcoming can be overcome by the use of bigger spheres (i.e., batch B). We try to compare batch A and batch B in the same state. In terms of scaled quantities, both batches should give the same result (cf., section 2.5.4). In the following, we characterize both batches with standard rheological tests.

Dynamic frequency sweeps are shown in figure 10.5 for batch A and batch B. The agreement is relatively good for both volume fractions (i.e., $\phi_1 = 0.57$ and $\phi_2 = 0.61$). In terms of Péclet, the overlap region is small since for the same Péclet ($\mathrm{Pe}_\omega = \omega\tau_B$) the oscillation frequencies ω differ by the factor $(R_A/R_B)^3 \approx 84$. Data

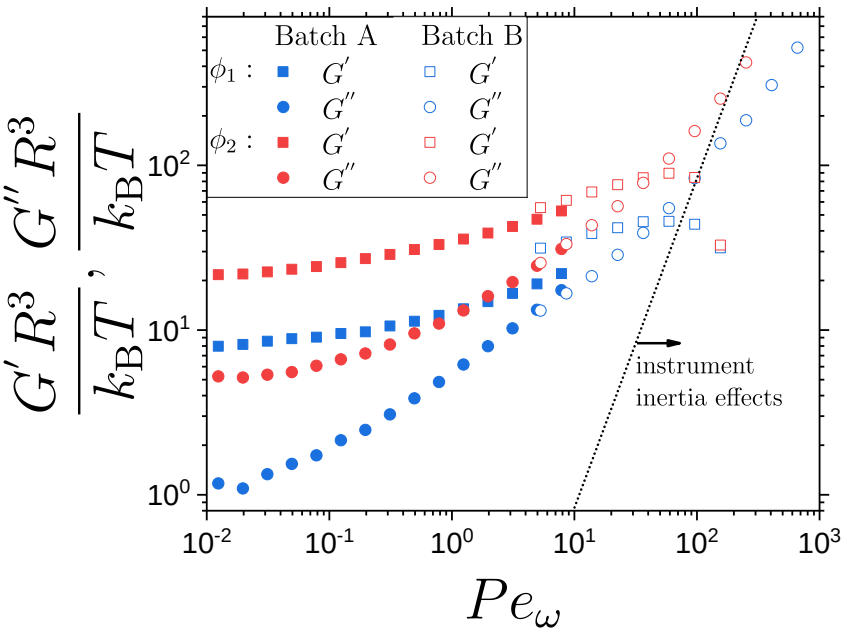

Fig. 10.5 DFS of batch A (filled symbols) and batch B (open symbols) for $\phi_1 = 0.57$ (blue) and $\phi_2 = 0.61$ (red). The dotted line refers to batch B and indicates inertia limits (equation (1.46)), with $\epsilon = 0.01$ as an additional correction factor (cf., [1, p.218]).

for both batches are available in a small region around $\mathrm{Pe}_\omega \approx 6$. There, the biggest rheological discrepancy between batch A and batch B can be seen in the scaled values of the elastic moduli G', especially at $\phi_1 = 0.57$.

Similar results are obtained from corresponding flow curves. Flow curves for botch batches are depicted in figure 10.6 and parameters of Herschel-Buckley fits are listed in table 10.2. The data of batch A shows a volume fraction dependence similar to what has been reported by Petekidis et al. for hard spheres [164] (cf., figure 2.16). For instance, at $\phi_2 = 0.61$, batch A exhibits a yield stress plateau at low rates and a sub-linear increase at higher rates. At high rates ($\mathrm{Pe} \gtrsim 1$) where only data of batch B is available, the slope of stress versus strain is higher than unity, which is indicative of shear thickening. In terms of Péclet, we have an overlap region between batch A and B over two orders of magnitude. This enables us to take a closer look at rheological similarities and differences between batch A and batch B: For the higher volume fraction (i.e., $\phi_2 = 0.61$) the agreement is very good: The scaled stress versus Péclet superimposes almost identical as expected for hard spheres. Small differences only arise for $\mathrm{Pe} \lesssim 0.02$. For the lower volume fraction (i.e., $\phi_1 = 0.57$) the picture is different: Starting from high Péclets (i.e., $Pe \gtrsim 1$), the response of batch A and batch B is still similar. But this changes dramatically at lower Péclets (i.e., $\mathrm{Pe} \lesssim 1$). As we go to smaller Péclets ($\mathrm{Pe} \lesssim 10^{-2}$), the relative difference between the (scaled) stresses of batch A and B increases up to $\sim 100\%$.

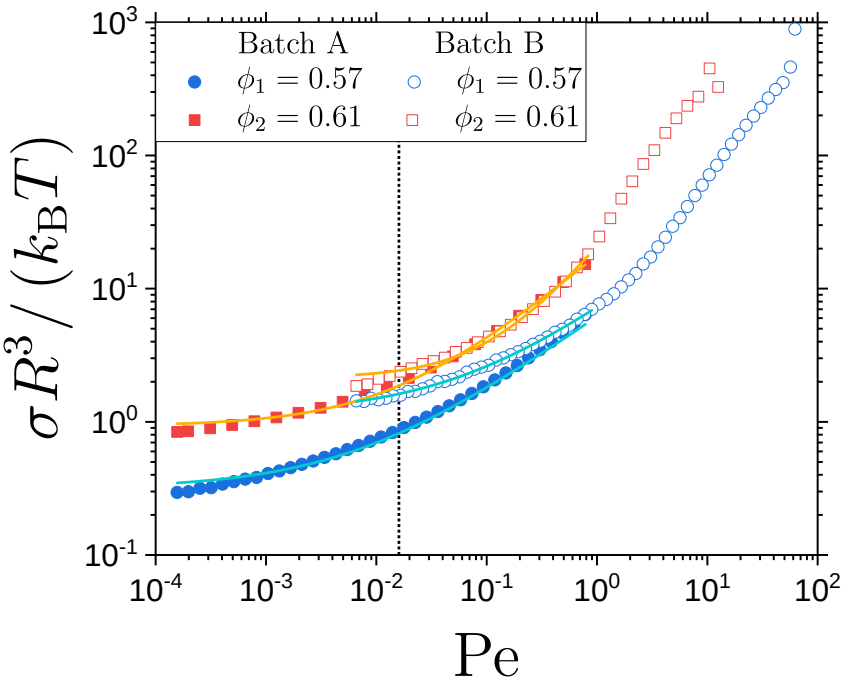

Fig. 10.6 Flow curves of batch A (filled symbols) and batch B (open symbols) for $\phi_1 = 0.57$ (blue cycles) and $\phi_2 = 0.61$) (red squares). Lines are fits to the Herschel-Buckley law. All fitting parameters are listed in table 10.2.

Batch	ϕ	$\sigma_y R^3/(k_B T)$	υ
A	0.57	0.32	0.59
A	0.61	0.93	0.70
B	0.57	1.1	0.62
B	0.61	2.1	1.0

Tab. 10.2 Parameters of Herschel-Buckley fits with $\sigma = \sigma_y + \kappa\dot{\gamma}^{\upsilon}$ for data of the flowcurves given in figure 10.6.

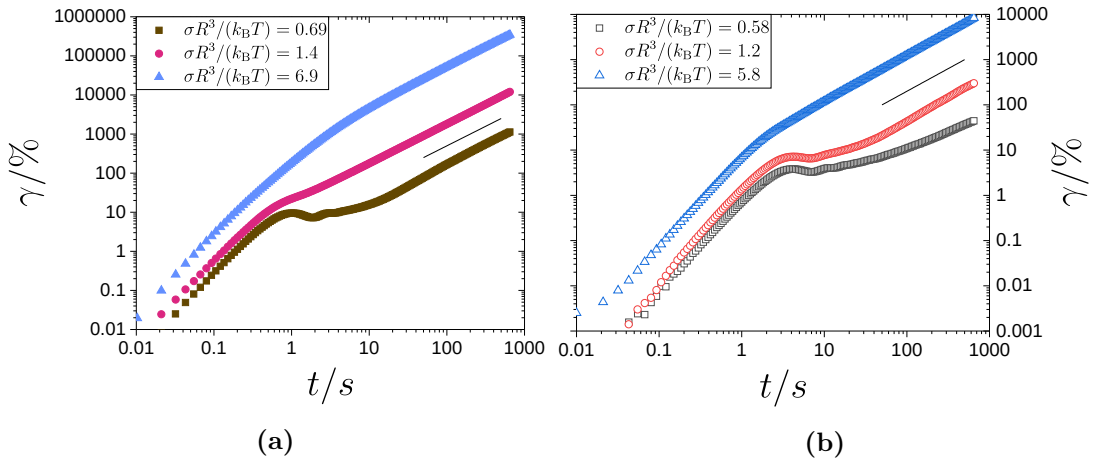

Fig. 10.7 Creep tests of (a) batch A and (b) batch B at $\phi_1 = 0.57$. Lines indicate slopes of unity.

A stress value for $\dot{\gamma} \to 0$ corresponds to the yield stress. Yield stresses are double-checked for $\phi_1 = 0.57$ by creep experiments as shown in figure 10.7. A slope of unity is reached for batch A for all investigated stresses. Batch B reaches a slope of unity only for $\sigma R^3/(k_BT) = 1.2$ and $\sigma R^3/(k_BT) = 5.8$. This is in reasonable agreement with the Herschel-Buckley fits to the flow curves.

A flow curve shows steady-state values of the stress for different Péclet numbers. We now look at a specific Péclet number and follow the transient response of the stress. In other words, the results of start-up experiments at $\mathrm{Pe} = 0.016$ are given in figure 10.8 for botch batch A and batch B. What we can learn from the start-up tests in figure 10.8 is that the steady-state values of batch B are actually fluctuating as a function of strain (or time). The measured stress $\sigma = F_\sigma M$ (cf., section 1.5.2) of bigger spheres is typically much noisier because bigger spheres produce less torque M. We emphasize that we tested different cones and plates and that the usage of smaller cones or small plates produces even noisier data.

Nevertheless, it is possible to deduce new insights from these start-up experiments: At both volume fractions, batch B shows a weaker stress overshoot with respect to batch A. Although the data of both batches does not exactly fall on top of each other, values are within the same order of magnitude and differ in the long-time regime by a factor of 1.4, in reasonable agreement with the previously shown flowcurves.

Let us now take a look at the velocity profiles of batch B. For $\phi_2 = 0.61$, a typical evolution of the velocity profiles is given in figure 10.9, for selected values of strain. Initially (i.e., at $\gamma \approx 1\%$) an almost ideal Newtonian profile is observed. With increasing strain, the velocity profile shifts to the left, that is, the velocity is smaller than expected for Newtonian flow. Above $\gamma \approx 100\%$, the system seems to reach a steady state and only small variations are observed until our maximum strain of $\gamma \approx 900\%$.

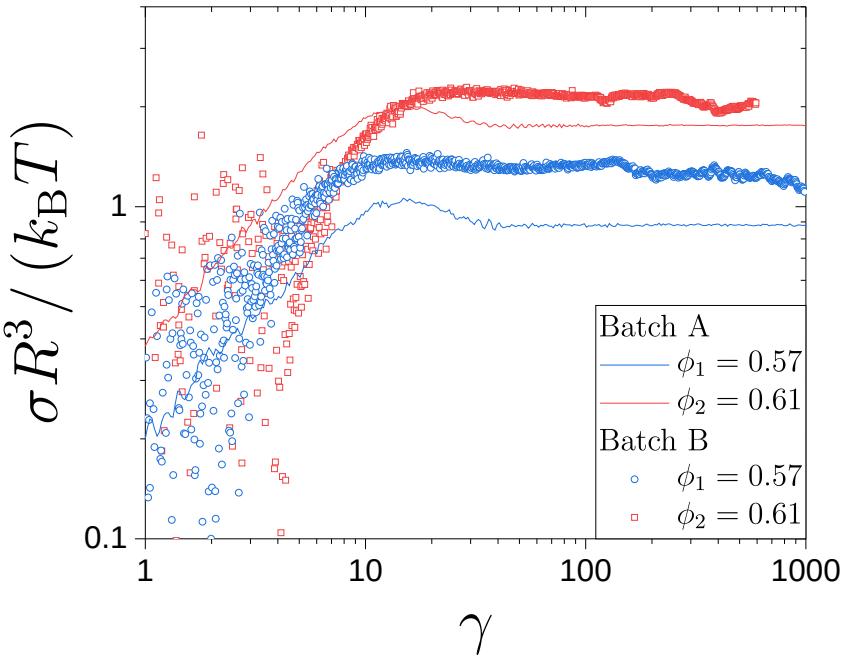

Fig. 10.8 Comparison of start-up tests of batch B (open symbols) together with previously shown start-up tests of batch A (solid lines) for $\phi_1 = 0.57$ (blue) and $\phi_2 = 0.61$ (red).

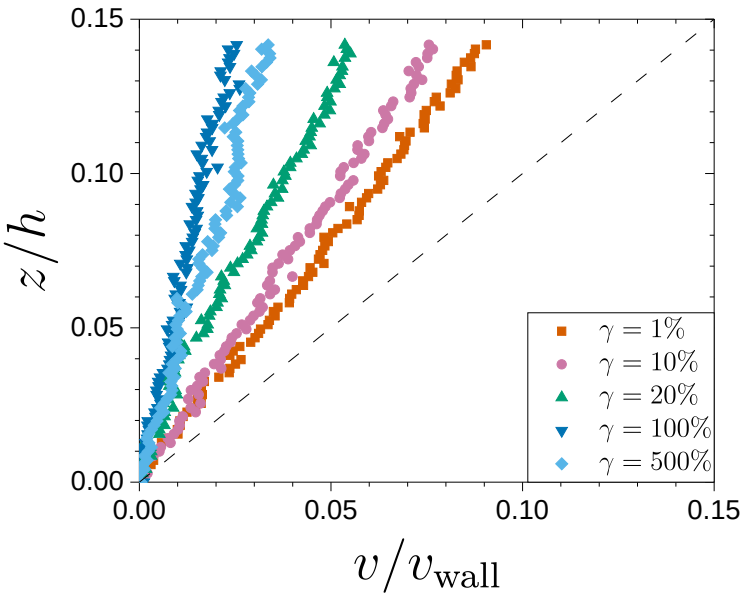

Fig. 10.9 Transient velocity profiles of batch B for $\phi_2 = 0.61$ at strains as indicated in the legend. The dashed black line corresponds to a Newtonian behavior with $v(z) = \dot{\gamma} z$, where $\dot{\gamma} = 0.0025\,\mathrm{s}^{-1}$ is the applied shear rate. The total gap height is $h = 529\,\mu\mathrm{m}$.

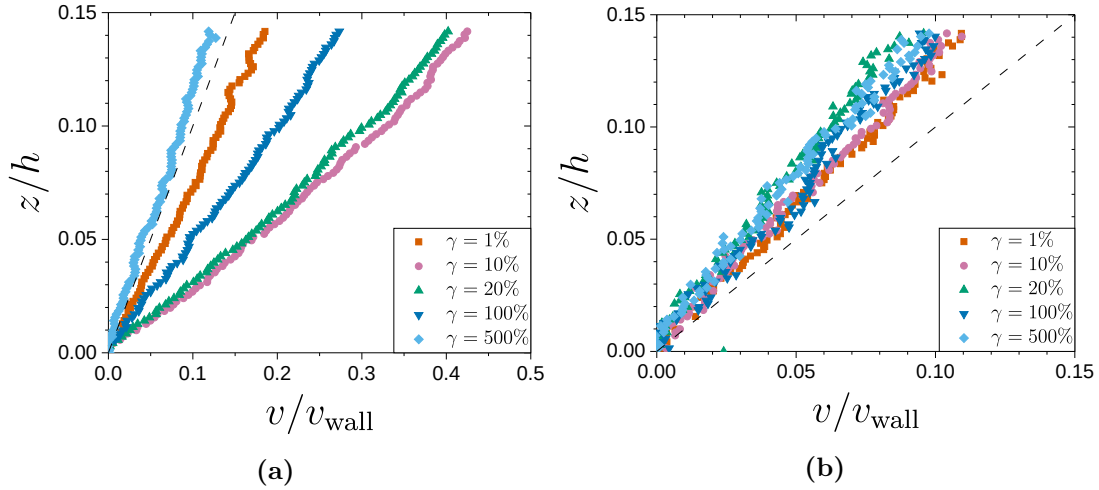

Fig. 10.10 Transient velocity profiles of batch B for $\phi_1 = 0.57$ at strains as indicated in the legend. In this case, batch B exhibits inhomogeneous flow, which depends on history. Velocity profiles in (a) will be denoted as *scenario 1* and profiles in (b) as *scenario 2* (see text). In both cases, the dotted black line corresponds to a Newtonian shear profile. Note the different scale of the x-axis in (a) and (b).

What we have to keep in mind is that we only have data from a fraction of the gap. In order to meet no-slip conditions at both boundaries (i.e., $v(z = 0) = 0$ and $v(h) = v_{\text{wall}}$) the profiles need to have a curvature or a kink at higher z. To clarify the terminology, we speak of ideal *Newtonian flow* if the condition

$$\frac{z}{h} = \frac{v(z)}{v_{\text{wall}}} \tag{10.2}$$

is true for all gap heights z. The velocity of the moving (top) wall is $v_{\text{wall}} = \dot{\gamma}h$, where $\dot{\gamma}$ is the applied shear rate and h the corresponding gap height.

Interestingly, velocity profiles in the case of $\phi_1 = 0.57$ show two different scenarios, that is, we observe *different* evolutions of the velocity profiles for the *same* externally applied shear rate ($\dot{\gamma} = 0.0025\,\text{s}^{-1}$, or Pe = 0.016). On the one hand, linear and almost time-independent profiles are observed as shown in figure 10.10b. In this case, the relation $z/h < v(z)/v_{\text{wall}}$ holds, that is, the velocity of the sample in the investigated heights is *smaller* than the velocity of a corresponding Newtonian fluid. For reasons that will become clear later on, this phenomenon will be denoted as *scenario 2*.

Performing the same experiment (i.e., a start-up with $\dot{\gamma} = 0.0025\,\text{s}^{-1}$) with literally the same sample can lead to a totally different microscopic picture, as shown in figure 10.10a. Note here that the x-axis needs to cover a much larger range to show all data points. What we observe is the following: For very small strains (i.e., $\gamma = 1\%$), the velocity profile is relatively close to an ideal Newtonian flow

i	protocol	observation
1	sample loading	
2	*RJ*	
3	start-up test	*scenario 1*
4	*RJ*	
5	start-up test	*scenario 2*

Tab. 10.3 Dependence of mesoscopic velocity profiles during start-up tests on the order of the experiments for batch B ($\phi_1 = 0.57$, Pe = 0.016). The order of the experiments is indicated by the index i. The rejuvenation protocol RJ, as well as the two types of velocity profiles (i.e., *scenario 1* and *2*), are explained in the text.

(dashed black line). A closer look reveals that the measured profile (at $\gamma = 1\%$) is to the right of the dotted black line, that is, particles locally move *faster* than expected for Newtonian flow. The difference between the measured and the ideal Newtonian velocity profile increases with increasing strain and reaches a maximum for $\gamma \approx 10 - 20\%$. Afterward (i.e., for $\gamma \gtrsim 20\%$), the velocity profile slowly "moves back to the left." For $\gamma = 100\%$, the profile is still to the right of the Newtonian line but it is not that far away anymore. At this relatively high strain, the velocity profile is still transient and changes further with increasing strain. Around $\gamma \approx 500\%$, the profile reaches its steady state that is to the left of the Newtonian line. We will refer to this second set of velocity profiles (figure 10.10a) as *scenario 1*.

Interestingly, the only difference for the set of velocity profiles that we observe for batch B and $\phi_1 = 0.57$ (i.e., *scenario 1* and *scenario 2*) is the order of the experiments. For instance, if we load the sample, apply our rejuvenation procedure (RJ) and then the start-up experiment, we observe *scenario 1*. If afterward we repeat the rejuvenation (RJ) and perform a second start-up, we find *scenario 2*. These findings are summarized in table 10.3.

While we speak about the velocity profiles, we have seen velocity profiles only for a small fraction within the gap so far (i.e., $z/h \lesssim 0.15$). To get an impression of what is happening in the whole gap we show a preliminary velocity profile of batch B at $\phi_1 = 0.57$ as obtained with another cone-plate geometry[1] in figure 10.11. Here, we clearly see that the profile has an s-shape at certain values of strain. Furthermore, wall slip seems to be absent both at the top and bottom.

Hence, determining a velocity profile once and assuming this velocity profile for further experiments appears risky. On the other hand, if we always need to

[1] To obtain a smaller gap height, a different cone ($d = 40\,\text{mm}$, $\beta = 0.97°$) is used and this cone is furthermore lowered below its correct measuring position by 32 µm. We measure velocity profiles between absolute heights of $z = 15 - 115\,\mu\text{m}$ by using the maximum range of the piezo (100 µm) and an additional offset with respect to the bottom plate by turning the focus knob on the microscope.

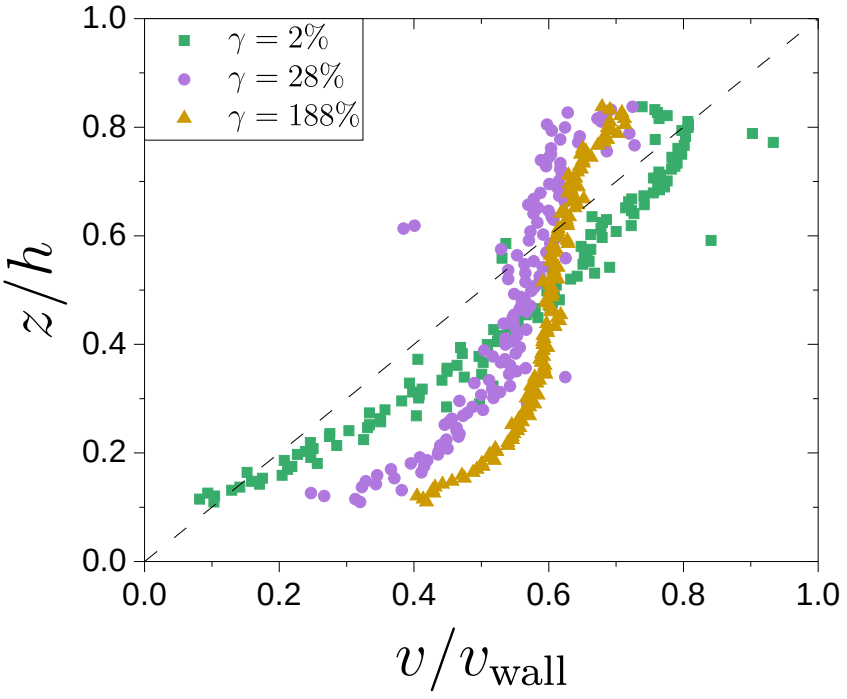

Fig. 10.11 Velocity profiles of batch B at $\phi_1 = 0.57$, measured with a smaller gap height ($h = 137\,\mu\text{m}$). At intermediate and higher strains, the profile is s-shaped.

determine a velocity profile, we cannot easily investigate single-particle motions in detail. The solution is to measure dynamics within a small volume and to deduce velocity profiles from properties within that small z-region. Figure 10.12 illustrates the principle: Three relatively "simple" velocity profiles are drawn in red, blue and black. The black line corresponds to the ideal Newtonian velocity profile and the red and blue curves represent, for instance, *scenarios 1* and *2*. The boundary conditions at $z = 0$ and $z = h$ are fixed by the no-slip condition. A third point within the gap (e.g., P1, P2 or P3) helps to shed light on the shape of the velocity profile. Note that not only the velocity $v(z)$ is known at these points but also the local shear rate. In a z-v-representation, the shear rate corresponds to the inverse slope. If we assume "simple" profiles, we can thus deduce the overall profile from local measures. In the following, we will quantify the deviation of the measured velocity profiles from Newtonian flow by the two normalized quantities

$$v_{\text{norm}} = v_{\text{norm}}(z) = \frac{v(z)}{\dot{\gamma} z} \tag{10.3}$$

and

$$\dot{\gamma}_{\text{norm}} = \dot{\gamma}_{\text{norm}}(z) = \frac{\dot{\gamma}(z)}{\dot{\gamma}}\,, \tag{10.4}$$

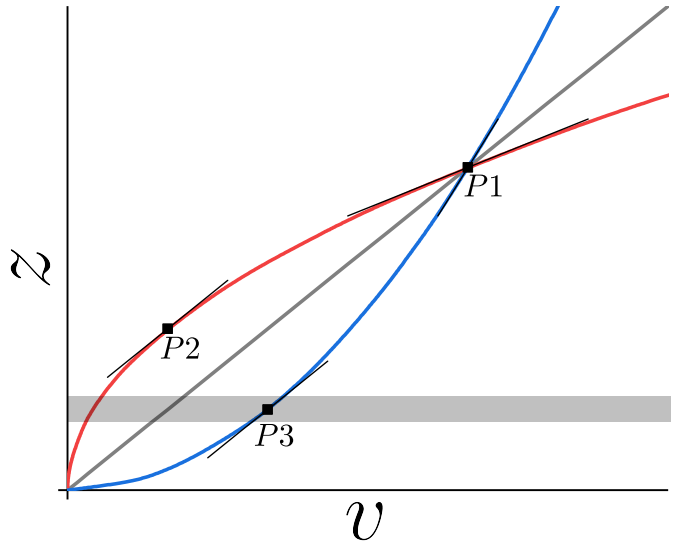

Fig. 10.12 Schematic shear profiles with different curvatures. At point $P1$ all velocities are identical whereas points $P2$ and $P3$ have identical shear rates. Local velocities and shear rates can be inferred from a time-series of 3D-stacks captured in a small volume (semi-transparent gray box).

where $v(z)$ and $\dot{\gamma}(z)$ are local measures at height z, and $\dot{\gamma}$ is the applied (macroscopic) shear rate.

We can now take a step forward and look at single-particle dynamics that are obtained by scanning a small 3D volume. Figure 10.13 depicts single-particle dynamics inside the 3D volume through the calculation of local properties, such as ensemble-averaged local velocities (c,d), ensemble-averaged local shear rates (e,f), and ensemble-averaged nonaffine motions $\langle D^2_{\text{min}} \rangle$ (g,h). In (a) and (b) of the same figure, we see two corresponding start-up experiments that are measured simultaneously. Interestingly, the macroscopic response of the start-up tests is similar but the microscopic dynamics are not that similar.

Let us first examine figure 10.13c,e,g, that is, *scenario 1*: For $\gamma \lesssim 6\%$, particles first follow the applied shear (i.e., $\langle v_{\text{norm}} \rangle \approx 1$ & $\langle \dot{\gamma}_{\text{norm}} \rangle \approx 1$). As the strain is increased further, the local ensemble-averaged velocity $\langle v_{\text{norm}} \rangle$ reaches a maximum at the peak of the stress overshoot ($\gamma \approx 20\%$) where the velocity is more than 3 times higher than expected for a linear velocity profile (figure 10.13c). By further increasing the strain, the local velocity decreases and subsequently becomes smaller than expected (i.e., $\langle v_{\text{norm}} \rangle < 1$). A similar trend is observed for $\langle \dot{\gamma}_{\text{norm}} \rangle$, which reaches almost a value of 3 at the peak of the stress overshoot and subsequently decreases with increasing strain (figure 10.13e). The trend of $\langle v_{\text{norm}} \rangle$ and $\langle \dot{\gamma}_{\text{norm}} \rangle$ is also depicted in the calculation of the ensemble averaged nonaffine displacement $\langle D^2_{\text{min}} \rangle$ (figure 10.13g). For $\gamma \lesssim 6\%$, the nonaffine displacements gradually increase.

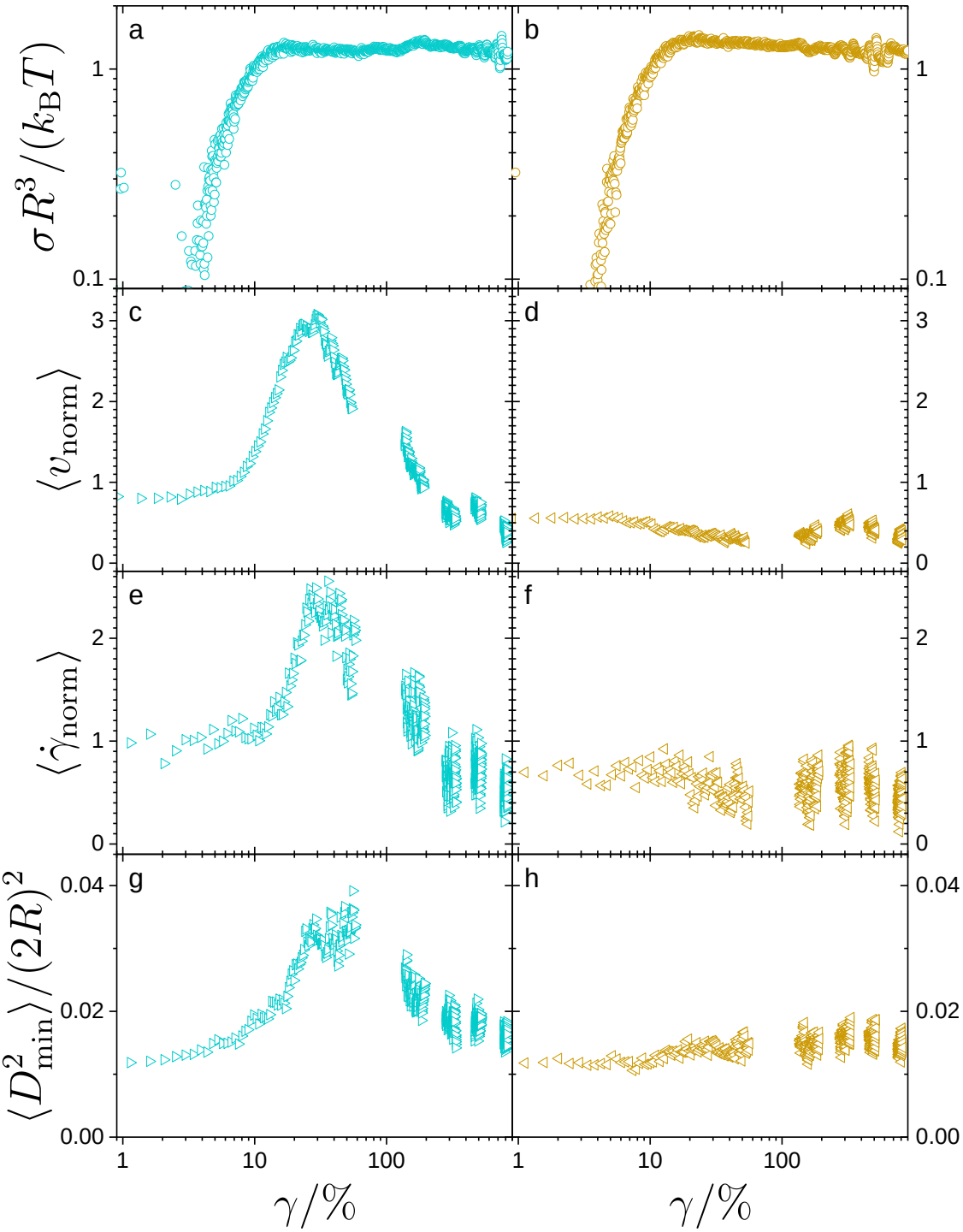

Fig. 10.13 Macroscopic rheological response together with local dynamical quantities of batch B at $\phi_1 = 0.57$. (a,b) Macroscopic stress response of a start-up experiment at $\dot{\gamma} = 0.0025\,\mathrm{s}^{-1}$. (c-h) Local quantities for *scenario 1* (left column) and *scenario 2* (right column). Further details in the text.

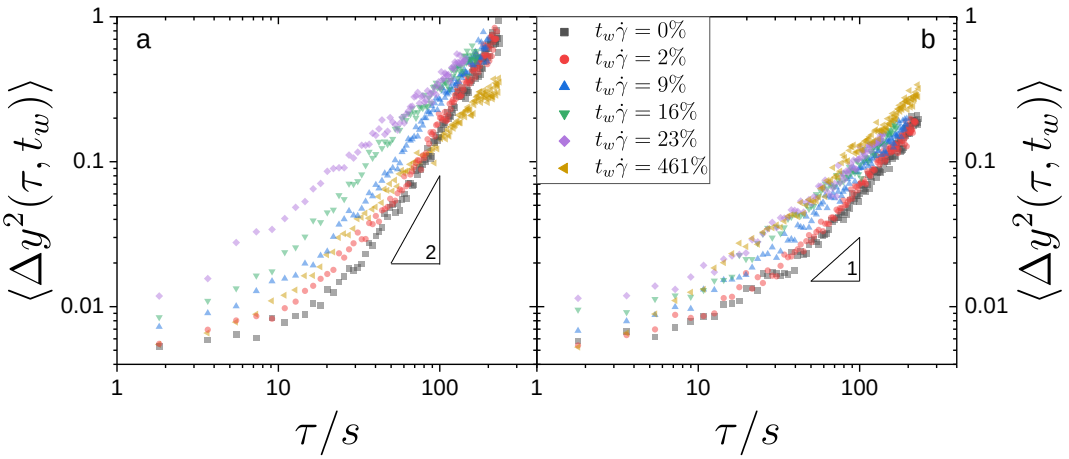

Fig. 10.14 MSDs of batch B at $\phi_1 = 0.57$ and Pe $= 0.016$ that correspond to (a) *scenario 1* and (b) *scenario 2*.

Afterward, they sharply increase to a maximum at $\gamma \approx 30\%$. Later on, $\langle D^2_{\text{min}} \rangle$ slowly decreases to its initial value.

Next, we step over to *scenario 2*: The averaged normalized velocity within the small 3D volume is always less than unity (figure 10.13d), which means that particles move slower than expected for Newtonian flow. At small strains, the ensemble-averaged velocity has a value of $\langle v_{\text{norm}} \rangle = 0.5 - 0.6$. It then decreases to about $\langle v_{\text{norm}} \rangle = 0.3$ at 100% strain and stays between 0.2 and 0.7 for larger strains. Similarly, the normalized shear rate (figure 10.13f) starts around $\langle \dot{\gamma}_{\text{norm}} \rangle = 0.7$, decreases down to $\langle \dot{\gamma}_{\text{norm}} \rangle = 0.2$ at intermediate strains, and fluctuates later on. Within the measured strain interval (i.e., $1 \leq \gamma \leq 900\%$), the normalized shear rate is always less than unity. In this *scenario 2*, the averaged nonaffine motion experiences small modulations between $\langle D^2_{\text{min}}/(2R)^2 \rangle = 0.01 - 0.02$. The values are relatively constant in the rheological linear regime, that is, for $\gamma \lesssim 12\%$. A tiny increase might be present in the vicinity of the stress overshoot ($\gamma \approx 20\%$), and larger fluctuations are observed above 50% strain.

If we would only knew *scenario 1* or figure 10.13a and (g), we could conclude that particles exhibit strong nonaffine motions close to the stress overshoot [263]. By comparing all data from figure 10.13, we might need to revise this picture and attribute (most of) the trend of $\langle D^2_{\text{min}} \rangle$ to the transient behavior of $\langle v_{\text{norm}} \rangle$ and $\langle \dot{\gamma}_{\text{norm}} \rangle$, that is, to the transient nonlinear velocity profiles.

Before we discuss possible explanations for the emergence of nonlinear velocity profiles, we end the current section with results of mean squared displacements (MSDs). Figure 10.14 shows MSDs in the vorticity direction for $\phi_1 = 0.57$ during start-up shear. Both MSDs belong to the same repeated experiments as the results that were shown in figure 10.13. Waiting times t_w are multiplied with the applied shear rate $\dot{\gamma} = 0.0025\text{s}^{-1}$ to obtain units of strain. These strain units can be directly

compared with figure 10.13a and b.

The MSDs in figure 10.14a belong to *scenario 1*. At $t_w\dot{\gamma} = 0\%$ (black squares), the MSD shows an initial sub-diffusive plateau. The initial sub-diffusive plateau vanishes for $t_w\dot{\gamma} \gtrsim 5\%$ and is followed by a super-diffusive behavior (with a slope close to two). Above $t_w\dot{\gamma} \approx 16\%$, the super-diffusive regime starts to disappear and the MSDs eventually become diffusive. For $t_w\dot{\gamma} = 23\%$ and $t_w\dot{\gamma} = 461\%$, the MSDs are essentially diffusive (slope 1) with the only difference that the absolute displacements are smaller at larger $t_w\dot{\gamma}$. The super-diffusive behavior found with batch B at $\phi_1 = 0.57$ occurs at intermediate strains close to the stress overshoot where also v_{norm} and $\dot{\gamma}_{\mathrm{norm}}$ have their maximum values (cf., figure 10.13).

We now turn to the MSDs in figure 10.14b that correspond to *scenario 2*: Independent of $t_w\dot{\gamma}$, all MSDs show a sub-diffusive behavior at small lag times τ (with a slope less than unity), followed by a diffusive behavior (slope 1). Despite the fact that there are some quantitative differences between the individual MSDs, all of them show essentially the same qualitative trend.

Last but not least we turn back to the case of $\phi_2 = 0.61$. For this larger volume fraction, we always observe *scenario 2* and thus all local quantities (i.e., $\langle v_{\mathrm{norm}}\rangle$, $\langle\dot{\gamma}_{\mathrm{norm}}\rangle$, $\langle D^2_{\mathrm{min}}\rangle$, $\langle\Delta y\rangle$) behave qualitatively like figure 10.13 (d,f,h) and figure 10.14b, respectively (not shown here).

10.5 Discussion

Different results are obtained for the two investigated batches. For batch A, the velocity profile is linear for all times investigated as has also been reported before in an experimental study of PMMA-spheres of similar size [186] (cf., figure 2.21).

In the case of batch B, different kinds of transient and nonlinear velocity profiles are observed. On the one hand, we find transient s-shaped velocity profiles (*scenario 1*) that have previously been observed, for instance, in colloidal glasses [186] and granular media [332]. On the other hand, we observe profiles where particles experience a shear rate that is lower than the applied one (*scenario 2*). Our *scenario 2* is typical for a system that exhibits shear banding (cf., figure 2.20). As with different trends of mesoscopic velocity profiles, we also observe different qualitative trends in local dynamical quantities. Is there a link between mesoscopic shear profiles and local particle dynamics?

Mean squared displacements are sensitive to the shear rate as observed, for example, by Chen et al. [245]. Higher shear rates $\dot{\gamma}$ lead to larger displacements Δy. Previous works report the relation $\tau^* \propto \dot{\gamma}^{-u}$, where τ^* is a diffusion time scale and the exponent is $u = 0.8$ [182] or $u = 1$ [245]. If we argue that the inverse diffusion time scale is proportional to the diffusion coefficient D then we can write $D \propto \dot{\gamma}^u$. Thus, a larger (local) shear rate should lead to larger (local) diffusion coefficients and hence to larger (local) displacements. If the (local) shear rate is increasing

with time then consequently super-diffusive behavior might be observed. Thus, it seems likely that the observed super-diffusion in our experiments is related to the strong increase of the local shear rate that is present in our *scenario 1* but absent in *scenario 2*.

To this end we have to distinguish at least three phenomena:

- Why is there a difference between batch A and batch B?

And, in the case of Batch B:

- Why is the steady-state behavior nonlinear?
- Why are there different transient pathways to the final state?

Possible explanations can be related to the yield stress, various kinds of inhomogeneities, aging and history dependence, as well as size effects. We will discuss them in the following.

The perhaps most obvious difference between batch A and batch B is their particle size. Colloids of different sizes exposed to the same (rescaled) shear should give the same (rescaled) results (cf., section 2.5.4). Uncertainties of absolute particle sizes can lead to uncertainties of rescaled physical quantities. We cannot rule out this argument completely. Nevertheless, it seems unlikely that the very different behavior between batch A and batch B can be explained by small differences in Péclet and volume fraction. For instance, the flow curves of batch A and B differ not only quantitatively as expected for different ϕ (cf., section 2.5.4) but they have qualitatively different shapes as seen in figure 10.6.

Related to the size difference of the two batches is a different absolute rheological signal since bigger spheres produce less torque. We used customized big tools (i.e., $d = 40.1\,\mathrm{mm}$, $\beta = 3.03°$) in order to increase the sample volume below the transducer. The total sample volume of batch A and B in the cone-plate geometries contains about $3 \cdot 10^{12}$ and $2 \cdot 10^{11}$ particles, respectively. If we only consider the number of particles along the z-direction then we end up with "only" 980 and 340 particles, respectively. Thus, there are fewer bigger particles (batch B) within the gap than smaller ones (batch A), even though we use one of the biggest available cones for batch B. Higher gap heights can be achieved with plate-plate geometries: A preliminary measurement with a large gap (i.e., $h = 1\,\mathrm{mm} \approx 640 R_B$) reveals an approximately Newtonian velocity profile for batch B (!). This could be related to wave propagation that is important in oscillatory measurements and depends on the gap height [333]. We also briefly studied particles of intermediate sizes and believe that future experiments could continue along these lines to systematically study the gap height and particle size dependence.

Another experimental detail may be of importance. Before each start-up test, we run our rejuvenation procedure where both batch A and batch B are subjected to the same dynamic strain sweep (i.e., the same oscillation frequency). Thus, samples

	ζ ($\phi = 0.57$)	ζ ($\phi = 0.61$)
Batch A	1.7	0.89
Batch B	0.16	0.011

Tab. 10.4 Distance from the yield stress as quantified with equation (10.5).

containing the larger spheres are relatively speaking prepared faster. This leads us to aging phenomena and history dependence of colloidal suspensions under shear: For samples beyond the glass transition, aging phenomena affect the sample's rheological properties [334–337]. For instance, the stress overshoot depends on age [338] and quenching speed [339]. Rogers et al. find that a previously fluidized system exhibits a metastable linear velocity profile while an aged sample shows the coexistence of a fluid and a solid band [331]. Indeed, if we add a flowcurve to our rejuvenation procedure, we *always* observe *scenario 1* for batch B and $\phi_1 = 0.57$. However, batch A always shows essentially Newtonian velocity profiles, independent of the rejuvenation procedure.

Colloidal glasses belong to the group of yield stress materials, which only flow above the yield stress σ_y. This suggests that nonlinear velocity profiles with regions of higher and regions of lower (local) shear rates might be related to yield stress phenomena. To quantify this a little bit further, we define

$$\zeta = \frac{\sigma_s - \sigma_y}{\sigma_y}\,, \tag{10.5}$$

where σ_s is the steady-state stress and σ_y the yield stress of the system. We take steady-state values from the start-up experiments (cf., figure 10.8) and estimate yield stresses with Herschel-Bulkley-fits of the flowcurve (cf., table 10.2). Corresponding values of ζ are given in table 10.4. We see that batch B is very close to the yield stress, especially for $\phi_1 = 0.57$. This is another possible explanation for the observed transient velocity profiles. What remains unclear is why batch B is in a state that is much closer to its yield stress than batch A.

We can only speculate that interactions such as attractive or repulsive forces or frictional/non-frictional contacts between particles might be of relevance. For instance, frictional contacts are found to be relevant for shear thickening, which in turn has an impact on flow properties, as shown in theoretical work [162]. Inhomogeneous flow below the static yield stress is also observed in simulations [187], and the softness of the interaction potential is thought to play a role. Shear localization below a critical shear rate is observed by another simulation [340] and leads, for a given shear rate, to higher shear stresses than homogeneous flow. In an experimental system that is very similar to our model system (i.e., PMMA-particles with $R = 850\,\mathrm{nm}$, cone-plate geometry), shear banding has been seen for small rates, that is, for $\dot{\gamma} < 0.01\,\mathrm{s}^{-1}$ [182]. Preliminary results with batch B at $\phi_1 = 0.57$

indicate inhomogeneous flow even for $\dot{\gamma} = 0.1\,\mathrm{s}^{-1}$. Unfortunately, local velocities at still higher shear rates are experimentally not accessible to us.

We may turn back to the question: "What is the reason for inhomogeneous flow for the given volume fractions and Péclet numbers?" A solution could also be that not only the velocities and shear rates have local inhomogeneities but also other quantities such as the volume fraction. Indeed, local changes in the volume fraction have been related to changes in the shear profiles [177, 341–344]. We do have some indications for density fluctuations within the gap but a conclusive answer to this effect needs further investigations, especially since particle sizes and thus local volume fractions are difficult to determine experimentally [64].

10.6 Conclusion

We have studied colloidal suspensions close to the glass transition under start-up shear. Two different batches with different particle sizes show different types of velocity profiles even though they are sheared at the same Péclet number. The batch of smaller spheres shows linear Newtonian velocity profiles for all volume fractions investigated, while the batch of bigger spheres exhibits transient and highly nonlinear flow that depends, among others, on volume fraction and history.

Transient nonlinear shear profiles seem to be coupled to local properties. In what we call *scenario 1*, particles (locally) move faster and are strained more with respect to an ideal Newtonian velocity profile. This is reflected in increasing nonaffine motions and super-diffusive mean squared displacements. Correspondingly, in what we call *scenario 2*, particles are (locally) moving slower and strained less than expected. Resulting nonaffine motions barely change with time and the MSDs show essentially diffusive behavior in the whole time (or strain) window.

Consequently, the comparison of differently sized spheres, as well as the extrapolation of local quantities to macroscopic variables, has to be treated with caution if the corresponding velocity profiles are unknown.

Acknowledgments

Thanks to A. B. Schofield, M. A. Escobedo Sánchez and J. P. Segovia Gutiérrez for the particles, the Center for Advanced Imaging (CAi) for the SEM image, and J. K. Dhont and J. Horbach for helpful discussions.

11

Preliminary Experiments: Episode XI: A New Hope

Preliminary experiments in this chapter are meant to provide an impression of further experiments that are related to soft systems under external load. Three small example projects will be presented: First, section 11.1 will deal with the ordering of PMMA-spheres under oscillatory and steady shear. This is reasonably close to one of the previous experimental chapters where we studied the shear-induced crystallization of binary mixtures (e.g., chapter 8). Then, in section 11.2, PMMA-particles will be subjected to another type of external load: indentation. Finally, in section 11.3, we will switch from colloidal spheres to gels and examine them with the rheo-confocal setup under start-up shear. There, we will see that the methods of this work can be readily applied to other systems.

11.1 Shear-Induced Ordering and Melting

11.1.1 Introduction

Shear can induce order, as we have seen in chapter 8. Ordering under oscillatory shear has also been studied extensively in previous work [228, 282, 285, 287, 290, 291]. We may recall that oscillation frequencies and strain amplitudes of the order one were found suitable to induce order [282, 286]. Experiments on two-dimensional colloidal polycrystals with intermediate volume fraction also demonstrate that small oscillatory strains lead to large defect-free crystals [257].

Experiments usually make use of shear cells [228, 239, 282, 290–292, 313]. Local ordering is then quantified by microscopy [239, 289], or scattering techniques [282, 286, 290–292]. The orientation of the crystals depends on the details of shear [228, 345, 346]. Often, rheology is performed separately and then compared to the microscopic results [289, 291, 292, 313]. Gap heights, geometries, sample volumes, and other parameters typically differ in shear cells and rheometers. Linking (macroscopic) flow properties to structural ordering is ideally done in a combined setup.

A few studies have combined rheology with simultaneous light scattering using optically transparent geometries [337, 347]. They revealed a drop of elastic and viscous moduli due to shear-induced crystallization [337], as well as a structure-dependent viscosity [347].

Here, the rheo-confocal setup will be used to provide simultaneous rheological and microscopic signatures of shear-induced structural changes under oscillatory and steady shear.

11.1.2 Materials and Methods

The sample under study is a colloidal suspension of PMMA-spheres ($R \approx 750\,\mathrm{nm}$, $\delta \approx 5\%$) suspended in *cis*-decahydronaphthalene, known to be a hard-sphere model system [240].

The PMMA-spheres are synthesized by M. A. Escobedo Sánchez and J. P. Segovia Gutiérrez and labeled with rhodamine B. The volume fraction is set by sedimentation of the sample to a random close packing (assumed to be $\phi_{\mathrm{rcp}} = 0.655$), followed by a subsequent dilution to $\phi \approx 0.56$, as verified with a Voronoi tessellation (cf., section 7.4) of particle coordinates.

Measurements are performed with the rheo-confocal setup (cf., section 4.2). It combines a stress-controlled rotational rheometer (Anton Paar, MCR 301 WESP) with an inverted microscope (Nikon Ti-U) that is connected to a confocal scan head (Visitech, VTEye). The sample is illuminated with a $\lambda = 488\,\mathrm{nm}$ laser and imaged through an oil-immersion objective (Nikon, Plan Apo VC, NA = 1.40, 100x). The rheometer is equipped with cone and plate geometry. The cone (Anton Paar, CP25/2-S, SN36375) is sandblasted and has a diameter of $d = 24.9826\,\mathrm{mm}$ and

a cone angle of $\beta = 2.001°$. A serrated glass coverslip (original thickness: #1.5, diameter: $d = 50\,\text{mm}$) acts as the bottom plate. The glass slide is supported by a stainless steel plate.

Two main tests are conducted: A dynamic strain sweep (DSS) with strain amplitudes from $\gamma_0 = 200\%$ to $\gamma_0 = 1\%$ at a frequency of $\omega = 1\,\text{rad/s}$, and a start-up test with a shear rate of $\dot{\gamma} = 10\,\text{s}^{-1}$. This corresponds to Péclet numbers of $\text{Pe}_\omega = 5$ and $\text{Pe} = 50$, respectively (cf., equation (2.23) and equation (2.22)). The sequence of tests is given in table 11.1 and lasts about two hours altogether.

Confocal image acquisition is triggered electronically at the start of each test. Under shear, two-dimensional time-series are recorded at heights of $z_1 = 7.7\,\mu\text{m}$ or $z_2 = 10\,\mu\text{m}$ above the bottom plate. The frame rate for the 2D series is one frame per second. Three-dimensional z-stacks are recorded under quiescent conditions with 51 frames per second from 7.7 µm to 22.7 µm, with a z-step of 0.15 µm. Individual images contain 512×512 pixels corresponding to $47.4\,\mu\text{m} \times 48.7\,\mu\text{m}$.

Particle tracking is done using standard routines [203]. Local order parameters $\overline{q}_6$ (cf., equation (7.23) or [266]) are calculated on a single-particle level. To this end, neighbors are defined with a cutoff-distance. The cutoff-distance is taken from the position of the first minimum of the pair correlation function. The ensemble-averaged quantity $\langle \overline{q}_6 \rangle$ serves as a measure for the overall degree of ordering. Particles close to the edges of the field of view are disregarded.

11.1.3 Results

Visual inspection of the sample during the measurements indicates that the sample changes its microscopic structure depending on the applied shear. Upon loading, the sample is amorphous. Order is then induced during oscillatory shear, especially at small strain amplitudes. An amorphous structure is recovered, for example, at large strains during a start-up test. In either case, the shear-induced structures persist after cessation of shear – at least within the experimental time window. Qualitative results from the full sequence of tests are given in table 11.1.

A few tests will now be analyzed quantitatively. First, we will take a closer look at shear-induced ordering during oscillatory shear (i.e., tests #3, #7, #9 of table 11.1). As a second step, we will have a brief look at shear-induced melting under steady shear (i.e., test #11).

11.1.3.1 Dynamic Strain Sweeps

The rheological results of the three executed dynamic strain sweeps are shown in figure 11.1. The strain sweeps are performed from large to small strain amplitudes. At any strain amplitude, the storage moduli G' are smaller than the loss moduli G'', indicating a liquid-like sample. The trends of the moduli differ from the typical response of colloidal glasses (cf., figure 2.18a). Furthermore, the moduli are largest

test	action	observation by eye
#1	sample loading	
#2	no action	amorphous sample
#3	DSS	crystallization under shear
#4	no action	mainly crystalline sample with some fluid zones
#5	manual shearing	melting of crystalline zones
#6	no action	amorphous sample
#7	DSS	crystallization under shear
#8	no action	mainly crystalline sample with some fluid zones
#9	DSS	amorphous at high, crystalline at low strains
#10	no action	mainly crystalline sample with some fluid zones
#11	start-up	melting of crystalline zones
#12	no action	amorphous sample

Tab. 11.1 Tabular list of executed tests together with qualitative observations from confocal microscopy. The first column specifies the running sequence, the second column describes what has been done and the third column provides a short observation note. Actions include a dynamic strain sweep (DSS) and a start-up test as described in the materials and methods. During "manual shearing," the cone is rotated by hand. The item "no action" means that no shear is applied and that the sample is left undisturbed.

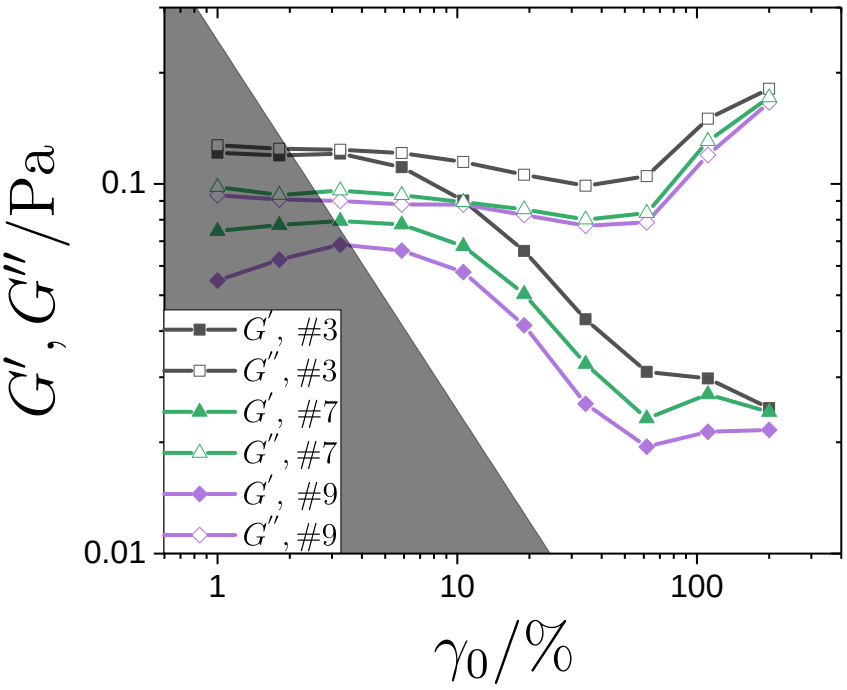

Fig. 11.1 Comparison of three DSSs, measured from large to small strain amplitudes. The numbers in the legend refer to the test sequence as introduced in table 11.1. Tests with lower numbers are executed before tests with higher numbers. The gray area indicates a region of low torque according to equation (1.43).

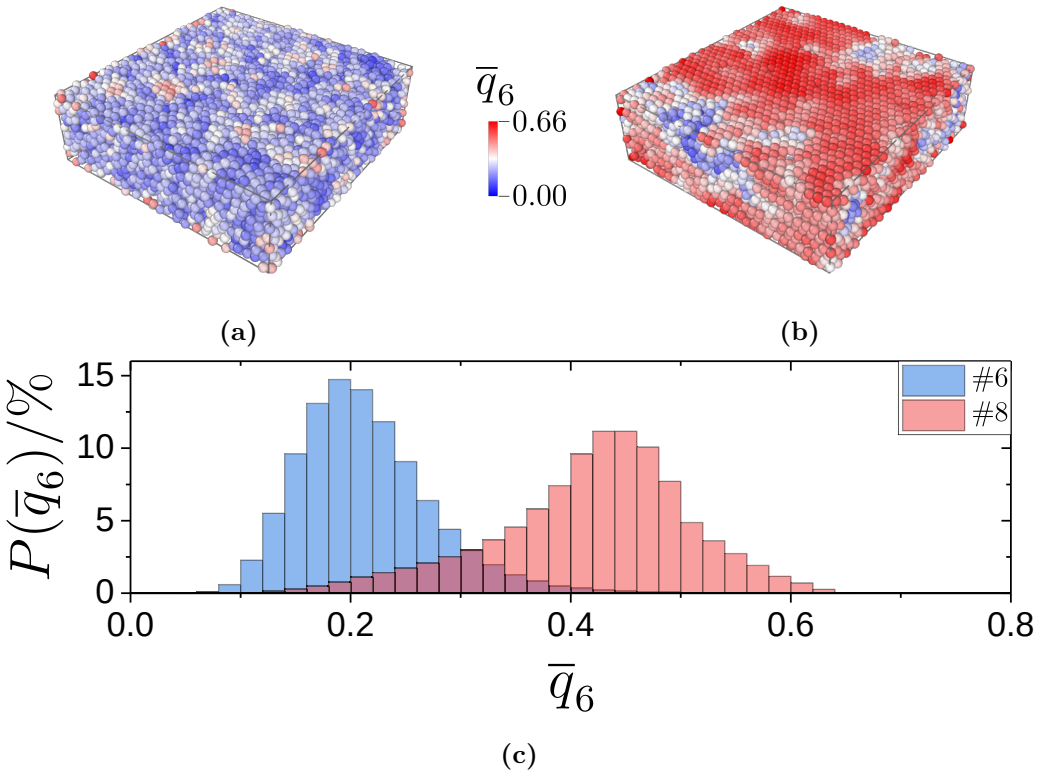

Fig. 11.2 (a,b) Renderings of particle positions showing the state of the sample before and after the DSS (test #7), that is, during test #6 (top left) and #8 (top right). The color coding of the $\overline{q}_6$-values goes from 0 (blue) via 0.33 (white) to 0.66 (red). (c) Histograms of corresponding $\overline{q}_6$-values for test #6 and #8, as indicated in the legend.

for test #3 and smallest for test #9, revealing a history dependence. Experimental limits are reached at small strains (i.e., $\gamma \lesssim 3\%$), where the inertia of the sample is comparable to the inertia of the rheometer, as indicated in figure 11.1 by the gray area. We will now pick the intermediate DSS (test #7) and have a closer look at the corresponding microscopic results. Renderings of reconstructed particle coordinates before and after this DSS are shown in figure 11.2, where particles are color-coded according to their $\overline{q}_6$-value. Fluid-like particles appear blue and crystalline particles red. Obviously, the local structure of the sample has changed during the DSS from an amorphous state to a more crystalline state. This is also revealed in the histogram of the $\overline{q}_6$-values (figure 11.2c). The threshold to distinguish between order and disorder is around $\overline{q}_6 = 0.33$ [266].

To elucidate the amount of ordering *during* the DSS, one can take a look at results

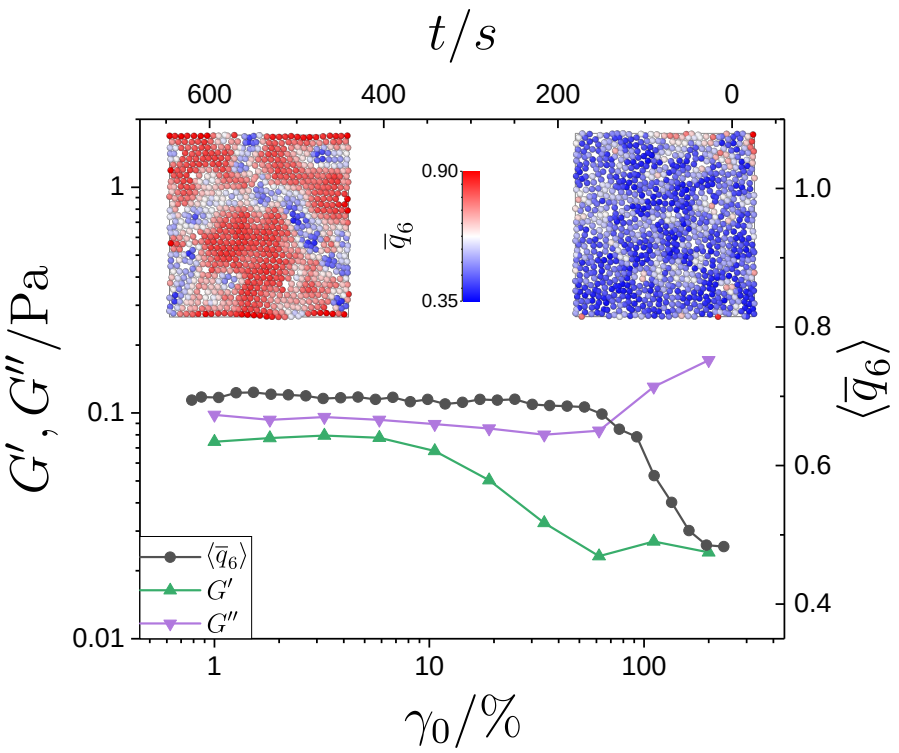

Fig. 11.3 DSS (test #7) at $\omega = 1\,\mathrm{rad/s}$. Inserted are snapshots of the particle positions for high ($\gamma_0 = 200\%$) and low strains ($\gamma_0 = 2\%$), acquired at $z = 7.7\,\mu\mathrm{m}$. The color coding inside the snapshots refers to the magnitude of the $\overline{q}_6$-values and ranges from 0.35 (blue) to 0.92 (red). The scale for the ensemble-averaged structure order parameter $\langle\overline{q}_6\rangle$ is shown on the right axis. The top-axis shows the elapsed time of this measurement.

from simultaneous rheology and confocal microscopy. In figure 11.3, the storage modulus G' and the loss modulus G'' are again plotted as a function of γ_0. This time, the rheological results are superimposed with the ensemble-averaged order parameter $\langle\overline{q}_6\rangle$ as calculated for all particles within the field of view during shear. The lowest $\langle\overline{q}_6\rangle$-values are found at the beginning of the experiment, that is, around $\gamma_0 = 200\%$. The $\langle\overline{q}_6\rangle$-values increase with decreasing strain until they are essentially constant for $\gamma_0 \lesssim 70\%$. With this microscopic information, we can understand that the sample undergoes a transition from an amorphous to a crystalline state at $\gamma_0 \approx 100\%$. Interestingly, $\langle\overline{q}_6\rangle$ and $(-1 \cdot G'')$ have very similar trends.

Information on the full series of raw-images indicates that the crystallization process starts with small nuclei that grow with time. Two renderings of particle positions at small ($\gamma_0 = 2\%$) and large strains ($\gamma_0 = 200\%$) are shown inside figure 11.3. In both cases, the x-axis corresponds to the direction of shear and the y-axis to the vorticity direction. One can, therefore, infer that crystalline particles are aligned parallel to the direction of shear.

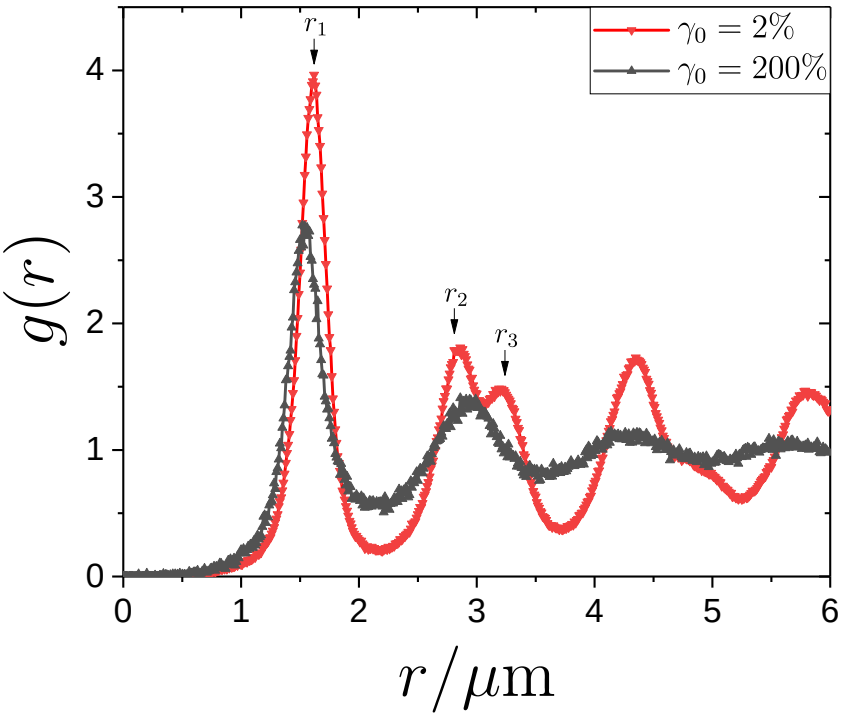

Fig. 11.4 Pair correlation function $g(r)$ as a function of distance r at different strain amplitudes during a DSS (test #7). The positions of the three tagged peaks are discussed in the text.

The structure of the sample can also be quantified by a pair correlation function. Figure 11.4 shows the pair correlation function $g(r)$ based on two-dimensional images for small ($\gamma_0 = 2\%$) and large ($\gamma_0 = 200\%$) strain amplitudes. At large strains, $g(r)$ shows the typical profile of a (concentrated) fluid. At small strains, however, the pair correlation function reveals signatures of a crystal, where particles occupy their lattice positions. The position of the first, second, and third peak is located at $r_1 = 1.62\,\mu\mathrm{m}$, $r_2 \approx \sqrt{3}\,r_1$, and $r_3 \approx 2\,r_1$. They correspond to the distances of the nearest, second nearest, and third nearest neighbors, as expected for a two-dimensional close-packed hexagonal lattice. The first peak is more pronounced and shifted to a slightly larger distance as compared to the amorphous sample. This means that the average inter-particle distance is larger in a crystalline than in a disordered state. The position of the first minimum is the same for both cases, which justifies the use of a fixed cutoff radius for the bond order analysis.

11.1.3.2 Start-Up Shear

We now take a look at the start-up experiment at $\dot{\gamma} = 10\,\mathrm{s}^{-1}$ (i.e., test #11 in table 11.1). Initially, the sample is in a crystalline state (similar to figure 11.2b)

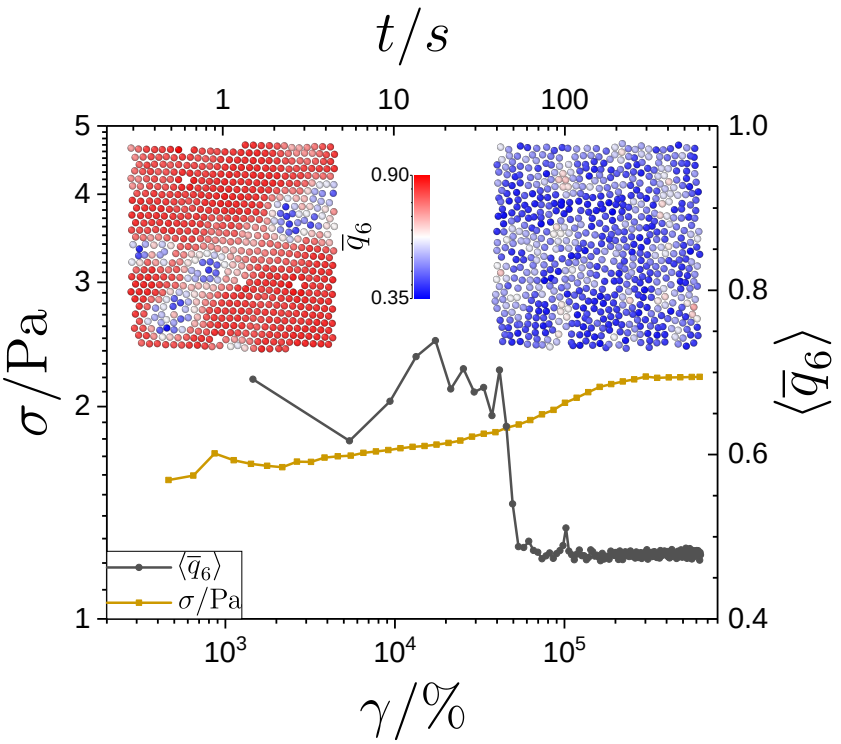

Fig. 11.5 Start-up experiment at $\dot{\gamma} = 10\,\mathrm{s}^{-1}$. Shown is the stress σ as a function of strain γ (bottom axis) and elapsed time (top axis), together with the ensemble-averaged quantity $\langle \overline{q}_6 \rangle$ as obtained from confocal microscopy. Inserted are renderings of the particle positions at short ($t = 1\,\mathrm{s}$, left inset) and long times ($t = 590\,\mathrm{s}$, right inset). The color coding of the particles is due to the $\overline{q}_6$-values as indicated.

that is interrupted by defects of various sizes and shapes. At the end of the start-up experiment, the crystalline regions are melted and the sample has an amorphous structure (comparable to figure 11.2a).

The degree of ordering *during* shear is quantified again by the ensemble-averaged order parameter $\langle \overline{q}_6 \rangle$ and shown together with the rheological response in figure 11.5. The stress response at small strains (short times) is noisy and not shown for clarity. The increase of σ at $\gamma \approx 5 \cdot 10^4\,\%$ coincides with a transition from a crystalline to a disordered structure of the sample as can be inferred from the abrupt drop of $\langle \overline{q}_6 \rangle$. The two renderings inside the figure are taken at $\gamma = 10^3\,\%$ and $\gamma = 6 \cdot 10^5\,\%$ and illustrate the ordered and disordered structure on a single-particle level. One can see that the crystalline structure at $t = 1\,\mathrm{s}$ is interrupted by small defects. In the experiment, defects of different sizes are passing through the field of view leading to the apparent fluctuations of $\langle \overline{q}_6 \rangle$ for $\gamma \lesssim 5 \cdot 10^4\,\%$. From $\gamma \approx 10^5\,\%$ onward, the ensemble-averaged bond order parameter is almost constant, and the system is amorphous as also directly observed from the raw images.

11.1.4 Discussion

The possibility of getting an ordered structure heavily depends on the properties of the probed sample. For spherical colloidal particles, polydispersity plays a crucial role (cf., section 2.4.3 and chapter 8). Here, the polydispersity is small enough ($\delta \approx 5\%$) such that ordered structures can appear.

The crystalline structures are aligned parallel to the direction of shear. This corresponds to an orientation previously found at high strains: Haw et al. observed an orientation parallel to shear at "high strains" ($\gamma > 50\%$) and perpendicular to shear at "low strains" ($\gamma < 50\%$) [228, 345]. Our preliminary experiments do not show any ordering perpendicular to shear even though also small strain amplitudes are applied to the system. A possible explanation is that previous work used fixed strain amplitudes, while experiments from this work are performed continuously from high to small strains. Hence, it seems plausible that the orientation is induced in the high-strain regime and persists until the cessation of shear. Low strains might not be able to revert the high-strain orientation. This is supported by the observation by Haw et al., stating that the orientation at low strains is not as pronounced as in the case of high strains [228]. In fact, Haw et al. find a distribution of orientations at low strains as well as "narrow bands of disorder" that separate individual crystals [228]. Narrow bands, small islands, and other shapes of disorder are also found in this work. It is expected that a mono-crystal can be obtained under a prolonged application of shear.

Particles in a crystalline state can slide along each other [228, 337, 345, 347], whereas larger rearrangements are necessary in the case of disordered systems. Similarly, our storage and loss moduli are larger for a disordered state than they would be expected in their ordered counterparts, in agreement with reference [337]. Koumakis et al. found that the elastic modulus G' of a shear aligned crystal is lower than the elastic modulus G' of a poly-crystal, which in turn is again lower than a completely amorphous sample [337]. The moduli can, therefore, serve as an indicator of the degree of ordering.

According to the train of thought of Koumakis et al., the results can be explained as follows [337]: Even though the ordered and disordered states have the same overall volume fraction, their distances to the corresponding maximum packing are different. While the maximum packing for a disordered system is at $0.64 \lesssim \phi_{\max} \lesssim 0.66$, it is at $\phi_{\max} = 0.74$ for a hexagonal close-packed system. This means that at a given volume fraction, a crystal is effectively further away from its maximum packing than its disordered counterpart. Accordingly, crystalline particles have a larger free volume and show less resistance to external shear than glasses at the same ϕ. Smaller stresses of crystals as compared to glasses at the same volume fraction have also been seen in numerical simulation [346]. This is in line with our start-up test, in which we also observe that the shear stress of the ordered state is lower than the shear stress of the amorphous state (cf., figure 11.5).

11.1.5 Conclusion

The results show shear-induced crystallization and melting. While oscillatory experiments at low and moderate strains facilitate ordering, tests at high rates and large strains destroy any ordered structure.

The transition from disorder to order is smooth in terms of the order parameter $\langle \overline{q}_6 \rangle$ and takes place in a relatively broad strain range, namely, from $\gamma_0 = 200\%$ to $\gamma_0 = 70\%$ (cf., figure 11.3). Instead, the transition from order to disorder is found to be rather abrupt (cf., figure 11.5).

Structural rearrangements are linked to rheological measures and and manifest themselves in moderate changes of the shear stress or modulus. The stress is found to be higher in the disordered than in the ordered state. This implies that it is easier to shear a crystal than a fluid of the same volume fraction.

11.2 Indentation

Indentation experiments have been performed at the Max Planck Institute for Polymer Research in Mainz in the group of G. K. Auernhammer.

11.2.1 Introduction

Besides shear, indentation is another method to mechanically probe a sample. A good overview including historical aspects as well as a more detailed description of indentation – mostly based on metallic glasses – may be provided in references [348–350]. Indentation is also frequently used in applied science, for instance, to test the endurance of a windshield.

Recently, indentation is also performed on a submicron scale. This is termed *nanoindentation* [351] and can be combined with in situ particle tracking in the case of colloids [352]. Preliminary experiments from this work follow previous studies on colloidal glasses and crystals [254, 353–355] and may be seen as a starting point for future investigations.

11.2.2 Materials and Methods

PMMA-spheres (synthesized by A. B. Schofield) are used for the indentation experiments. The particles have a radius of $R = 720\,\mathrm{nm}$, a polydispersity of $\delta = 6\%$, and are labeled with 4-methylaminoethylmethacrylate-7-nitro-benzo-2-oxal,3-diazol (NBD). They are dispersed in a density and refractive index matching mixture of *cis*-decalin and cycloheptyl bromide. The sample cell consists of a PTFE-cylinder (with an inner diameter of 6 mm and a height of about 5 mm) that is glued onto a coverslip. The sample is filled from the top and placed into the home-build setup at MPI Mainz. The temperature inside the setup is $T = 28\,^{\circ}\mathrm{C}$. The sample is

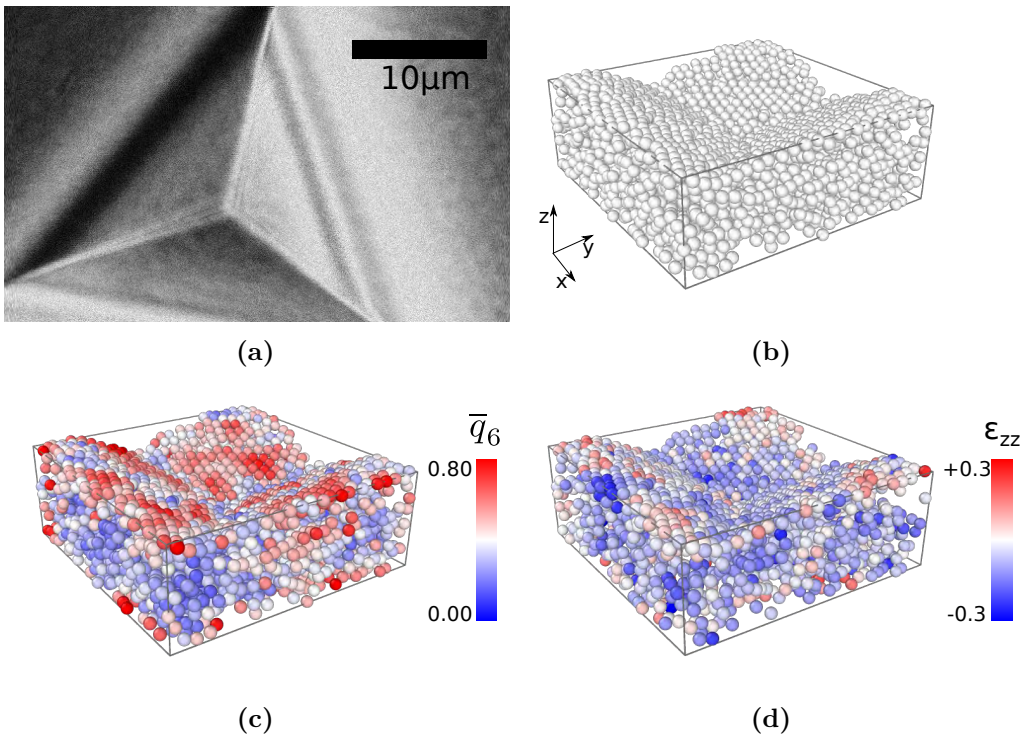

Fig. 11.6 (a) Raw image with the tip of the Berkovich indentor. The image is cut and a scale bar of 10 µm added. (b) Rendering of particle positions. "Missing" particles indicate the position of the indentor. Particles in (c) are color-coded according to their $\overline{q}_6$-values and in (d) according to their ϵ_{zz}-values. For the latter, particles having positive values are colored in red and particles with negative ones in blue.

illuminated from below with a $\lambda = 468\,\text{nm}$ laser. Confocal image-stacks consist of $512 \times 512 \times 96$ pixels, corresponding to a volume of $40 \times 40 \times 15\,\mu\text{m}$. It takes roughly $\Delta t_{3D} = 170\,\text{s}$ to capture a full 3D-stack and a total of 100 3D-stacks are recorded. A Berkovich tip indents the sample. The indentor is lowered by $z_{\text{step}} = 0.15\,\mu\text{m}$ between two consecutive 3D-stacks, and the motion is paused during image acquisition.

Particle coordinates are obtained using standard routines [203, 204] (cf., section 6.1.1). The structure and dynamics of the sample are analyzed using bond order parameters (equation (7.23)) and local strains (equation (7.18), with $\delta t = \Delta t_{3D}$). Neighbors are defined using a cutoff-distance of $1.4R$ for the bond order parameters and $2.8R$ for the calculation of local strains, respectively.

11.2.3 Results

The preliminary results are summarized in figure 11.6: The image in figure 11.6a shows a part of the raw data in which the Berkovich indentor is visible. A corresponding reconstruction of particle coordinates is given in figure 11.6b. One can see

in the rendering that particles do not fill the entire box. Missing particles at the top indicate the presence of the indentor. The shape of the indentor is clearly visible from the arrangement of particles. Wetting is observed close to the (smooth) surface of the indentor. This is quantified in figure 11.6c, where each particle is color-coded according to its $\overline{q}_6$-value. The color range goes from blue over white to red and ranges from $\overline{q}_6 = 0$ to $\overline{q}_6 = 0.66$. One can see that the majority of particles next to the (invisible) indentor are red, and particles in the bulk are blue. Thus, indentation explicitly affects the structure of the sample close to the tip of the indentor.

Besides the structure, also the dynamics can be investigated. It is very common, to evaluate shear strains during indentation. Similar to reference [354], we also plot the strains ϵ_{zz} on a single-particle level (figure 11.6d). The ϵ_{zz} quantify the extension and compression along the z-axis. Positive values (extension) are marked red and negative values (compression) are marked blue. Intuitively, the sample should be compressed along the z-direction since the indentor is pushed downwards. This is indeed observed here since the mean value over all ϵ_{zz}-values is negative.

11.2.4 Discussion

Rahmani et al. find that histograms of strain values differ close to and further away from the indentor [354]. One needs to admit that the quality of the given set of data is not suitable for quantitative analysis. Particles move too far between two consecutive images. The Brownian time of the particles is $\tau_B = 5\,\mathrm{s}$, which is very small compared to the time it takes to capture a 3D-stack.

In terms of data analysis, new insights might be obtained by calculating D^2_{min}. Varying systematically volume fraction, sample composition or the distance of the field of view with respect to the indentor are further possibilities for future studies.

11.2.5 Conclusion

Nanoindentation of colloids can serve as a fruitful technique to study colloidal materials. The preliminary results give an impression of what can be done. Confocal microscopy allows for in situ observation of structural and dynamical properties. Once the particle coordinates have been determined, many local properties can be calculated. As proof of principle, this was done for $\overline{q}_6$ and ϵ_{zz}.

11.3 Gels under Shear

So far, results were entirely based on colloidal spheres. We will use this final section to slightly change perspective and take a look at another model system: gels.

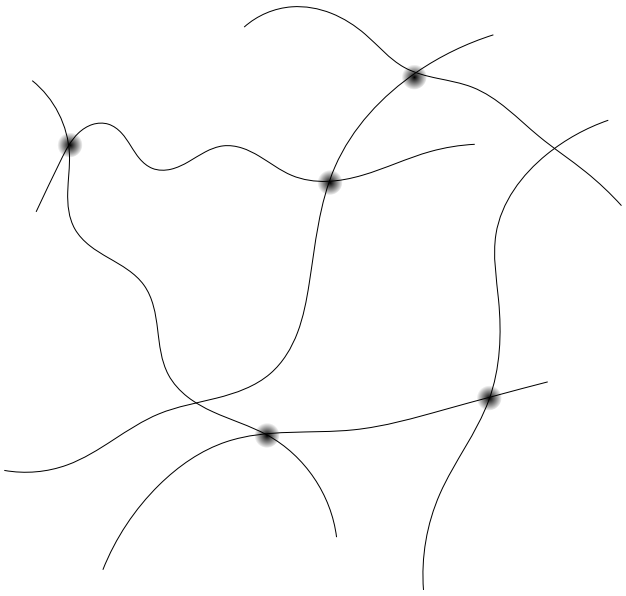

Fig. 11.7 Schematic representing a gel that consists of linear polymer chains (lines) connected by cross-links (small black blobs).

11.3.1 Introduction

There are a variety of gels and their applications range from food additives over pharmaceuticals to synthetic tissues and biomedical implants [356–358].

A relevant subgroup is made up of hydrophilic gels or in short: hydrogels. Everyday examples include wound dressings and contact lenses. Hydrogels are based on polymer networks and can store a large amount of water due to hydrophilic functional groups. A schematic of a hydrogel is given in figure 11.7. A hydrogel can be, for example, based on the monomer acrylamide (AAm) and the cross-linker N,N'-methylenebis(acrylamide) (MBAAm). The properties of these gels can be tuned by varying the polymer concentration and the cross-linking density [359]. Other synthetic hydrogels are so-called polyisocyanopeptide hydrogels (PIC), which resemble intermediate filaments and can thus be used to mimic the natural environment of biological cells [360].

The physics of gels strongly depends on the details of the individual constituents and the bonding between them. One may separate the bonds into "physical" and "chemical" bonds. While the latter are strong and permanent, the former are much weaker and can easily break and reform at thermal energies.

Gel networks have been studied experimentally with rheology [360], a combined setup consisting of a tensile stage and confocal microscopy [361], and boundary stress microscopy [362]. Gels often show strain stiffening. Mechanical failure manifests itself in cracks [361], slip [363], plastic events [364], and breaking of bonds [365]. More details are beyond the scope of this section and further reading is, for example,

Gel	Objective	magn	NA	FOV / px^3	FOV / µm^3
AAm	Plan Fluor (oil)	100x	1.30	$512 \times 512 \times 134$	$49 \times 49 \times 100$
PIC	Plan Apo VC (water)	60x	1.20	$512 \times 512 \times 134$	$79 \times 77 \times 100$

Tab. 11.2 Parameters for the confocal image acquisition. The water-immersion objective was lent by Nikon GmbH, Düsseldorf.

provided in one out of many recent reviews [356–358, 366, 367]. It was stated by Brink et al. in 2007 that "there is clearly a need of sophisticated measurement techniques for fracture dynamics at the microscopic level in addition to traditional large-scale rheological methods in order to fully map the structural dynamics leading to failure" [361].

In the following, we will study a polyisocyanopeptide hydrogel (PIC-gel) as an example of a gel with weak bonds, and an acrylamide-based hydrogel (AAm-gel) with strong bonds.

11.3.2 Materials and Methods

The AAm-gel is prepared by cross-linking polymerization of the monomer acrylamide (AAm) (Sigma, A8887) with the cross-linker N,N'-methylenebis(acrylamide) (Sigma-Aldrich, 146072). The cross-linker to monomer ratio is 1 : 60. The reaction is stated with ammonium peroxydisulphate (Roth, 9592.2) and accelerated with N,N,N',N'-Tetramethyl ethylenediamine (Merck, 110732). For an aqueous solution of $V = 2\,\mathrm{ml}$, 75 mg of AAm is used. The solution contains 0.1% (V/V) fluorescently labeled polystyrene-spheres (Thermo Scientific, R0200) that have a radius of $R_{\mathrm{tracer}} = 2\,\mu\mathrm{m}$.

The PIC-gel has a catalyst to monomer ratio of 1 : 4000 and a molecular weight of 562 kg/mol. Sample preparation yields a 2 mg/ml solution of polyisocyanide. The solution contains 0.25% (V/V) fluorescently labeled spheres (Thermo Scientific, R0200) – the same as used for the AAm-gel.

The confocal rheometer is equipped with a parallel plate geometry (Anton Paar, PP25, SN34724) with a diameter of $d = 25.0\,\mathrm{mm}$. Shear is applied by means of a start-up experiment with a shear rate of $\dot{\gamma} = 0.0025\,\mathrm{s}^{-1}$. Gap heights and temperatures in the case of the AAm-hydrogel and the PIC-hydrogel are $h_{\mathrm{AAm}} = 675\,\mu\mathrm{m}$, $T_{\mathrm{AAm}} = 20.5\,^{\circ}\mathrm{C}$ and $h_{\mathrm{PIC}} = 85\,\mu\mathrm{m}$, $T_{\mathrm{PIC}} = 24\,^{\circ}\mathrm{C}$, respectively. Further parameters for confocal image acquisition are given in table 11.2.

Tracer particles are tracked using modifications of standard routines [203] as described in section 6.1.1 and section 6.2. Local shear rates and nonaffine motions are calculated following section 7.2. To this end, neighbors are defined via a cutoff-distance of 60 µm and 13 µm, respectively.

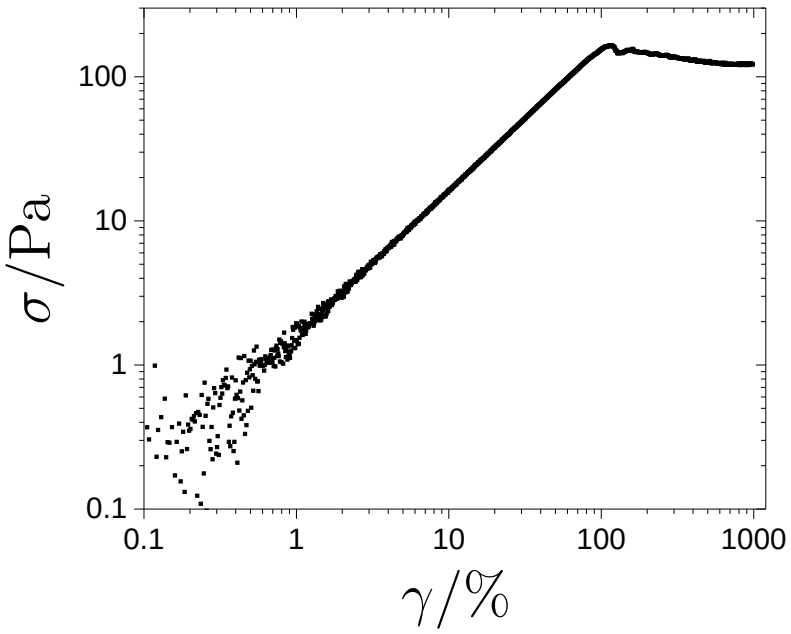

Fig. 11.8 Rheological stress response of the AAm-gel as a function of strain during a start-up test at $\dot{\gamma} = 0.0025\,\mathrm{s}^{-1}$.

11.3.3 Results

11.3.3.1 AAm-Gel

We start with the rheological response of the acrylamide-hydrogel. Figure 11.8 shows the stress as a function of strain during the start-up experiment. The AAm-gel exhibits a long linear regime until about 100% strain where it reaches its maximum stress value. Stress values of the order of 100 Pa are much higher than found in colloidal suspensions. From $\gamma \approx 100\%$ on, the stress decreases slowly and shows evidence of a steady-state plateau at high strains.

Keeping the rheological results in mind, we may step over to results from confocal microscopy. Renderings of tracer particles at $\gamma = 38\%$, $\gamma = 108\%$ and $\gamma = 188\%$ are shown in figure 11.9. The direction of shear is from left to right and all particle positions are projected into the velocity-gradient plane. For clarity, some – at first sight arbitrary – particles are highlighted in green. These particles are chosen because they can be connected by a straight line. Moreover, they represent the sample in different heights within the gap. One can see that the highlighted particles, which are aligned along an imaginary straight line at $\gamma = 38\%$ (figure 11.9a), are still arranged along a straight line at $\gamma = 108\%$ (figure 11.9b). Thus, the sample moves affine during the strain interval of 38% to 108%. At $\gamma = 189\%$, the highlighted particles are still arranged along a straight line but they are strained less than one would expect. Compared to $\gamma = 108\%$, particles actually move in the opposite

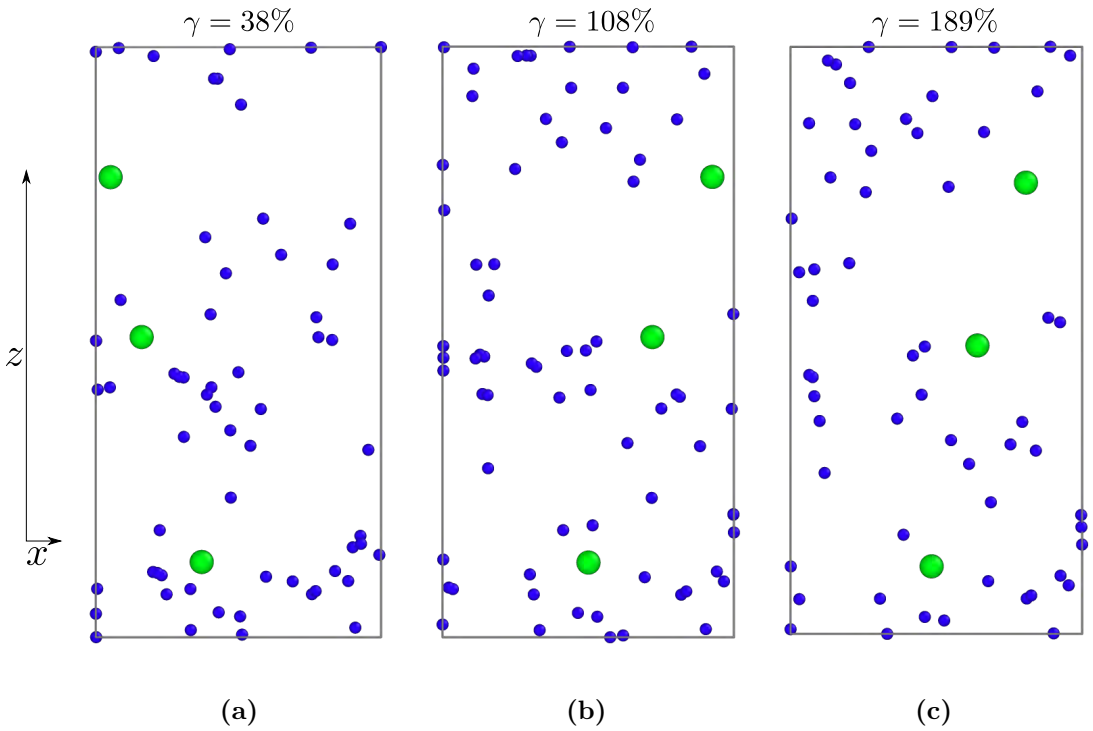

Fig. 11.9 Renderings of tracer particles inside the AAm-gel at (a) $\gamma = 38\%$, (b) $\gamma = 108\%$ and (c) $\gamma = 189\%$. All renderings are projections in the velocity-gradient direction. The direction of shear is in positive x-direction and the field of view covers a z-range from 0 µm to 100 µm. The bottom plate at $z = 0$ µm is stationary. In each rendering, three particles (green color) are highlighted to indicate the overall motion. The radii of the three highlighted particles are doubled for clarity. Between (a) and (b), particles move affine and follow the imposed shear. Between (b) and (c), the gel does not follow the shear anymore as can be inferred from the (almost stationary) particle positions.

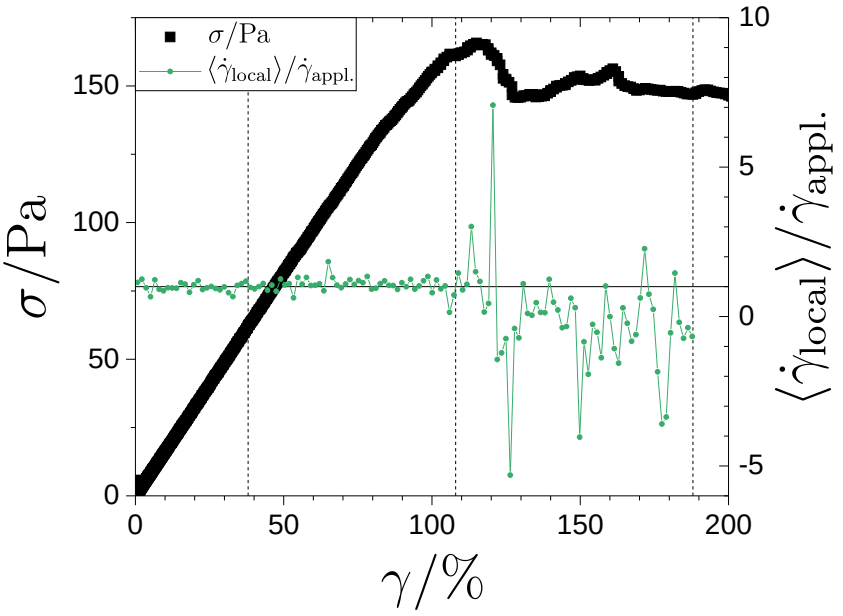

Fig. 11.10 Combined results of the AAm-gel as obtained from simultaneous rheology and confocal microscopy. The stress is the same as in figure 11.8 but plotted here in a linear scale for better comparison. The local shear rate is obtained from tracer particle trajectories. Dashed lines are located at $\gamma \in [38\%, 108\%, 189\%]$, that is, at the same strains as in figure 11.9.

direction of shear. Examination of particle reconstructions over the whole strain range reveals that particles move smooth and affine for $\gamma \lesssim 108\%$ and discontinuous at higher strains.

This will be quantified in the following: From the single-particle displacements, one can calculate local shear rates $\dot{\gamma}_{\text{local}}$. We now calculate the ensemble-averaged quantity $\langle\dot{\gamma}_{\text{local}}\rangle$ and normalize it with the macroscopic shear rate $\dot{\gamma}_{\text{appl.}}$ that is applied. The quantity $\langle\dot{\gamma}_{\text{local}}\rangle/\dot{\gamma}_{\text{appl.}}$ is plotted together with the macroscopic stress response in figure 11.10. The data of the shear stress is the same as in figure 11.8 and plotted here in a lin-lin representation for better comparison with confocal results. Dashed vertical lines indicate the corresponding strains of the renderings (cf., figure 11.9). We now see that the local shear rate for strains below $\gamma \approx 108\%$ is as expected, i.e., $\langle\dot{\gamma}_{\text{local}}\rangle/\dot{\gamma}_{\text{appl.}} \eqsim 1$. This changes dramatically above $\gamma \gtrsim 108\%$ where the local shear rate exhibits several peaks in both positive and negative directions. In particular, there are a number of strong recoils and in most of the time, $\langle\dot{\gamma}_{\text{local}}\rangle/\dot{\gamma}_{\text{appl.}}$ is now less than unity. Thus, the AAm-gel is not sheared properly anymore at high strains. From the confocal data, it can be inferred that the AAm-gel exhibits a behavior that is reminiscent of a stick-slip phenomenon. Since no slip is observed at the bottom plate, slip needs to take place entirely at the top plate. The stress-overshoot at $\gamma \approx 100\%$ marks the onset of the stick-slip regime.

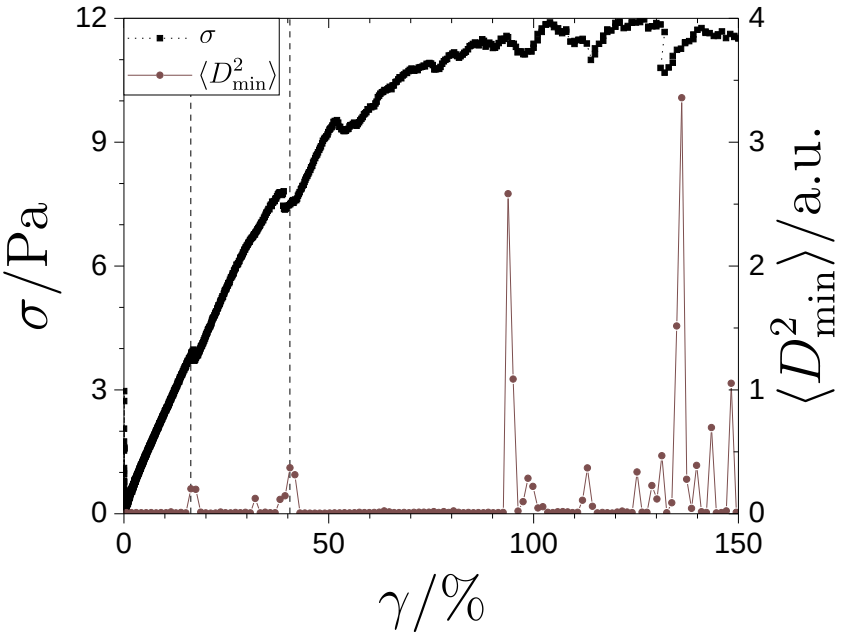

Fig. 11.11 Combined macroscopic and microscopic results of the PIC-gel. The figure shows a lin-lin plot of the stress (left axis) and local nonaffine motion (right axis) as a function of strain. Dashed vertical lines are located at $\gamma_1 = 16.3\%$ and $\gamma_2 = 40.5\%$, that is, where the first two stress drops are observed.

11.3.3.2 PIC-Gel

We can now turn to the PIC-gel. The use of a smaller gap height provides the opportunity to image tracer particles throughout the entire gap. Slip is observed neither at the top nor at the bottom plate. Yet, we have another interesting observation: The motion of the tracer particles is nonaffine. In figure 11.11, the ensemble-averaged nonaffine motion $\langle D^2_{\text{min}} \rangle$ is plotted together with the measured shear stress σ as a function of strain. The stress increases from $\sigma = 0\,\text{Pa}$ up to a maximum of about $\sigma = 12\,\text{Pa}$. The increase is not monotonic, but there are several stress fluctuations together with sharply increasing nonaffine motions. For example, the first two stress drops are indicated by dashed lines and located at $\gamma_1 = 16.3\%$ and $\gamma_2 = 40.5\%$. At the same time, a peak in $\langle D^2_{\text{min}} \rangle$ is observed.

Renderings of tracer particles at γ_1 and γ_2 are shown in figure 11.12. All particle positions are projected into the velocity-gradient plane. The direction of shear is from left to right and the gradient axis covers the full gap from the bottom plate to the top plate. Tracer particles are color-coded according to their amount of nonaffine motion. Here, blue indicates small and red large D^2_{min}-values, respectively. What we can see is that nonaffine events take place in localized spots. The first event (cf., figure 11.12a) is located in the velocity-vorticity plane at a height of $z \approx 33\mu\text{m}$ and

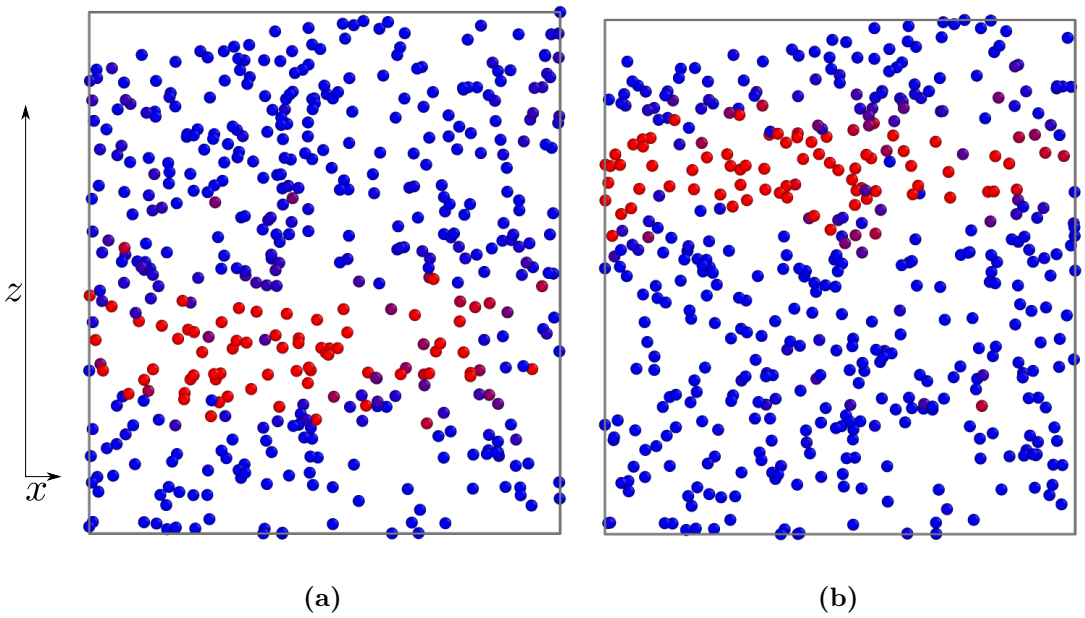

Fig. 11.12 Renderings of tracer particles inside the PIC-gel at (a) $\gamma_1 = 16.3\%$ and (b) $\gamma_2 = 40.5\%$. The positions of tracer particles are projected into the velocity-gradient plane. Blue particles are in zones of negligible nonaffine motion whereas red particles are in regions of large nonaffine motion.

the second event (cf., figure 11.12b) takes place at $z \approx 63\,\mu m$. Nonaffine events at higher strains show very similar results. These events are spread in the velocity-vorticity-plane and occur anywhere within the gap. Inspection of confocal data suggests that the gel fractures at these places.

11.3.4 Discussion

We have seen two different scenarios for the AAm- and the PIC-gel. The AAm-hydrogel shows a long linear increase of the stress as a function of strain between $\gamma = 0\%$ and $\gamma \approx 100\%$. In this regime, the local shear rate is equal to the macroscopic shear rate and the gel behaves elastic ($\sigma \propto \gamma$). Further deformation of the AAm-gel is then prevented by strong chemical bonds. The apparent overshoot and steady state are the consequence of a stick-slip phenomenon as revealed by confocal microscopy. The results are in good agreement with experiments on a carbopol microgel, where Divoux et al. identify four regimes [363]: Initially, they observe a regime of homogeneous deformation. Then, they find a maximum value of the stress that coincides with the emergence of a lubrication layer. Third, their gel experiences a recoil and finally enters a regime of total wall slip [363]. Similarly, plug flow of a hydrogel is observed in a recent rheo-confocal study [367].

The PIC-gel shows a different behavior. Simultaneous rheology and confocal

microscopy show a strong correlation between shear stresses on the one hand and local nonaffine motion on the other hand. Microscopically, it is observed that the PIC-gel locally fractures, as indicated by significant nonaffine motions. This is macroscopically reflected in a reduction of the shear stress. Stress drops have previously been related to plastic events [364] and breaking of bonds [365]. Breaking of bonds takes place in a plane parallel to the velocity-vorticity direction (figure 11.12), as previously observed in amorphous solids [364].

11.3.5 Conclusion

We can relate the two observations to the material properties of the two gels. To do so, we recognize that the AAm-gel has "strong, chemical bonds," while the PIC-gel has "weak, physical bonds." This leads to the following conclusion: Initially, (all) gels behave elastically. Any non-elastic behavior stems from small, microscopic cracks between subunits of the gel. Depending on the amount of external load, bonds may break or resist. If they withstand the external load, then further shearing is impossible, and the sample will eventually exhibit slip. Once connections break, the sample deforms plastically, and the stress is reduced.

Part IV

Conclusion and Perspectives

This work investigated the flow of concentrated colloidal suspensions of hard spheres. External shear can crystallize or melt the system and thereby change the internal structure, which in turn affects the macroscopic rheological response (section 11.1). The size distribution of the colloidal particles plays a crucial role in determining this behavior. For instance, binary mixtures at $\phi = 0.58$ were observed to crystallize under shear unless the size difference between the individual constituents is larger than about 15% (chapter 8). For much smaller size differences, the system forms a substitutional crystal with a random mixture of fcc and hcp stackings. Therefore, samples with high enough polydispersity were used to investigate the yielding and flow of colloidal glasses ($0.56 \leq \phi \leq 0.65$).

Yielding under oscillatory shear is reflected macroscopically in the transition from elastic to viscous behavior, microscopically in the transition from reversible to irreversible particle motions, and takes place at strain amplitudes of around $2 - 20\%$ (chapter 9), depending on the volume fraction. At these strains, the system shows rheological signatures of intra-cycle shear thickening. Strain amplitudes were monitored by confocal microscopy and corrected if slip occurred.

Start-up experiments at low shear rates (chapter 10) suggest that colloidal glasses obey the principles of simple shear only in a specific parameter range that is smaller than previously expected. Transient and highly nonlinear shear profiles are found together with transient and nonlinear dynamics on a single particle-level. Interestingly, the nature of the flow of colloidal glasses does not only depend on the external shear but also on the experimental conditions and the sample itself. The direct real-space observation of microscopic and mesoscopic quantities provided useful evidence that is barely accessible by rheology alone. Future work could extend the results using different volume fractions, Péclet numbers, and particle sizes to reveal the corresponding regions of homogeneous and inhomogeneous flow.

Further studies could also tackle different mechanical tests, and preliminary experiments for this have already been performed (section 11.2). For instance, the rheo-confocal setup (section 4.2) could be extended for indentation experiments if an indentor tip replaces the measuring geometry. Then, indentation steps with a precision of 1 µm, and normal forces measurements down to 5 mN are technically feasible.

Furthermore, a set of rheo-confocal experiments with a sinusoidal stress input (instead of strain) could be performed, since the respective material response can differ significantly [368]. Similarly, creep tests are straightforward to perform on the rheo-confocal setup.

Yielding, flow, and other phenomena are not limited to systems of hard spheres. A simple step would be to include other soft systems (e.g., gels (section 11.3)) that can, for instance, change their interaction potential as a function of temperature. A temperature-controlled sample cell for the rheo-confocal setup has already been developed and is available for future research.

Acknowledgements

First of all, my thanks go to Stefan, my supervisor, who has been teaching me physics since my bachelor studies. It has been a pleasure to work with you because you are always in a good mood and never hesitate to explain even the simplest things over and over again. Not only did you make discussions of physical problems great fun but you were also very helpful when it came to topics outside physics. I really appreciate it.

Second, many, many thanks to my mentor and second supervisor, Thomas, especially for your support in the last few weeks of my PhD.

Furthermore, I wish to thank Marco for teaching me colloidal suspension rheology during my bachelor and master studies. And many thanks to you and Stefan for giving me the opportunity to visit the soft matter summer school in Varenna in 2015. Special thanks also to Günter, Regina and Laurent for giving me the chance to visit your lab at the MPI in Mainz as well as for experimental support. A very inspiring cooperation also arose from a research visit by Jan. His colleague, Petri, came for a second research visit and I had definitely a great time with both of you.

I had the pleasure of sharing the soft matter lab at HHU Düsseldorf with many great people and my thanks go to all (current and former, staff and honorary, long- and short-term) members of the soft matter group (Alejandro, Alina, Andreas, Anne, Angel, Arjun, Caroline, Carolyn, Christoph, Dana, Debasish, Erick, Florian, Frau Vobis, George, Götz, Helen, Ingo, Ingo, Jan, Jasper, Julia, Juan Pablo, Jörg, Katrin, Katherine, Kevin, Laura, Lisa, Lorena, Mahnoush, Manuel, Marco, Milana, Patrick, Payam, Ramón, René, Ronja, Sebastian, Stefan, Stella, Tanja, Tatjana, and many more). Special thanks to Andreas, Debasish, Jan, Juan Pablo, Katherine, Florian, Manuel and Patrick for proof-reading single chapters.

Und außerdem bin ich natürlich sehr, sehr dankbar über die gemeinsamen Abende, Urlaube, Feste, sportlichen Aktivitäten, Spiele und viele weitere lustige Unternehmungen mit meinen Freunden. Auch ohne Euch namentlich zu nennen, sei Euch gesagt, dass ihr mir sehr wichtig seid. Der größte Dank geht schließlich an meine Familie für das aufgebrachte Verständnis und die Unterstützung in den letzten Jahren! Auch an diejenigen, die die Fertigstellung dieser Arbeit leider nicht mehr miterleben konnten. Ohne Euch wäre dies so nicht möglich gewesen. Danke!

Bibliography

[1] R. H. Ewoldt, M. T. Johnston, and L. M. Caretta. "Experimental Challenges of Shear Rheology: How to Avoid Bad Data". In: *Complex Fluids in Biological Systems*. Ed. by S. E. Spagnolie. Biological and Medical Physics, Biomedical Engineering. New York, NY: Springer New York, 2015, pp. 207–241. ISBN: 978-1-4939-2064-8. DOI: 10.1007/978-1-4939-2065-5_6.

[2] H. A. Barnes, J. F. Hutton, and K. Walters. *An introduction to rheology*. Vol. 3. Amsterdam: Elsevier, 1989. ISBN: 0-444-87140-3.

[3] C. W. Macosko. *Rheology: Principles, measurements, and applications*. Advances in interfacial engineering series. New York: Wiley-VCH, 1994. ISBN: 978-0-471-18575-8.

[4] G. Strobl. *Physik kondensierter Materie*. Berlin, Heidelberg: Springer Berlin Heidelberg, 2002. ISBN: 978-3-540-43217-3. DOI: 10.1007/978-3-642-55986-0.

[5] S. E. Spagnolie. *Complex Fluids in Biological Systems*. New York, NY: Springer New York, 2015. ISBN: 978-1-4939-2064-8. DOI: 10.1007/978-1-4939-2065-5.

[6] X. Oliver and C. Agelet de Saracibar. *Continuum Mechanics for Engineers. Theory and Problems (First edition)*. 2016. DOI: 10.13140/RG.2.2.25821.20961.

[7] J. Mewis and N. J. Wagner. *Colloidal suspension rheology*. Cambridge series in chemical engineering. Cambridge and New York: Cambridge University Press, 2012. ISBN: 978-0-521-51599-3. URL: http://catdir.loc.gov/catdir/enhancements/fy1114/2011029383-b.html.

[8] H. Späth. "Fitting affine and orthogonal transformations between two sets of points". In: *Mathematical Communications* 9 (2004), pp. 27–34.

[9] X. Roca, J. Sarrate, and A. Huerta. "A new least-squares approximation of affine mappings for sweep algorithms". In: *Engineering with Computers* 26 (2010), pp. 327–337. DOI: 10.1007/s00366-009-0161-2.

[10] *The schematic is inspired and reproduced with permission from a lecture given by Johan Bergenholtz, Göteborg, Sweden.*

[11] T. Mezger. *Das Rheologie-Handbuch*. 4. Aufl. Hannover: Vincentz Network, 2010. ISBN: 3-86630-863-9.

[12] P. Ballesta and G. Petekidis. "Creep and aging of hard-sphere glasses under constant stress". In: *Physical review. E* 93 (2016), p. 042613. DOI: 10.1103/PhysRevE.93.042613.

[13] A. J. Giacomin and J. M. Dealy. "Large-Amplitude Oscillatory Shear". In: *Techniques in Rheological Measurement*. Ed. by A. A. Collyer. Dordrecht: Springer Netherlands, 1993, pp. 99–121. ISBN: 978-94-010-4937-5. DOI: 10.1007/978-94-011-2114-9_4.

[14] T. F. Tadros. *Formulation of disperse systems: Science and technology / Tharwat F. Tadros*. Weinheim: Wiley-VCH, 2014. ISBN: 978-3-527-33682-1.

[15] N. Bowditch. “LII.” In: *American Academy of Arts and Sciences, Boston. Memoirs of the American Academy of Arts and Sciences (1785-1902)* 3 (1815), p. 413.

[16] S. A. Rogers et al. “A sequence of physical processes determined and quantified in LAOS: Application to a yield stress fluid”. In: *Journal of Rheology* 55 (2011), pp. 435–458. DOI: 10.1122/1.3544591.

[17] K. Hyun et al. “Nonlinear response of complex fluids under LAOS (large amplitude oscillatory shear) flow”. In: *Korea-Australia Rheology Journal* 15 (2003), pp. 97–105.

[18] K. Hyun et al. “A review of nonlinear oscillatory shear tests: Analysis and application of large amplitude oscillatory shear (LAOS)”. In: *Progress in Polymer Science* 36 (2011), pp. 1697–1753. DOI: 10.1016/j.progpolymsci.2011.02.002.

[19] M. Wilhelm, D. Maring, and H.-W. Spiess. “Fourier-transform rheology”. In: *Rheologica Acta* 37 (1998), pp. 399–405. DOI: 10.1007/s003970050126.

[20] M. Wilhelm, P. Reinheimer, and M. Ortseifer. “High sensitivity Fourier-transform rheology”. In: *Rheologica Acta* 38 (1999), pp. 349–356. DOI: 10.1007/s003970050185.

[21] M. Wilhelm. “Fourier-Transform Rheology”. In: *Macromolecular Materials and Engineering* 287 (2002), pp. 83–105. DOI: 10.1002/1439-2054(20020201)287:2%3C83::AID-MAME83%3E3.0.CO;2-B.

[22] C. Storm et al. “Nonlinear elasticity in biological gels”. In: *Nature* 435 (2005), pp. 191–194. DOI: 10.1038/nature03521.

[23] C. O. Klein et al. “Separation of the Nonlinear Oscillatory Response into a Superposition of Linear, Strain Hardening, Strain Softening, and Wall Slip Response”. In: *Macromolecules* 40 (2007), pp. 4250–4259. DOI: 10.1021/ma062441u.

[24] K. S. Cho et al. “A geometrical interpretation of large amplitude oscillatory shear response”. In: *Journal of Rheology* 49 (2005), pp. 747–758. DOI: 10.1122/1.1895801.

[25] R. H. Ewoldt, A. E. Hosoi, and G. H. McKinley. “New measures for characterizing nonlinear viscoelasticity in large amplitude oscillatory shear”. In: *Journal of Rheology* 52 (2008), pp. 1427–1458. DOI: 10.1122/1.2970095.

[26] M. D. Graham. “Wall slip and the nonlinear dynamics of large amplitude oscillatory shear flows”. In: *Journal of Rheology* 39 (1995), pp. 697–712. DOI: 10.1122/1.550652.

[27] P. Tapadia, S. Ravindranath, and S.-Q. Wang. “Banding in entangled polymer fluids under oscillatory shearing”. In: *Physical Review Letters* 96 (2006), p. 196001. DOI: 10.1103/PhysRevLett.96.196001.

[28] J. Läuger and H. Stettin. “Effects of instrument and fluid inertia in oscillatory shear in rotational rheometers”. In: *Journal of Rheology* 60 (2016), pp. 393–406. DOI: 10.1122/1.4944512.

[29] S. Rathgeber. “Practical Rheology”. In: ed. by J. Dhont, G. Gompper, and D. Richter. ISBN: 3-89336-297-5. Forschungszentrum Jülich, 2002.

[30] G. Petekidis, D. Vlassopoulos, and P. N. Pusey. "Yielding and flow of colloidal glasses". In: *Faraday discussions* 123 (2003), pp. 287–302. DOI: 10.1039/b207343a.

[31] P. Ballesta et al. "Slip and flow of hard-sphere colloidal glasses". In: *Physical review letters* 101 (2008), p. 258301. DOI: 10.1103/PhysRevLett.101.258301.

[32] G. Bossis et al. "Discontinuous shear thickening in the presence of polymers adsorbed on the surface of calcium carbonate particles". In: *Rheologica Acta* 56 (2017), pp. 415–430. DOI: 10.1007/s00397-017-1005-4.

[33] D. Bonn et al. "Yield stress materials in soft condensed matter". In: *Reviews of Modern Physics* 89 (2017), p. 15. DOI: 10.1103/RevModPhys.89.035005.

[34] H. P. Sdougos, S. R. Bussolari, and C. F. Dewey. "Secondary flow and turbulence in a cone-and-plate device". In: *Journal of Fluid Mechanics* 138 (1984), p. 379. DOI: 10.1017/S0022112084000161.

[35] G. V. Vinogradov et al. "The flow of plastic disperse systems in the presence of the wall effect". In: *Rheologica Acta* 14 (1975), pp. 765–775. DOI: 10.1007/BF01521405.

[36] P. Ballesta et al. "Wall slip and flow of concentrated hard-sphere colloidal suspensions". In: *Journal of Rheology* 56 (2012), pp. 1005–1037. DOI: 10.1122/1.4719775.

[37] T. Graham. "Liquid Diffusion Applied to Analysis". In: *Philosophical Transactions of the Royal Society of London* 151 (1861), pp. 183–224. DOI: 10.1098/rstl.1861.0011.

[38] J. Stauff. *Kolloidchemie*. Berlin, Heidelberg: Springer Berlin Heidelberg, 1960. ISBN: 978-3-642-87210-5. DOI: 10.1007/978-3-642-87209-9.

[39] W. Ostwald. *Die Welt der vernachlässigten Dimensionen: Eine Einführung in die Kolloidchemie*. bearb. Ausg. Hamburg: Severus Verlag, 2015. ISBN: 978-3-95801-220-2.

[40] R. A. L. Jones. *Soft condensed matter*. Vol. 6. Oxford master series in condensed matter physics. Oxford: Oxford University Press, 2002. ISBN: 9780198505891.

[41] C. Likos et al., eds. *Soft matter self-assembly*. Vol. Course 193. International School of Physics Enrico Fermi, 0074-784X. Amsterdam, The Netherlands: IOS Press, 2016. ISBN: 978-1-61499-661-3.

[42] R. Brown. "XXVII. A brief account of microscopical observations made in the months of June, July and August 1827, on the particles contained in the pollen of plants; and on the general existence of active molecules in organic and inorganic bodies". In: *The Philosophical Magazine* 4 (2009), pp. 161–173. DOI: 10.1080/14786442808674769.

[43] P. W. Van der Pas. "The discovery of the Brownian motion". In: *Scientiarum Historia: Tijdschrift voor de Geschiedenis van de Wetenschappen en de Geneeskunde* 13 (1971), pp. 27–35.

[44] A. Einstein. "Über die von der molekularkinetischen Theorie der Wärme geforderte Bewegung von in ruhenden Flüssigkeiten suspendierten Teilchen". In: *Annalen der Physik* 322 (1905), pp. 549–560. DOI: 10.1002/andp.19053220806.

[45] D. S. Lemons and A. Gythiel. “Paul Langevin’s 1908 paper “On the Theory of Brownian Motion” [“Sur la théorie du mouvement brownien,” C. R. Acad. Sci. (Paris) 146 , 530–533 (1908)]”. In: *American Journal of Physics* 65 (1997), pp. 1079–1081. DOI: 10.1119/1.18725.

[46] R. Cerbino. “Quantitative optical microscopy of colloids: The legacy of Jean Perrin”. In: *Current Opinion in Colloid & Interface Science* 34 (2018), pp. 47–58. DOI: 10.1016/j.cocis.2018.03.003.

[47] P. A. Hassan, S. Rana, and G. Verma. “Making sense of Brownian motion: Colloid characterization by dynamic light scattering”. In: *Langmuir : the ACS journal of surfaces and colloids* 31 (2015), pp. 3–12. DOI: 10.1021/la501789z.

[48] J. Stenhammar et al. “An exact calculation of the van der Waals interaction between two spheres of classical dipolar fluid”. In: *The journal of physical chemistry. B* 114 (2010), pp. 13372–13380. DOI: 10.1021/jp105754t.

[49] P. S. Yadav et al. “Effective refractive index and intermolecular forces associated with a phase of functional groups”. In: *Surface Science* 601 (2007), pp. 4582–4585. DOI: 10.1016/j.susc.2007.07.012.

[50] R. Piazza. *Statistical Physics*. Cham: Springer International Publishing, 2017. ISBN: 978-3-319-44536-6. DOI: 10.1007/978-3-319-44537-3.

[51] A. Yethiraj and A. van Blaaderen. “A colloidal model system with an interaction tunable from hard sphere to soft and dipolar”. In: *Nature* 421 (2003), pp. 513–517. DOI: 10.1038/nature01328.

[52] G. N. Smith, J. E. Hallett, and J. Eastoe. “Celebrating Soft Matter’s 10th Anniversary: Influencing the charge of poly(methyl methacrylate) latexes in nonpolar solvents”. In: *Soft matter* 11 (2015), pp. 8029–8041. DOI: 10.1039/c5sm01190f.

[53] B. Derjaguin and L. Landau. “Theory of the stability of strongly charged lyophobic sols and of the adhesion of strongly charged particles in solutions of electrolytes”. In: *Progress in Surface Science* 43 (1993), pp. 30–59. DOI: 10.1016/0079-6816(93)90013-L.

[54] E. J. W. Verwey and J. T. G. Overbeek. *Theory of the Stability of Lyophobic Colloids: The Interaction of Sol Particles Having an Electric Double Layer*. Elsevier, 1948.

[55] P. J. Flory. “Thermodynamics of High Polymer Solutions”. In: *The Journal of Chemical Physics* 10 (1942), pp. 51–61. DOI: 10.1063/1.1723621.

[56] M. L. Huggins. “Solutions of Long Chain Compounds”. In: *The Journal of Chemical Physics* 9 (1941), p. 440. DOI: 10.1063/1.1750930.

[57] D. J. Walbridge and J. A. Waters. “Rheology of sterically stabilized dispersions of poly(methyl methacrylate) in aliphatic hydrocarbons”. In: *Discussions of the Faraday Society* 42 (1966), p. 294. DOI: 10.1039/DF9664200294.

[58] D. H. Napper. “Colloid Stability”. In: *Industrial & Engineering Chemistry Product Research and Development* 9 (1970), pp. 467–477. DOI: 10.1021/i360036a005.

[59] K. E. J. Barrett. “Dispersion polymerisation in organic media”. In: *British Polymer Journal* 5 (1973), pp. 259–271. DOI: 10.1002/pi.4980050403.

[60] L. Antl et al. “The preparation of poly(methyl methacrylate) latices in non-aqueous media”. In: *Colloids and Surfaces* 17 (1986), pp. 67–78. DOI: 10.1016/0166-6622(86)80187-1.

[61] M. N. van der Linden et al. “Charging of poly(methyl methacrylate) (PMMA) colloids in cyclohexyl bromide: Locking, size dependence, and particle mixtures”. In: *Langmuir : the ACS journal of surfaces and colloids* 31 (2015), pp. 65–75. DOI: 10.1021/la503665e.

[62] U. Gasser et al. “Real-space imaging of nucleation and growth in colloidal crystallization”. In: *Science* 292 (2001), pp. 258–262. DOI: 10.1126/science.1058457.

[63] C. P. Royall, W. C. K. Poon, and E. R. Weeks. “In search of colloidal hard spheres”. In: *Soft matter* 9 (2013), pp. 17–27. DOI: 10.1039/C2SM26245B.

[64] W. C. K. Poon, E. R. Weeks, and C. P. Royall. “On measuring colloidal volume fractions”. In: *Soft matter* 8 (2012), pp. 21–30. DOI: 10.1039/C1SM06083J.

[65] P. N. Pusey and W. van Megen. “Observation of a glass transition in suspensions of spherical colloidal particles”. In: *Physical review letters* 59 (1987), pp. 2083–2086. DOI: 10.1103/PhysRevLett.59.2083.

[66] W. van Megen and P. N. Pusey. “Dynamic light-scattering study of the glass transition in a colloidal suspension”. In: *Physical Review A* 43 (1991), pp. 5429–5441. DOI: 10.1103/PhysRevA.43.5429.

[67] P. N. Pusey and W. van Megen. “The glass transition of hard-sphere colloids”. In: *Physica Scripta* T45 (1992), pp. 261–264. DOI: 10.1088/0031-8949/1992/T45/056.

[68] T. E. Kodger et al. “Stable, Fluorescent Polymethylmethacrylate Particles for the Long-Term Observation of Slow Colloidal Dynamics”. In: *Langmuir : the ACS journal of surfaces and colloids* 33 (2017), pp. 6382–6389. DOI: 10.1021/acs.langmuir.7b00852.

[69] T. E. Kodger, R. E. Guerra, and J. Sprakel. “Precise colloids with tunable interactions for confocal microscopy”. In: *Scientific reports* 5 (2015), p. 14635. DOI: 10.1038/srep14635.

[70] P. N. Pusey and W. van Megen. “Phase behaviour of concentrated suspensions of nearly hard colloidal spheres”. In: *Nature* 320 (1986), pp. 340–342. DOI: 10.1038/320340a0.

[71] L. V. Woodcock. “GLASS TRANSITION IN THE HARD-SPHERE MODEL AND KAUZMANN’S PARADOX”. In: *Annals of the New York Academy of Sciences* 371 (1981), pp. 274–298. URL: https://nyaspubs.onlinelibrary.wiley.com/doi/abs/10.1111/j.1749-6632.1981.tb55667.x.

[72] W. van Megen and S. M. Underwood. "Glass transition in colloidal hard spheres: Measurement and mode-coupling-theory analysis of the coherent intermediate scattering function". In: *Physical Review E* 49 (1994), pp. 4206–4220. DOI: 10.1103/PhysRevE.49.4206.

[73] W. G. Hoover and F. H. Ree. "Melting Transition and Communal Entropy for Hard Spheres". In: *The Journal of Chemical Physics* 49 (1968), pp. 3609–3617. DOI: 10.1063/1.1670641.

[74] J. F. Lutsko and M. Baus. "Can the thermodynamic properties of a solid be mapped onto those of a liquid?" In: *Physical review letters* 64 (1990), pp. 761–763. DOI: 10.1103/PhysRevLett.64.761.

[75] D. Frenkel. "Order through entropy". In: *Nature materials* 14 (2015), pp. 9–12. DOI: 10.1038/nmat4178.

[76] V. N. Manoharan. "COLLOIDS. Colloidal matter: Packing, geometry, and entropy". In: *Science (New York, N.Y.)* 349 (2015), p. 1253751. DOI: 10.1126/science.1253751.

[77] T. C. Lubensky. "Soft condensed matter physics". In: *Solid State Communications* 102 (1997), pp. 187–197. DOI: 10.1016/S0038-1098(96)00718-1.

[78] P. N. Pusey. "Colloidal Suspensions". In: *Liquides, cristallisation et transition vitreuse = Liquids, freezing and glass transition*. Ed. by J.-P. Hansen, D. Levesque, and J. Zinn-Justin. Amsterdam: North-Holland, 1991, pp. 763–942. ISBN: 978-0444889287.

[79] A. K. Sood. "Structural Ordering in Colloidal Suspensions". In: *Solid State Physics*. Ed. by H. Ehrenreich and D. Turnbull. Vol. 45. Solid State Physics. Elsevier, 1991, pp. 1–73. ISBN: 9780126077452. DOI: 10.1016/S0081-1947(08)60143-5.

[80] P. Bartlett and W. van Megen. "Physics of Hard-Sphere Colloidal Suspensions". In: *Granular Matter*. Ed. by A. Mehta. New York, NY: Springer New York, 1994, pp. 195–257. ISBN: 978-1-4612-8725-4. DOI: 10.1007/978-1-4612-4290-1{_}7.

[81] Z. Cheng. "Colloidal Crystallization". In: *Fluids, Colloids and Soft Materials*. Ed. by A. Fernandez-Nieves and A. M. Puertas. Hoboken, NJ, USA: John Wiley & Sons, Inc, 2016. ISBN: 9781119220510. DOI: 10.1002/9781119220510.ch12.

[82] T. Hales. "A proof of the Kepler conjecture". In: *Annals of Mathematics* 162 (2005), pp. 1065–1185. DOI: 10.4007/annals.2005.162.1065.

[83] S. Auer and D. Frenkel. "Suppression of crystal nucleation in polydisperse colloids due to increase of the surface free energy". In: *Nature* 413 (2001), pp. 711–713. DOI: 10.1038/35099513.

[84] S. Auer and D. Frenkel. "Prediction of absolute crystal-nucleation rate in hard-sphere colloids". In: *Nature* 409 (2001), pp. 1020–1023. DOI: 10.1038/35059035.

[85] P. N. Pusey et al. "Structure of crystals of hard colloidal spheres". In: *Physical review letters* 63 (1989), pp. 2753–2756. DOI: 10.1103/PhysRevLett.63.2753.

[86] A. Santos et al. "Simple effective rule to estimate the jamming packing fraction of polydisperse hard spheres". In: *Physical review. E, Statistical, nonlinear, and soft matter physics* 89 (2014), p. 040302. DOI: 10.1103/PhysRevE.89.040302.

[87] S. E. Phan et al. "Effects of polydispersity on hard sphere crystals". In: *The Journal of Chemical Physics* 108 (1998), pp. 9789–9795. DOI: 10.1063/1.476453.

[88] P. Bartlett and P. B. Warren. "Reentrant Melting in Polydispersed Hard Spheres". In: *Physical Review Letters* 82 (1999), pp. 1979–1982. DOI: 10.1103/PhysRevLett.82.1979.

[89] P. Sollich. "Predicting phase equilibria in polydisperse systems". In: *Journal of Physics: Condensed Matter* 14 (2002), R79–R117. DOI: 10.1088/0953-8984/14/3/201.

[90] M. Fasolo and P. Sollich. "Equilibrium phase behavior of polydisperse hard spheres". In: *Physical review letters* 91 (2003), p. 068301. DOI: 10.1103/PhysRevLett.91.068301.

[91] W. Schaertl and H. Sillescu. "Brownian dynamics of polydisperse colloidal hard spheres: Equilibrium structures and random close packings". In: *Journal of Statistical Physics* 77 (1994), pp. 1007–1025. DOI: 10.1007/BF02183148.

[92] P. N. Pusey et al. "Hard spheres: Crystallization and glass formation". In: *Philosophical transactions. Series A, Mathematical, physical, and engineering sciences* 367 (2009), pp. 4993–5011. DOI: 10.1098/rsta.2009.0181.

[93] M. Fasolo and P. Sollich. "Fractionation effects in phase equilibria of polydisperse hard-sphere colloids". In: *Physical review. E, Statistical, nonlinear, and soft matter physics* 70 (2004), p. 041410. DOI: 10.1103/PhysRevE.70.041410.

[94] E. Zaccarelli et al. "Crystallization of hard-sphere glasses". In: *Physical Review Letters* 103 (2009), p. 135704. DOI: 10.1103/PhysRevLett.103.135704.

[95] P. G. Bolhuis and D. A. Kofke. "Numerical study of freezing in polydisperse colloidal suspensions". In: *Journal of Physics: Condensed Matter* 8 (1996), pp. 9627–9631. DOI: 10.1088/0953-8984/8/47/074.

[96] D. A. Kofke and P. G. Bolhuis. "Freezing of polydisperse hard spheres". In: *Physical Review E* 59 (1999), pp. 618–622. DOI: 10.1103/PhysRevE.59.618.

[97] T. Narumi et al. "Spatial and temporal dynamical heterogeneities approaching the binary colloidal glass transition". In: *Soft matter* 7 (2011), pp. 1472–1482. DOI: 10.1039/C0SM00756K.

[98] N. Hunt, R. Jardine, and P. Bartlett. "Superlattice formation in mixtures of hard-sphere colloids". In: *Physical Review E* 62 (2000), pp. 900–913. DOI: 10.1103/PhysRevE.62.900.

[99] P. N. Pusey. "The effect of polydispersity on the crystallization of hard spherical colloids". In: *Journal de Physique* 48 (1987), pp. 709–712. DOI: 10.1051/jphys:01987004805070900.

[100] C. Chakravarty, P. G. Debenedetti, and F. H. Stillinger. "Lindemann measures for the solid-liquid phase transition". In: *The Journal of Chemical Physics* 126 (2007), p. 204508. DOI: 10.1063/1.2737054.

[101] P. Bartlett. "Thermodynamic properties of polydisperse hard spheres". In: *Molecular Physics* 97 (1999), pp. 685–693. DOI: 10.1080/002689799163523.

[102] V. Ogarko and S. Luding. "Equation of state and jamming density for equivalent bi- and polydisperse, smooth, hard sphere systems". In: *The Journal of Chemical Physics* 136 (2012), p. 124508. DOI: 10.1063/1.3694030.

[103] J. L. Lebowitz and J. S. Rowlinson. "Thermodynamic Properties of Mixtures of Hard Spheres". In: *The Journal of Chemical Physics* 41 (1964), pp. 133–138. DOI: 10.1063/1.1725611.

[104] J. L. Barrat, M. Baus, and J. P. Hansen. "Density-functional theory of freezing of hard-sphere mixtures into substitutional solid solutions". In: *Physical review letters* 56 (1986), pp. 1063–1065. DOI: 10.1103/PhysRevLett.56.1063.

[105] C. N. Likos and C. L. Henley. "Complex alloy phases for binary hard-disc mixtures". In: *Philosophical Magazine B* 68 (1993), pp. 85–113. DOI: 10.1080/13642819308215284.

[106] A. B. Hopkins et al. "Phase diagram and structural diversity of the densest binary sphere packings". In: *Physical review letters* 107 (2011), p. 125501. DOI: 10.1103/PhysRevLett.107.125501.

[107] P. Bartlett, R. H. Ottewill, and P. N. Pusey. "Freezing of binary mixtures of colloidal hard spheres". In: *The Journal of Chemical Physics* 93 (1990), pp. 1299–1312. DOI: 10.1063/1.459142.

[108] T. Sentjabrskaja, M. Laurati, and S. U. Egelhaaf. "One- and two-component colloidal glasses under transient shear". In: *The European Physical Journal Special Topics* 226 (2017), pp. 3023–3037. DOI: 10.1140/epjst/e2017-70076-0.

[109] S. W. Rick and A. D. J. Haymet. "Density functional theory for the freezing of Lennard–Jones binary mixtures". In: *The Journal of Chemical Physics* 90 (1989), pp. 1188–1199. DOI: 10.1063/1.456175.

[110] A. R. Denton and N. W. Ashcroft. "Weighted-density-functional theory of nonuniform fluid mixtures: Application to freezing of binary hard-sphere mixtures". In: *Physical Review A* 42 (1990), pp. 7312–7329. DOI: 10.1103/PhysRevA.42.7312.

[111] X. C. Zeng and D. W. Oxtoby. "Density functional theory for freezing of a binary hard sphere liquid". In: *The Journal of Chemical Physics* 93 (1990), pp. 4357–4363. DOI: 10.1063/1.458719.

[112] W. Kranendonk and D. Frenkel. "Computer simulation of solid-liquid coexistence in binary hard sphere mixtures". In: *Molecular Physics* 72 (1991), pp. 679–697. DOI: 10.1080/00268979100100501.

[113] A. Imhof and J. K. G. Dhont. "Experimental Phase Diagram of a Binary Colloidal Hard-Sphere Mixture with a Large Size Ratio". In: *Physical review letters* 75 (1995), pp. 1662–1665. DOI: 10.1103/PhysRevLett.75.1662.

[114] T. Biben and J. P. Hansen. "Phase separation of asymmetric binary hard-sphere fluids". In: *Physical review letters* 66 (1991), pp. 2215–2218. DOI: 10.1103/PhysRevLett.66.2215.

[115] X. Cottin and P. A. Monson. "Substitutionally ordered solid solutions of hard spheres". In: *The Journal of Chemical Physics* 102 (1995), pp. 3354–3360. DOI: 10.1063/1.469209.

[116] W. Paskowicz. "Contribution of a hard-spheres packing model to the determination of binary alloy phase diagrams". In: *Journal of Physics F: Metal Physics* 18 (1988), pp. 1761–1785. DOI: 10.1088/0305-4608/18/8/014.

[117] W. Hume-Rothery, G. W. Mabbott, and K. M. C. Evans. "The Freezing Points, Melting Points, and Solid Solubility Limits of the Alloys of Silver, and Copper with the Elements of the B Sub-Groups". In: *Philosophical Transactions of the Royal Society A: Mathematical, Physical and Engineering Sciences* 233 (1934), pp. 1–97. DOI: 10.1098/rsta.1934.0014.

[118] R. P. Sear. "Nucleation: Theory and applications to protein solutions and colloidal suspensions". In: *Journal of Physics: Condensed Matter* 19 (2007), p. 033101. DOI: 10.1088/0953-8984/19/3/033101.

[119] S. Torquato. *Random Heterogeneous Materials*. Vol. 16. New York, NY: Springer New York, 2002. ISBN: 978-1-4757-6357-7. DOI: 10.1007/978-1-4757-6355-3.

[120] M. Hermes and M. Dijkstra. "Jamming of polydisperse hard spheres: The effect of kinetic arrest". In: *EPL (Europhysics Letters)* 89 (2010), p. 38005. DOI: 10.1209/0295-5075/89/38005.

[121] R. S. Farr and R. D. Groot. "Close packing density of polydisperse hard spheres". In: *The Journal of Chemical Physics* 131 (2009), p. 244104. DOI: 10.1063/1.3276799.

[122] J. G. Berryman. "Random close packing of hard spheres and disks". In: *Physical Review A* 27 (1983), pp. 1053–1061. DOI: 10.1103/PhysRevA.27.1053.

[123] K. W. Desmond and E. R. Weeks. "Influence of particle size distribution on random close packing of spheres". In: *Physical review. E, Statistical, nonlinear, and soft matter physics* 90 (2014), p. 022204. DOI: 10.1103/PhysRevE.90.022204.

[124] A. J. Liu and S. R. Nagel. "Jamming is not just cool any more". In: *Nature* 396 (1998), pp. 21–22. DOI: 10.1038/23819.

[125] S. Torquato and F. H. Stillinger. "Jammed hard-particle packings: From Kepler to Bernal and beyond". In: *Reviews of Modern Physics* 82 (2010), pp. 2633–2672. DOI: 10.1103/RevModPhys.82.2633.

[126] M. A. Klatt and S. Torquato. "Characterization of maximally random jammed sphere packings. II. Correlation functions and density fluctuations". In: *Physical review. E* 94 (2016), p. 022152. DOI: 10.1103/PhysRevE.94.022152.

[127] J. Zhu et al. “Crystallization of hard-sphere colloids in microgravity”. In: *Nature* 387 (1997), pp. 883–885. DOI: 10.1038/43141.

[128] Z. Cheng et al. “Phase diagram of hard spheres”. In: *Materials & Design* 22 (2001), pp. 529–534. DOI: 10.1016/S0261-3069(01)00015-2.

[129] L. Berthier and G. Biroli. “Theoretical perspective on the glass transition and amorphous materials”. In: *Reviews of Modern Physics* 83 (2011), pp. 587–645. DOI: 10.1103/RevModPhys.83.587.

[130] A. Cavagna. “Supercooled liquids for pedestrians”. In: *Physics Reports* 476 (2009), pp. 51–124. DOI: 10.1016/j.physrep.2009.03.003.

[131] S. I. Henderson et al. “Effect of particle size distribution on crystallisation and the glass transition of hard sphere colloids”. In: *Physica A: Statistical Mechanics and its Applications* 233 (1996), pp. 102–116. DOI: 10.1016/S0378-4371(96)00153-7.

[132] W. K. Kegel. “Direct Observation of Dynamical Heterogeneities in Colloidal Hard-Sphere Suspensions”. In: *Science* 287 (2000), pp. 290–293. DOI: 10.1126/science.287.5451.290.

[133] V. Chikkadi et al. “Long-range strain correlations in sheared colloidal glasses”. In: *Physical review letters* 107 (2011), p. 198303. DOI: 10.1103/PhysRevLett.107.198303.

[134] D. V. Denisov et al. “Sharp symmetry-change marks the mechanical failure transition of glasses”. In: *Scientific reports* 5 (2015), p. 14359. DOI: 10.1038/srep14359.

[135] T. G. Mason and D. A. Weitz. “Linear viscoelasticity of colloidal hard sphere suspensions near the glass transition”. In: *Physical review letters* 75 (1995), pp. 2770–2773. DOI: 10.1103/PhysRevLett.75.2770.

[136] K. N. Pham et al. “Yielding of colloidal glasses”. In: *EPL (Europhysics Letters)* 75 (2006), pp. 624–630. DOI: 10.1209/epl/i2006-10156-y.

[137] P. Chaudhuri et al. “Equilibrium glassy phase in a polydisperse hard-sphere system”. In: *Physical Review Letters* 95 (2005), p. 248301. DOI: 10.1103/PhysRevLett.95.248301.

[138] J. M. Brader et al. “Nonlinear response of dense colloidal suspensions under oscillatory shear: Mode-coupling theory and Fourier transform rheology experiments”. In: *Physical review. E, Statistical, nonlinear, and soft matter physics* 82 (2010), p. 061401. DOI: 10.1103/PhysRevE.82.061401.

[139] T. Kawasaki, A. Ikeda, and L. Berthier. “Thinning or thickening? Multiple rheological regimes in dense suspensions of soft particles”. In: *EPL (Europhysics Letters)* 107 (2014), p. 28009. DOI: 10.1209/0295-5075/107/28009.

[140] K. Chen et al. “Strain heterogeneity in sheared colloids revealed by neutron scattering”. In: *Physical chemistry chemical physics : PCCP* 20 (2018), pp. 6050–6054. DOI: 10.1039/c7cp07197c.

[141] H. Löwen. “Melting, freezing and colloidal suspensions”. In: *Physics Reports* 237 (1994), pp. 249–324. DOI: 10.1016/0370-1573(94)90017-5.

[142] G. L. Hunter and E. R. Weeks. "The physics of the colloidal glass transition". In: *Reports on progress in physics. Physical Society (Great Britain)* 75 (2012), p. 066501. DOI: 10.1088/0034-4885/75/6/066501.

[143] W. van Megen et al. "Measurement of the self-intermediate scattering function of suspensions of hard spherical particles near the glass transition". In: *Physical Review E* 58 (1998), pp. 6073–6085. DOI: 10.1103/PhysRevE.58.6073.

[144] R. S. L. Stein and H. C. Andersen. "Scaling analysis of dynamic heterogeneity in a supercooled Lennard-Jones liquid". In: *Physical Review Letters* 101 (2008), p. 267802. DOI: 10.1103/PhysRevLett.101.267802.

[145] E. R. Weeks and D. Weitz. "Subdiffusion and the cage effect studied near the colloidal glass transition". In: *Chemical Physics* 284 (2002), pp. 361–367. DOI: 10.1016/S0301-0104(02)00667-5.

[146] E. R. Weeks and D. A. Weitz. "Properties of cage rearrangements observed near the colloidal glass transition". In: *Physical Review Letters* 89 (2002), p. 095704. DOI: 10.1103/PhysRevLett.89.095704.

[147] E. R. Weeks. "Three-Dimensional Direct Imaging of Structural Relaxation Near the Colloidal Glass Transition". In: *Science* 287 (2000), pp. 627–631. DOI: 10.1126/science.287.5453.627.

[148] G. Adam and J. H. Gibbs. "On the Temperature Dependence of Cooperative Relaxation Properties in Glass–Forming Liquids". In: *The Journal of Chemical Physics* 43 (1965), pp. 139–146. DOI: 10.1063/1.1696442.

[149] L. Berthier et al. "Direct experimental evidence of a growing length scale accompanying the glass transition". In: *Science (New York, N.Y.)* 310 (2005), pp. 1797–1800. DOI: 10.1126/science.1120714.

[150] L. M. C. Janssen. "Mode-Coupling Theory of the Glass Transition: A Primer". In: *Frontiers in Physics* 6 (2018), p. 259. DOI: 10.3389/fphy.2018.00097.

[151] W. Kob et al. "Dynamical Heterogeneities in a Supercooled Lennard-Jones Liquid". In: *Physical Review Letters* 79 (1997), pp. 2827–2830. DOI: 10.1103/PhysRevLett.79.2827.

[152] R. Candelier et al. "Spatiotemporal hierarchy of relaxation events, dynamical heterogeneities, and structural reorganization in a supercooled liquid". In: *Physical review letters* 105 (2010), p. 135702. DOI: 10.1103/PhysRevLett.105.135702.

[153] S. Franz and G. Parisi. "On non-linear susceptibility in supercooled liquids". In: *Journal of Physics: Condensed Matter* 12 (2000), pp. 6335–6342. DOI: 10.1088/0953-8984/12/29/305.

[154] Y. Gao and M. L. Kilfoil. "Direct imaging of dynamical heterogeneities near the colloid-gel transition". In: *Physical review letters* 99 (2007), p. 078301. DOI: 10.1103/PhysRevLett.99.078301.

[155] A. Coniglio et al. "Dynamical heterogeneities: From glasses to gels". In: *Journal of Physics: Condensed Matter* 20 (2008), p. 494239. DOI: 10.1088/0953-8984/20/49/494239.

[156] P. Chaudhuri and L. Berthier. "Ultra-long-range dynamic correlations in a microscopic model for aging gels". In: *Physical review. E* 95 (2017), p. 060601. DOI: 10.1103/PhysRevE.95.060601.

[157] M. L. Falk and J. S. Langer. "Dynamics of viscoplastic deformation in amorphous solids". In: *Physical Review E* 57 (1998), pp. 7192–7205. DOI: 10.1103/PhysRevE.57.7192.

[158] V. Chikkadi and P. Schall. "Nonaffine measures of particle displacements in sheared colloidal glasses". In: *Physical review. E, Statistical, nonlinear, and soft matter physics* 85 (2012), p. 031402. DOI: 10.1103/PhysRevE.85.031402.

[159] I. M. Krieger. "Rheology of monodisperse latices". In: *Advances in colloid and interface science* 3 (1972), pp. 111–136. DOI: 10.1016/0001-8686(72)80001-0.

[160] D. Quemada. "Rheology of concentrated disperse systems and minimum energy dissipation principle". In: *Rheologica Acta* 16 (1977), pp. 82–94. DOI: 10.1007/BF01516932.

[161] W. B. Russel, N. J. Wagner, and J. Mewis. "Divergence in the low shear viscosity for Brownian hard-sphere dispersions: At random close packing or the glass transition?" In: *Journal of Rheology* 57 (2013), pp. 1555–1567. DOI: 10.1122/1.4820515.

[162] M. Wyart and M. E. Cates. "Discontinuous shear thickening without inertia in dense non-Brownian suspensions". In: *Physical review letters* 112 (2014), p. 098302. DOI: 10.1103/PhysRevLett.112.098302.

[163] B. M. Guy, M. Hermes, and W. C. K. Poon. "Towards a Unified Description of the Rheology of Hard-Particle Suspensions". In: *Physical review letters* 115 (2015), p. 088304. DOI: 10.1103/PhysRevLett.115.088304.

[164] G. Petekidis, D. Vlassopoulos, and P. N. Pusey. "Yielding and flow of sheared colloidal glasses". In: *Journal of Physics: Condensed Matter* 16 (2004), S3955–S3963. DOI: 10.1088/0953-8984/16/38/013.

[165] M. Ballauff et al. "Residual stresses in glasses". In: *Physical review letters* 110 (2013), p. 215701. DOI: 10.1103/PhysRevLett.110.215701.

[166] A. S. Poulos et al. "Large amplitude oscillatory shear (LAOS) in model colloidal suspensions and glasses: Frequency dependence". In: *Rheologica Acta* 54 (2015), pp. 715–724. DOI: 10.1007/s00397-015-0865-8.

[167] V. Carrier and G. Petekidis. "Nonlinear rheology of colloidal glasses of soft thermosensitive microgel particles". In: *Journal of Rheology* 53 (2009), pp. 245–273. DOI: 10.1122/1.3045803.

[168] M. Laurati et al. "Transient dynamics in dense colloidal suspensions under shear: Shear rate dependence". In: *Journal of physics. Condensed matter : an Institute of Physics journal* 24 (2012), p. 464104. DOI: 10.1088/0953-8984/24/46/464104.

[169] N. Koumakis et al. "Yielding of hard-sphere glasses during start-up shear". In: *Physical review letters* 108 (2012), p. 098303. DOI: 10.1103/PhysRevLett.108.098303.

[170] A. Nicolas et al. "Deformation and flow of amorphous solids: Insights from elastoplastic models". In: *Reviews of Modern Physics* 90 (2018), p. 341. DOI: 10.1103/RevModPhys.90.045006.

[171] N. J. Wagner and J. F. Brady. "Shear thickening in colloidal dispersions". In: *Physics Today* 62 (2009), pp. 27–32. DOI: 10.1063/1.3248476.

[172] C. P. Hsu et al. "Roughness-dependent tribology effects on discontinuous shear thickening". In: *Proceedings of the National Academy of Sciences of the United States of America* 115 (2018), pp. 5117–5122. DOI: 10.1073/pnas.1801066115.

[173] T. Kawasaki and L. Berthier. "Discontinuous shear thickening in Brownian suspensions". In: *Physical review. E* 98 (2018), p. 012609. DOI: 10.1103/PhysRevE.98.012609.

[174] H. A. Barnes. "Shear–Thickening ("Dilatancy") in Suspensions of Nonaggregating Solid Particles Dispersed in Newtonian Liquids". In: *Journal of Rheology* 33 (1989), pp. 329–366. DOI: 10.1122/1.550017.

[175] G. Ovarlez et al. "Phenomenology and physical origin of shear localization and shear banding in complex fluids". In: *Rheologica Acta* 48 (2009), pp. 831–844. DOI: 10.1007/s00397-008-0344-6.

[176] L. Berthier. "Yield stress, heterogeneities and activated processes in soft glassy materials". In: *Journal of Physics: Condensed Matter* 15 (2003), S933–S943. DOI: 10.1088/0953-8984/15/11/317.

[177] T. Divoux et al. "Shear Banding of Complex Fluids". In: *Annual Review of Fluid Mechanics* 48 (2016), pp. 81–103. DOI: 10.1146/annurev-fluid-122414-034416.

[178] F. Spaepen. "A microscopic mechanism for steady state inhomogeneous flow in metallic glasses". In: *Acta Metallurgica* 25 (1977), pp. 407–415. DOI: 10.1016/0001-6160(77)90232-2.

[179] A. Argon. "Plastic deformation in metallic glasses". In: *Acta Metallurgica* 27 (1979), pp. 47–58. DOI: 10.1016/0001-6160(79)90055-5.

[180] J. Bokeloh et al. "Tracer measurements of atomic diffusion inside shear bands of a bulk metallic glass". In: *Physical review letters* 107 (2011), p. 235503. DOI: 10.1103/PhysRevLett.107.235503.

[181] V. Schmidt et al. "Quantitative Measurement of Density in a Shear Band of Metallic Glass Monitored Along its Propagation Direction". In: *Physical review letters* 115 (2015), p. 035501. DOI: 10.1103/PhysRevLett.115.035501.

[182] R. Besseling et al. "Three-dimensional imaging of colloidal glasses under steady shear". In: *Physical review letters* 99 (2007), p. 028301. DOI: 10.1103/PhysRevLett.99.028301.

[183] T. Divoux et al. “Transient shear banding in a simple yield stress fluid”. In: *Physical review letters* 104 (2010), p. 208301. DOI: 10.1103/PhysRevLett.104.208301.

[184] T. Divoux, C. Barentin, and S. Manneville. “Stress overshoot in a simple yield stress fluid: An extensive study combining rheology and velocimetry”. In: *Soft matter* 7 (2011), p. 9335. DOI: 10.1039/c1sm05740e.

[185] J. D. Martin and Y. Thomas Hu. “Transient and steady-state shear banding in aging soft glassy materials”. In: *Soft matter* 8 (2012), p. 6940. DOI: 10.1039/c2sm25299f.

[186] R. Besseling et al. “Shear banding and flow-concentration coupling in colloidal glasses”. In: *Physical review letters* 105 (2010), p. 268301. DOI: 10.1103/PhysRevLett.105.268301.

[187] J. M. Brader. “Nonlinear rheology of colloidal dispersions”. In: *Journal of physics. Condensed matter : an Institute of Physics journal* 22 (2010), p. 363101. DOI: 10.1088/0953-8984/22/36/363101.

[188] V. Chikkadi et al. “Shear banding of colloidal glasses: Observation of a dynamic first-order transition”. In: *Physical review letters* 113 (2014), p. 208301. DOI: 10.1103/PhysRevLett.113.208301.

[189] I. Fuereder and P. Ilg. “Transient inhomogeneous flow patterns in supercooled liquids under shear”. In: *Soft matter* 13 (2017), pp. 2192–2200. DOI: 10.1039/c7sm00178a.

[190] M. Siebenbürger et al. “Viscoelasticity and shear flow of concentrated, noncrystallizing colloidal suspensions: Comparison with mode-coupling theory”. In: *Journal of Rheology* 53 (2009), pp. 707–726. DOI: 10.1122/1.3093088.

[191] A. Jain et al. “Role of inertia and thixotropy in start-up flows of aging soft materials: Transient dynamics and shear banding in a rate-controlled flow field”. In: *Journal of Rheology* 62 (2018), pp. 1001–1016. DOI: 10.1122/1.5023305.

[192] E. Abbe. “Beiträge zur Theorie des Mikroskops und der mikroskopischen Wahrnehmung”. In: *Archiv für Mikroskopische Anatomie* 9 (1873), pp. 413–418. DOI: 10.1007/BF02956173.

[193] M. Minsky. *U.S. Patent #3013467, Microscopy Apparatus.* 1957.

[194] C. J. Sheppard. “Scanning confocal microscopy”. In: *Encyclopedia of Optical Engineering* (2003).

[195] P. Maßhoff. “Das rheologische Verhalten von Kolloiden in eingeschränkter Geometrie”. Bachelor thesis. Heinrich-Heine-Universität Düsseldorf, 2012.

[196] J. B. Pawley. *Handbook of biological confocal microscopy.* 2nd ed. New York and London: Plenum Press, 1995. ISBN: 0-306-44826-2.

[197] E. Sezgin. “Super-resolution optical microscopy for studying membrane structure and dynamics”. In: *Journal of physics. Condensed matter : an Institute of Physics journal* 29 (2017), p. 273001. DOI: 10.1088/1361-648X/aa7185.

[198] R. H. Webb. "Theoretical basis of confocal microscopy". In: *Confocal Microscopy*. Vol. 307. Methods in enzymology. Elsevier, 1999, pp. 3–20. ISBN: 9780121822088. DOI: 10.1016/S0076-6879(99)07003-2.

[199] S. Inoué. "Foundations of Confocal Scanned Imaging in Light Microscopy". In: *Handbook Of Biological Confocal Microscopy*. Ed. by J. B. Pawley. Boston, MA: Springer US, 2006, pp. 1–19. ISBN: 978-0-387-45524-2. DOI: 10.1007/978-0-387-45524-2_1.

[200] T. H. Besseling, J. Jose, and A. van Blaaderen. "Methods to calibrate and scale axial distances in confocal microscopy as a function of refractive index". In: *Journal of microscopy* 257 (2015), pp. 142–150. DOI: 10.1111/jmi.12194.

[201] F. Giavazzi et al. "Tracking-Free Determination of Single-Cell Displacements and Division Rates in Confluent Monolayers". In: *Frontiers in Physics* 6 (2018), p. 4714. DOI: 10.3389/fphy.2018.00120.

[202] M. K. Cheezum, W. F. Walker, and W. H. Guilford. "Quantitative Comparison of Algorithms for Tracking Single Fluorescent Particles". In: *Biophysical Journal* 81 (2001), pp. 2378–2388. DOI: 10.1016/S0006-3495(01)75884-5.

[203] J. C. Crocker and D. G. Grier. "Methods of Digital Video Microscopy for Colloidal Studies". In: *Journal of Colloid and Interface Science* 179 (1996), pp. 298–310. DOI: 10.1006/jcis.1996.0217.

[204] J. C. Crocker and E. R. Weeks. *Particle tracking using IDL*. URL: http://www.physics.emory.edu/faculty/weeks//idl/ (visited on 02/18/2015).

[205] Y. Gao and M. L. Kilfoil. "Accurate detection and complete tracking of large populations of features in three dimensions". In: *Optics Express* 17 (2009), p. 4685. DOI: 10.1364/OE.17.004685.

[206] M. C. Jenkins and S. U. Egelhaaf. "Confocal microscopy of colloidal particles: Towards reliable, optimum coordinates". In: *Advances in colloid and interface science* 136 (2008), pp. 65–92. DOI: 10.1016/j.cis.2007.07.006.

[207] R. Besseling et al. "Quantitative imaging of colloidal flows". In: *Advances in colloid and interface science* 146 (2009), pp. 1–17. DOI: 10.1016/j.cis.2008.09.008.

[208] M. H. G. Duits, S. Ghosh, and F. Mugele. "Measuring advection and diffusion of colloids in shear flow". In: *Langmuir : the ACS journal of surfaces and colloids* 31 (2015), pp. 5689–5700. DOI: 10.1021/acs.langmuir.5b01369.

[209] M. Leocmach and H. Tanaka. "A novel particle tracking method with individual particle size measurement and its application to ordering in glassy hard sphere colloids". In: *Soft matter* 9 (2013), pp. 1447–1457. DOI: 10.1039/C2SM27107A.

[210] C. van der Wel and D. J. Kraft. "Automated tracking of colloidal clusters with sub-pixel accuracy and precision". In: *Journal of physics. Condensed matter : an Institute of Physics journal* 29 (2017), p. 044001. DOI: 10.1088/1361-648X/29/4/044001.

[211] D. Allan et al. *Trackpy: Trackpy V0.3.2*. 2016. DOI: 10.5281/zenodo.60550.

[212] M. Bierbaum et al. “Light Microscopy at Maximal Precision”. In: *Physical Review X* 7 (2017), p. 81. DOI: 10.1103/PhysRevX.7.041007.

[213] R. Kurita, D. B. Ruffner, and E. R. Weeks. “Measuring the size of individual particles from three-dimensional imaging experiments”. In: *Nature communications* 3 (2012), p. 1127. DOI: 10.1038/ncomms2114.

[214] G. Petekidis et al. “Shear-induced yielding and ordering in concentrated particle suspensions”. In: *Physica A: Statistical Mechanics and its Applications* 306 (2002), pp. 334–342. DOI: 10.1016/S0378-4371(02)00510-1.

[215] J. Zausch et al. “From equilibrium to steady state: The transient dynamics of colloidal liquids under shear”. In: *Journal of Physics: Condensed Matter* 20 (2008), p. 404210. DOI: 10.1088/0953-8984/20/40/404210.

[216] P. A. Smith. “Colloidal Gels under Oscillatory Shear”. Dissertation. Edinburgh: University of Edinburgh, 2004. URL: http://hdl.handle.net/1842/11924.

[217] P. Maßhoff. “Konstruktion und Test eines Rheoskops zur gleichzeitigen Durchführung von konfokaler Mikroskopie und Rheologie”. Master thesis. Düsseldorf: Heinrich Heine University Düsseldorf, 2014.

[218] E. D. Knowlton, D. J. Pine, and L. Cipelletti. “A microscopic view of the yielding transition in concentrated emulsions”. In: *Soft matter* 10 (2014), pp. 6931–6940. DOI: 10.1039/c4sm00531g.

[219] A. Schofield. *https://www2.ph.ed.ac.uk/~abs/, 24.06.2018.*

[220] N. Koumakis et al. “Direct comparison of the rheology of model hard and soft particle glasses”. In: *Soft matter* 8 (2012), p. 4271. DOI: 10.1039/c2sm07113d.

[221] T. Sentjabrskaja et al. “Yielding of binary colloidal glasses”. In: *Soft matter* 9 (2013), p. 4524. DOI: 10.1039/C3SM27903K.

[222] D. Derks et al. “Confocal microscopy of colloidal dispersions in shear flow using a counter-rotating cone–plate shear cell”. In: *Journal of Physics: Condensed Matter* 16 (2004), S3917–S3927. DOI: 10.1088/0953-8984/16/38/010.

[223] I. Cohen et al. “Slip, yield, and bands in colloidal crystals under oscillatory shear”. In: *Physical review letters* 97 (2006), p. 215502. DOI: 10.1103/PhysRevLett.97.215502.

[224] C. Patrick Royall et al. “Direct observation of a local structural mechanism for dynamic arrest”. In: *Nature materials* 7 (2008), pp. 556–561. DOI: 10.1038/nmat2219.

[225] T. H. Besseling et al. “Oscillatory shear-induced 3D crystalline order in colloidal hard-sphere fluids”. In: *Soft matter* 8 (2012), p. 6931. DOI: 10.1039/c2sm07156h.

[226] I. Ríos de Anda et al. “Long-lived non-equilibrium interstitial solid solutions in binary mixtures”. In: *The Journal of Chemical Physics* 147 (2017), p. 124504. DOI: 10.1063/1.4985917.

[227] M. Hassani et al. "Long-range strain correlations in 3D quiescent glass forming liquids". In: *EPL (Europhysics Letters)* 124 (2018), p. 18003. DOI: 10.1209/0295-5075/124/18003.

[228] M. D. Haw, W. C. K. Poon, and P. N. Pusey. "Direct observation of oscillatory-shear-induced order in colloidal suspensions". In: *Physical Review E* 57 (1998), pp. 6859–6864. DOI: 10.1103/PhysRevE.57.6859.

[229] A. I. Campbell and P. Bartlett. "Fluorescent Hard-Sphere Polymer Colloids for Confocal Microscopy". In: *Journal of Colloid and Interface Science* 256 (2002), pp. 325–330. DOI: 10.1006/jcis.2002.8669.

[230] F. Varnik et al. "Correlations of plasticity in sheared glasses". In: *Physical review. E, Statistical, nonlinear, and soft matter physics* 89 (2014), p. 040301. DOI: 10.1103/PhysRevE.89.040301.

[231] A. Ghosh et al. "Direct Observation of Percolation in the Yielding Transition of Colloidal Glasses". In: *Physical review letters* 118 (2017), p. 148001. DOI: 10.1103/PhysRevLett.118.148001.

[232] T. Sentjabrskaja et al. "Creep and flow of glasses: Strain response linked to the spatial distribution of dynamical heterogeneities". In: *Scientific reports* 5 (2015), p. 11884. DOI: 10.1038/srep11884.

[233] E. Lázaro-Lázaro et al. "Glassy dynamics in asymmetric binary mixtures of hard spheres". In: *Physical review. E* 99 (2019), p. 042603. DOI: 10.1103/PhysRevE.99.042603.

[234] M. Leocmach and H. Tanaka. "Roles of icosahedral and crystal-like order in the hard spheres glass transition". In: *Nature communications* 3 (2012), p. 974. DOI: 10.1038/ncomms1974.

[235] L. C. Hsiao et al. "Role of shear-induced dynamical heterogeneity in the nonlinear rheology of colloidal gels". In: *Soft matter* 10 (2014), pp. 9254–9259. DOI: 10.1039/c4sm01375a.

[236] N. Y. C. Lin and I. Cohen. "Relating microstructure and particle-level stress in colloidal crystals under increased confinement". In: *Soft matter* 12 (2016), pp. 9058–9067. DOI: 10.1039/c6sm02079h.

[237] M. C. Jenkins. "Quantitative confocal microscopy of dense colloidal systems". Ph.D. thesis. University of Edinburgh, 2006. URL: http://hdl.handle.net/1842/1347.

[238] D. Heckendorf et al. "Size-Dependent Localization in Polydisperse Colloidal Glasses". In: *Physical review letters* 119 (2017), p. 048003. DOI: 10.1103/PhysRevLett.119.048003.

[239] Y. L. Wu et al. "Melting and crystallization of colloidal hard-sphere suspensions under shear". In: *Proceedings of the National Academy of Sciences of the United States of America* 106 (2009), pp. 10564–10569. DOI: 10.1073/pnas.0812519106.

[240] G. Bryant et al. “How hard is a colloidal "hard-sphere" interaction?” In: *Physical review. E, Statistical, nonlinear, and soft matter physics* 66 (2002), p. 060501. DOI: 10.1103/PhysRevE.66.060501.

[241] S. Weyhe. *Wägetechnik im Labor: Technologie und Anwendung*. Vol. Bd. 4. Die Bibliothek der Wissenschaft. Landsberg/Lech: Verl. Moderne Industrie, 1997. ISBN: 3-478-93160-6.

[242] M. Leocmach. *The colloid toolkit*. 2015. DOI: 10.5281/zenodo.31286.

[243] A. Stukowski. “Visualization and analysis of atomistic simulation data with OVITO–the Open Visualization Tool”. In: *Modelling and Simulation in Materials Science and Engineering* 18 (2010), p. 015012. DOI: 10.1088/0965-0393/18/1/015012.

[244] J. Olafsen. *Experimental and Computational Techniques in Soft Condensed Matter Physics*. Cambridge: Cambridge University Press, 2010. ISBN: 9780511760549. DOI: 10.1017/CBO9780511760549.

[245] D. Chen et al. “Microscopic structural relaxation in a sheared supercooled colloidal liquid”. In: *Physical review. E, Statistical, nonlinear, and soft matter physics* 81 (2010), p. 011403. DOI: 10.1103/PhysRevE.81.011403.

[246] D. S. Martin, M. B. Forstner, and J. A. Käs. “Apparent Subdiffusion Inherent to Single Particle Tracking”. In: *Biophysical Journal* 83 (2002), pp. 2109–2117. DOI: 10.1016/S0006-3495(02)73971-4.

[247] I. E. Abdou. “Practical approach to the registration of multiple frames of video images”. In: *IS&T/SPIE Conference on Visual Communications and Image Processing '99*. San Jose, California, 1999, pp. 371–382. DOI: 10.1117/12.334685.

[248] J. P. Lewis. “Fast Template Matching”. In: *Vision Interface '95*. Ed. by Laurendeau, D. and Cédras, C. Canadian Image Processing and Pattern Recognition Society, 1995, pp. 120–123.

[249] E. Gladilin and R. Eils. “On the role of spatial phase and phase correlation in vision, illusion, and cognition”. In: *Frontiers in computational neuroscience* 9 (2015), p. 45. DOI: 10.3389/fncom.2015.00045.

[250] A. Kaso. “Computation of the normalized cross-correlation by fast Fourier transform”. In: *PloS one* 13 (2018), e0203434. DOI: 10.1371/journal.pone.0203434.

[251] B. Pan, H. Xie, and Z. Wang. “Equivalence of digital image correlation criteria for pattern matching”. In: *Applied Optics* 49 (2010), pp. 5501–5509. DOI: 10.1364/AO.49.005501.

[252] B. Utter and R. P. Behringer. “Experimental measures of affine and nonaffine deformation in granular shear”. In: *Physical Review Letters* 100 (2008), p. 208302. DOI: 10.1103/PhysRevLett.100.208302.

[253] R. M. Lee et al. “Quantifying stretching and rearrangement in epithelial sheet migration”. In: *New journal of physics* 15 (2013). DOI: 10.1088/1367-2630/15/2/025036.

[254] P. Schall et al. “Visualizing dislocation nucleation by indenting colloidal crystals”. In: *Nature* 440 (2006), pp. 319–323. DOI: 10.1038/nature04557.

[255] P. Schall, D. A. Weitz, and F. Spaepen. “Structural rearrangements that govern flow in colloidal glasses”. In: *Science (New York, N.Y.)* 318 (2007), pp. 1895–1899. DOI: 10.1126/science.1149308.

[256] A. van Blaaderen and P. Wiltzius. “Real-Space Structure of Colloidal Hard-Sphere Glasses”. In: *Science* 270 (1995), pp. 1177–1179. DOI: 10.1126/science.270.5239.1177.

[257] I. Buttinoni et al. “Colloidal polycrystalline monolayers under oscillatory shear”. In: *Physical review. E* 95 (2017), p. 012610. DOI: 10.1103/PhysRevE.95.012610.

[258] W. Mickel et al. “Shortcomings of the bond orientational order parameters for the analysis of disordered particulate matter”. In: *The Journal of Chemical Physics* 138 (2013), p. 044501. DOI: 10.1063/1.4774084.

[259] M. O’Keeffe. “A proposed rigorous definition of coordination number”. In: *Acta Crystallographica Section A: Crystal Physics, Diffraction, Theoretical and General Crystallography* 35 (1979), pp. 772–775. DOI: 10.1107/S0567739479001765.

[260] A. Malins et al. “Identification of structure in condensed matter with the topological cluster classification”. In: *The Journal of Chemical Physics* 139 (2013), p. 234506. DOI: 10.1063/1.4832897.

[261] J. Haeberle, M. Sperl, and P. Born. *Distinguishing noisy crystalline structures using bond orientational order parameters*. arXiv: 1906.08111.

[262] W. Brostow, J.-P. Dussault, and B. L. Fox. “Construction of Voronoi polyhedra”. In: *Journal of Computational Physics* 29 (1978), pp. 81–92. DOI: 10.1016/0021-9991(78)90110-9.

[263] M. Laurati et al. “Long-Lived Neighbors Determine the Rheological Response of Glasses”. In: *Physical review letters* 118 (2017), p. 018002. DOI: 10.1103/PhysRevLett.118.018002.

[264] C. H. Rycroft. “VORO++: A three-dimensional voronoi cell library in C++”. In: *Chaos (Woodbury, N.Y.)* 19 (2009), p. 041111. DOI: 10.1063/1.3215722.

[265] P. J. Steinhardt, D. R. Nelson, and M. Ronchetti. “Bond-orientational order in liquids and glasses”. In: *Physical Review B* 28 (1983), pp. 784–805. DOI: 10.1103/PhysRevB.28.784.

[266] W. Lechner and C. Dellago. “Accurate determination of crystal structures based on averaged local bond order parameters”. In: *The Journal of Chemical Physics* 129 (2008), p. 114707. DOI: 10.1063/1.2977970.

[267] A. Stukowski. “Structure identification methods for atomistic simulations of crystalline materials”. In: *Modelling and Simulation in Materials Science and Engineering* 20 (2012), p. 045021. DOI: 10.1088/0965-0393/20/4/045021.

[268] P. Rein ten Wolde, M. J. Ruiz–Montero, and D. Frenkel. "Numerical calculation of the rate of crystal nucleation in a Lennard–Jones system at moderate undercooling". In: *The Journal of Chemical Physics* 104 (1996), pp. 9932–9947. DOI: 10.1063/1.471721.

[269] W. Brostow et al. "Voronoi polyhedra and Delaunay simplexes in the structural analysis of molecular-dynamics-simulated materials". In: *Physical Review B* 57 (1998), pp. 13448–13458. DOI: 10.1103/PhysRevB.57.13448.

[270] H. S. M. Coxeter. *Introduction to geometry*. 2nd ed. New York and Chichester: Wiley, 1969. ISBN: 9780471182832.

[271] G. Racah. "Theory of Complex Spectra. I". In: *Physical Review* 61 (1942), pp. 186–197. DOI: 10.1103/PhysRev.61.186.

[272] G. Racah. "Theory of Complex Spectra. II". In: *Physical Review* 62 (1942), pp. 438–462. DOI: 10.1103/PhysRev.62.438.

[273] L. Landau and E. Lifshitz. "Quantum mechanics, vol. 3". In: *Course of theoretical physics* 3 (1977).

[274] P. K. Bommineni et al. "Complex Crystals from Size-Disperse Spheres". In: *Physical Review Letters* 122 (2019). DOI: 10.1103/PhysRevLett.122.128005.

[275] S. Martin, G. Bryant, and W. van Megen. "Crystallization kinetics of polydisperse colloidal hard spheres. II. Binary mixtures". In: *Physical review. E, Statistical, nonlinear, and soft matter physics* 71 (2005), p. 021404. DOI: 10.1103/PhysRevE.71.021404.

[276] S. Mader. "Metastable Alloy Films". In: *Journal of Vacuum Science and Technology* 2 (1965), pp. 35–41. DOI: 10.1116/1.1492396.

[277] A. S. Nowick and S. R. Mader. "A Hard-Sphere Model to Simulate Alloy Thin Films". In: *IBM Journal of Research and Development* 9 (1965), pp. 358–374. DOI: 10.1147/rd.95.0358.

[278] W. Kob and H. C. Andersen. "Testing mode-coupling theory for a supercooled binary Lennard-Jones mixture I: The van Hove correlation function". In: *Physical Review E* 51 (1995), pp. 4626–4641. DOI: 10.1103/PhysRevE.51.4626.

[279] A. B. Schofield. "Binary hard-sphere crystals with the cesium chloride structure". In: *Physical review. E, Statistical, nonlinear, and soft matter physics* 64 (2001), p. 051403. DOI: 10.1103/PhysRevE.64.051403.

[280] T. Hamanaka and A. Onuki. "Transitions among crystal, glass, and liquid in a binary mixture with changing particle-size ratio and temperature". In: *Physical review. E, Statistical, nonlinear, and soft matter physics* 74 (2006), p. 011506. DOI: 10.1103/PhysRevE.74.011506.

[281] D. J. Koeze et al. "Mapping the jamming transition of bidisperse mixtures". In: *EPL (Europhysics Letters)* 113 (2016), p. 54001. DOI: 10.1209/0295-5075/113/54001.

[282] B. J. Ackerson and P. N. Pusey. "Shear-induced order in suspensions of hard spheres". In: *Physical review letters* 61 (1988), pp. 1033–1036. DOI: 10.1103/PhysRevLett.61.1033.

[283] A. V. Mokshin and J.-L. Barrat. "Shear-induced crystallization of an amorphous system". In: *Physical review. E, Statistical, nonlinear, and soft matter physics* 77 (2008), p. 021505. DOI: 10.1103/PhysRevE.77.021505.

[284] A. V. Mokshin and J.-L. Barrat. "Shear induced structural ordering of a model metallic glass". In: *The Journal of Chemical Physics* 130 (2009), p. 034502. DOI: 10.1063/1.3058433.

[285] B. J. Ackerson. "Shear induced order of hard sphere suspensions". In: *Journal of Physics: Condensed Matter* 2 (1990), SA389–SA392. DOI: 10.1088/0953-8984/2/S/061.

[286] F. R. Molino et al. "Identification of flow mechanisms for a soft crystal". In: *The European Physical Journal B* 3 (1998), pp. 59–72. DOI: 10.1007/s100510050284.

[287] N. Duff and D. J. Lacks. "Shear-induced crystallization in jammed systems". In: *Physical review. E, Statistical, nonlinear, and soft matter physics* 75 (2007), p. 031501. DOI: 10.1103/PhysRevE.75.031501.

[288] T. Kanai et al. "Air-Pulse-Drive Fabrication of Photonic Crystal Films of Colloids with High Spectral Quality". In: *Advanced Functional Materials* 15 (2005), pp. 25–29. DOI: 10.1002/adfm.200305160.

[289] A. Imhof, A. van Blaaderen, and J. K. G. Dhont. "Shear Melting of Colloidal Crystals of Charged Spheres Studied with Rheology and Polarizing Microscopy". In: *Langmuir* 10 (1994), pp. 3477–3484. DOI: 10.1021/la00022a020.

[290] P. Panine et al. "Structure and rheology during shear-induced crystallization of a latex suspension". In: *Physical review. E, Statistical, nonlinear, and soft matter physics* 66 (2002), p. 022401. DOI: 10.1103/PhysRevE.66.022401.

[291] L. B. Chen et al. "Structural changes and orientaional order in a sheared colloidal suspension". In: *Physical review letters* 69 (1992), pp. 688–691. DOI: 10.1103/PhysRevLett.69.688.

[292] L. B. Chen, B. J. Ackerson, and C. F. Zukoski. "Rheological consequences of microstructural transitions in colloidal crystals". In: *Journal of Rheology* 38 (1994), pp. 193–216. DOI: 10.1122/1.550498.

[293] I. Biazzo et al. "Theory of amorphous packings of binary mixtures of hard spheres". In: *Physical Review Letters* 102 (2009), p. 195701. DOI: 10.1103/PhysRevLett.102.195701.

[294] N. Y. C. Lin et al. "Tunable shear thickening in suspensions". In: *Proceedings of the National Academy of Sciences of the United States of America* 113 (2016), pp. 10774–10778. DOI: 10.1073/pnas.1608348113.

[295] S. R. Williams, C. P. Royall, and G. Bryant. "Crystallization of dense binary hard-sphere mixtures with marginal size ratio". In: *Physical Review Letters* 100 (2008), p. 225502. DOI: 10.1103/PhysRevLett.100.225502.

[296] X. Cottin and P. A. Monson. "A cell theory for solid solutions: Application to hard sphere mixtures". In: *The Journal of Chemical Physics* 99 (1993), pp. 8914–8921. DOI: 10.1063/1.465560.

[297] M. Ozawa, G. Parisi, and L. Berthier. "Configurational entropy of polydisperse supercooled liquids". In: *The Journal of Chemical Physics* 149 (2018), p. 154501. DOI: 10.1063/1.5040975.

[298] P. Bartlett. "Fractionated crystallization in a polydisperse mixture of hard spheres". In: *The Journal of Chemical Physics* 109 (1998), pp. 10970–10975. DOI: 10.1063/1.477753.

[299] P. Sollich and N. B. Wilding. "Crystalline phases of polydisperse spheres". In: *Physical review letters* 104 (2010), p. 118302. DOI: 10.1103/PhysRevLett.104.118302.

[300] W. van Megen and S. M. Underwood. "Change in crystallization mechanism at the glass transition of colloidal spheres". In: *Nature* 362 (1993), pp. 616–618. DOI: 10.1038/362616a0.

[301] W. G. T. Kranendonk and D. Frenkel. "Computer simulation of solid-liquid coexistence in binary hard-sphere mixtures". In: *Journal of Physics: Condensed Matter* 1 (1989), pp. 7735–7739. DOI: 10.1088/0953-8984/1/41/026.

[302] J. D. Bernal. "A Geometrical Approach to the Structure Of Liquids". In: *Nature* 183 (1959), pp. 141–147. DOI: 10.1038/183141a0.

[303] T. Egami. "Universal criterion for metallic glass formation". In: *Materials Science and Engineering: A* 226-228 (1997), pp. 261–267. DOI: 10.1016/S0921-5093(97)80041-X.

[304] M. L. Mansfield, L. Rakesh, and D. A. Tomalia. "The random parking of spheres on spheres". In: *The Journal of Chemical Physics* 105 (1996), pp. 3245–3249. DOI: 10.1063/1.472166.

[305] S. J. Smithline and A. D. J. Haymet. "Density functional theory for the freezing of 1: 1 hard sphere mixtures". In: *The Journal of Chemical Physics* 86 (1987), pp. 6486–6494. DOI: 10.1063/1.452439.

[306] D. J. Pine et al. "Chaos and threshold for irreversibility in sheared suspensions". In: *Nature* 438 (2005), pp. 997–1000. DOI: 10.1038/nature04380.

[307] N. Y. C. Lin et al. "Far-from-equilibrium sheared colloidal liquids: Disentangling relaxation, advection, and shear-induced diffusion". In: *Physical review. E, Statistical, nonlinear, and soft matter physics* 88 (2013), p. 062309. DOI: 10.1103/PhysRevE.88.062309.

[308] G. Petekidis, A. Moussaïd, and P. N. Pusey. "Rearrangements in hard-sphere glasses under oscillatory shear strain". In: *Physical review. E, Statistical, nonlinear, and soft matter physics* 66 (2002), p. 051402. DOI: 10.1103/PhysRevE.66.051402.

[309] I. Regev, T. Lookman, and C. Reichhardt. "Onset of irreversibility and chaos in amorphous solids under periodic shear". In: *Physical review. E, Statistical, nonlinear, and soft matter physics* 88 (2013), p. 062401. DOI: 10.1103/PhysRevE.88.062401.

[310] P. Hébraud et al. "Yielding and Rearrangements in Disordered Emulsions". In: *Physical Review Letters* 78 (1997), pp. 4657–4660. DOI: 10.1103/PhysRevLett.78.4657.

[311] X. Qiu et al. "Self-diffusion of interacting colloids far from equilibrium". In: *Physical review letters* 61 (1988), pp. 2554–2557. DOI: 10.1103/PhysRevLett.61.2554.

[312] C. W. Lee and S. A. Rogers. "A sequence of physical processes quantified in LAOS by continuous local measures". In: *Korea-Australia Rheology Journal* 29 (2017), pp. 269–279. DOI: 10.1007/s13367-017-0027-x.

[313] B. J. Ackerson. "Shear induced order and shear processing of model hard sphere suspensions". In: *Journal of Rheology* 34 (1990), pp. 553–590. DOI: 10.1122/1.550096.

[314] T. Palberg. "Crystallization kinetics of repulsive colloidal spheres". In: *Journal of Physics: Condensed Matter* 11 (1999), R323–R360. DOI: 10.1088/0953-8984/11/28/201.

[315] IDL Astronomy Library. URL: https://github.com/wlandsman/IDLAstro.git (visited on 02/18/2015).

[316] K. Miyazaki et al. "Nonlinear viscoelasticity of metastable complex fluids". In: *EPL (Europhysics Letters)* 75 (2006), pp. 915–921. DOI: 10.1209/epl/i2006-10203-9.

[317] N. Koumakis. "A study on the effects of interparticle interactions on the dynamics, rheology and aging of colloidal systems out of equilibrium". PhD thesis. Greece: University of Crete, 2011. URL: http://hdl.handle.net/10442/hedi/30129.

[318] D. Fiocco, G. Foffi, and S. Sastry. "Oscillatory athermal quasistatic deformation of a model glass". In: *Physical review. E, Statistical, nonlinear, and soft matter physics* 88 (2013), p. 020301. DOI: 10.1103/PhysRevE.88.020301.

[319] W. van Megen and Underwood. "Glass transition in colloidal hard spheres: Mode-coupling theory analysis". In: *Physical review letters* 70 (1993), pp. 2766–2769. DOI: 10.1103/PhysRevLett.70.2766.

[320] J. M. Brader et al. "Glass rheology: From mode-coupling theory to a dynamical yield criterion". In: *Proceedings of the National Academy of Sciences of the United States of America* 106 (2009), pp. 15186–15191. DOI: 10.1073/pnas.0905330106.

[321] P. Sollich. "Rheological constitutive equation for a model of soft glassy materials". In: *Physical Review E* 58 (1998), pp. 738–759. DOI: 10.1103/PhysRevE.58.738.

[322] M. Priya and T. Voigtmann. "Nonlinear rheology of dense colloidal systems with short-ranged attraction: A mode-coupling theory analysis". In: *Journal of Rheology* 58 (2014), pp. 1163–1187. DOI: 10.1122/1.4871474.

[323] C. P. Amann et al. "Shear-induced breaking of cages in colloidal glasses: Scattering experiments and mode coupling theory". In: *The Journal of Chemical Physics* 143 (2015), p. 034505. DOI: 10.1063/1.4926932.

[324] J. F. Brady. "The rheological behavior of concentrated colloidal dispersions". In: *The Journal of Chemical Physics* 99 (1993), pp. 567–581. DOI: 10.1063/1.465782.

[325] F. Varnik. "Structural relaxation and rheological response of a driven amorphous system". In: *The Journal of Chemical Physics* 125 (2006), p. 164514. DOI: 10.1063/1.2363998.

[326] D. R. Foss and J. F. Brady. "Structure, diffusion and rheology of Brownian suspensions by Stokesian Dynamics simulation". In: *Journal of Fluid Mechanics* 407 (2000), pp. 167–200. DOI: 10.1017/S0022112099007557.

[327] N. Koumakis et al. "Start-up shear of concentrated colloidal hard spheres: Stresses, dynamics, and structure". In: *Journal of Rheology* 60 (2016), pp. 603–623. DOI: 10.1122/1.4949340.

[328] G. P. Shrivastav, P. Chaudhuri, and J. Horbach. "Yielding of glass under shear: A directed percolation transition precedes shear-band formation". In: *Physical review. E* 94 (2016), p. 042605. DOI: 10.1103/PhysRevE.94.042605.

[329] A. Nicolas, J. Rottler, and J. L. Barrat. "Spatiotemporal correlations between plastic events in the shear flow of athermal amorphous solids". In: *The European physical journal. E, Soft matter* 37 (2014), p. 9. DOI: 10.1140/epje/i2014-14050-1.

[330] G. Picard et al. "Simple model for heterogeneous flows of yield stress fluids". In: *Physical review. E, Statistical, nonlinear, and soft matter physics* 66 (2002), p. 051501. DOI: 10.1103/PhysRevE.66.051501.

[331] S. A. Rogers, D. Vlassopoulos, and P. T. Callaghan. "Aging, yielding, and shear banding in soft colloidal glasses". In: *Physical Review Letters* 100 (2008), p. 128304. DOI: 10.1103/PhysRevLett.100.128304.

[332] P. G. Rognon et al. "Long-range wall perturbations in dense granular flows". In: *Journal of Fluid Mechanics* 764 (2015), pp. 171–192. DOI: 10.1017/jfm.2014.707.

[333] J. L. Schrag. "Deviation of Velocity Gradient Profiles from the "Gap Loading" and "Surface Loading" Limits in Dynamic Simple Shear Experiments". In: *Transactions of the Society of Rheology* 21 (1977), pp. 399–413. DOI: 10.1122/1.549445.

[334] J. L. Barrat. "Ageing, rheology and effective temperature in a glass-forming system". In: *Journal of Physics: Condensed Matter* 15 (2003), S1–S9. DOI: 10.1088/0953-8984/15/1/301.

[335] S. M. Fielding, P. Sollich, and M. E. Cates. "Aging and rheology in soft materials". In: *Journal of Rheology* 44 (2000), pp. 323–369. DOI: 10.1122/1.551088.

[336] C. Christopoulou et al. "Ageing and yield behaviour in model soft colloidal glasses". In: *Philosophical transactions. Series A, Mathematical, physical, and engineering sciences* 367 (2009), pp. 5051–5071. DOI: 10.1098/rsta.2009.0166.

[337] N. Koumakis, A. B. Schofield, and G. Petekidis. "Effects of shear induced crystallization on the rheology and ageing of hard sphere glasses". In: *Soft matter* 4 (2008), p. 2008. DOI: 10.1039/b805171b.

[338] R. L. Moorcroft, M. E. Cates, and S. M. Fielding. "Age-dependent transient shear banding in soft glasses". In: *Physical review letters* 106 (2011), p. 055502. DOI: 10.1103/PhysRevLett.106.055502.

[339] S. Patinet, D. Vandembroucq, and M. L. Falk. "Connecting Local Yield Stresses with Plastic Activity in Amorphous Solids". In: *Physical review letters* 117 (2016), p. 045501. DOI: 10.1103/PhysRevLett.117.045501.

[340] F. Varnik et al. "Shear localization in a model glass". In: *Physical review letters* 90 (2003), p. 095702. DOI: 10.1103/PhysRevLett.90.095702.

[341] J. K. G. Dhont et al. "Nonuniform flow in soft glasses of colloidal rods". In: *Physical Review Fluids* 2 (2017), p. 291. DOI: 10.1103/PhysRevFluids.2.043301.

[342] M. A. Fardin et al. "Shear-banding in wormlike micelles: Beware of elastic instabilities". In: *Journal of Rheology* 60 (2016), pp. 917–926. DOI: 10.1122/1.4960333.

[343] A. Fall et al. "Shear thickening and migration in granular suspensions". In: *Physical review letters* 105 (2010), p. 268303. DOI: 10.1103/PhysRevLett.105.268303.

[344] S. Mandal et al. "Heterogeneous shear in hard sphere glasses". In: *Physical review letters* 108 (2012), p. 098301. DOI: 10.1103/PhysRevLett.108.098301.

[345] M. D. Haw et al. "Colloidal glasses under shear strain". In: *Physical Review E* 58 (1998), pp. 4673–4682. DOI: 10.1103/PhysRevE.58.4673.

[346] N. Koumakis, J. F. Brady, and G. Petekidis. "Amorphous and ordered states of concentrated hard spheres under oscillatory shear". In: *Journal of Non-Newtonian Fluid Mechanics* 233 (2016), pp. 119–132. DOI: 10.1016/j.jnnfm.2016.02.004.

[347] S. E. Paulin, B. J. Ackerson, and M. S. Wolfe. "Microstructure-dependent viscosity in concentrated suspensions of soft spheres". In: *Physical Review E* 55 (1997), pp. 5812–5819. DOI: 10.1103/PhysRevE.55.5812.

[348] C. A. Schuh and T. G. Nieh. "A survey of instrumented indentation studies on metallic glasses". In: *Journal of Materials Research* 19 (2004), pp. 46–57. DOI: 10.1557/jmr.2004.19.1.46.

[349] G. Subhash et al. "Recent Advances in Dynamic Indentation Fracture, Impact Damage and Fragmentation of Ceramics". In: *Journal of the American Ceramic Society* 91 (2008), pp. 2777–2791. DOI: 10.1111/j.1551-2916.2008.02624.x.

[350] N. K. Mukhopadhyay and P. Paufler. "Micro- and nanoindentation techniques for mechanical characterisation of materials". In: *International Materials Reviews* 51 (2013), pp. 209–245. DOI: 10.1179/174328006X102475.

[351] C. A. Schuh. “Nanoindentation studies of materials”. In: *Materials Today* 9 (2006), pp. 32–40. DOI: 10.1016/S1369-7021(06)71495-X.

[352] M. Roth et al. “Colloidal aggregates tested via nanoindentation and quasi-simultaneous 3D imaging”. In: *The European physical journal. E, Soft matter* 35 (2012), p. 124. DOI: 10.1140/epje/i2012-12124-8.

[353] P. Schall and F. Spaepen. “Chapter 96 Dislocations in Colloidal Crystals”. In: vol. 16. Dislocations in Solids. Elsevier, 2010, pp. 233–261. ISBN: 9780444534439. DOI: 10.1016/S1572-4859(09)01605-2.

[354] Y. Rahmani et al. “Probing incipient plasticity by indenting colloidal glasses”. In: *Scientific reports* 3 (2013), p. 1064. DOI: 10.1038/srep01064.

[355] Y. Rahmani et al. “Visualizing the strain evolution during the indentation of colloidal glasses”. In: *Physical review. E, Statistical, nonlinear, and soft matter physics* 89 (2014), p. 012304. DOI: 10.1103/PhysRevE.89.012304.

[356] E. M. Ahmed. “Hydrogel: Preparation, characterization, and applications: A review”. In: *Journal of advanced research* 6 (2015), pp. 105–121. DOI: 10.1016/j.jare.2013.07.006.

[357] E. Caló and V. V. Khutoryanskiy. “Biomedical applications of hydrogels: A review of patents and commercial products”. In: *European Polymer Journal* 65 (2015), pp. 252–267. DOI: 10.1016/j.eurpolymj.2014.11.024.

[358] J. Malda et al. “25th anniversary article: Engineering hydrogels for biofabrication”. In: *Advanced materials (Deerfield Beach, Fla.)* 25 (2013), pp. 5011–5028. DOI: 10.1002/adma.201302042.

[359] O. Okay. “General Properties of Hydrogels”. In: *Hydrogel Sensors and Actuators: Engineering and Technology*. Ed. by G. Gerlach and K.-F. Arndt. Berlin, Heidelberg: Springer Berlin Heidelberg, 2010, pp. 1–14. ISBN: 978-3-540-75645-3. DOI: 10.1007/978-3-540-75645-3_1.

[360] P. H. J. Kouwer et al. “Responsive biomimetic networks from polyisocyanopeptide hydrogels”. In: *Nature* 493 (2013), pp. 651–655. DOI: 10.1038/nature11839.

[361] J. Brink et al. “Simultaneous analysis of the structural and mechanical changes during large deformation of whey protein isolate/gelatin gels at the macro and micro levels”. In: *Food Hydrocolloids* 21 (2007), pp. 409–419. DOI: 10.1016/j.foodhyd.2006.04.012.

[362] R. C. Arevalo et al. “Stress heterogeneities in sheared type-I collagen networks revealed by Boundary Stress Microscopy”. In: *PloS one* 10 (2015), e0118021. DOI: 10.1371/journal.pone.0118021.

[363] T. Divoux, C. Barentin, and S. Manneville. “Stress overshoot in a simple yield stress fluid: An extensive study combining rheology and velocimetry”. In: *Soft matter* 7 (2011), p. 9335. DOI: 10.1039/c1sm05740e.

[364] R. Dasgupta et al. “Shear localization in three-dimensional amorphous solids”. In: *Physical review. E, Statistical, nonlinear, and soft matter physics* 88 (2013), p. 032401. DOI: 10.1103/PhysRevE.88.032401.

[365] M. Bouzid et al. “Elastically driven intermittent microscopic dynamics in soft solids”. In: *Nature communications* 8 (2017), p. 15846. DOI: 10.1038/ncomms15846.

[366] J. Maitra and V. K. Shukla. “Cross-linking in Hydrogels - A Review”. In: *American Journal of Polymer Science* 4 (2014), pp. 25–31.

[367] S. Sathaye et al. “Rheology of peptide- and protein-based physical hydrogels: Are everyday measurements just scratching the surface?” In: *Wiley interdisciplinary reviews. Nanomedicine and nanobiotechnology* 7 (2015), pp. 34–68. DOI: 10.1002/wnan.1299.

[368] J. Läuger and H. Stettin. “Differences between stress and strain control in the non-linear behavior of complex fluids”. In: *Rheologica Acta* 49 (2010), pp. 909–930. DOI: 10.1007/s00397-010-0450-0.